

Searching for a Dark Photon in the HPS Experiment

Sebouh Jacob Paul

Vienna, Virginia

Master of Science, Christopher Newport University, 2012  
Bachelor of Science, Christopher Newport University, 2010

A Dissertation presented to the Graduate Faculty  
of The College of William & Mary in Candidacy for the Degree of  
Doctor of Philosophy

Department of Physics

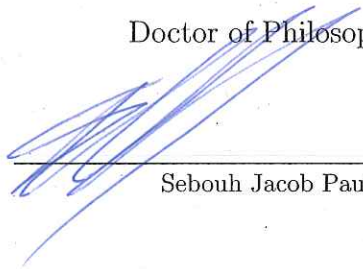
College of William & Mary  
May 2018



## APPROVAL PAGE

This Dissertation is submitted in partial fulfillment of  
the requirements for the degree of

Doctor of Philosophy



---

Sebouh Jacob Paul

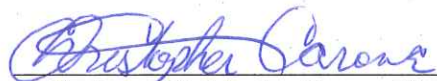
Approved by the Committee, March 2018



---

Committee Chair

Professor Keith Griffioen, Physics  
College of William & Mary



---

Professor Christopher Carone, Physics  
College of William & Mary



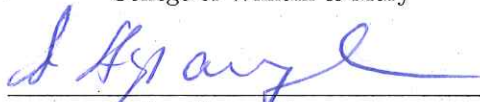
---

Assistant Professor Justin Stevens, Physics  
College of William & Mary



---

Professor David Armstrong, Physics  
College of William & Mary



---

Dr. Stepan Stepanyan

Thomas Jefferson National Accelerator Facility

## ABSTRACT

The Heavy Photon Search (HPS) experiment at Jefferson Lab is designed to search for a hypothesized elementary particle called a dark (heavy) photon. Such a particle would behave as a mediator between dark matter and the Standard Model through kinetic mixing with the Standard Model photon. The search is performed by scattering GeV-scale electrons off tungsten nuclei in a fixed target and looking for a resonance and/or displaced vertices amidst a background of radiative QED trident events. These background events are kinematically identical to the events in which dark photons are produced and decay into lepton pairs. Several other types of reactions take place in this experiment, such as Bethe-Heitler tridents, Møller scattering, wide-angle bremsstrahlung and elastic scattering off the nucleus. Each of these types of background reactions are used for calibration of the detector. For one of these calibration studies, we have measured the form factors for electrons scattering elastically and nearly-elastically off a carbon target and compared these to predicted values. A resonance search, performed on 10% of the dataset taken in 2016 with a 2.306 GeV beam, shows no sign of a dark photon in the mass range 45-200 MeV. Preliminary upper limits on the square of the dark-photon's kinetic coupling to the Standard Model photon have been set in the  $10^6 - 10^5$  range at 95% confidence for every mass hypothesis in this mass range.

## TABLE OF CONTENTS

Acknowledgments . . . . .	v
Dedication . . . . .	vi
List of Tables . . . . .	vii
List of Figures . . . . .	viii
 CHAPTER	
1 Introduction . . . . .	2
1.1 Motivation for Dark Matter . . . . .	2
1.2 Formalism and Motivation of a Dark-Photon Model . . . . .	3
1.3 Searches for Dark Photons . . . . .	6
2 Overview of the Heavy Photon Search Experiment . . . . .	10
2.1 Experimental Apparatus . . . . .	13
2.1.1 Targets . . . . .	13
2.1.2 Magnets and Beamline . . . . .	14
2.1.3 Silicon Vertex Tracker . . . . .	17
2.1.4 Electronic Calorimeter . . . . .	20
2.1.5 Trigger System . . . . .	20
2.2 Event Reconstruction . . . . .	26
3 Dark-Photon Signal and Background Reactions . . . . .	31
3.1 Radiative Tridents and $A'$ Production . . . . .	33
3.2 Bethe-Heitler Tridents . . . . .	35
3.3 Wide-Angle Bremsstrahlung . . . . .	38

3.4	Møller Scattering . . . . .	39
3.5	Full-Energy Electrons . . . . .	41
4	Monte-Carlo Simulations . . . . .	42
4.1	Event Generators . . . . .	42
4.2	Interaction Between Particles and Detector Elements . . . . .	43
4.3	Readout . . . . .	44
4.4	Reconstruction . . . . .	45
5	Data Taken in HPS . . . . .	46
5.1	Calibration Methods . . . . .	49
5.2	Event Flags . . . . .	51
6	Efficiency Measurements Using Full-Energy Electrons . . . . .	52
6.1	Model . . . . .	53
6.1.1	Elastic Scattering . . . . .	55
6.1.2	Quasielastic Scattering . . . . .	56
6.1.3	Delta resonance . . . . .	59
6.1.4	Radiative Corrections and Multiple Scattering . . . . .	60
6.2	Cross Section Measurement . . . . .	62
6.2.1	Event Selection . . . . .	62
6.2.2	Normalization . . . . .	67
6.3	Comparison to model . . . . .	71
6.4	Interpretation . . . . .	76
7	Resonance Search Part 1: Preparing a Mass Spectrum . . . . .	78
7.1	Bump-Hunt Algorithm Overview . . . . .	78
7.2	Dataset . . . . .	79
7.3	Event Selection . . . . .	84

7.4	Composition of the $e^+e^-$ Event Sample . . . . .	95
7.5	Mass Resolution and Signal Shape . . . . .	101
8	Resonance Search Part 2: Fitting the Mass Spectrum . . . . .	109
8.1	Formalization of Likelihood-Ratio Test . . . . .	110
8.2	Background and Signal Models . . . . .	114
8.3	Look-Elsewhere Effect . . . . .	119
8.4	Exclusion-Region Calculation . . . . .	121
9	Results of Resonance Search . . . . .	124
10	Conclusion and Outlook . . . . .	129
10.1	The Future of HPS . . . . .	129
APPENDIX A		
	Muon Detector . . . . .	131
A.1	Description of Research Instrumentation and Needs . . . . .	132
A.1.1	Conceptual Design . . . . .	138
A.1.2	Absorbers and Scintillators . . . . .	140
A.1.3	Background Reducing Features . . . . .	144
A.1.4	Readout and Electronics . . . . .	145
A.2	Trigger Conditions . . . . .	146
A.3	Methods of Simulation . . . . .	148
A.4	Background Sources . . . . .	149
A.4.1	QED Reactions Producing Muons . . . . .	150
A.4.2	Pions . . . . .	150
A.4.3	Beam Background . . . . .	152
A.5	Additional Filters on Events . . . . .	153
A.6	Optimization of Dimensions . . . . .	153
A.6.1	Angular Coverage . . . . .	154

A.6.2	Sheet-of-Flame Window . . . . .	156
A.6.3	Inner Tungsten Shield . . . . .	161
A.6.4	Tungsten Backsplash Shield . . . . .	164
A.6.5	Scintillator Thickness . . . . .	168
APPENDIX B		
	Optimization of Resonance-Search Cuts in the 2016 HPS Dataset . . . . .	169
B.1	Track-Cluster Matching . . . . .	170
B.2	Accidental Reduction . . . . .	175
B.3	Track $\chi^2$ . . . . .	179
B.4	WAB and Bethe-Heitler Reductions . . . . .	181
APPENDIX C		
	List of Abbreviations . . . . .	185
	Bibliography . . . . .	190
	Vita . . . . .	197



## ACKNOWLEDGMENTS

The research included in this dissertation could not have been performed if not for the assistance, patience, and support of many individuals. I would like to extend my gratitude first and foremost to my thesis advisor Keith Griffioen for mentoring me over the course of my graduate studies. He introduced me to the HPS project, and helped me find a dissertation project within there. He has helped me through difficult times over the course of the analysis and the writing of the dissertation and for that I sincerely thank him for his confidence in me. I would also like to thank the rest of my committee members for their comments and corrections for the dissertation.

I would also like to thank David and Anna Elefant for their hospitality all the times I stayed at their house while doing research for HPS and/or collaboration meetings at SLAC, and likewise, Aram and Ginny Kerovpian, for their hospitality during the HPS collaboration meeting in Paris.

This research would not have been possible without the assistance of the HPS experimental collaboration who constructed the experimental apparatus and built the foundations for the data analysis. Especially, I would like to thank Rafayel Paremuzyan and Nathan Baltzell for teaching me how to use tools such as the ROOT software package and the SQL database for analysis, and Holly Szumilla-Vance for her explanations of everything related to the calorimeter, and for her help in preparing my dissertation defense talk. Additionally, I would like to thank Omar Moreno and Mathew Graham for guiding me in the bump hunt analysis. I would also like to thank Miriam Diamond for all her hard work and patience with working on the tracking software, and for brightening everyone's day with her sense of humor.

There are also a few Jefferson Lab colleagues outside of the HPS collaboration whom I would like to thank, namely Vardan Gyurjyan, Carlos Ayerbe-Gayoso and Douglas Higinbotham, for their support and advice in my research.

I would also like to thank the Jefferson Science Associates, LLC, for providing funds for my research, including travel to SLAC as well as other locations.

Finally I would like to extend my deepest gratitude to my mother Roxanne Paul without whose love, support and understanding I could never have completed this doctoral degree.

I present this thesis in honor of my mother, Roxanne Paul, and my late father Aram Paul.

## LIST OF TABLES

2.1	Trigger configuration summary for the 2015 run period. . . . .	24
2.2	Trigger configuration summary for the 2016 run period. . . . .	25
2.3	SSP prescale factors for the Single 1 trigger used in the 2016 dataset.	26
5.1	Data taking parameters for the 2015 and 2016 HPS runs. . . . .	48
6.1	Calculations of the radiative correction factors. . . . .	62
6.2	Weighting events by brescale in FEE analysis (2016 dataset only). . .	68
7.1	List of “golden” runs from the 2016 HPS physics dataset used in the bump-hunt analysis. . . . .	80
7.1	List of “golden” runs from the 2016 HPS physics run used in this analysis. (continued) . . . . .	81
7.1	List of “golden” runs from the 2016 HPS physics run used in this analysis. (continued) . . . . .	82
7.1	List of “golden” runs from the 2016 HPS physics run used in this analysis. (continued) . . . . .	83
7.2	Comparison of event acceptance after each cut on the data and on several Monte-Carlo simulations: . . . . .	87
A.1	Ranges of acceptable pairs of $x$ indices for paired tracks. . . . .	147

## LIST OF FIGURES

1.1	Example of a one-loop diagram that could create kinetic mixing. . . .	5
1.2	Existing constraints on a dark photon decaying into Standard Model particles. . . . .	9
2.1	$A'$ production from a target nucleus of charge $Z$ , followed by the decay of the $A'$ into an electron-positron pair. . . . .	11
2.2	Setup of the HPS experiment. . . . .	12
2.3	HPS target mounting apparatus. . . . .	13
2.4	Schematic of CEBAF. . . . .	15
2.5	Location of HPS in the downstream alcove of Hall B . . . . .	16
2.6	Chicane Magnet System. . . . .	18
2.7	Silicon Vertex Tracker and enclosing vacuum box. . . . .	19
2.8	Ecal crystal schematics. . . . .	21
2.9	Electronic Calorimeter schematics viewed from upstream. . . . .	22
2.10	Hits per cluster in the Ecal for events triggered by the Pair 1 trigger .	27
3.1	Examples of Feynman diagrams of background and signal reactions in HPS. . . . .	32
3.2	Feynman diagrams for radiative tridents. . . . .	34
3.3	Feynman diagrams for $A'$ production. . . . .	34
3.4	Feynman diagrams for Bethe-Heitler tridents. . . . .	36
3.5	Comparison of kinematics of Bethe-Heitler tridents and radiative tridents in a Monte-Carlo simulation using MadGraph5 [1]. . . . .	37
3.6	Feynman diagrams for Wide-Angle Bremsstrahlung (WAB). . . . .	38
3.7	Illustration of a WAB conversion. . . . .	39
3.8	Feynman diagrams for Møller scattering. . . . .	41
5.1	Estimated integrated charge and event count during 2015 (top) and 2016 (bottom) HPS runs, not corrected for data quality. . . . .	49

6.1	Modeled cross sections for FEEs produced on a $^{12}\text{C}$ target, . . . . .	54
6.2	Cluster energy spectra for runs 5779 (top, 1.056 GeV beam) and 8054 (bottom, 2.306 GeV beam). . . . .	64
6.3	Angular distribution of particles passing FEE cuts in run 5779. . . . .	65
6.4	Angular distribution of particles passing FEE Cuts in run 8054. . . . .	66
6.5	Overall prescale factors of the Single 0 and Single 1 triggers used in 2016. . . . .	69
6.6	Prescale-weighted angular distribution of particles passing FEE Cuts in run 8054. . . . .	70
6.7	Ratio of measured to predicted cross-sections for FEEs in run 5779 (1.056 GeV). . . . .	72
6.8	Ratio of measured to predicted cross-sections for FEEs in run 8054 (2.306 GeV). . . . .	73
6.9	Ratio of measured to predicted cross-sections for FEEs in run 5779 (1.056 GeV), projected in $u_x$ . . . . .	74
6.10	Ratio of measured to predicted cross-sections for FEEs in run 8054 (2.306 GeV), projected in $u_x$ . . . . .	75
7.1	Time spectra of clusters in Ecal. . . . .	85
7.2	Cutflow of the invariant-mass spectrum of $e^+e^-$ pairs. . . . .	88
7.3	Cutflow of the time difference between cluster times of paired particles. . . . .	89
7.4	Cutflow of the electron momentum. . . . .	90
7.5	Cutflow of the positron momentum. . . . .	91
7.6	Cutflow of the total momentum of $e^+e^-$ pairs. . . . .	92
7.7	Cutflow of the track fit $\chi^2$ values. . . . .	93
7.8	Cutflow of the difference in cluster-track time difference . . . . .	94
7.9	Comparison of pair momentum (top) and invariant-mass (bottom) spectra of $e^+e^-$ events between data and Monte Carlo. . . . .	96
7.10	Comparison of particle momenta in $e^+e^-$ events between data and Monte Carlo. . . . .	97
7.11	Comparison of particle initial direction (in $x$ ) in $e^+e^-$ events between data and Monte Carlo. . . . .	98
7.12	Comparison of particle initial direction (in $y$ ) in $e^+e^-$ events between data and Monte Carlo. . . . .	99

7.13	Dependency of the radiative fraction on the invariant mass, as calculated using Monte-Carlo simulations. The red curve represents the parameterization in Equation 7.1. At large masses, statistics are limited both in simulations and data, due to the small cross-sections. Since there is very little sensitivity to dark photons with mass more than 120 MeV, the large uncertainties on $f_{\text{rad}}$ are not as important as at smaller masses. . . . .	100
7.14	Invariant mass spectrums for $A'$ Monte Carlo . . . . .	103
7.15	Fitted mass spectra for Møller pairs in data (top) and Monte Carlo (bottom). . . . .	106
7.16	Fit parameters of the reconstructed mass spectra of simulated $A'$ events, as well as Møller pairs in both data and simulations. . . . .	107
7.17	Fit parameters of the reconstructed mass spectra of simulated $A'$ events, as well as Møller pairs in both data and simulations . . . . .	108
8.1	Illustration a signal+background fit (blue, left) and background-only fit (green, right) for a simulated mass spectrum. . . . .	113
8.2	Relationship between the test-statistic $q_0$ and the associated $p$ -value. . . . .	113
8.3	Function used for generating pseudo-datasets . . . . .	115
8.4	Residuals of the global fit . . . . .	116
8.5	Comparison of various choices of background polynomial order and window sizes. . . . .	118
8.6	Relationship between global and local $p$ -values. . . . .	120
8.7	Upper limits on the signal yield at each mass hypothesis. . . . .	122
9.1	Local $p$ -values as a function of the mass hypothesis. . . . .	125
9.2	Fits to signal plus background models for mass hypotheses of 62.25 (upper plot) and 135 MeV (lower plot), . . . . .	126
9.3	Spectra of test statistics $q_0$ (top) and $p$ -values (bottom) of the signal+background vs. background-only tests for each mass hypothesis, . . . . .	127
9.4	Preliminary exclusion region from bump hunt on 10% of the 2016 HPS dataset (purple), . . . . .	128
A.1	$A'$ detection efficiency . . . . .	133
A.2	Pion rejection in the muon detector. . . . .	135

A.3	Additional reach from the muon detector. . . . .	136
A.4	Position of the proposed muon detector in relation to other components of HPS. . . . .	137
A.5	Schematic diagram detailing the various components of the muon detector. . . . .	139
A.6	Schematic for the iron absorbers. . . . .	141
A.7	Schematics of scintillators and their backboards . . . . .	142
A.8	Layout of scintillators. . . . .	143
A.9	Dimensions and position of the sheet-of-flame window cut. . . . .	145
A.10	Dimensions of tungsten shields. . . . .	146
A.11	Beam background hit rates . . . . .	152
A.12	Angular coverage of the muon detector. . . . .	155
A.13	Background rates on each channel for various thicknesses of the aluminum plate covering the sheet-of-flame window. . . . .	157
A.14	Background rates on each channel for various heights of the sheet-of-flame window. . . . .	158
A.15	Background rates on each channel for various positions of the upstream end of the sheet-of-flame window. . . . .	159
A.16	Background rates on each channel for various positions of the downstream end of the sheet-of-flame window. . . . .	160
A.17	Background rates on each channel for various thicknesses of the inner tungsten shields. . . . .	162
A.18	Background rates on each channel for various starting positions of the inner tungsten shield. . . . .	163
A.19	Background rates on each channel for various backslash shield heights. . . . .	165
A.20	Background rates on each channel for various backslash shield thicknesses. . . . .	166
A.21	Background rates on each channel for various backslash shield widths. . . . .	167
A.22	Comparison of background rates on each channel with 3 cm and 1 cm thick scintillators. . . . .	168
B.1	Time difference between clusters and tracks for “signal-like” (blue) and “background-like” (brown) events for fine-tuning the cut on $n_\sigma$ in the track-cluster matching. . . . .	171
B.2	$n_\sigma$ spectra for “signal-like” (blue) and “background-like” (brown) events. . . . .	172
B.3	$n_\sigma$ values for “signal-like” (blue) and “background-like” (brown) events for fine-tuning the track-cluster time difference cut. . . . .	173

B.4	Track-cluster time difference spectra for “signal-like” (blue) and “background-like” (brown) events. . . . .	174
B.5	Cluster-time difference spectra for “signal-like” (blue) and “background-like” (brown) events for fine-tuning the accidental-reduction cuts. . .	176
B.6	Electron momentum spectra for background-like (brown) and signal-like (blue) events. . . . .	177
B.7	Total momentum spectra for background-like (brown) and signal-like (blue) events. . . . .	178
B.8	Track fit $\chi^2$ vs Møller invariant masses. . . . .	180
B.9	Comparison of the cross sections of events with/without SVT Layer 1 (L1) hits in data and Monte Carlo simulations. . . . .	182
B.10	Comparison of positron track’s distance of closest approach in data and Monte Carlo. . . . .	183
B.11	Comparison of $e^+e^-$ pair sum momenta in data and Monte Carlo. . .	184



SEARCHING FOR A DARK PHOTON IN THE HPS EXPERIMENT

# CHAPTER 1

## Introduction

### 1.1 Motivation for Dark Matter

One of the most successful theories in physics today is the Standard Model (SM), which describes the interactions between all of the known elementary particles, the fundamental building blocks of the universe. These particles include the leptons, quarks, photon, W&Z bosons, the gluons and the Higgs boson. The Higgs was the last of the SM particles to be discovered [2, 3], about half a century after its namesake Peter Higgs predicted its existence. There are only a handful of anomalies in particle physics that the Standard Model fails to predict. For instance, it fails to provide a candidate for the so-called “dark matter” [4–9].

In the 1930’s, Swiss astronomer Fritz Zwicky found that the velocities of the galaxies in the Coma cluster were too dispersed for it to be held together by the gravitational attraction of luminous matter alone. As a solution to this problem, he proposed that only a fraction of the cluster’s total mass consists of luminous matter, and that an unseen *dunkel Materie* (dark matter) constitutes the remaining mass [4].

Since then, other astronomers have found further evidence of dark matter. For instance, consider the rotational velocities of the stars in a galaxies as a function of distance from the galactic center. The observed velocities drop off more slowly at increasing distance than predicted in models that only include the gravitational effects from visible matter. When a halo of dark matter is included in the model, it matches the observed data. Observations of this discrepancy have been found in other galaxies [5] as well as our own Milky Way galaxy [6]. Gravitational lensing effects [7] and microwave background radiation [10] have provided further evidence of dark matter’s existence.

Eight decades have passed since Zwicky’s proposal of *dunkel Materie*, and despite ample evidence for dark matter’s existence, its composition remains a mystery. Any possible candidate for the dark matter must neither emit nor absorb electromagnetic radiation, otherwise it would have already been observed. Most models of dark matter suggest that it consists of particles outside of the Standard Model, which only feebly interact with Standard Model particles (if at all). “Direct-detection” experiments, searching for interactions between dark matter in galactic halos and terrestrial-based detectors, have strongly constrained the interaction strength between dark matter and the Standard Model [8, 9].

## 1.2 Formalism and Motivation of a Dark-Photon Model

Some of the models of dark matter include a  $U'(1)$  gauge symmetry mediated by a massive spin-1 boson called a “dark photon” (abbreviated herein as  $A'$ , pronounced “A Prime”). This dark photon would mediate interactions between dark-matter particles

and it could also kinetically mix with the Standard-Model photon by a very small coupling  $\epsilon$ , through the following Lagrangian term:

$$\mathcal{L}_{A'\gamma} = \frac{1}{2}\epsilon F_{\mu\nu}F'^{\mu\nu} \quad (1.1)$$

where  $F_{\mu\nu}$  and  $F'_{\mu\nu}$  are the field strengths of the standard model photon and the dark photon field strengths respectively. Through this mixing, the dark photon would couple to electromagnetically-charged SM particles analogously to the SM photon (although the coupling would be a factor of  $\epsilon$  weaker). Therefore a dark photon could be created and detected in laboratory settings, provided sufficiently large luminosity in a dedicated experiment. In such a case, it would be useful as a gateway into observing more elusive hidden-sector dark matter. Cross sections of reactions between SM particles producing the dark photon would be suppressed by a factor of  $\epsilon^2$  [11]. Similarly, if the dark photon decays into SM particles, then its decay width would also be suppressed by the same factor.

The kinetic mixing could arise from a high-energy loop diagram such as the one in Figure 1.1 [12]. However, the dark photon model is independent of any higher energy field theory of which the Standard Model is an effective field theory. Moreover, the dark photon model is one of only a few “dark portal” candidates: interactions between dark matter and the Standard Model through a mediator which do not break any of the existing gauge and Lorentz symmetries of the Standard Model. The Lagrangian terms of other three dark portals (as discussed in the Dark Sectors Workshop 2016: Community Report [8]) are:

- Higgs portal:  $(\mu\phi + \lambda\phi^2)H^\dagger H$ , where  $\phi$  is the scalar mediator field,  $\lambda$  and  $\mu$  are couplings, and  $(H, H^\dagger)$  are the Higgs doublet and its hermitian conjugate.

- Neutrino portal:  $y_n L H N$ : where  $y_n$  is the coupling,  $L$  is any generation of lepton doublets, and  $N$  is a fermionic DM or mediator field (e.g. a right-handed neutrino).
- Axion portal:  $\frac{a}{f_a} F_{\mu\nu} \tilde{F}^{\mu\nu}$ : where  $a$  is a (pseudoscalar) axion field,  $f_a$  is a high mass scale, and  $F_{\mu\nu}$  and  $\tilde{F}^{\mu\nu}$  are the SM photon field and its dual. Of the four portals discussed in [8], this is the only one that is non-renormalizable (dimension-5); the others are renormalizable (dimension-4).

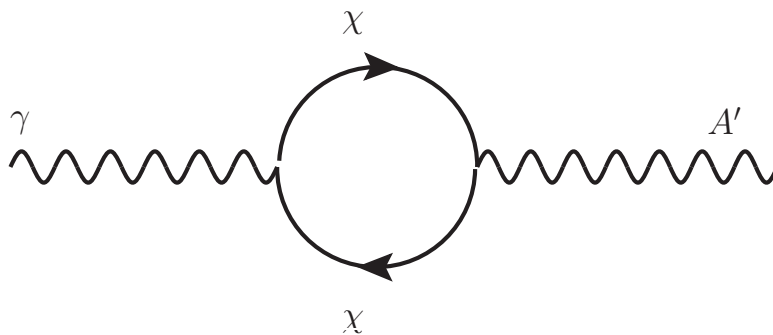


FIG. 1.1: Example of a one-loop diagram that could create kinetic mixing. In this case, the massive particle  $\chi$  has both electromagnetic charge and dark charge.

A strong argument can be made for the presence of a mediator by the “core-cusp” problem [13]. Collisionless models of dark matter predict that the density of the dark matter sharply increases near the center of a galaxy, in a feature known as a “cusp”. However, measurements of the galactic rotational velocities suggests that the dark-matter density is nearly constant near the center (core). If the dark matter is self-interacting, then dark matter particles could elastically scatter off one another in the dense galactic core, redistributing energy and angular momentum among particles, preventing a cusp from forming. The cross section required for this to happen is on the order of  $1 \text{ barn}/\text{GeV} \times m_D$ , where  $m_D$  is the mass of the dark-matter particle.

Another motivation is that cosmological “freeze-out” requires a mediator for

interactions between dark matter and SM matter. The present-day isotropic distribution of dark matter throughout the universe suggests that the dark matter and SM matter were in thermal equilibrium with one another at some point in the early stages in the universe just after the Big Bang. The freeze-out model predicts that this early equilibrium was maintained by SM particles annihilating with one another into dark-matter particles and vice versa. Eventually, as the universe cooled and expanded, there was not enough kinetic energy available, and the mean free paths between particles was too long, for these sorts of reactions to occur. At that point, the dark matter and the SM matter became thermally decoupled from one another, and the relic abundance of the dark matter has remained constant since then. This model, combined with cosmological measurements of the present abundance of dark matter, provides lower-bound constraints on the couplings of the mediator to the standard model ( $\epsilon$ ) and to the dark matter ( $g_D$ ); if these couplings are too weak, then the universe would have failed to reach thermal equilibrium.

### 1.3 Searches for Dark Photons

Over a dozen experiments [8, 14, 15, 15–20, 20–23, 23, 24, 24, 25, 25–44] have run and/or have been proposed within the past decade to search for the dark photon using a wide variety of experimental setups, dark photon production methods and detection techniques. Since neither the mass of the dark photon nor its coupling are known *a priori*, each experiment’s design is tailored to search for it in a specific range in the mass vs. coupling parameter space. A few of these experiments are highlighted below to exemplify various experimental techniques. More details on the individual experiments may be found in [8] and its references.

In the DarkLight experiment at Jefferson Lab [14], for example, beam electrons

scatter off protons in a windowless hydrogen-gas target, possibly producing dark photons via bremsstrahlung ( $e^-p \rightarrow e^-pA'$ ). The dark photon could either decay into a detectable  $e^+e^-$  pair, or into dark matter  $\chi\chi$  if the dark photon is more than twice as massive as the dark-matter particles. In the former case, a “visible-search” bump hunt searches the spectrum of  $e^+e^-$  invariant masses for a small narrow peak. For the latter case, an additional “invisible-search” bump hunt searches for a peak in the missing-mass spectrum. This requires high efficiency for detection of particles (for vetoing other types of reactions) as well as precise knowledge of the kinematics of the initial particles (in DarkLight, this is  $e^-p$ ) and measurement of the scattered electron and recoiling proton momenta.

The BaBar experiment at SLAC used an electron-positron collider to search for  $e^+e^- \rightarrow \gamma A'$  reactions, where the  $A'$  would decay into detectable  $e^+e^-$  or  $\mu^+\mu^-$  pairs or into dark matter ( $\chi\chi$ ). Bump-hunts were performed on both the invariant-mass spectra of lepton decays [15] and “invisible” decays [16].

In the LHCb experiment at CERN [17–20], two proton beams collide with one another with a center-of-mass energy of 13 TeV. Dark photons may be produced via meson decays (such as  $D^* \rightarrow D^0 A'$  or  $B \rightarrow K^* A'$ ) or Drell-Yan processes. They would then decay (either promptly, or after traveling a few cm if they are long-lived) into  $e^+e^-$  or  $\mu^+\mu^-$  pairs found by the detector. A bump-hunt algorithm searches for bumps in the dilepton invariant-mass spectra assuming prompt decay. The regions surrounding known resonances are avoided. Additionally, a displaced-vertex search algorithm looks for dilepton pairs where the vertex of the reconstructed pair was further from the  $pp$  collision point than allowed by detector resolution.

Beam-dump experiments are another class of experiments to search for very long-lived dark photons. These experiments typically run commensal to other experiments further upstream and can search for neutrinos and many types of long-lived beyond-

standard-model particles. For example, the IHEP-JINR detector was originally designed to study neutrinos produced by protons in the U70 accelerator interacting with the beam dump [21, 22]. However, the data were later reanalyzed to set limits on the dark photon mass-coupling [23]. While the constraints on dark photons from early beam-dump experiments such as U70, E137[24] and E141[25] were calculated *post-facto*, newer beam-dump experiments, such as the proposed BDX at JLab [26, 27] and a proposed experiment at the LBNF [28], are specially dedicated to finding dark photons.

Figure 1.2 summarizes the present experimentally-excluded regions of the dark-photon parameter space. So far, none of these experiments have found conclusive evidence of a dark photon.



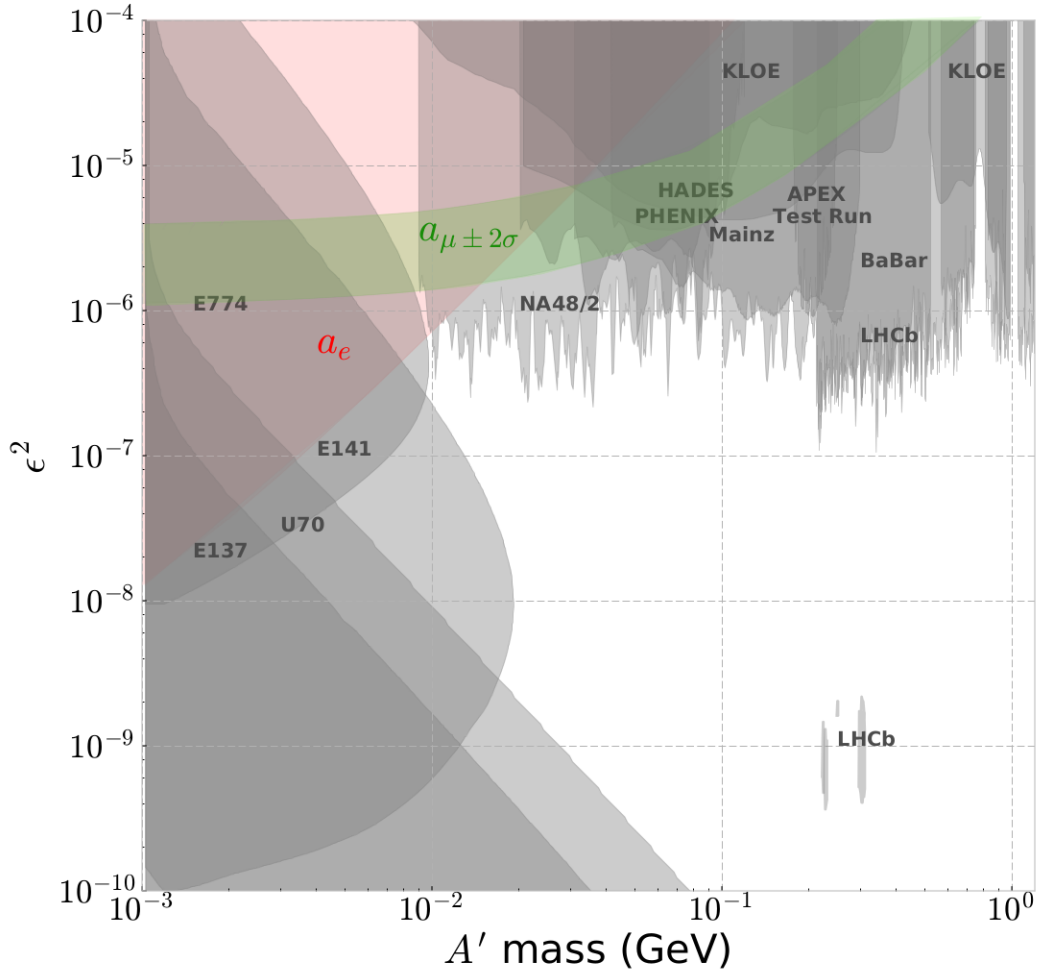


FIG. 1.2: Existing constraints on a dark photon decaying into Standard Model particles. The shaded regions are parts of the  $A'$  parameter space which other experiments have excluded with  $2\sigma$  confidence. The bright green band is the region where the effect of a dark photon could have explained the muon’s anomalous magnetic moment [45], however this has since been ruled out experimentally. The constraints on the lower left-hand side are from beam-dump experiments [23–25, 29, 30], while the “stalactitic” constraints at the top of the plot are from bump-hunt experiments [15, 20, 31–44]. The red region in the upper left is excluded because of the effect a dark photon would have on the electron magnetic moment measurements [45]. The island-shaped exclusion regions are from displaced vertex searches [20].

## CHAPTER 2

# Overview of the Heavy Photon Search Experiment

The Heavy Photon Search<sup>1</sup> (HPS) experiment at the Thomas Jefferson National Accelerator Facility (JLab) searches for dark photons in the mass range 20 MeV to 1 GeV with  $\epsilon^2$  as low as  $10^{-10}$ , which would be produced through bremsstrahlung of an electron beam scattering off a tungsten foil target (Figure 2.1). The experimental apparatus was designed to search for two possible signatures of dark photons decaying into  $e^+e^-$  amidst the much larger QED background. If the coupling  $\epsilon$  is sufficiently small, then the decay length of the  $A'$  is larger than the vertex-reconstruction resolution of the detector, and the signal would manifest itself as displaced vertices of paired  $e^+e^-$  tracks. If the coupling is much larger, then the  $A'$ -production cross section will be larger, and the signal would manifest itself as a small narrow peak (“bump”) in the spectrum of  $e^+e^-$  pair masses. Both of these two analyses require very good resolution in tracking variables.

---

<sup>1</sup>Another name for dark photons is “heavy photons”, since the dark-photon model requires that their mass be non-zero.

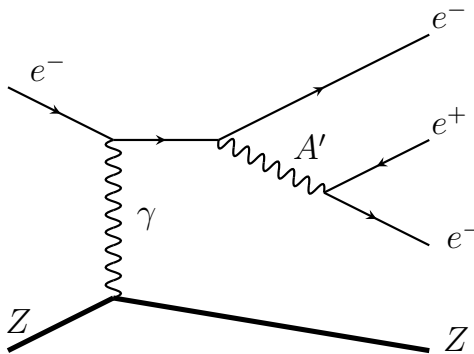


FIG. 2.1:  $A'$  production from a target nucleus of charge  $Z$ , followed by the decay of the  $A'$  into an electron-positron pair.

Figure 2.2 shows the setup of the experiment. HPS utilizes a continuous electron beam of up to 500 nA, which hits a 4  $\mu\text{m}$  thick tungsten target. Between 10 cm and 90 cm downstream of the target is the Silicon Vertex Tracker (SVT), which tracks charged particles. Further downstream ( $\sim 130$  cm) is an Electronic Calorimeter (Ecal) which measures the energy deposited by electrons, positrons and photons, and provides information for making the triggering decision.

A large Pair-Spectrometer (PS) magnet surrounds the target and the SVT, so that the radius of curvature of the tracks can be used to determine the momentum of the particles. This magnet is part of a beam-line chicane system, along with two other dipole magnets, which is described in more detail in Section 2.1.2.

The electrons from the beam that lose energy in the target bend more in the PS magnet than the rest of the beam, and therefore their trajectories spread out into a horizontal plane called the “sheet of flame”. Since high background makes it impractical to place any sensitive detector elements in front of the sheet of flame, both the SVT and the Ecal are split into two halves, top and bottom, with a gap in between them, creating a  $\sim 15$  mrad dead-zone in the detector’s geometric acceptance.

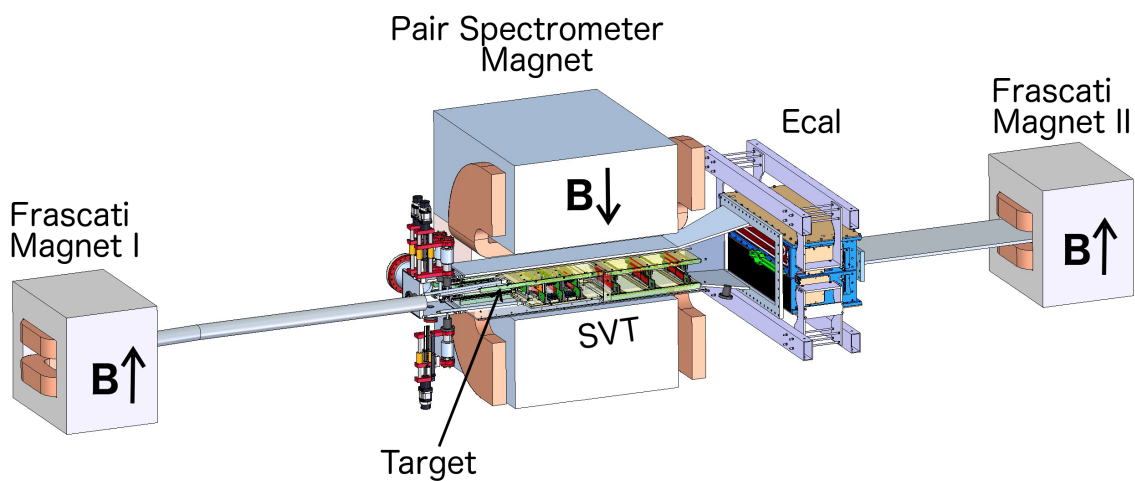


FIG. 2.2: Setup of the HPS experiment. The components of the HPS, along the beam direction (left to right), are the upstream Frascati magnet, the target, the Pair-Spectrometer magnet and the Silicon Vertex Tracker (SVT), the Electromagnetic Calorimeter (Ecal), and the downstream Frascati magnet.

## 2.1 Experimental Apparatus

### 2.1.1 Targets

The primary target in HPS is a 4  $\mu\text{m}$  thick tungsten foil. Additionally, HPS has three other available targets, which we have only used for special calibration runs: an 8  $\mu\text{m}$  tungsten target, a carbon target and a  $\text{CH}_2$  target, all mounted in a retractable apparatus shown in Figure 2.3.

The tungsten targets consist of a naturally occurring mixture of isotopes, with an average atomic mass of 183.84 amu. Its thickness is nominally 4  $\mu\text{m}$  and its areal density is 0.0078125 g/cm<sup>2</sup>. The graphite carbon target consists of pure  $^{12}\text{C}$  and has an areal density of 0.0441 g/cm<sup>2</sup>. The areal density of the  $\text{CH}_2$  target is 0.0706 g/cm<sup>2</sup>.

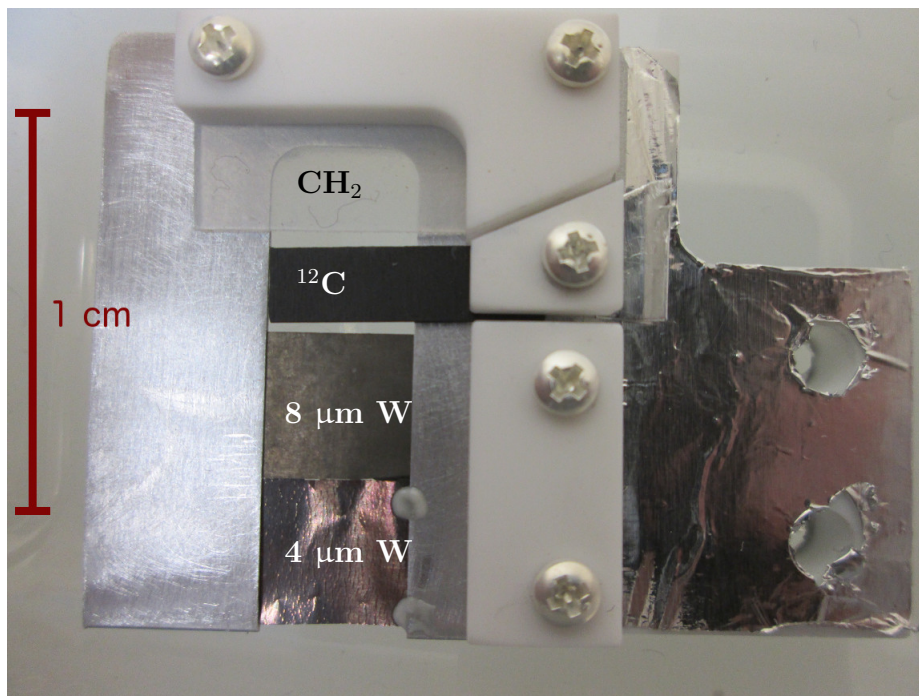


FIG. 2.3: HPS target mounting apparatus. The targets, from top to bottom, are  $\text{CH}_2$ , carbon, 8  $\mu\text{m}$  tungsten and 4  $\mu\text{m}$  tungsten.

### 2.1.2 Magnets and Beamline

HPS uses the electron beam from Jefferson Lab’s CEBAF (Continuous Electron-Beam Accelerator Facility) accelerator, a recirculating linac that allows electrons to pass multiple times through the same set of accelerating cavities. The accelerator can provide continuous beam to 4 experimental halls (named Halls A-D) simultaneously through a RF splitter system. Depending on the needs of the experiments in the halls, the accelerator may provide different beam energies, corresponding to different number of passes through the linac. CEBAF recently underwent an upgrade to increase maximum beam energy up to 12 GeV; however, HPS can only run at energies up to 6.6 GeV, due to limitations on its chicane-magnet system. Figure 2.4 shows the schematic of CEBAF.

HPS is installed in an alcove of Hall B, downstream of the Hall’s main experimental-detector system, the CEBAF Large-Acceptance Spectrometer (CLAS), as is shown in Figure 2.5. CLAS is currently undergoing major upgrades to allow the maximum-beam energy conditions for the detector to be increased from 6 GeV to 12 GeV. Because of this, our data-taking time-slots in 2015 were limited to night shifts and weekends, when the construction crews were not in the Hall. In 2016, in order to compensate for delays in CLAS construction, the construction crews worked week-day night shifts in addition to morning and afternoon shifts, limiting our data-taking time-slots to weekends only.

Several precautions were taken to prevent damage to the SVT, whose first layer is only 0.5 mm from the beamline. We used CEBAF’s Fast-Shutdown (FSD) system to turn off the injector whenever the beam-halo counters near HPS recorded unusually high rates. Secondly, we obtained, upon request, a very narrow beam profile (a few tens of microns along either axis) with low beam halo (a part in  $10^{-5}$ ). Thirdly, we

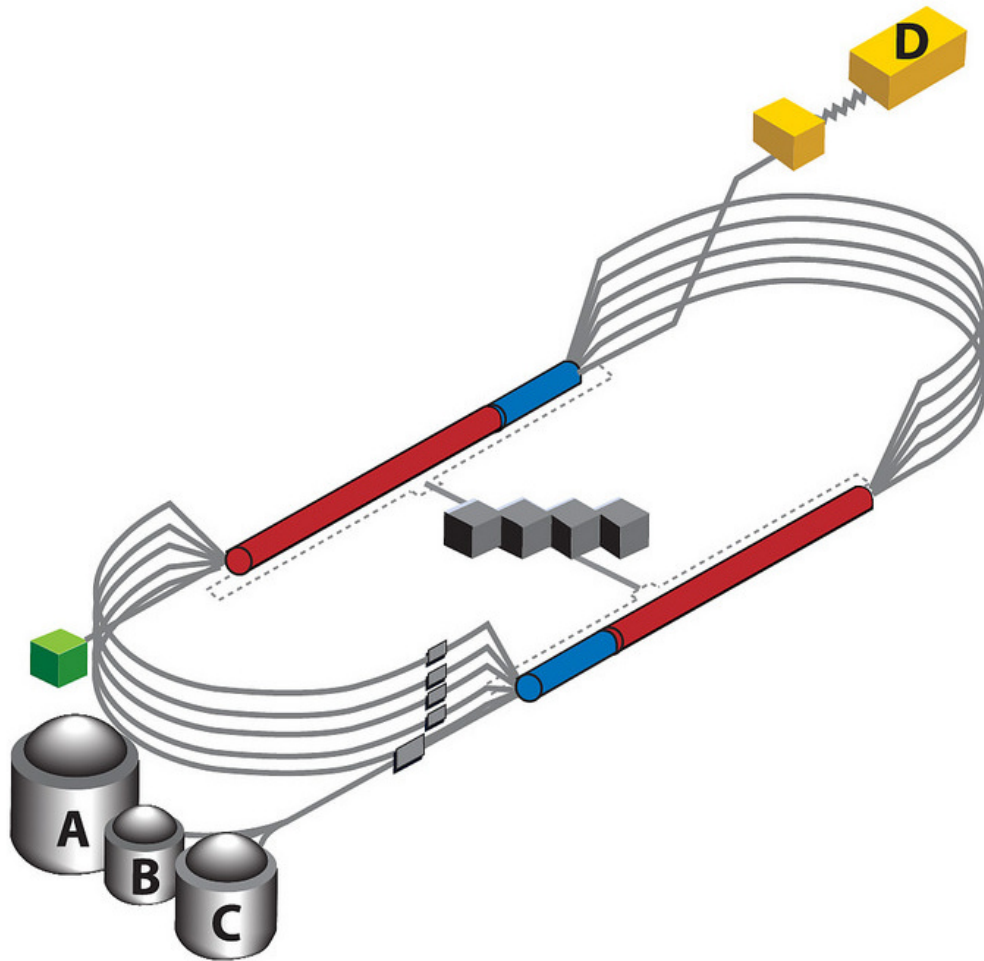


FIG. 2.4: Schematic of CEBAF. The electrons enter the loop from the injector (green) and circulate through the linacs (red and blue) and magnetic arcs several times before reaching the experimental halls A-D. At the time of the 12 GeV upgrade, 5 extra cryomodules (blue) were added to each linac, in addition to the 20 cryomodules that were in each linac prior to the upgrade (red).

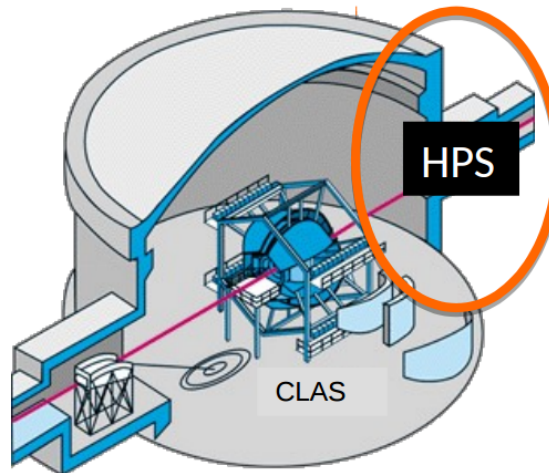


FIG. 2.5: Location of HPS in the downstream alcove of Hall B

placed a collimator upstream of the SVT to passively reduce beam halo hitting the target.

The electrons from the beam arrive in bunches at 2 ns intervals, which is commensurate with the timing resolution of the Ecal. This bunching structure is a product of the linac system, which we are able to exploit in order to reduce background from pairs of clusters from different beam bunches.

HPS utilizes a beam-line chicane system consisting of three dipole magnets with vertical magnetic fields. The central and largest of these magnets is the Pair-Spectrometer dipole magnet, which curves the trajectories of the particles passing through the SVT so that their momenta can be measured. The other two dipole magnets, the “Frascati” magnets, are placed equidistantly upstream and downstream of the Pair-Spectrometer magnet, and each have  $-1/2$  of the field path integral  $\int Bdl$  of the Pair-Spectrometer magnet. This causes the beam trajectory downstream of the chicane to be independent of whether or not the magnets are activated. This setup is shown in Figure 2.6. Downstream of the chicane is a Faraday Cup, which captures



beam-line electrons and measures the charge accumulated. In 2016, we inserted a retractable beam-blocker in front of the Faraday cup to prevent overheating due to the higher beam current.

### 2.1.3 Silicon Vertex Tracker

The SVT consists of six layers of silicon strip detectors located inside of the vacuum box. The first three layers have only one module in each half of the detector, whereas layers 4-6 have two modules in each half side-by-side in  $x$  (horizontal) from one another. Each module contains two sublayers of silicon strips: the “axial” sublayer, where the strips are oriented along the horizontal ( $x$ ) axis, and the “stereo” sublayer, where the strips are tilted with a small angle (100 mrad for the first 3 layers, and 50 mrad for layers 4-6) relative to the  $x$  axis. The dimensions of the sensitive regions of each module are  $\approx 100 \times 40$  mm and the silicon sublayers are each 320  $\mu\text{m}$  thick, with readout strip pitch 60  $\mu\text{m}$ . Each of the 18 modules has 1278 channels (639 on the axial sublayer and 639 in the stereo sublayer), totaling to 23,004 channels in this system. The SVT layers are located at approximately 10, 20, 30, 50, 70 and 90 cm downstream of the target. Studies on elastically scattered electrons show that the momentum resolution of the SVT is  $\sim 7\%$ . Figure 2.7 shows the geometry of the SVT system inside its enclosing structure.

The first layer of the SVT is very close to the beamline (only 0.5 mm, with an opening angle of 15 mrad) in order to increase acceptance in the case that the  $A'$  has a relatively low mass (in which case the opening angle between the electron and positron trajectories will be very small). When a beam trip occurs or there is excessive halo-counter noise (indicating beam motion), the SVT bias voltage automatically turns off, and a set of precision linear shifts retracts the detector to a safe position. After the

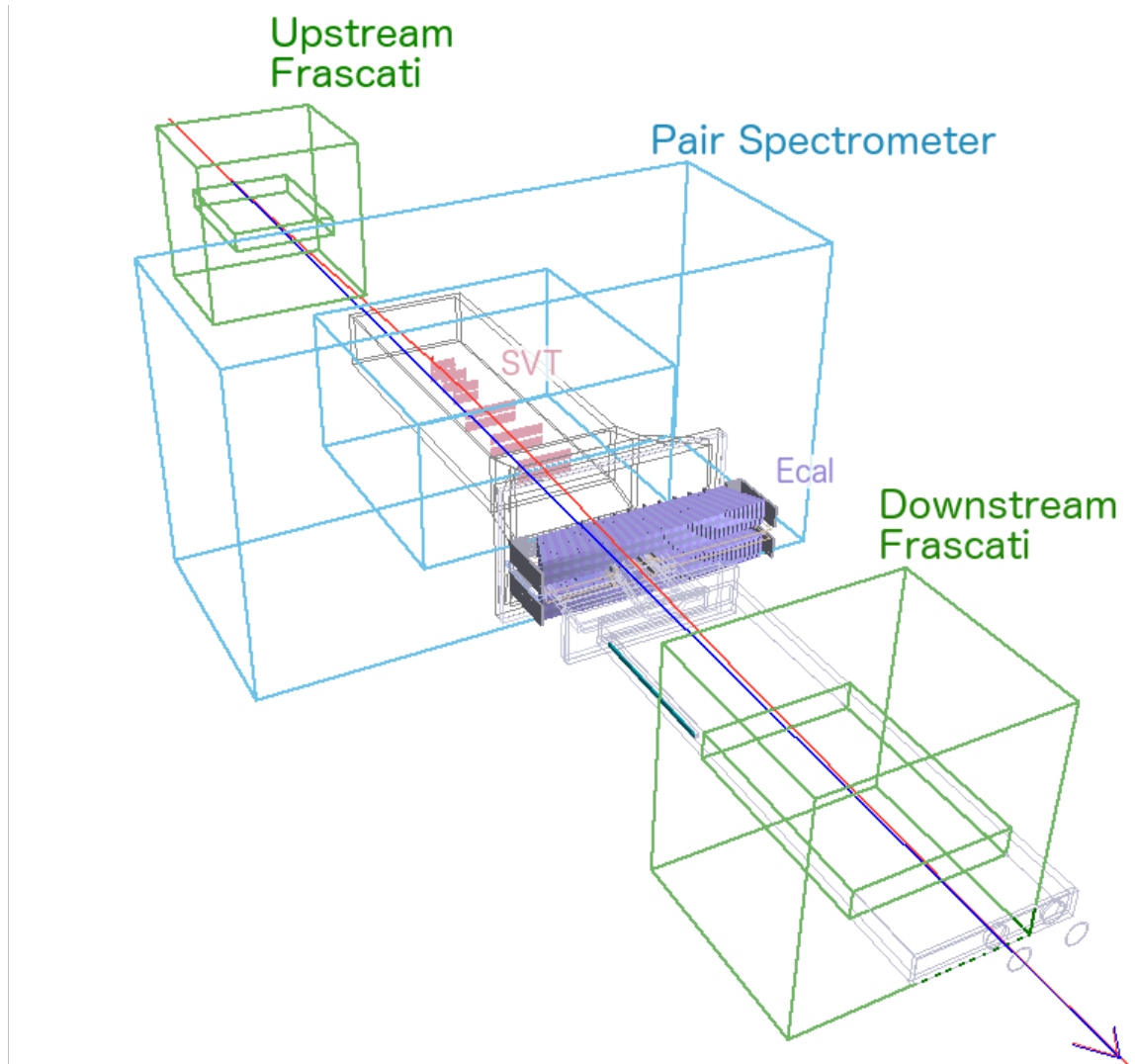


FIG. 2.6: Chicane Magnet System. In this rendering, the 3 magnets are shown as green and teal wireframes. When the magnets are activated, the beam follows the chicane path (red); when they are off, the beam follows a straight line (blue).

beam is restored to safe, stable conditions, the bias voltage can be turned back on and the detector moved back to its nominal position. (During the 2016 run, we disabled the automatic retraction of the SVT and only under rare circumstances retracted it manually). Since the amount of time needed to retract the SVT and return it to its nominal position is much smaller than the typical amount of time between beam-trips, the luminosity lost during this procedure is minimized.

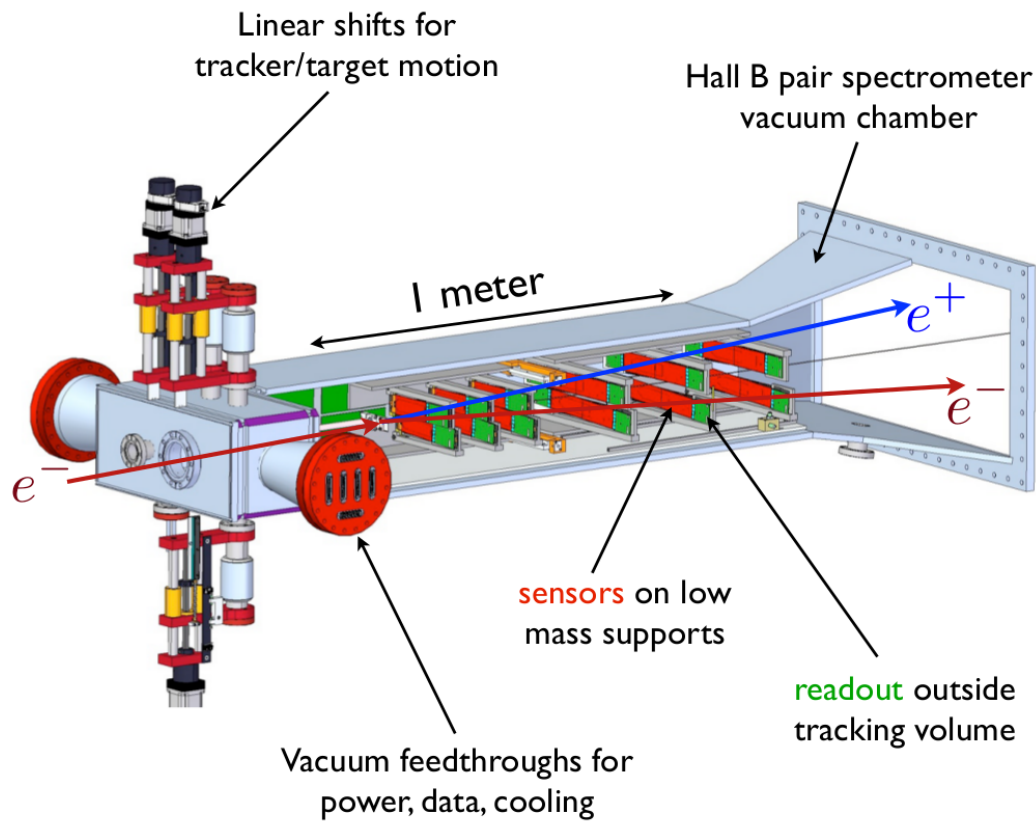


FIG. 2.7: Silicon Vertex Tracker and enclosing vacuum box.

### 2.1.4 Electronic Calorimeter

The sensitive parts of the Ecal are the lead-tungstate ( $\text{PbWO}_4$ ) crystals which are arranged in a grid. As a particle passes through a crystal, other particles are produced in an electromagnetic shower. If the initial particle is an electron or positron, then photons are produced via bremsstrahlung. If the initial particle is a photon, then electrons and positrons are produced via pair production. These secondary particles in turn produce more particles through bremsstrahlung and pair production, and the cycle continues to produce more particles. This continues until their photons do not have enough energy for pair production. As the electron and positron energies decrease, other processes besides bremsstrahlung dominate, and their remaining energy is deposited via excitation and ionization. The photons are collected in the avalanche photodiodes (APDs) where they are converted to an electrical signal. This signal is then amplified by the preamplifier before being digitized on one of the 16-channel Flash Analog to Digital Converter (FADC) boards, which read out samples every 4 ns.

An LED monitoring system employs bicolor LEDs mounted to each crystal in order to quickly monitor the performance of the entire Ecal. The schematics of a single crystal and its associated electronics and supports are shown in Figure 2.8 and the geometry of the Ecal as a whole is shown in Figure 2.9. Further details of the design, calibration, performance and operations of the Ecal may be found in [46].

### 2.1.5 Trigger System

When the Ecal's FADC signals cross a set threshold, then a fixed number of samples before and after the threshold crossing are summed, and the energy is calculated by multiplying the sum by the calibrated gain for that channel. Every 16 ns, the two

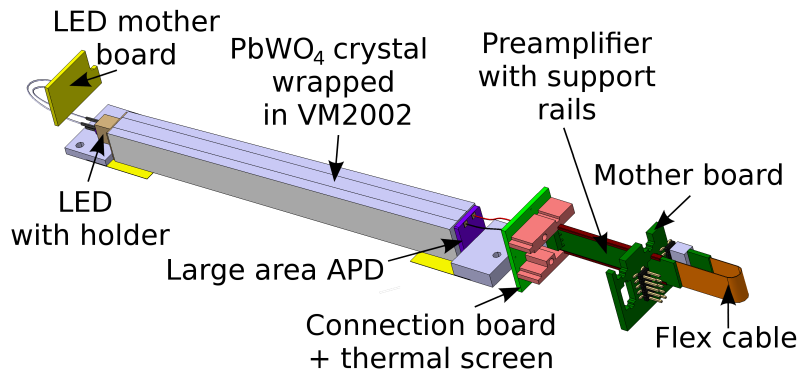


FIG. 2.8: Ecal crystal schematics. On the upstream side of each crystal is an LED for monitoring. The downstream end of the crystal is on the right. The crystals are wrapped in VM2002 foil in order to increase the yield of photons in the APDs at the downstream end of the crystal. The shape of the crystals is trapezoidal: 16 cm deep,  $1.3 \times 1.3$  cm in the front and  $1.6 \times 1.6$  cm in the back.

General Trigger Processor (GTP) boards take these crossing times and energies and searches for clusters consisting of a “seed” hit (whose energy is greater than all its neighbors) and the hits on neighboring crystals within a time coincidence window. The cluster information is then sent to the Subsystem Processor (SSP) board to make a trigger decision.

The SSP allows several triggers to run concurrently. The primary trigger, Pair 1, is optimized to find pairs of triggers consistent with the kinematics of  $A' \rightarrow e^+e^-$  events. The other triggers are used for calibration and diagnostics: Pair 0 (similar to the Pair 1 except with looser cuts), Single 0 and Single 1 (which require only one cluster matching certain criteria to trigger) and Pulser (which records a trigger after a fixed time interval regardless of whether the trigger finds a cluster). By default, the pulser interval is 10 ms, although there were special pulser runs where we used a higher pulser frequency.

When a trigger occurs, the trigger information is sent to the Trigger Interface

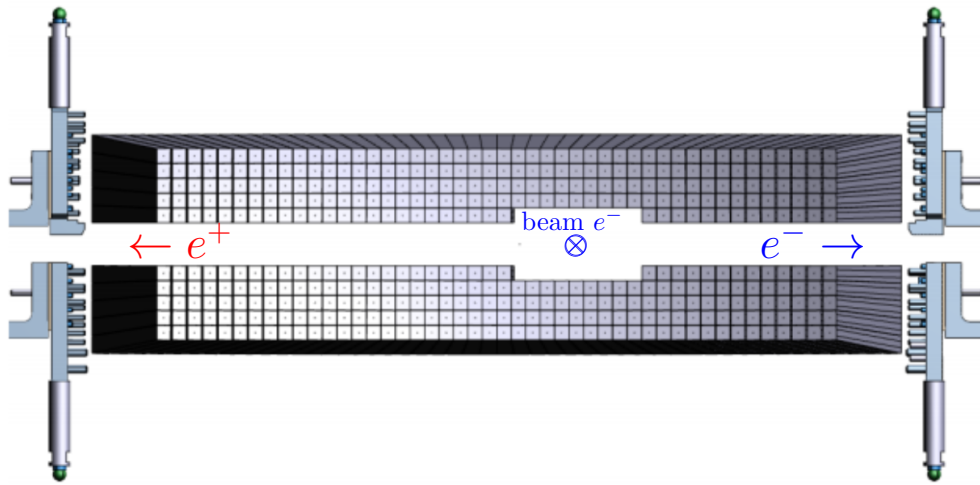


FIG. 2.9: Electronic Calorimeter schematics viewed from upstream. 9 crystals are removed from the innermost row in each half of the detector, due to high background rates near the beamline. The directions of curvature of positrons and electrons are shown as arrows. Also shown is the (approximate) position of the beam as it passes between the two halves of the Ecal. The beam electrons' trajectory is curved by a smaller amount than the rest of the electrons due to their higher momentum. The Ecal is not centered around the beamline, but rather about the line tangential to the beam at the target. This maximizes geometric acceptance, because dark photons are expected to be produced along the tangent line and to decay isotropically; thus the hit positions of the  $e^+$  and the  $e^-$  on the detector would be on opposite sides of that line.

(TI) board, which then sends out the trigger signal for all readout to be sent to file. In order to prioritize the Pair 1 trigger, the TI applies prescaling to the Single 1, Single 0 and Pair 0 triggers, recording only every  $N^{\text{th}}$  event, where  $N$  is the prescale factor for that trigger.

The Pair triggers require two clusters on opposite halves of the Ecal satisfying the following criteria (where the thresholds depend on the trigger configuration):

- $E_{\min} < E_{1,2} < E_{\max}$
- $|t_1 - t_2| < \Delta t_{\max}$
- $E_{\text{sum\_min}} < E_1 + E_2 < E_{\text{sum\_max}}$
- $|E_1 - E_2| < \Delta E_{\max}$
- $|\tan^{-1} \frac{x_1}{y_1} - \tan^{-1} \frac{x_2}{y_2}| < \theta_{\text{coplanarity}}$
- both clusters have  $\geq N_{\min}$  hits.
- $E + \sqrt{x^2 + y^2} F > E_{\text{dist\_slope}}$  for the cluster with the least energy<sup>2</sup>.

where  $E_{1,2}$ ,  $t_{1,2}$ ,  $x_{1,2}$  and  $y_{1,2}$  are the energies<sup>3</sup>, times, and positions in  $x$  and  $y$  of the top and bottom clusters,  $E_{\min}$ ,  $E_{\max}$ ,  $\Delta t_{\max}$ ,  $E_{\text{sum\_min}}$ ,  $E_{\text{sum\_max}}$ ,  $\Delta E_{\max}$ ,  $\theta_{\text{coplanarity}}$ ,  $N_{\min}$ ,  $F$  and  $E_{\text{dist\_slope}}$  are configurable parameters.

The Single 0 and Single 1 triggers only require one cluster with at least  $N_{\min}$  hits within energy between  $E_{\max}$  and  $E_{\min}$ .

---

<sup>2</sup>This cut is primarily meant to reduce wide-angle bremsstrahlung (WAB) reactions with low-energy photons produced at small angles (but just wide enough to enter the acceptance of the Ecal).

<sup>3</sup>The energies used in the trigger decision are calculated in the GTP using  $3 \times 3$  square groups of crystals, and do not take into account the energy deposited in crystals outside of the  $3 \times 3$  square, nor shower loss outside of the Ecal. Therefore, the energies calculated in the GTP are considerably smaller than the actual energy of the incident particles. The offline event reconstruction, detailed in Section 2.2, corrects for these effects.

Tables 2.1 and 2.2 summarize the configuration of each of the available triggers with default settings that we used in the 2015 and 2016 experimental run periods respectively. In 2016, we ran with different trigger settings to accommodate the higher beam energy in the latter run (2.3 GeV instead of 1.056 GeV). Additionally, the Single 1 trigger was modified so that the SSP applies a prescale to the triggers, dependent on the column of the seed hit of the triggering cluster, in conjunction to the TI prescale factor, which was 2. We did this so that the number of events seeded in each column on the Ecal would be on the same order of magnitude after prescaling. The different sections of the Ecal with their 2016 Single 1 prescale factors are listed in Table 2.3.

TABLE 2.1: Trigger configuration summary for the 2015 run period. These are the values of the variables defined in the version 7 trigger configuration, which was the default used in the 2015 Engineering Run period, during which the beam energy was 1.056 MeV.

Trigger Name	Single 0	Single 1	Pair 0	Pair 1	Pulser
TI Prescale	8192	2048	2048	1	1
$E_{\min}$ (MeV)	60	400	54	54	—
$E_{\max}$ (MeV)	2500	1100	1100	630	—
$N_{\min}$	3	3	1	1	—
$\Delta t_{\max}$ (ns)	—	—	16	12	—
$E_{\text{sum\_min}}$ (MeV)	—	—	120	180	—
$E_{\text{sum\_max}}$ (MeV)	—	—	2000	860	—
$\Delta E_{\max}$ (MeV)	—	—	1000	540	—
$\theta_{\text{coplanarity}}$ (deg)	—	—	180	30	—
$F$ (MeV/mm)	—	—	5.5	5.5	—
$E_{\text{dist\_slope}}$ (MeV)	—	—	100	600	—
Pulser Rate (Hz)	—	—	—	—	100



TABLE 2.2: Trigger configuration summary for the 2016 run period. These are the values of the variables defined in the version 8 trigger configuration, which we used during most of the 2016 Physics Run period, during which the beam energy was 2.3 GeV. For the first  $\sim 20\%$  of the production data we took in 2016, we were using a slightly looser trigger configuration (version 7<sup>4</sup>). The only two things we changed were in the Pair 1 trigger, increasing the  $E_{\text{dist.slope}}$  variable from 600 MeV to 700 MeV, and lowering the maximum coplanarity ( $\theta_{\text{coplanarity}}$ ) from 40 degrees to 35 degrees. \*The total prescale factor for the Single 1 trigger is the product of the TI's global prescale (2) and the SSP's cluster-position-dependent prescale (listed in Table 2.3).

Trigger Name	Single 0	Single 1	Pair 0	Pair 1	Pulser
TI Prescale	4097	2*	33	1	1
$E_{\text{min}}$ (MeV)	100	1300	150	150	—
$E_{\text{max}}$ (MeV)	2700	2600	1400	1400	—
$N_{\text{min}}$	3	3	2	2	—
$\Delta t_{\text{max}}$ (ns)	—	—	8	12	—
$E_{\text{sum.min}}$ (MeV)	—	—	500	600	—
$E_{\text{sum.min}}$ (MeV)	—	—	1900	2000	—
$\Delta E_{\text{max}}$ (MeV)	—	—	1100	1100	—
$\theta_{\text{coplanarity}}$ (deg)	—	—	180	35	—
$F$ (MeV/mm)	—	—	5.5	5.5	—
$E_{\text{dist.slope}}$ (MeV)	—	—	400	700	—
Pulser Rate (Hz)	—	—	—	—	100

TABLE 2.3: SSP prescale factors for the Single 1 trigger used in the 2016 dataset. The total prescale factor is the product of the SSP prescale factors in this table and the TI’s global prescale factor (which was 2).

column range	SSP prescale
-23 -13	1
-12 -9	80
-8 -7	1300
-6 -3	18000
-2 1	1300
2 5	80
6 23	1

## 2.2 Event Reconstruction

The reconstruction of events is performed offline using software based on the LC-SIM framework [47], which was originally developed for the Linear Collider Detector at SLAC. Here, the chain of reconstruction for HPS is outlined. The reconstruction of HPS events is currently being documented in more detail [48].

The first stage of the reconstruction chain is the Ecal reconstruction. This begins by fitting the raw ADC waveforms from the Ecal hits to a 3-pole function pulse shape,

$$ADC(t) = P + \frac{A}{2\tau^2}(t - t_0)^2 e^{-(t-t_0)/\tau}, \quad (2.1)$$

with width  $\tau$ , start time  $t_0$  and pedestal  $P$ . The measured energy of the hit is the product of the integral of the fitted pulse with the crystal’s gain factor. The time of the hit is then determined by the beginning of the fitted pulse-shape, with a small correction for the threshold crossing. Groups of hits on contiguous crystals of the Ecal

within a short time window (8 ns) are combined to make clusters. Figure 2.10 shows the number of hits per cluster. A preliminary calculation of the clusters' energy is performed by adding up the energies of the individual hits. Since the timing resolution of a hit is proportional to the energy of the cluster, the cluster time is defined to be the time of the most energetic hit (called the “seed hit”).

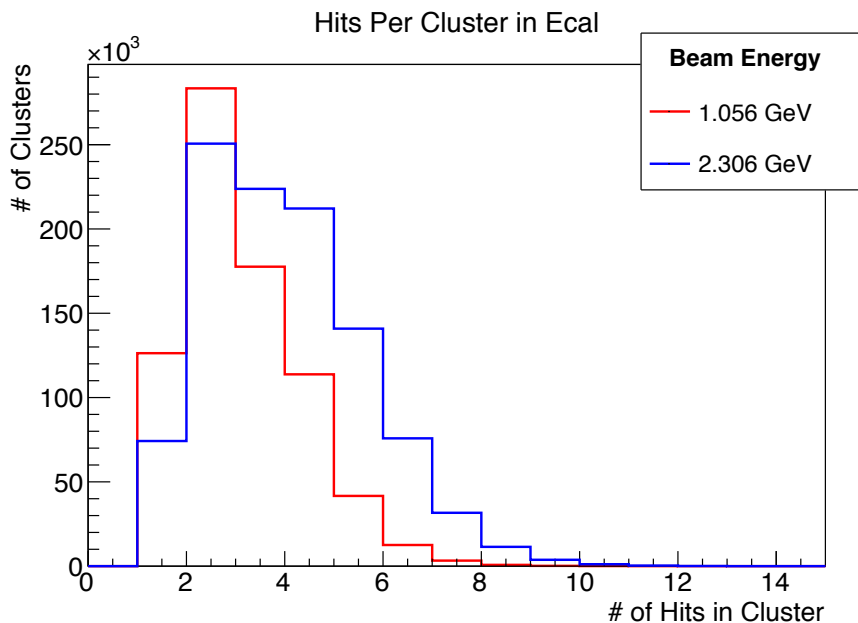


FIG. 2.10: Hits per cluster in the Ecal for events triggered by the Pair 1 trigger in the 2015 dataset (red, 1.056 GeV) and the 2016 dataset (blue, 1.056 GeV).

The next stage is the reconstruction of tracks in the SVT. Similar to the Ecal reconstruction, this begins by fitting ADC waveforms to a pulse shape. Since the response of the silicon strips is much slower than that of the Ecal modules, it is not uncommon for there to be more than one pulse within the fitting time-window on a given channel. If a fit to a single pulse fails, a fit with two pulses is performed, and then this becomes two fitted hits. If there are hits on adjacent strips within a short time window, then they are combined into a single hit. Then pairs of hits on the

stereo sublayers are combined with those on the axial sublayers to form 3 dimensional hits.

The track-finding algorithm uses four strategies for finding the track, each of which specifies a set of three layers on which to find a “seed” of three hits, another layer for “confirming” the seed track, and the remaining layers to “extend” the fit. The tracking begins by finding combinations of 3d hits on the three “seed” layers, and then fits the three hits to a helical trajectory. Next, the helix is extrapolated to the “confirm” layer. If there is a hit on the “confirm” layer consistent with the extrapolated trajectory, then the hit is added to the track candidate, and the helix fit is updated. If no hit is found on the confirm layer consistent with the trajectory, the candidate is rejected. The updated helix is then extrapolated to the “extend” layers and if there are hits in either of the “extend” layers that are consistent with the new extrapolated trajectory, then they are added to the track candidate and refit. If neither of the two “extend” layers has a hit consistent with the extrapolated trajectory, then the track candidate is rejected.

We allow tracks to have 5 or six hits because sometimes a hit will be missing from one layer of the track due to geometric acceptance or hit reconstruction inefficiency. The use of four strategies helps reduce the number of tracks that are lost due to missing a single hit. Duplicate versions of tracks that were found using more than one strategy are removed. Next, each of the tracks are refit using a “Generalized Broken Lines” (GBL) [49] algorithm to account for scattering inside the detector by treating the track’s trajectory not as a single helix, but as a collection of helical segments with small kinks (scattering angles) between them at each layer, and then minimizing both the hit residuals and the kinks.

The third stage of reconstruction is to match the clusters in the Ecal with tracks in the SVT. For each track, a loop is performed over all the clusters on the same half

of the detector as the track. The goodness of the track-cluster matching is quantified by

$$n_{\sigma}^2 = \left[ \frac{x_{\text{cluster}} - x_{\text{extrap}} - \mu_x(p)}{\sigma_x(p)} \right]^2 + \left[ \frac{y_{\text{cluster}} - y_{\text{extrap}} - \mu_y(p)}{\sigma_y(p)} \right]^2 \quad (2.2)$$

where  $x_{\text{cluster}}$  and  $y_{\text{cluster}}$  are the reconstructed position of the cluster, and  $x_{\text{extrap}}$  and  $y_{\text{extrap}}$  are the extrapolated position of the track at the Ecal face. We determined the functions  $\mu_{x,y}(p)$  and  $\sigma_{x,y}(p)$  by taking a large sample of clean tracks and clusters and then calculating the mean and standard deviations of the residuals of the difference in position between clusters and extrapolated track positions. These functions are calculated separately depending on whether the track is on the top or on the bottom, if it's positively or negatively charged, and whether or not the track has a hit in layer 6; each of them were fit to a 5th-order polynomial of the track momentum  $p$ . Under special circumstances, the second term in Equation 2.2 (the normalized residual in  $y$ ) is dropped from the calculation. This only happens if  $y_{\text{extrap}}$  is closer to the upper (lower) edge of the Ecal than  $y_{\text{cluster}}$  and all the hits in that cluster are on the row closest to the upper (lower) edge of the Ecal<sup>5</sup>. We do this because the reconstructed cluster position cannot be closer to the edge in  $y$  than the center of the edge crystal.

For every matched track-cluster pair, a correction factor for shower loss is then applied to the cluster. This correction factor depends on the distance of the extrapolated track from both the top and the bottom edge of the Ecal in  $y$ , and on whether the track is positively or negatively charged.

The final stage of reconstruction is fitting pairs of tracks on opposite halves of the detector as vertices. There are two configurations of pairs of tracks that are considered:  $e^+e^-$  (trident/ $A'$  candidates) and  $e^-e^-$  (Moller candidates). Three variations

---

<sup>5</sup>In columns -10 through -2, where the row-1 crystal is removed, the row-2 crystals are considered “edge” crystals.

of the vertex-fitting algorithm (one for each set of constraints) are performed for each track pair:

- Unconstrained: no constraints on the position of the common vertex of the two tracks.
- Beamspot-Constrained: the vertex position must be along a straight line from the target in the direction of the vector sum of the particles' momenta.
- Target-Constrained: the vertex must be at the target.

The reason for including three versions of the vertex fitting is that different analyses have different requirements. For instance, a bump-hunt analysis will require the target-constrained fit, whereas a displaced-vertex analysis would require either the beamspot-constrained or the unconstrained fit. The output of each of these fits includes the vertex-position, the refit track parameters, the invariant mass and momentum sum of the two particles, and a  $\chi^2$  statistic of the fits.

## CHAPTER 3

# Dark-Photon Signal and Background Reactions

The primary goal of HPS is to find  $A'$  events amidst a background of Bethe-Heitler and radiative trident events. However, several other types of reactions take place in this experiment, such as Møller events and elastic scattering off the nucleus, whose kinematics and cross-sections are useful for calibration in HPS by comparing the data to theoretical models and to Monte-Carlo simulation. This chapter describes each of the types of reactions that are important to this experiment. The Feynman diagrams of these reactions are shown in Figure 3.1. Chapter 4 describes the Monte-Carlo software and algorithms we use for simulating all of these events.

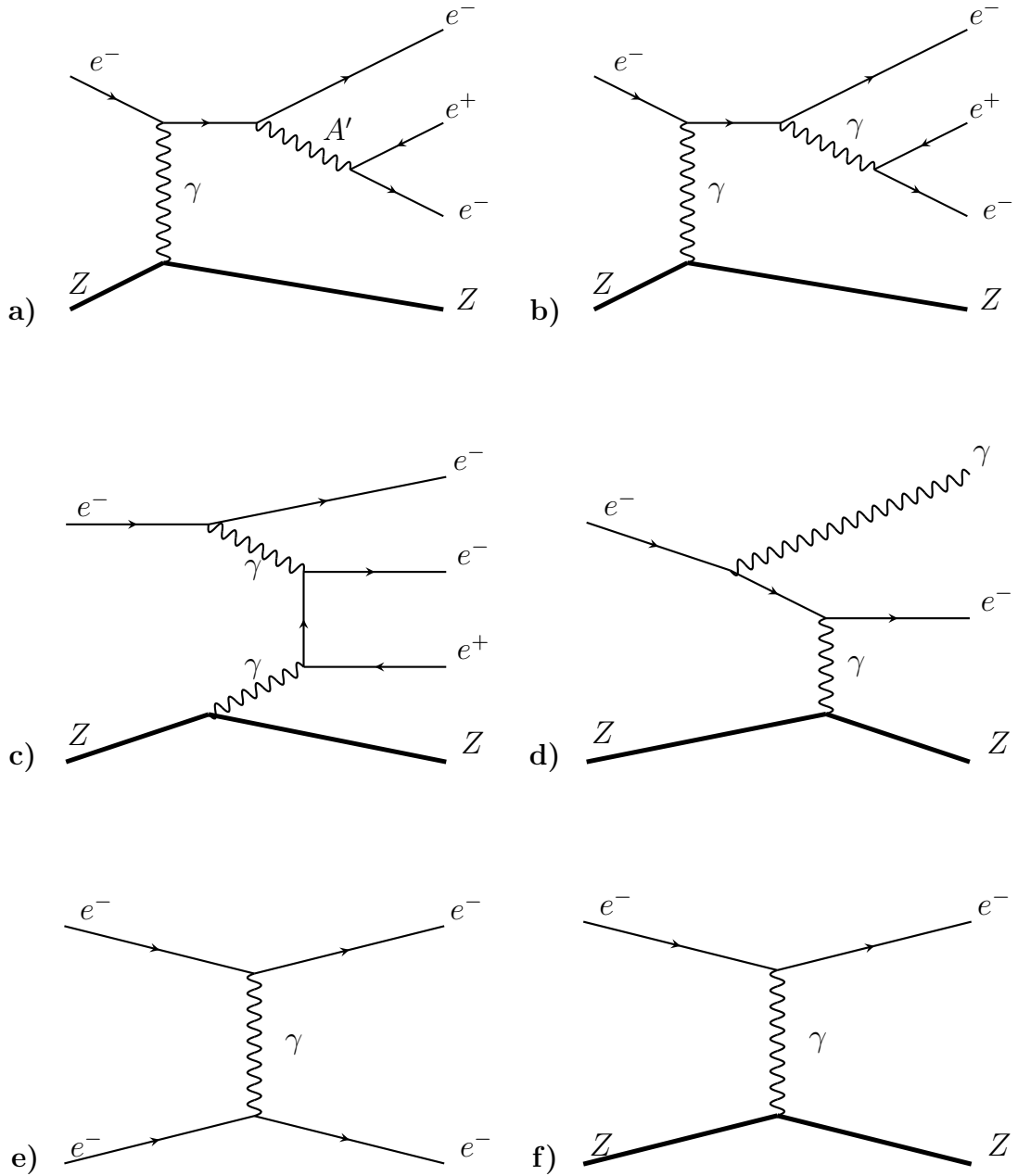


FIG. 3.1: Examples of Feynman diagrams of background and signal reactions in HPS. The thick line labeled represents the target nucleus, with charge  $Z$ . The diagrams shown represent: **a)**  $A'$  production followed by the decay of the  $A'$  into an electron positron pair, **b)** Radiative trident, **c)** Bethe-Heitler trident, **d)** Wide-angle bremsstrahlung (WAB), **e)** Møller scattering, and **f)** Elastic scattering off nuclei.



### 3.1 Radiative Tridents and $A'$ Production

The kinematics of radiative-trident events are identical to those of the  $A'$  signal we are looking for, except instead of having an on-shell dark photon, there is an off-shell ordinary photon. In both cases, an  $e^+e^-$  pair is produced, and the pair receives most of the beam's energy, while the scattered electron has a small energy and is usually not detected. The cross section of the  $A'$  events is proportional to that of the radiative tridents within a small invariant-mass window of width  $dm$  centered on the dark photon mass  $m_{A'}$  by Equation 3.1 (adapted from [11]).

$$\sigma_{A'} = \frac{d\sigma_{\text{rad}}}{dm} \frac{3\pi\epsilon^2 m_{A'}}{2N_{\text{eff}}\alpha} \quad (3.1)$$

In the above equation,  $N_{\text{eff}}$  is the effective number of decay modes (which equals 1 for masses below the muon-production threshold ( $m < 2m_\mu$ )),  $\frac{d\sigma_{\text{rad}}}{dm}$  is the differential cross-section of the radiative events as a function of mass, and  $\alpha$  is the fine-structure constant  $\approx \frac{1}{137}$ .

The dark photon (or a virtual photon in a radiative trident) may be produced before or after the electron scatters off the nucleus, leading to two diagrams for each type of reaction. These are shown in Figures 3.2 and 3.3.

There is a cutoff on the pair emission angle at  $\approx \max\left(\frac{\sqrt{m_{A'}m_e}}{E_0}, \frac{m_{A'}^{3/2}}{E_0^{3/2}}\right)$ , which is always smaller than the opening angle  $\approx \frac{m_{A'}}{E_0}$  for any kinematically-allowed  $A'$  mass ( $2m_e < m_{A'} < E_0$ ) [11].

HPS is primarily designed to detect electrons and positrons, but it may also be possible (with future upgrades, such as the muon detector proposed in Appendix A) to find  $\mu^+\mu^-$  pairs produced in the same way as the  $e^+e^-$  pairs. The muon detector in Appendix A was proposed in 2015, but was never built, since the results from BaBar

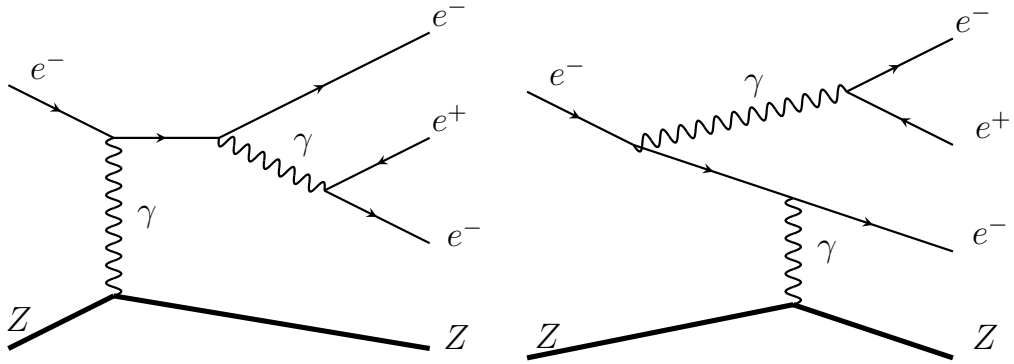


FIG. 3.2: Feynman diagrams for radiative tridents. When taking into account exchange diagrams, where the two final state electrons are swapped, there are actually 4 different diagrams contributing to the radiative cross-section.

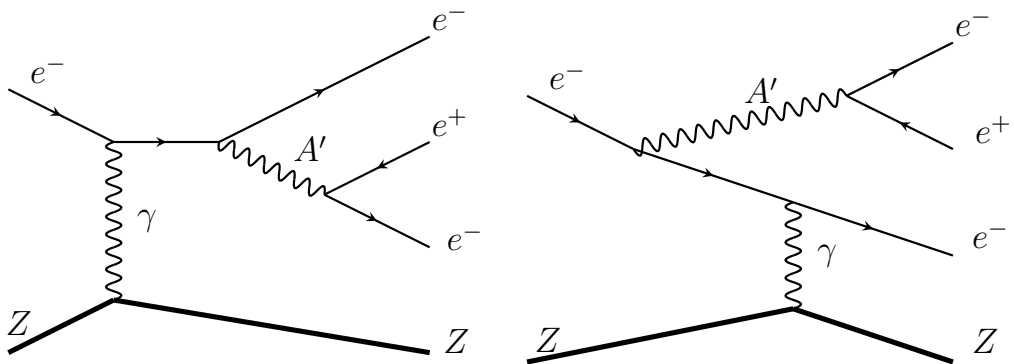


FIG. 3.3: Feynman diagrams for  $A'$  production. Unlike the virtual photon in a radiative trident, the dark photon produced in one of these reactions is on-shell, and depending on its coupling, it may travel several cm before decaying into the lepton pair.

[50], which were released at about the same time of the proposal, excluded the region of  $A'$  phase space that the muon detector would have enabled HPS to reach.

## 3.2 Bethe-Heitler Tridents

In addition to the radiative-trident events, there are also Bethe-Heitler tridents, which have the same types of final-state particles. The difference between these two types of events is that the former has one time-like virtual photon and one space-like virtual photon, whereas in the latter reaction, both virtual photons are space-like. Figure 3.4 shows the Bethe-Heitler tridents' Feynman diagrams. The Bethe-Heitler cross-section favors the kinematic range where the recoiling electron keeps most of the beam energy. The radiative cross section, on the other hand, favors the region of phase space with low-energy recoiling electrons and where the paired leptons's combined energy is at least 80% of the beam energy. Figure 3.5 compares the kinematics of the two types of tridents. While Bethe-Heitler events have a higher overall cross-section than their radiative counterparts, the ratio of Bethe-Heitler events to radiative events decreases with higher summed energy of the paired leptons. Therefore, to reduce the contribution of Bethe-Heitler events, we make a cut on the paired lepton energy sum.

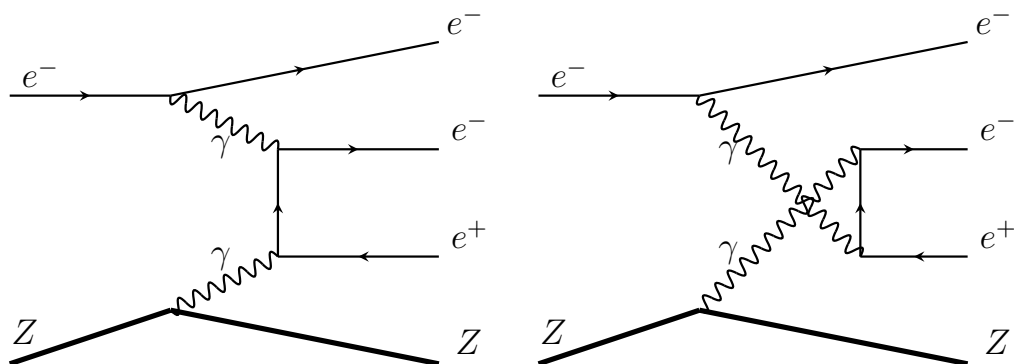


FIG. 3.4: Feynman diagrams for Bethe-Heitler tridents. Like the radiative events, there are exchange diagrams not shown here, where the two final-state electrons are swapped.

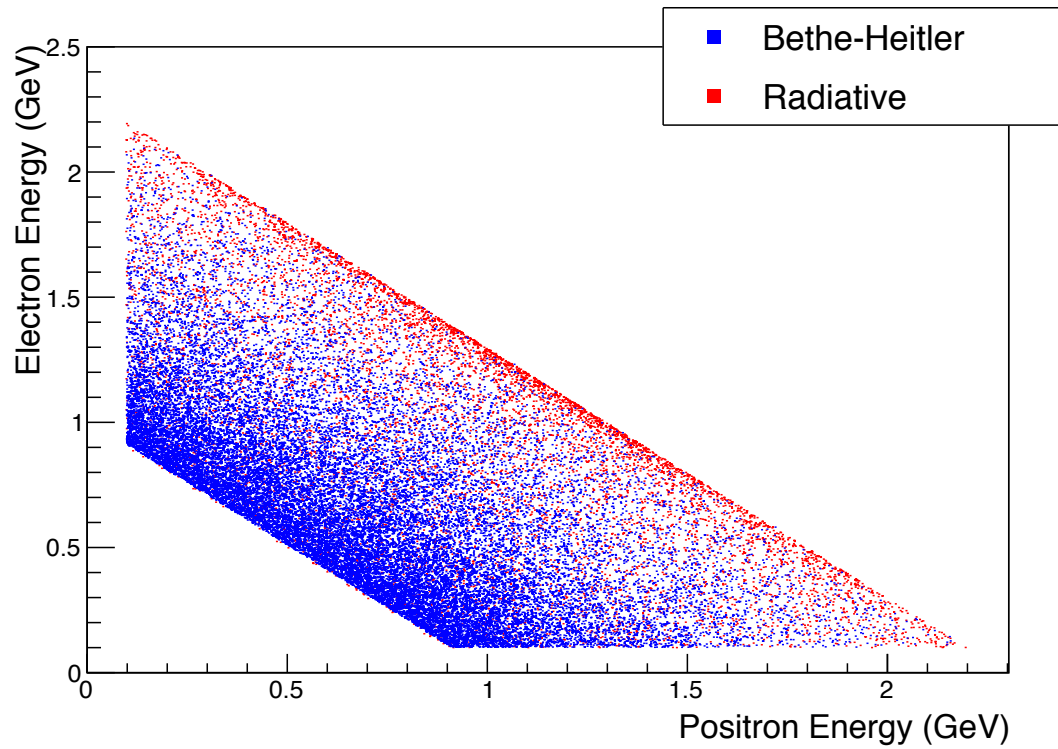


FIG. 3.5: Comparison of kinematics of Bethe-Heitler tridents and radiative tridents in a Monte-Carlo simulation using MadGraph5 [1]. Events where the  $e^+e^-$  pair's energy is less than 1 GeV, or where one of the particles has energy less than 100 MeV are removed from this plot due to generator-level cuts. The beam energy in this simulation is 2.3 GeV

### 3.3 Wide-Angle Bremsstrahlung

Wide-angle bremsstrahlung (WAB) events are another common type of background in HPS. In these events, a photon is produced in a reaction with the target, as shown in Figure 3.6. In our case, a bremsstrahlung reaction is considered “wide-angle” if both the scattered electron and the photon enter into the acceptance of the detector. If no other reaction takes place in the event, then we can easily exclude these events from the  $e^+e^-$  sample, since there is only one lepton found in the SVT, which is only sensitive to charged particles.

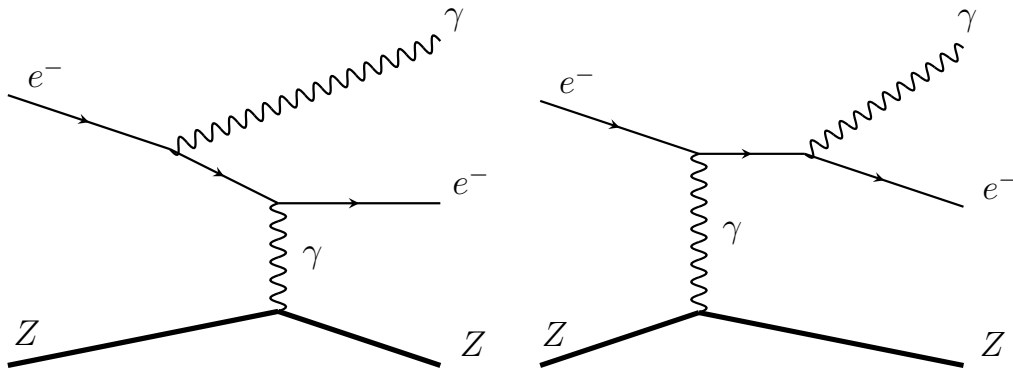


FIG. 3.6: Feynman diagrams for Wide-Angle Bremsstrahlung (WAB). The WAB photon may be emitted before or after the electron scatters off the target.

Often the photon reacts with material further downstream (either in the target or one of the SVT layers), converting to an electron-positron pair, as is illustrated in Figure 3.7. If the positron produced in this reaction receives most of the energy of the photon, then the electron produced will often have too little momentum to be reconstructed in tracking. In such a case, the two particles that will be detected are the positron and the original electron. The rate of these “converted WAB” events is comparable to that of tridents, and therefore they contribute significantly to the background in HPS. The contribution from the converted WABs to the total  $e^+e^-$

sample can be reduced by requiring that the positron track have a hit in the first layer of the SVT, and also by requiring that the positron track extrapolates to the beam-spot on the target.

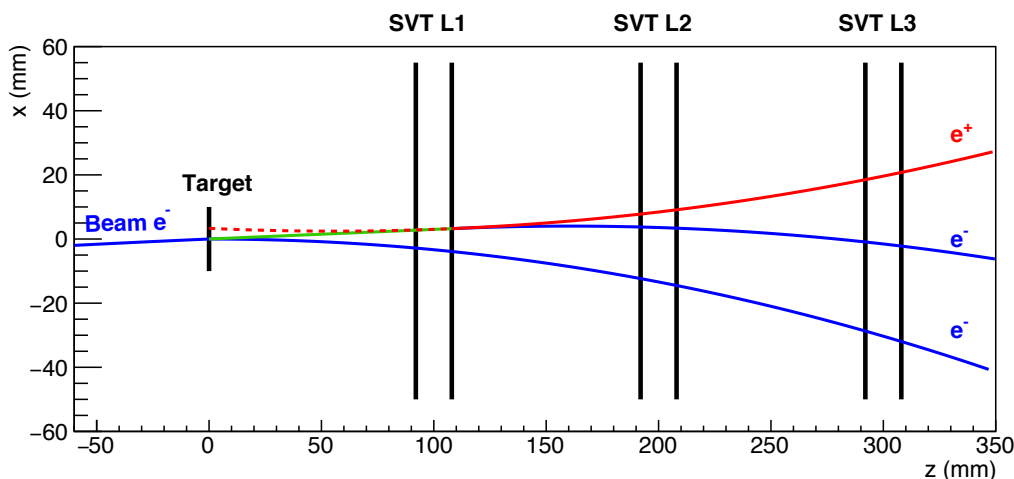


FIG. 3.7: Illustration of a WAB conversion. Blue tracks indicate the electron tracks, and the red curve is the positron track. The beam electron scatters off the target, producing a photon (green) via bremsstrahlung. The photon converts in the first SVT layer into an electron-positron pair. The red dashed curve shows the extrapolation of the positive track back to the target  $z$  position. Curvatures of tracks have been exaggerated in this illustration to visualize the offset in  $x$  of the extrapolated positron track. Only layers 1-3 are shown.

### 3.4 Møller Scattering

In Møller events, an electron from the beam scatters elastically off of one of the electrons in the target (Figure 3.8). Both of these two electrons may be detected and they are indistinguishable from one another. The scattering angles  $\theta_{1,2}$  and energies  $E_{1,2}$  (or momenta  $\mathbf{p}_{1,2}$ ) of the two electrons in the lab frame are related to one another by Equations 3.2 and 3.3. It is interesting to note that if one measures just one of

these 4 variables, it is possible to predict the value of all three of the other kinematic variables. That is,

$$E_i = \frac{E}{1 + \frac{2E}{m_e} \sin^2\left(\frac{\theta_i}{2}\right)} \quad (3.2)$$

$$E_1 + E_2 = E \quad (3.3)$$

$$\mathbf{p}_1 + \mathbf{p}_2 = \mathbf{p}$$

where  $E$  and  $\mathbf{p}$  are the beam energy and momentum. From these equations, one can derive the relation between the angles of the two particles,

$$\sin\left(\frac{\theta_1}{2}\right) \sin\left(\frac{\theta_2}{2}\right) = \frac{m_e}{2E}, \quad (3.4)$$

as well as calculate the invariant mass of the electron pair:

$$m_{\text{Møller}} = \sqrt{2m_e(E + m_e)}. \quad (3.5)$$

Since invariant mass of the pair depends only on the beam energy, it serves as a useful reference point in determining the resolution of HPS's mass reconstruction. This formula yields an invariant mass of 32.9 (48.4) MeV when the beam energy is 1.056 (2.306) GeV. In future HPS runs with higher beam energies (4.4 and 6.6 GeV), the opening angle between Møller pairs will be too small for us to be able to detect both electrons without modifications to the detector.



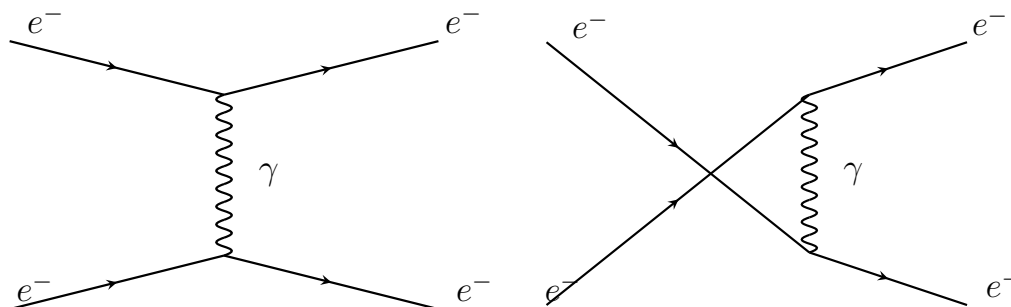


FIG. 3.8: Feynman diagrams for Møller scattering.

### 3.5 Full-Energy Electrons

There are three types of scattering in which the energy difference between the beam and the scattered electron is much smaller than the resolution of our detectors:

- elastic scattering of a beam electron off a nucleus in the target,
- quasielastic scattering of the beam electron scatters off one of the nucleons in a target nucleus, knocking it out of the nucleus,
- inelastic scattering of the beam electron off the target nucleus, leaving the nucleus in an excited state, a few MeV above the ground state.

Collectively, these reactions are called “Full Energy Electron” (FEE) reactions. Section 6.1 describes all three types of FEE reactions in detail.

# CHAPTER 4

## Monte-Carlo Simulations

In order to understand our detector, we simulated all types of reactions described in Chapter 3 following a 4-step procedure. First, a large number of events are generated for reactions between beam electrons and the target, producing the final 3-dimensional momenta of all of the output particles. Then the interactions between the particles and the detector elements are simulated as the particles travel through the detector and the magnetic field. Thirdly, the readout of signals is simulated along with the trigger. Finally, the simulated event files are reconstructed using the same code as used to reconstruct the actual data.

### 4.1 Event Generators

We employ six generators for various types of reactions:

**tritrig** Bethe-Heitler and radiative tridents. The name is short for “**trident trigger**”, and refers to the fact that this generator contains loose kinematic cuts to select only the events that might create a trigger.

**RAD** Radiative tridents only.

**wab** Wide-angle bremsstrahlung.

**ap**  $A'$  production, with decay into an electron positron pair.

**beam** miscellaneous interactions between the beam and the target, including elastic and quasielastic scattering off the nuclei, as well as Møller scattering.

**moller** Møller scattering ( $e^-e^- \rightarrow e^-e^-$ ). This generator is the same as the beam generator, except it requires at least two final-state electrons. This generator also produces some events with background electrons in addition to the Møller pair.

Our trident generators “tritrig” and “RAD” are based on MadGraph5 [1]. We attempted to use MadGraph5 for the WABs and  $A'$  production events as well, however there were problems with this generator, so we have continued to use the MadGraph4 [51] for our generator for those types of events. For “beam” interactions (ie, full-energy electrons) and Møller electron pairs we used EGS5 [52].

We generated our  $A'$  both with prompt decay (for the bump hunt analysis) and with decay length  $c\tau = 10$  mm (for the displaced-vertex analysis). For the 2.3 GeV beam energy, our generated  $A'$  masses are 50, 55, 60, 65, 70, 75, 80, 85, 90, 95, 100, 125, 150, 175, 200, 225 and 250 MeV.

## 4.2 Interaction Between Particles and Detector Elements

We used an executable called SLIC [53] to simulate the motion of the particles through the detector elements and the magnetic field. A model of the detector geometry is provided using a GDML file. SLIC handles the curvature of the particles’ paths

through the magnetic fields, energy loss, and multiple scattering using the Geant4 [54–56] software package. It also handles the conversion of WAB photons into electron positron pairs (see Figure 3.7). SLIC also records the energy deposition in each sensitive detector element for every particle above a small threshold energy.

Before running SLIC, we change coordinate systems from the generator frame to the lab frame by rotating all particles’ initial momenta by 30.5 mrad in the  $xz$  plane, since the nominal angle between the beam and the  $z$  axis is 30.5 mrad at its intersection with the target.

### 4.3 Readout

We used our own proprietary readout simulation program (based on the LCSIM framework [47]) for reading out simulated waveform signals from the detector and simulating the triggers. For tridents,  $A'$  and WAB simulations, we simulated the Pair 1 trigger. For the Møller simulations, we used the Single 0 trigger<sup>1</sup>, since the opening angle for Møller pairs with a 2.3 GeV beam is so small that usually only one of the electrons hits the Ecal.

For further realism, we included an option in the readout to add additional reactions from the wab, beam and tritrig generators mixed into the same events. These dirty versions are known as “wbt” versions of the readout, after the first letters of the names of the generators. The number of additional reactions per event is Poisson distributed, with the mean of the distribution equal to the number of additional reactions expected for incident particles within the same beam bucket (2 ns), given the event cross-sections, beam current, and target thickness. One purpose for simulating this is to study the effects of pile-up; that is, when particles from more

---

<sup>1</sup>which requires only one cluster with a very loose energy cut.

than one reaction hit the same channel in either the SVT or the Ecal and the signal waveforms from the two particles overlap. If the particles are sufficiently separated from each other in time, it is possible to reconstruct both signals. Otherwise, the fit to the signal waveform fails, and the hit is lost. Since we require both stereo and axial hits in at least five out of six tracking layers, pileup could significantly reduce our efficiency.

## 4.4 Reconstruction

Monte-Carlo simulations use the same reconstruction code as the data<sup>2</sup>, with a few small changes. First, since all our simulations assume proper run conditions, the filter for good event flags is disabled. Secondly, when reconstructing data, running averages of the pedestals are calculated for each channel of the Ecal. These pedestal values are then used in pulse fitting. This is necessary for the data, since the pedestals change on time scales much longer than the trigger window. However, the Monte Carlo does not simulate these changes in pedestal, so its reconstruction does not include the pedestal averaging. Since sample-noise is not simulated in the Ecal readout, the cluster-time resolutions are much better in Monte Carlo than in the data. Therefore, the Monte-Carlo reconstruction includes additional code to smear out the cluster time in order to match the resolution in the data.

Since simulated readout does not include channel-dependent time delays in the SVT, the Monte-Carlo reconstruction does not include corrections for these delays. Similarly, since we simulate the pulse-shapes in the Ecal with the same widths for all channels at readout, the reconstruction code fits the pulse-shapes with that same width, rather than using channel-dependent calibrated widths from a database.

---

<sup>2</sup>which is described in Section 2.2.

# CHAPTER 5

## Data Taken in HPS

HPS has taken preliminary data at two beam energies: 1.056 GeV in 2015, and 2.306 GeV in 2016. Due to technical difficulties and scheduling issues, the sizes of the datasets at both beam energies are only a small fraction of our goal. Nonetheless, these preliminary runs have allowed us to calibrate our detectors, debug and develop our reconstruction software and analysis framework, and will therefore be useful for much larger future datasets at the same and higher beam energies. Table 5.1 summarizes the conditions of these two data-taking periods. In each dataset, we took data in  $\sim 2$  hour chunks called “runs”. The raw data in each run are divided into EVIO format [57] files, of up to  $\sim 2$  GB ( $\sim 400$  million events) per file.

We employed a blinding policy, using every tenth file in each run for calibration of our analyses (with the exception of special calibration runs with different run conditions than usual). This protects us from biasing ourselves towards certain results. Once our collaboration is satisfied with all aspects of the analyses, we “unblind” the analysis, rerunning it on the full dataset<sup>1</sup>. We have already unblinded the 2015

---

<sup>1</sup>Strictly speaking, a “pure” blinding policy would only use the 90% in the final analysis that is not part of the 10% used in the blinded analysis. However, our collaboration had already agreed

dataset for both the bump-hunt analysis and the displaced-vertex analysis. We found that the 2015 dataset was too small to exclude any values of the  $A'$  mass and couplings for the displaced-vertex analysis [58, 59]. For the bump-hunt analysis on 2015 data, we were only able to exclude a region in mass-coupling phase space that had already been excluded by earlier experiments. However, with a much larger future dataset ( $\sim 4$  PAC weeks<sup>2</sup> at each beam energy), and several proposed upgrades, HPS could exclude regions in the mass-coupling phase space through both displaced-vertex and bump-hunt analyses that have not been excluded by other experiments.

As of the time of this writing, we have not unblinded the 2016 dataset for a displaced-vertex search nor the bump hunt. All results of the bump-hunt analysis for the 2016 dataset presented in this dissertation use 10% of the data, rather than the full dataset. With the full 2016 dataset, we expect to set upper limits on  $\epsilon^2$  that are marginally better than obtained in other experiments at some masses.

Figure 5.1 shows the integrated beam charge during each of the two run periods.

In both run periods, we took special calibration runs in addition to the production running, using different run conditions than usual, for instance, using a carbon target instead of a tungsten target. These carbon-target runs were useful for comparing the measured elastic scattering cross sections to a model and estimating the overall efficiency of the detector (Chapter 6). Additionally, it is easier to select Møller scattering events in carbon-target runs, since the cross-sections of Møller scattering is proportional to the atomic number  $Z$ , whereas most cross-sections of electron-nucleus scattering scale with  $Z^2$ .

During the beam down-time, two other types of calibration runs were performed in order to calibrate the gains in the Ecal. In the “LED” runs, LEDs mounted inside

---

upon using the full 100% in the final unblinded analysis.

<sup>2</sup>That is, 4 weeks with Physics Acceptable Conditions, ie, the beam is on, the SVT bias voltage is on and the SVT is at its nominal position.

TABLE 5.1: Data taking parameters for the 2015 and 2016 HPS runs. The first 0.47 PAC days ( $362.7 \text{ nb}^{-1}$ ) of the 2015 dataset were taken with the SVT Layer 1 at  $\pm 1.5 \text{ mm}$  in  $y$  from the beam line, out of caution to avoid exposing the SVT to excessive beam background. Afterward, when we found that it was safe to move it to the nominal position ( $\pm 0.5 \text{ mm}$  in  $y$  from the beam line), we did so and took the remainder of the 2015 data at the 0.5 mm position. The values in the table represent the total at both SVT positions. The entire 2016 dataset had the SVT at the 0.5 mm position.

Run period #	2015	2016
Beam energy (GeV)	1.056	2.306
Nominal beam current (nA)	50	200
Target	$4.4 \mu\text{m W}$	$4.4 \mu\text{m W}$
PAC days	2.17	3.9
Luminosity ( $\text{nb}^{-1}$ )	1529	10753

the Ecal were used to produce a signal in each Ecal crystal with a known energy. In the “cosmic” runs, the source of the signals were cosmic rays, which deposit a predictable amount of energy in the Ecal due to minimum ionization. These were our initial source of calibration for the Ecal gains; subsequent fine tuning was done using full-energy electrons as well as the  $e\gamma$  energy sums in wide-angle bremsstrahlung events.

During our data-taking periods, we set up a data quality management (DQM) system that generates histograms using a fraction (roughly 20%) of the data we took. There was a latency of only a few days between when the data was taken and when it was processed using DQM, allowing us to make informed decisions about whether or not to tweak certain data-taking parameters, such as beam current and trigger configurations to maximize the number of good events taken per hour. Some examples of these histograms include the position, energy and size of clusters in the Ecal, the sum of the energies of paired clusters, the direction, curvature and initial



positions of the tracks, and the momenta of reconstructed particles.

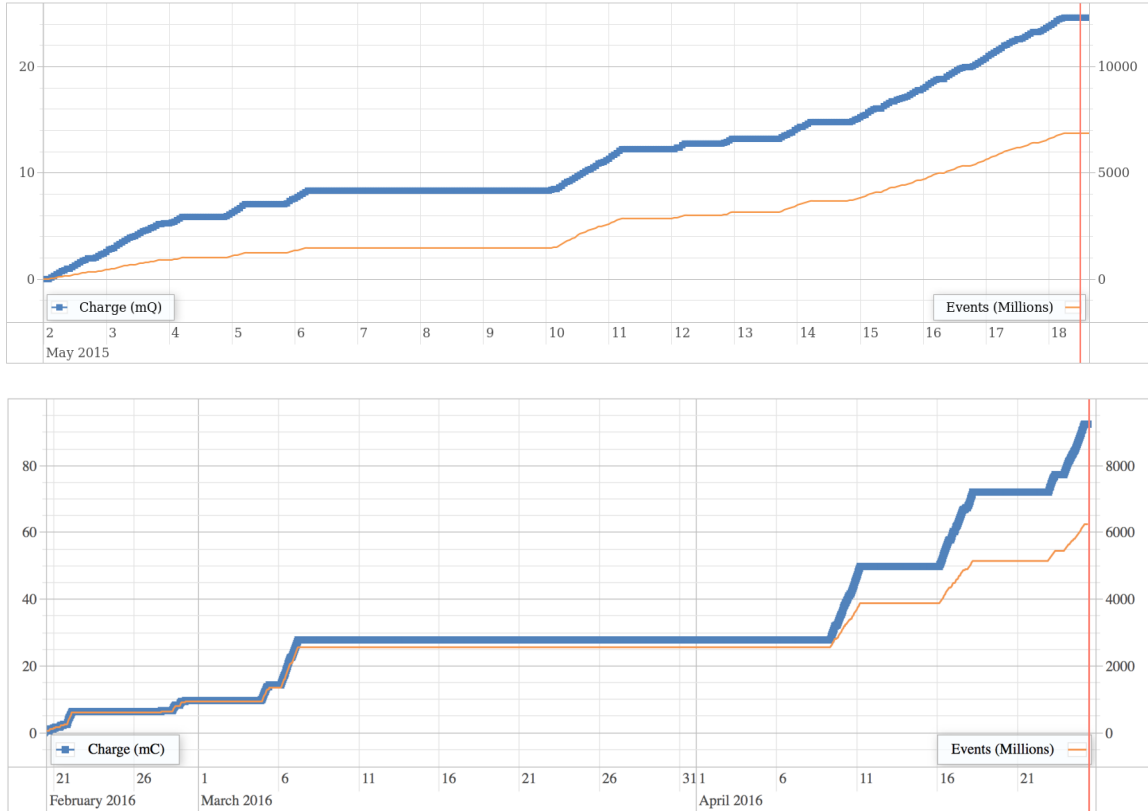


FIG. 5.1: Estimated integrated charge and event count during 2015 (top) and 2016 (bottom) HPS runs, not corrected for data quality. HPS was only assigned limited time-slots in which to collect data, when workers were not in Hall-B doing construction on CLAS-12. In the 2015, our time-slots consisted of nights and weekends, but in 2016 our data-taking time-slots were restricted to weekends only.

## 5.1 Calibration Methods

For our preliminary energy calibrations of the Ecal, we triggered the Ecal on cosmic ray muons coming from above the detector during our accelerator downtimes. The spectrum of energy deposition by the muons in the Ecal is sharply peaked, since

the muons minimally ionize the crystal. After taking some data and reconstructing it we fine-tuned the energy calibrations using elastically scattered electrons and WABs. The energy spectrum of elastically scattered electron energies should peak at the beam energy. Additionally, in WAB events, the energies of the electron and the photon should add up to the beam energy. (Nuclear recoil is negligible in both these two cases). After taking into account that these two types of measurements should peak at the beam energy, we adjusted the gains of each crystal of the Ecal accordingly.

We determined the correction factor to use for shower loss near the edges of the calorimeter using Monte-Carlo simulations. For the timing calibration of the Ecal, we compared the times of the radio-frequency signal from the accelerator with the start times of the pulses in each crystal's channel and adjusted the time offsets for each channel accordingly. Additionally, we employed a monitoring system using red and blue LEDs mounted to each crystal. This allowed us to generate pulses on each crystal individually with variable widths and amplitudes at two different wavelengths of light, and measure the response for each channel [46].

For the SVT alignment (i.e., to compensate for deviations between the nominal positions of the SVT sensors and their actual positions), we ran the program Millipede [60, 61] on our datasets using both curved tracks (from normal runs when the Pair Spectrometer magnet was on) and straight tracks (from special calibration runs when the magnet was turned off) as our input. The program then determined if there were any residuals to the fits that needed to be compensated. Additional constraints required that the elastic peak of the momentum distribution be at the beam energy and that the invariant mass of the Møller electron pairs be  $\sqrt{2E_{\text{beam}}m_{\text{electron}}}$ . The alignment for the 2016 dataset is in a preliminary stage and work is underway to try to improve beyond the current alignment for future reconstruction passes on the data.

## 5.2 Event Flags

Within good runs in both datasets, there were some events of poor quality that have been omitted from our analyses. For instance, events taken when the SVT was retracted from its nominal position or the bias voltage was turned off (which was the case just after a beam trip), are flagged. Also,  $\mathcal{O}(2\%)$  of events were affected by burstmode noise; that is when an event hasn't finished being read out through the DAQ before the next event is being read in. There were also some files with event header problems that needed to be omitted. Finally, during a large portion of the 2015 run, there was a latency bug affecting events with 2 out of 6 trigger phases, which was fixed just after it was discovered. Events with any of the problems listed here were flagged as “bad” and omitted from analysis.

## CHAPTER 6

# Efficiency Measurements Using Full-Energy Electrons

A bump-hunt analysis can viably find a resonance (or set limits on the size of the resonance) only if the invariant mass spectrum in the background-only case is smooth. Irregularities in the efficiency of the detector at specific angular ranges may cause unwanted bumps, jumps or dips in the invariant mass spectrum. The analysis in this chapter looks for such irregularities in the combined efficiency of the Ecal and SVT, by comparing the measured cross-sections of full-energy electrons (FEEs) to a theoretical model. The data used for this analysis were the carbon-target calibration runs (#5779 for the 1.056 GeV dataset and #8054 for the 2.306 GeV dataset) since the  $^{12}\text{C}$  nucleus has been more extensively studied than tungsten's five naturally occurring isotopes, and therefore it is easier to model the predicted cross sections for carbon than for tungsten. In my model, I included contributions from elastic scattering, quasielastic scattering, inelastic scattering to the two most significant<sup>1</sup>

---

<sup>1</sup>i.e., the ones with the largest cross sections

discrete excited states of the carbon nucleus, and  $\Delta$  resonances. I performed this analysis separately for the 2015 (1.056 GeV beam) and the 2016 (2.306 GeV beam) datasets. For both datasets, the modeled cross sections are expected to be accurate to within 15%.

## 6.1 Model

There are several types of processes that contribute to the total FEE cross section. The most common type of reaction is elastic scattering off the nucleus. There are also quasi-elastic scattering, where the electron elastically scatters off only one of the nucleons in the nucleus (knocking it out of the nucleus), and inelastic scattering, in which the nucleus enters an excited final state which is a few MeV above the ground-state. In other electron-nucleus scattering experiments, it is possible to distinguish between these three types of events using the energy loss; however, neither the energy resolution in HPS’s Ecal ( $\sim \frac{4\%}{\sqrt{E/(1 \text{ GeV})}}$ ), nor the momentum resolution of the SVT ( $\sim 7\%$ ), is precise enough to make this distinction.

Additionally, there is the  $\Delta$  resonance, where an individual nucleon is excited to a spin 3/2 state. This resonance is wide enough that a non-negligible number of  $\Delta$ -resonance reactions occur which pass our energy cut, despite the nearly 300 MeV separation between the elastic and  $\Delta$ -resonance peaks. Finally, sometimes a low-energy photon is produced via bremsstrahlung in any one of these types of events. To account for this, we need to apply “radiative corrections” to the data. This involves multiplying each component of the cross section by a factor of  $(1+\delta)$ , where  $\delta$  depends on the energy cut, the type of event and the energy resolution of the event.

Figure 6.1 shows the cross sections from the models for each dataset, divided by the Mott-scattering cross section.

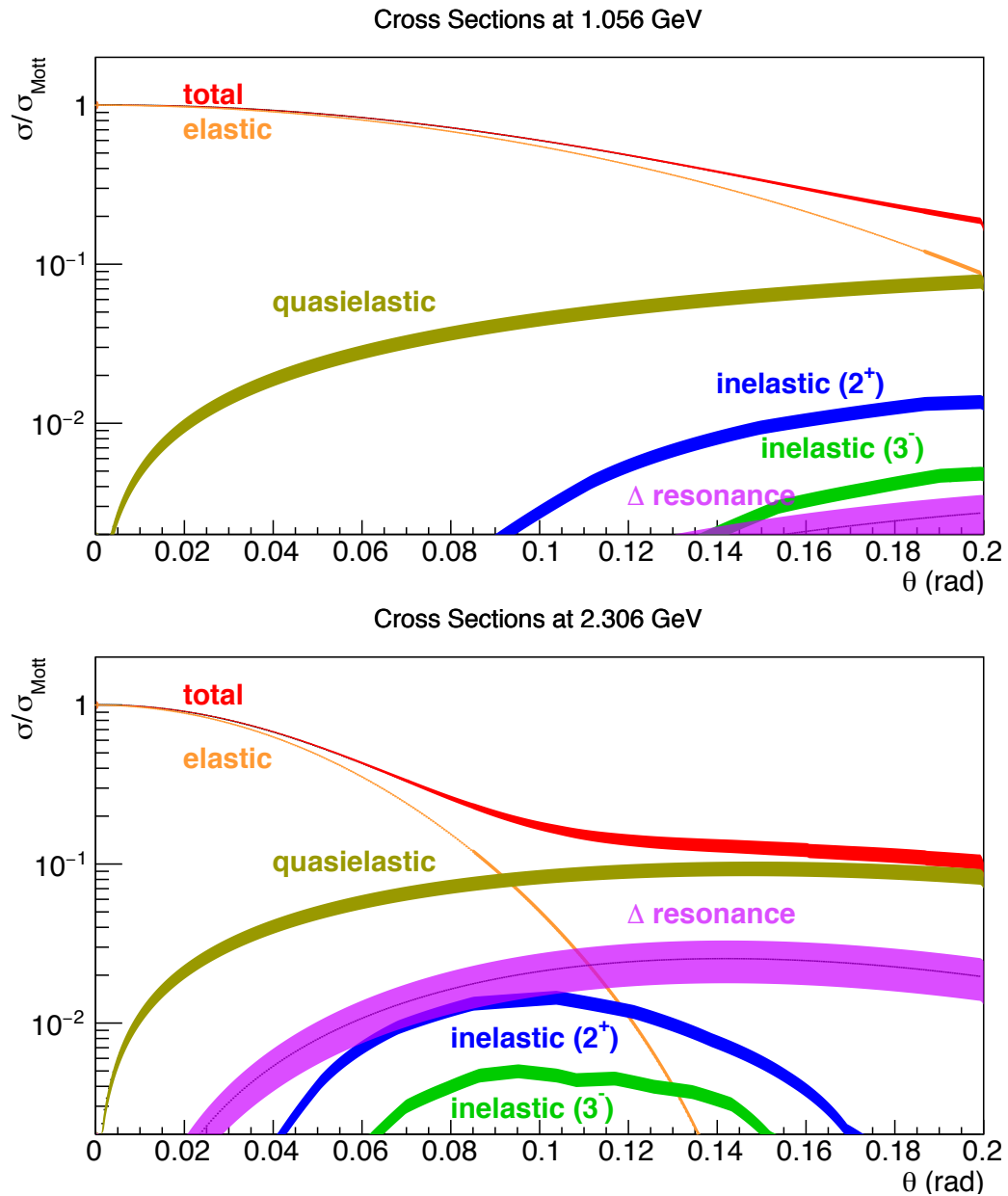


FIG. 6.1: Modeled cross sections for FEEs produced on a  $^{12}\text{C}$  target, evaluated for a 1.056 GeV beam (top) and a 2.306 GeV beam (bottom). Shaded regions show systematic uncertainties on each component of the total cross section. Radiative corrections are not included in this plot. The inelastic scattering reactions shown excite the nucleus to the  $2_1^+$  (4.43 MeV) and  $3_1^-$  (9.6 MeV) excited states.

### 6.1.1 Elastic Scattering

If the momentum transfer is very small ( $q \ll \hbar c/R_{rms}$ , where  $R_{rms}$  is the rms charge radius of the nucleus), then the elastic cross section may be approximated using the Mott-scattering cross section,

$$\left(\frac{d\sigma}{d\Omega}\right)_{\text{Mott}} = \frac{Z^2\alpha^2}{4E^2 \sin^4 \frac{\theta}{2}} \cos^2 \frac{\theta}{2} \left( \frac{1}{1 + \frac{2E}{M} \sin^2 \frac{\theta}{2}} \right), \quad (6.1)$$

which is a relativistic extension of the Rutherford scattering formula. Here  $E$  is the beam energy,  $M$  is the nucleus mass,  $\theta$  is the scattering angle, and  $Z$  is the atomic number of the nucleus.

It should be noted that Equation 6.1 is only valid for very small energy transfer, and does not take into account the internal structure of the nucleus or nucleon. The more appropriate formula for the cross section for elastic scattering off a nucleus or a nucleon is called the Born approximation:

$$\frac{d\sigma}{d\Omega} = \left(\frac{d\sigma}{d\Omega}\right)_{\text{Mott}} |F(Q^2)|^2 \quad (6.2)$$

where  $F(Q^2)$  is the elastic form factor, a function that describes the nucleus or nucleon's internal structure, which depends on the square of the momentum transfer,  $Q^2$ . For elastic scattering, the momentum transfer is given by

$$Q^2 = 4E^2 \sin^2 \frac{\theta}{2} \left( 1 + \frac{2E}{M} \sin^2 \frac{\theta}{2} \right)^{-1}. \quad (6.3)$$

$F(Q^2)$  is related to the electric charge density by a Fourier transformation<sup>2</sup>:

$$F(Q^2) = \frac{4\pi}{q} \int_0^\infty r \rho(r) dr \quad (6.4)$$

## Form Factors of Carbon

The elastic form factor for the  $^{12}\text{C}$  nucleus can be parameterized by [62]:

$$F(Q^2) = \sum_{i=1} a_i (-1)^{i+1} \frac{4\pi R^2 \hbar c \sin \frac{QR}{\hbar c}}{Q \left( i^2 \pi^2 - \left( \frac{QR}{\hbar c} \right)^2 \right)} \quad (6.5)$$

where  $a_i$  are the Fourier-Bessel coefficients and  $R$  is the cutoff radius, which in this parameterization is 8 fm.

At the range in  $Q^2$  accessible to HPS with up to a 2.306 GeV beam energy, the only inelastic transitions with a significant cross section are from the ground state to the  $2_1^+$  (4.43 MeV) and the  $3_1^-$  (9.6 MeV) excited states. The form factors I used for these transitions are from [63] and [64], respectively. Both cross sections are very small compared to the combined elastic and quasielastic cross section.

### 6.1.2 Quasielastic Scattering

The cross section of quasielastic scattering off an individual nucleon is then analogous to elastic scattering off a nucleus with a few modifications. First, the atomic number  $Z$  is replaced with one, and the nucleus's form factor is replaced with that of the nucleon. Secondly, the quasielastic cross section is suppressed by ‘‘Pauli blocking’’; that is, the Pauli exclusion principle prevents the nucleons from entering an already occupied state, thereby decreasing the overall cross-section.

---

<sup>2</sup>Strictly speaking, this is only true in the Breit frame, where the initial and final momentum of the electron are the reverse of one another. However, since the beam energy is much smaller than the mass of the nucleus, using this as an approximation is valid



To calculate the amount of Pauli-blocking, I use the shell approximation, which treats the nucleus as if it is a Fermi gas at the ground state. In this approximation, all the nucleon momentum states up to the Fermi momentum,  $k_F$ , ( $= 220 \pm 5$  MeV for  $^{12}\text{C}$  [65]) are occupied.

If the magnitude of the sum of the initial momentum of the nucleon  $\mathbf{k}_i$  and the transferred momentum  $\mathbf{q}$  is less than the Fermi momentum, then the scattering cannot take place, since such a scattering would place it in an already occupied momentum state. The fraction of the nucleons to which the electron can transfer momentum  $\mathbf{q}$  without putting them in an already occupied momentum state is:

$$\frac{\int d^3\mathbf{k}_i \theta(k_F - |\mathbf{k}_i|)\theta(|\mathbf{k}_i + \mathbf{q}| - k_F)}{\int d^3\mathbf{k}_i \theta(k_F - |\mathbf{k}_i|)}, \quad (6.6)$$

where  $\theta(x)$  is the step function. The function evaluates to

$$f(x) = \begin{cases} \frac{3x}{4} - \frac{x^3}{16}, & x < 2 \\ 1, & x \geq 2 \end{cases} \quad \text{where } x = \frac{|\mathbf{q}|}{k_F}, \quad (6.7)$$

where the momentum transferred,  $|\mathbf{q}|$  is given by

$$|\mathbf{q}|^2 = 4EE' \sin^2\left(\frac{\theta}{2}\right), \quad (6.8)$$

where  $E'$  is the scattered energy (in this case,  $E \left[1 + \frac{2E}{M_{\text{nucleon}}}\right]^{-1} - \bar{\epsilon}$ ) and  $\bar{\epsilon}$  is the average nucleon interaction energy ( $25 \pm 3$  MeV for  $^{12}\text{C}$  [65]).

In the ‘‘shell approximation’’ described above, the quasi-elastic scattering cross sections is equal to the elastic-scattering cross section off a free nucleon multiplied by  $f(x)$ . However, this does not account for the fact that the nucleon wave function is

non-zero above  $k_F$ , and therefore this function must be multiplied by a spectroscopic factor  $y$  to get an accurate estimate of the quasielastic cross section. Based on private communication [66], I use  $y = 0.8 \pm 0.1$  for this value.

### Form Factors of Nucleons

The form factor  $F(Q^2)$  for quasielastic scattering is related to two other form factors, the electric form factor  $G_E(Q^2)$  and the magnetic form factor  $G_M(Q^2)$  via

$$|F(Q^2)|^2 = \frac{G_E^2 + \frac{\tau}{\epsilon} G_M^2}{1 + \tau}, \quad (6.9)$$

where  $\tau = \frac{Q^2}{4M^2}$  and  $\epsilon = (1 + 2(1 + \tau) \tan^2 \frac{\theta}{2})^{-1}$  are kinematic factors. Since our experiment's geometric acceptance restricts us to small angles ( $< 160$  mrad), and the mass of the nucleus is much greater than the beam energy, the value of  $\tau$  is small, no more than 0.03 within our experiment's kinematic range of interest. For small  $Q^2$ , the neutron's electric form factor is near zero. Thus, the dominant part of the quasielastic scattering is from the proton's electric form factor. Nevertheless, I take both the electric and magnetic form factors of both types of nucleons into account.

I followed J. J. Kelly's parameterizations in [67] of the nucleon form factors. Kelly's fits use rank [1/3] Padé approximants for three of the four form factors. The one exception is the neutron electric moment,  $G_{En}$ , for which there was not enough data available to accurately fit in the same manner. Therefore Kelly parameterized the ratio  $G_{En}/G_D$ , where  $G_D$  is the so-called standard dipole form factor,  $\left(1 + \frac{Q^2}{0.71 \text{ GeV}^2}\right)^{-2}$ . Kelly's parameterizations of the electric and magnetic form factors

for the proton and neutron are:

$$\begin{aligned}
G_{Ep} &= \frac{1 - 0.24\tau}{1 + 10.98\tau + 12.82\tau^2 + 21.97\tau^3} \\
G_{Mp} &= \left( \frac{1 + 0.12\tau}{1 + 10.97\tau + 18.86\tau^2 + 6.55\tau^3} \right) \mu_p \\
G_{En} &= \left( \frac{1.7\tau}{1 + 3.3\tau} \right) \left[ 1 + \frac{Q^2}{0.71 \text{ GeV}^2} \right]^{-2} \\
G_{Mn} &= \left( \frac{1 + 2.33\tau}{1 + 14.72\tau + 24.2\tau^2 + 84.1\tau^3} \right) \mu_n
\end{aligned} \tag{6.10}$$

where  $\mu_p$  and  $\mu_n$  are the magnetic moments of the proton and neutron, 2.793 and -1.913 respectively. From these parameterizations, I use Equation 6.9 to calculate the elastic form factor  $F(Q^2)$  of the nucleons.

### 6.1.3 Delta resonance

The  $\Delta$  resonance has a mass of  $1232 \pm 2$  MeV with a width of  $117 \pm 3$  MeV [68].

The  $\Delta$  resonance does not contribute substantially in the 1.056 GeV dataset, and the peak energy for a scattered electron in a  $\Delta$ -producing reaction ( $\approx E_{\text{beam}} - (M_{\Delta} - M_p) = 762$  MeV) is about one resonance width less than the energy cutoff in my analysis ( $85\% \times E_{\text{beam}} = 897$  MeV). For the 2.306 GeV dataset, the peak scattered-electron energy is 2012 MeV, which is just above the energy cutoff in my event selection,  $85\% \times E_{\text{beam}} = 1960$  MeV. The peak from the  $\Delta$  resonance may be seen in Figure 6.2 as a bulge at about  $M_{\Delta} - M_p$  ( $\approx 300$  MeV) below the beam energy.

I used a parameterization for the  $\Delta$ -resonance production from J. Lightbody et.

al. [69]. This is given by

$$\begin{aligned} \sigma_{\Delta} = & \sigma_{\text{Mott}} \int_{\omega_{\text{thr}}}^{E_{\text{beam}} - E_{\text{cut}}} d\omega \left( \frac{Q^2}{q^2} + \tan^2 \frac{\theta}{2} \right) K q^2 \left[ 1 + \frac{Q^2}{a^2} \right]^{-4} \\ & \times \left[ \frac{W^2 \Gamma_{\Delta}^2}{(W^2 - M_{\Delta}^2)^2 + \Gamma_{\Delta}^2 W^2} \right] \left[ 1 - \exp \frac{\omega - \omega_{\text{thr}}}{\Gamma_{\text{thr}}} \right], \end{aligned} \quad (6.11)$$

where the kinematic variables  $\omega$ ,  $W$ ,  $Q$  and  $q$  are defined as follows:  $\omega$  is the difference in energy between the initial and final electron energies.  $Q^2$  is the invariant momentum transfer, defined as usual,  $4E_{\text{beam}}(E_{\text{beam}} - \omega) \sin^2 \frac{\theta}{2}$ .  $q^2$  is the spacial part of the momentum transfer, equal to  $Q^2 + \omega^2$ .  $W^2$  is invariant mass, defined as  $M_p^2 + 2M_p(\omega - \frac{Q^2}{2M_p})$ .

Lightbody's parameterization uses 700 MeV for the dipole parameter  $a$ . The width  $\Gamma_{\Delta}$  is the quadrature sum of the  $\Delta$  resonance's intrinsic width 117 MeV, a term accounting for the Fermi motion of nucleons ( $1.1 \times qk_F/M_p$ ), and a third term that depends on the nuclear medium, which equals 140 MeV for nuclei with atomic numbers  $A > 4$ . The threshold width,  $\Gamma_{\text{thr}}$  is 5 MeV and the threshold value  $\omega_{\text{thr}}$  equals  $\frac{Q^2}{2(M_p + M_{\pi})}$ . The overall scale  $K$  is  $31.3 \text{ GeV}^{-3}$ . I estimate the systematic error for the  $\Delta$  cross section to be 20%.

### 6.1.4 Radiative Corrections and Multiple Scattering

In order to relate the measured cross section to the Born approximation, several things must be taken into account. First, when I make cuts on the particle's measured energy (in this case, the energy measured in the Ecal), some of the events fail this cut due to energy loss either in the target or between the target and the Ecal, or due to bremsstrahlung. Secondly, there are next-to-leading-order corrections to the elastic (as well as quasi- and inelastic) cross sections, caused by vertex and vacuum-

loop corrections. Finally, the measured energy spectrum is smeared out by resolution effects.

In my treatment of these corrections, I neglect the straggling inside of the target (approximately  $10^{-3}$  radiation lengths), but retain the effects of straggling inside of the SVT (about 0.04 radiation lengths) prior to hitting the Ecal. Equation 6.12 below (based on the work of Mo and Tsai [70]) gives the ratio of the measured cross section to the Born cross section, with a cutoff on the energy measured by the Ecal at  $x_{\min}E_{\text{beam}}$  to  $x_{\min}E_{\text{beam}}$ :

$$f(\theta) = \frac{\sigma_{\text{measured}}}{\sigma_{\text{Born}}} = \int_0^1 x_1 \int_0^1 dx_2 \int_{x_{\min}}^{x_{\max}} dx_3 g(x_3 - x_1 x_2, \sigma_x) p_{\text{brem}}(x_1) p_{\text{strag}}(x_2), \quad (6.12)$$

where  $x_1$  is the fraction of the electron's energy retained after bremsstrahlung,  $x_2$  is the fraction of the energy remaining after straggling through the SVT (out of the energy just after the target),  $x_3$  is the ratio of the energy measured in the Ecal to the beam energy,  $g(\mu, \sigma)$  is the normalized gaussian function,  $p_{\text{strag}}(x)dx$  is the probability of energy loss via straggling from  $E$  into the interval  $xE$  to  $(x + dx)E$ , and likewise  $p_{\text{brem}}(x)dx$  is the probability of energy loss via bremsstrahlung from  $E$  into the interval  $xE$  to  $(x + dx)E$ . The two probability density functions are given by:

$$p_{\text{brem}}(x) = -\frac{d}{dx} \exp \left[ \frac{-2\alpha}{\pi} \left( \left( \log \frac{1}{x} - \frac{13}{12} \right) \left( \log \frac{Q^2}{m^2} - 1 \right) + \frac{17}{36} + \frac{1}{2} f(\sin^2 \frac{\theta}{2}) \right) \right] \quad (6.13)$$

$$p_{\text{strag}}(x) = \frac{bt}{1-x} \left( x + \frac{3}{4}(1-x)^2 \right) \left( \log \frac{1}{x} \right)^{bt},$$

where  $f(y) = \log(y) \log(1 - y) + \text{Li}_2(-y)$ , and  $b$  is given by

$$b = \frac{4}{3} \left[ 1 + \frac{Z + 1}{9(Z \log(183Z^{-1/3}) + \log(1440Z^{-2/3}))} \right]. \quad (6.14)$$

I numerically integrated Equation 6.12 using the Mathematica package [71]. The constants used in the integrals, as well as the values of the integral at selected angles, are listed in Table 6.1. I calculated this for 3 different values of the energy cut (83%, 85% and 87%) in order to estimate the systematic errors.

TABLE 6.1: Calculations of the radiative correction factors.

$\Delta E/E$	.83		.85		.87	
$E_{\text{beam}}$	1.056	2.306	1.056	2.306	1.056	2.306
$\sigma_x = \frac{\sigma_E}{E_{\text{beam}}}$	4.5%	3.3%	4.5%	3.3%	4.5%	3.3%
$t$	0.042					
$Z$ (silicon)	14					
$b$	1.34					
$f(40 \text{ mrad})$ (%)	86.3	86.2	85.3	85.1	83.9	84.0
$f(100 \text{ mrad})$ (%)	86.0	85.8	84.8	84.6	83.3	83.4
$f(160 \text{ mrad})$ (%)	85.7	85.5	84.5	84.3	83.0	83.0

Thus the ratio between the measured cross-section and the Born cross section, about 85%, has very little angular dependence.

## 6.2 Cross Section Measurement

### 6.2.1 Event Selection

I selected events in calibration runs 5779 (1.056 GeV beam,  $^{12}\text{C}$  target) and 8054 (2.306 GeV beam,  $^{12}\text{C}$  target) according to the following criteria for this analysis:

First, all events must have all of the SVT event status flags be good (see Section

5.2). For the 2015 dataset I used only the events with the Single 1 trigger. For the 2016 dataset, due to extreme prescaling of Single 1 triggered events in the central region of the Ecal, I used a combination of Single 1-triggered events and Single 0 events. This is further explained in Section 6.2.2.

The next step is to find clusters in the event that fulfill the following criteria: first, the cluster must be within the trigger window (40-55 ns in 2015, 52-62 ns in 2016). This reduces the number of accidental particles passing the cuts. Secondly, the reconstructed cluster position must be within the fiducial region of the Ecal (no more than 3/4 of a crystal width from any edge), since the energy resolution degrades near the edge of the Ecal, and there must be at least 3 hits in the cluster. Finally, the measured energy of the cluster must be greater than 85% of the beam energy. Figure 6.2 shows the cluster energy spectra of both datasets just before and just after making the cut on the cluster energies.

I then require that the cluster be matched to a track in the SVT fulfilling the following criteria:

- The track curves to the right in the magnetic field (that is, the particle is negatively charged),
- The goodness of track-cluster matching<sup>3</sup>,  $n_\sigma$ , must be less than 5,
- The  $\chi^2$  value of the track fit is less than 40.

I then calculated the initial polar and azimuthal angles,  $\theta$  and  $\phi$ , as well as the slopes  $u_x = dx/dz$  and  $u_y = dy/dz$ , in the beamline frame, where  $z$  is along the beam-line.

Figures 6.3 and 6.4 show the angular distributions of the events that pass these cuts.

---

<sup>3</sup>See Equation 2.2.

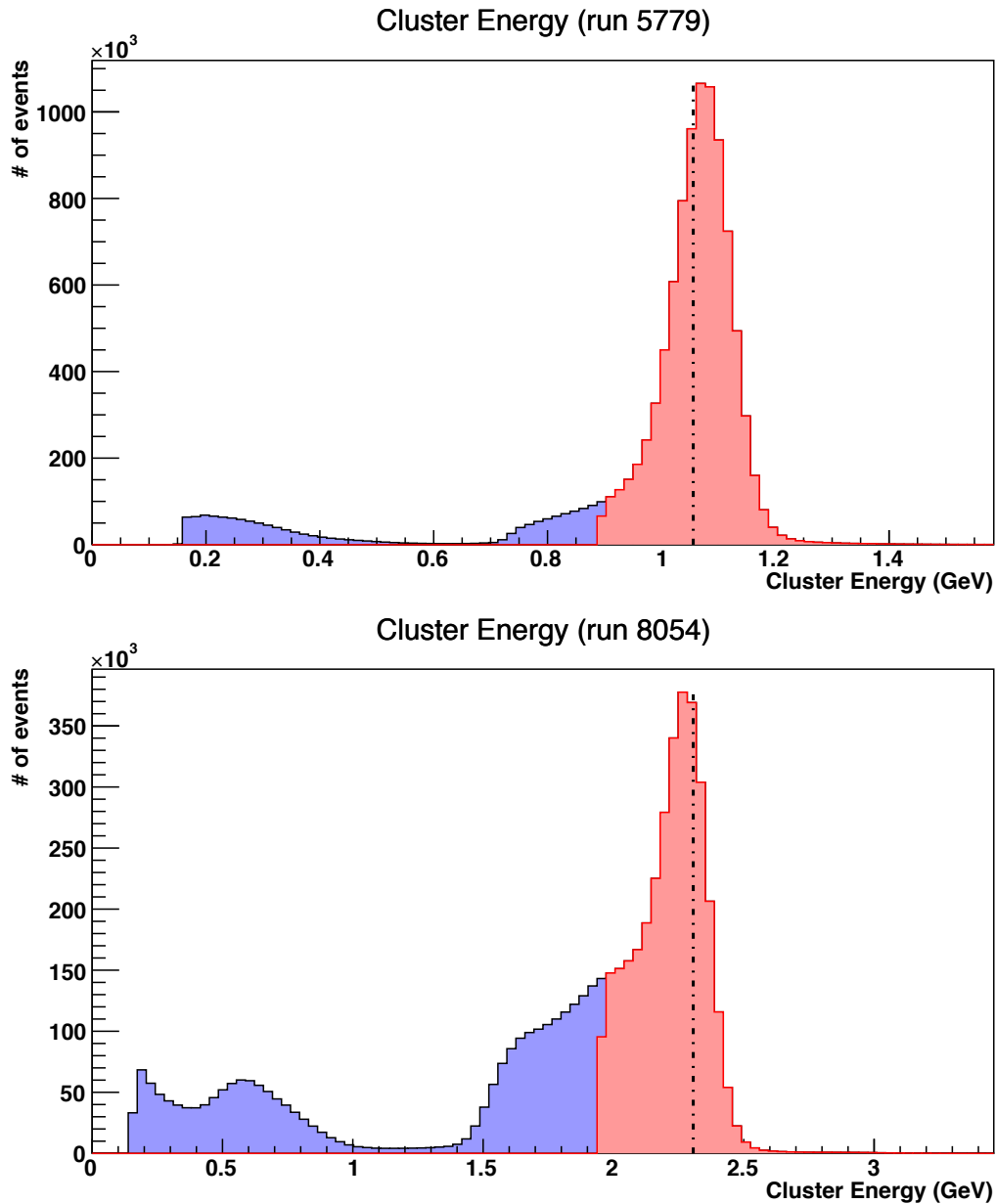


FIG. 6.2: Cluster energy spectra for runs 5779 (top, 1.056 GeV beam) and 8054 (bottom, 2.306 GeV beam). The red (blue) region represents events that have been retained (cut out) by the cluster energy cut. The beam energy is represented by the black vertical dashed line. It is unknown why the peak cluster energy is slightly greater than the beam energy in the former dataset and slightly less than the beam energy in the latter. Since the Ecal energy measurements are not used in HPS's bump-hunt and displaced-vertex searches for dark photons, this discrepancy does not affect the results of those analyses.



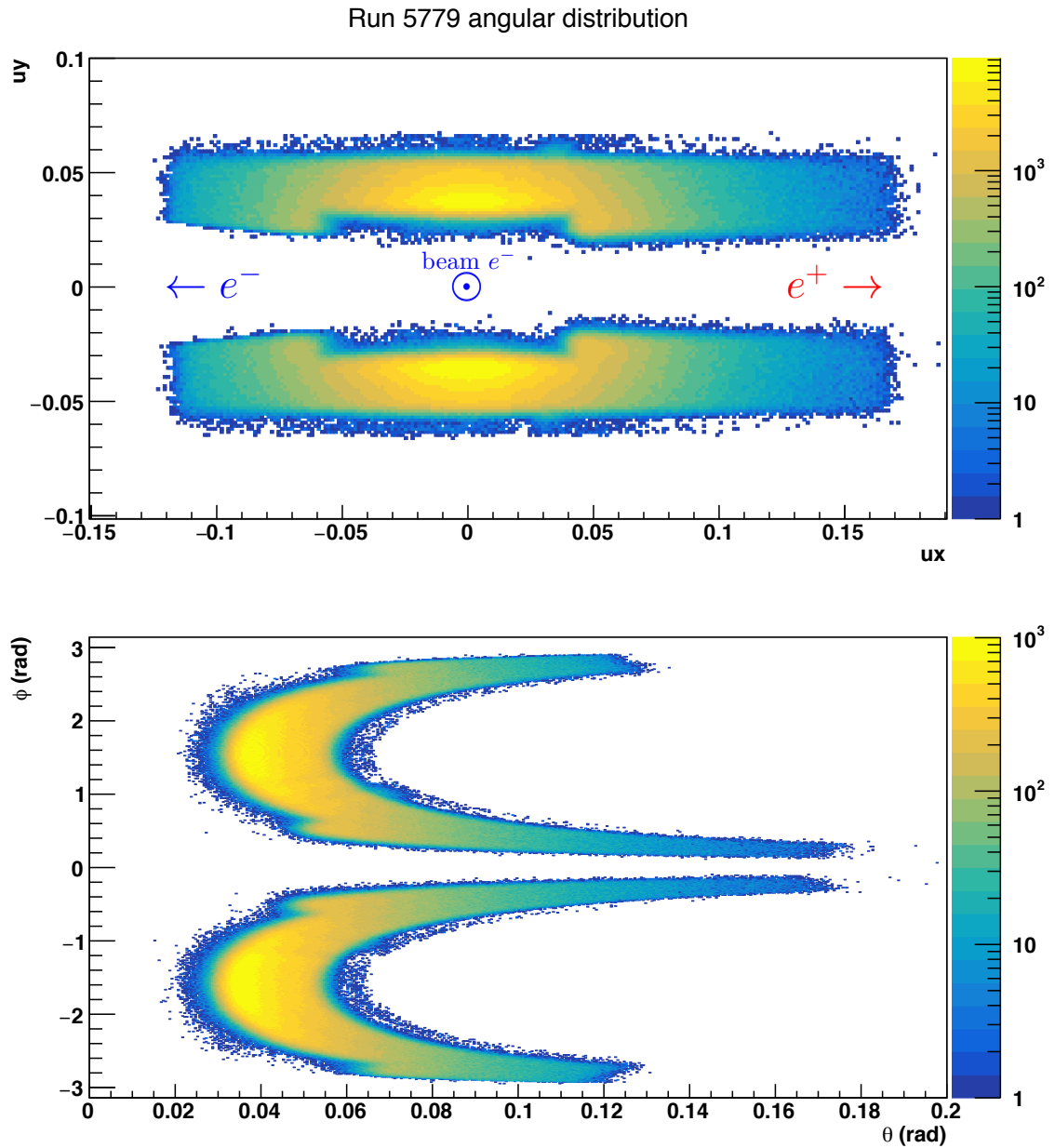


FIG. 6.3: Angular distribution of particles passing FEE cuts in run 5779. Initial directions of tracks are expressed in Cartesian coordinates  $u_x$  and  $u_y$  (top) and polar coordinates  $\theta$  and  $\phi$  (bottom). In the top plot of this Figure (as well as in Figures 6.4 and 6.6-6.8), the angular distribution of the tracks that pass the cuts follows the outline of the Ecal. Superimposed for reference are the direction of the beam line and the directions of curvature of the electrons and positrons.

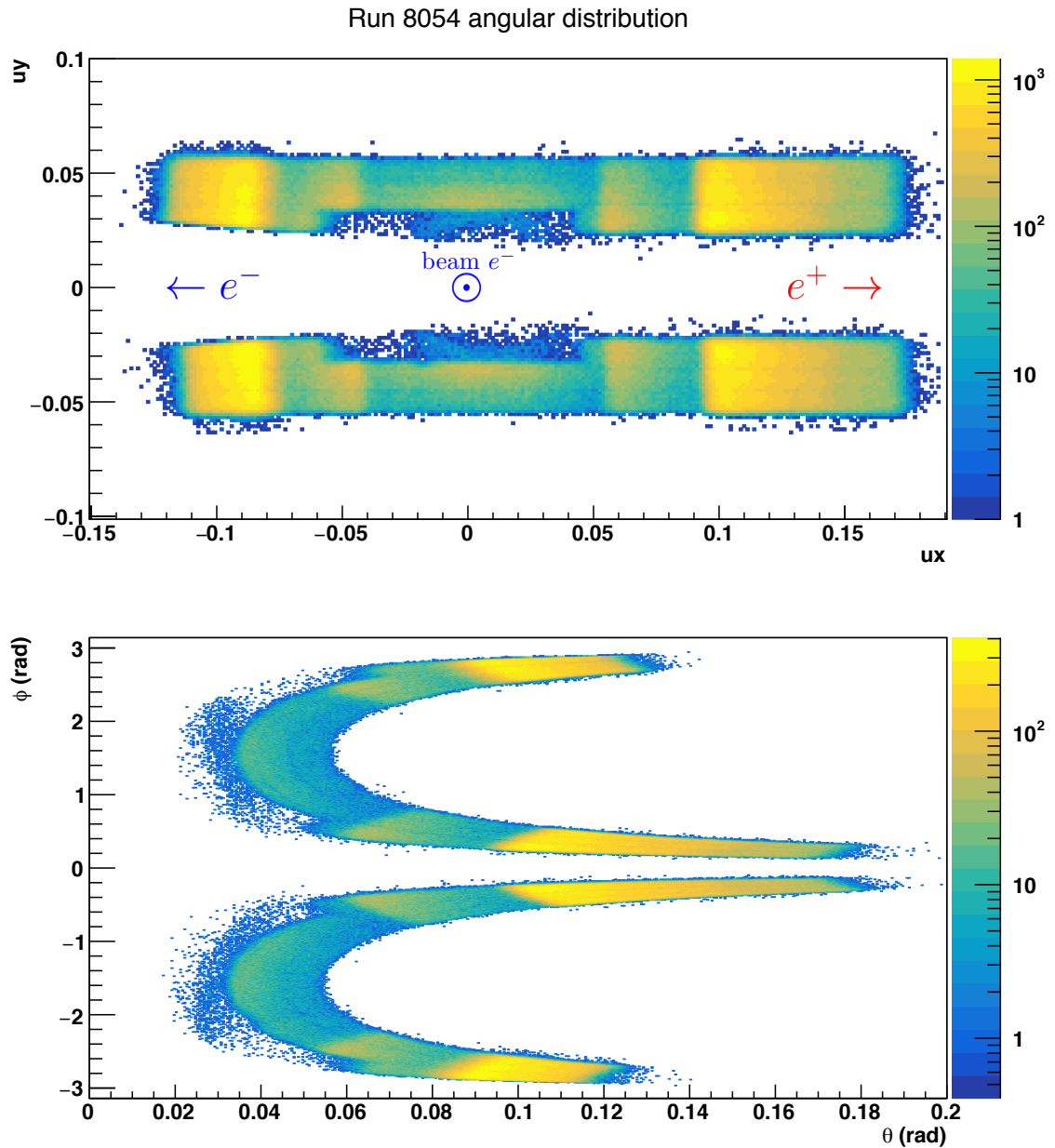


FIG. 6.4: Angular distribution of particles passing FEE Cuts in run 8054. Initial directions of tracks are expressed in Cartesian coordinates  $u_x$  and  $u_y$  (top) and polar coordinates  $\theta$  and  $\phi$  (bottom). There are more events at large positive or negative  $u_x$  because the trigger prescale factors depend on the position of the triggering cluster.

## 6.2.2 Normalization

The charges for each run were calculated by integrating the current measured in the Faraday cup, omitting intervals where the SVT was retracted from its nominal position or its bias voltage was off. The integrands of these integrals are then scaled to take data acquisition live-time and burst-mode noise into account. For runs in 2016, the charge that hits the Faraday cup needed to be multiplied by 61.98 to account for the attenuation of the beam from the beam-blocker in front of the Faraday cup.

In both datasets, all of the triggers except Pair 1 are prescaled, that is, the DAQ only recorded the events at every  $f_p^{\text{th}}$  occurrence of the trigger, where  $f_p$  is a trigger configuration parameter called the “prescale factor”. The prescale factor for run 5779 was globally 128 for the Single 1 trigger<sup>4</sup>. In the 2016 dataset, the Single 1 trigger was modified so that its prescale factor depended on the position of the triggering cluster. This prescale factor ranged from 2 to 36000 (Both the trigger interface (TI) and the subsystem processor (SSP) prescaled the triggers independent of one another. The SSP prescale factors were 1, 80, 1300 and 18000, depending on the cluster position, which, when multiplied by the TI’s global prescale factor of 2, ranges from 2 to 36000). The small prescale factors in the outer crystals gave priority to the regions of the Ecal where the cross-sections are much smaller. However, a prescale factor of 36000 in the central region yields very low statistics, much less than the looser Single 0 trigger, which has a global prescale factor of 4097. Figure 6.5 compares the total prescale factors of the 2016 Single 1 and Single 0 triggers.

For the 2016 dataset, I combined the event sets with Single 1 and the Single 0, weighting each event by the weights in Table 6.2 below. This scales all Single 1 events by a factor proportional to the prescale factor, except for the central region. For the

---

<sup>4</sup>In the other runs in 2015, the Single 1 prescale factor was 2048. The Pair 1 and Pair 0 triggers were disabled for run 5779 in order to allow for a smaller prescale factor for Single 1.

central region, I used the Single 0 trigger events, which I likewise scaled according to their prescale factor. Figure 6.6 shows the angular distributions shown in Figure 6.4 after applying the weighting factors.

TABLE 6.2: Weighting events by brescale in FEE analysis (2016 dataset only). Column ranges are inclusive.

Trigger	Columns	Weight
Single 1	-23 to -13; 6 to 23	2
Single 1	-12 to -9; 2 to 5	160
Single 1	-8 to -7; -2 to 1	2600
Single 0	-6 to -3	4097
	anything else	0

The measured areal density of the carbon target was 0.044 g/cm<sup>2</sup>. The luminosity is then:

$$\ell = \frac{\rho_A N_A Q}{A q_e} \frac{1 \text{ cm}^2}{10^{24} \text{ barn}} \quad (6.15)$$

where  $Q$  is the accumulated beam charge,  $q_e$  is the electron charge,  $N_A$  is Avogadro's number, and  $A$  is the atomic mass number of the nucleus. Carrying out these calculations, the integrated luminosities of runs 5779 and 8054 are then 45839.273 nb<sup>-1</sup> and 142582.897 nb<sup>-1</sup> respectively.

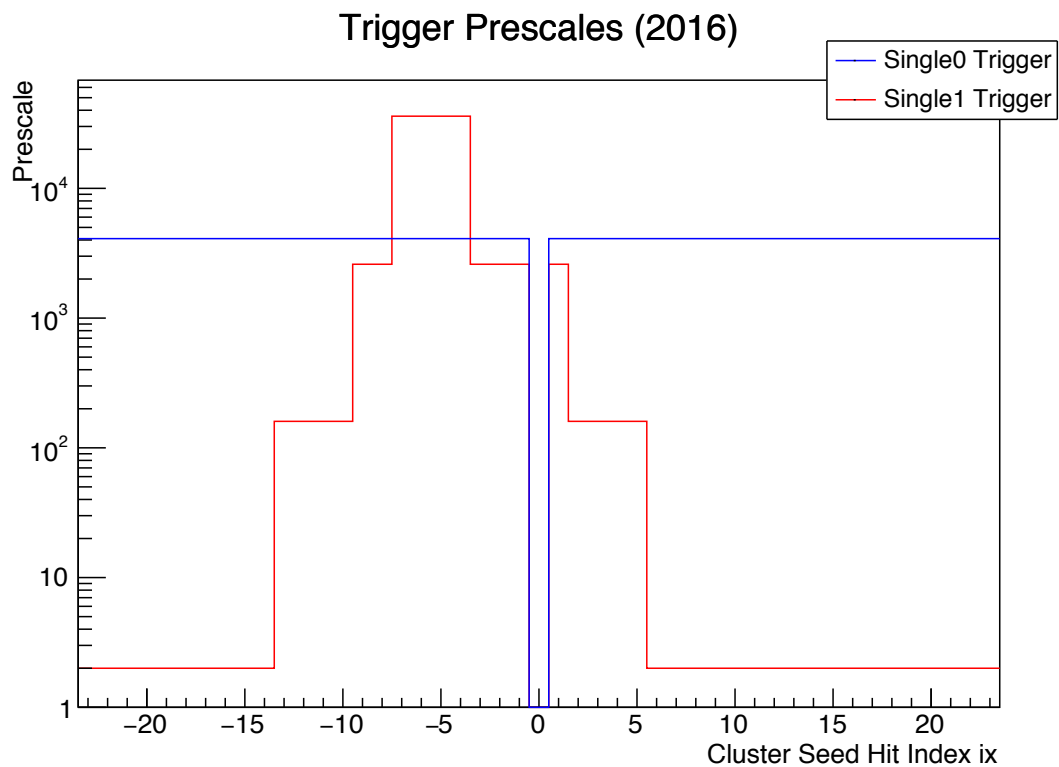


FIG. 6.5: Overall prescale factors of the Single 0 and Single 1 triggers used in 2016. There is no crystal index zero, due to the crystal numbering scheme.

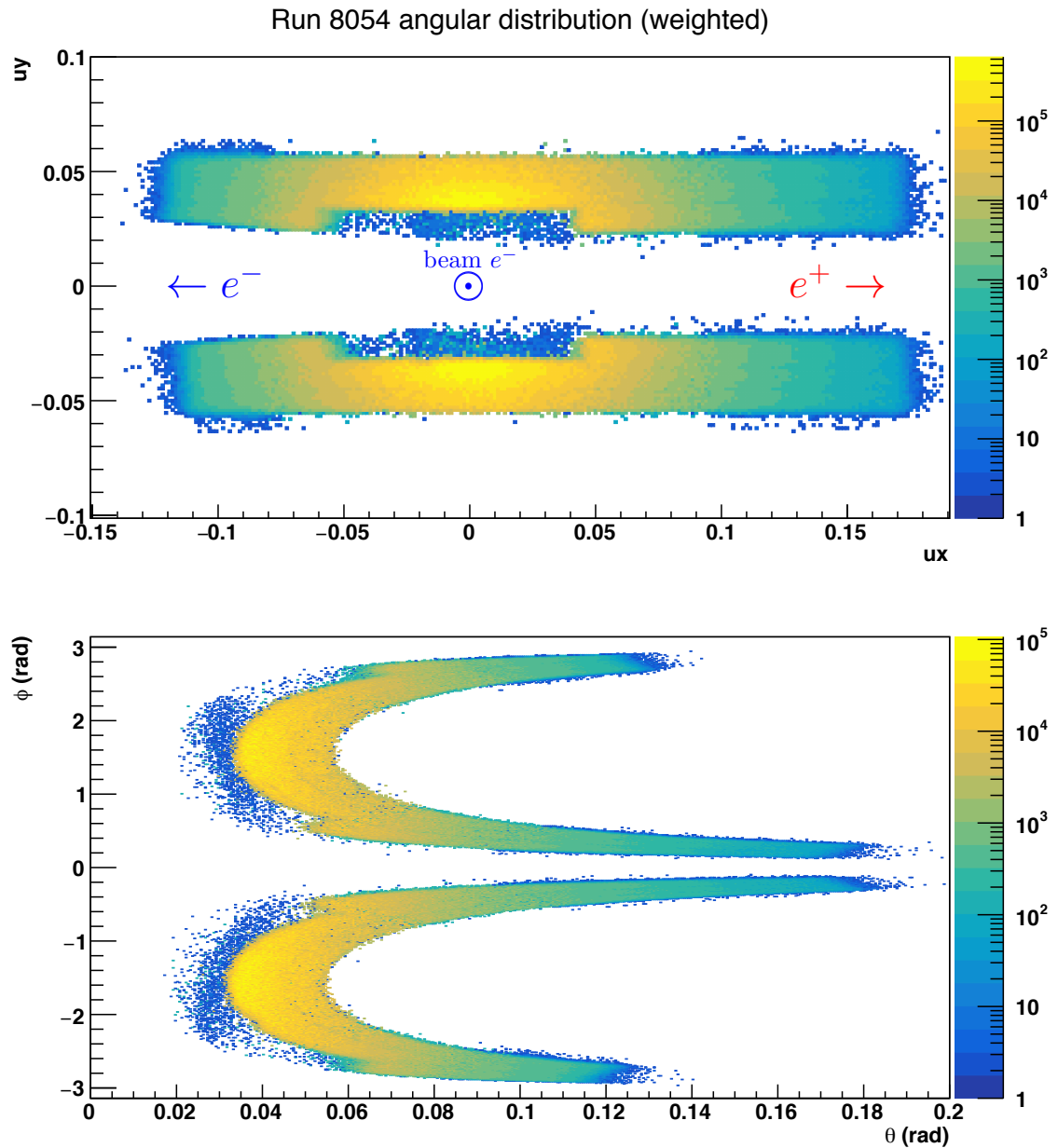


FIG. 6.6: Prescale-weighted angular distribution of particles passing FEE Cuts in run 8054. Events are weighted by the prescale factors,  $f_p$ , which are determined by the position of the triggering cluster. Initial directions of tracks are expressed in Cartesian coordinates  $u_x$  and  $u_y$  (top) and polar coordinates  $\theta$  and  $\phi$  (bottom).

### 6.3 Comparison to model

The ratio of the number of particles that pass the cut to the predicted number of particles within a given angular bin can be used as a proxy for the efficiency of the detector. The predicted number is given by:

$$N = \frac{\ell}{f_p} \frac{d\sigma}{d\Omega} d\Omega, \quad (6.16)$$

where  $f_p$  is the prescale factor, and  $\ell$  is the luminosity of the run and  $d\Omega$  equals  $d\theta d\phi \sin(\theta)$  for the polar graphs and  $\cos^2(\theta) du_y du_x$  for the Cartesian graphs. The detection/model ratios are shown as two-dimensional plots in Figures 6.7 and 6.8. Figures 6.9 and 6.10 show projections in the  $u_x$  direction of the Cartesian graphs in Figures 6.7 and 6.8 respectively.

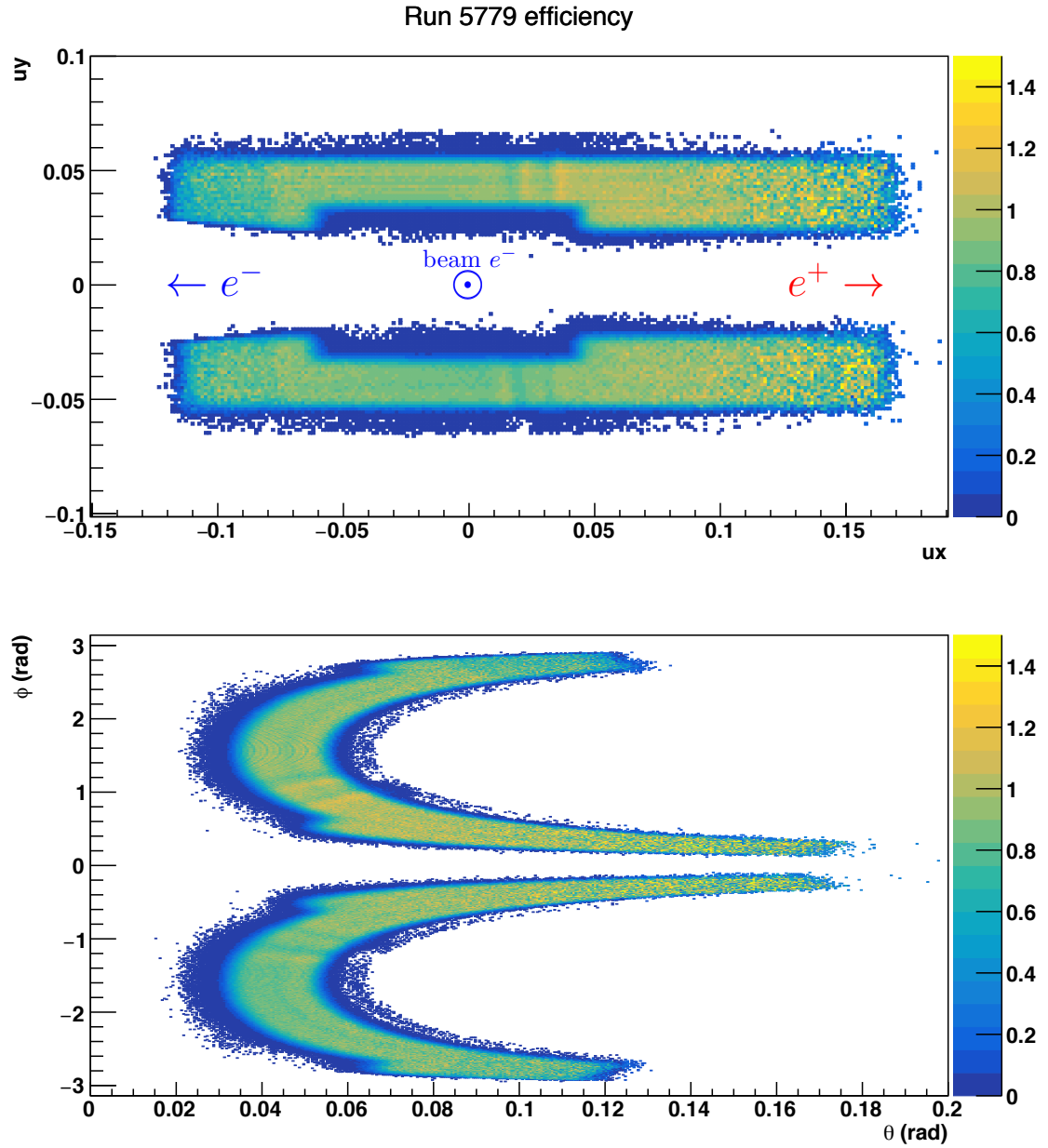


FIG. 6.7: Ratio of measured to predicted cross-sections for FEEs in run 5779 (1.056 GeV). Initial directions of tracks are expressed in Cartesian coordinates  $u_x$  and  $u_y$  (top) and polar coordinates  $\theta$  and  $\phi$  (bottom).



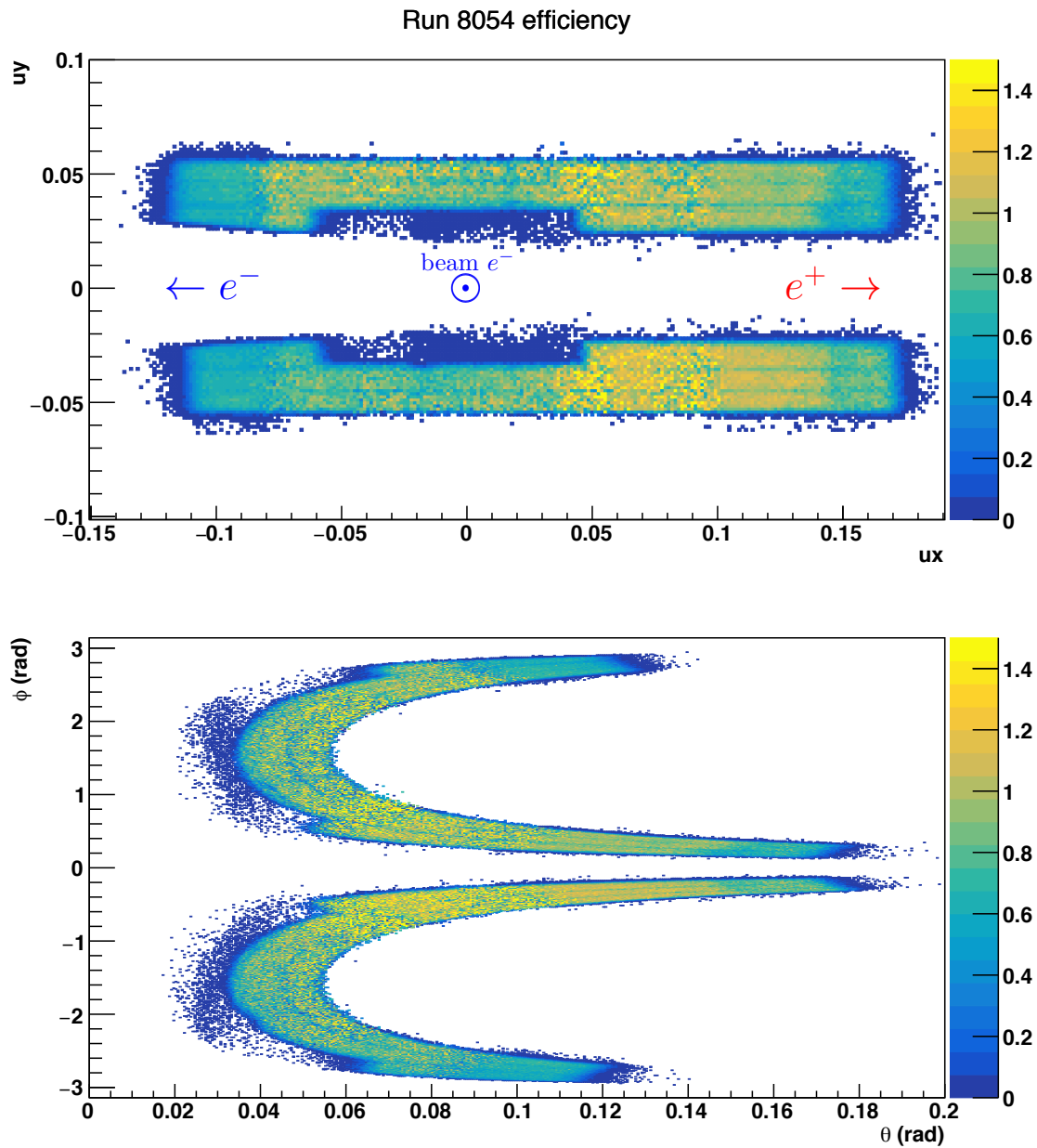


FIG. 6.8: Ratio of measured to predicted cross-sections for FEEs in run 8054 (2.306 GeV). Initial directions of tracks are expressed in Cartesian coordinates  $u_x$  and  $u_y$  (top) and polar coordinates  $\theta$  and  $\phi$  (bottom).

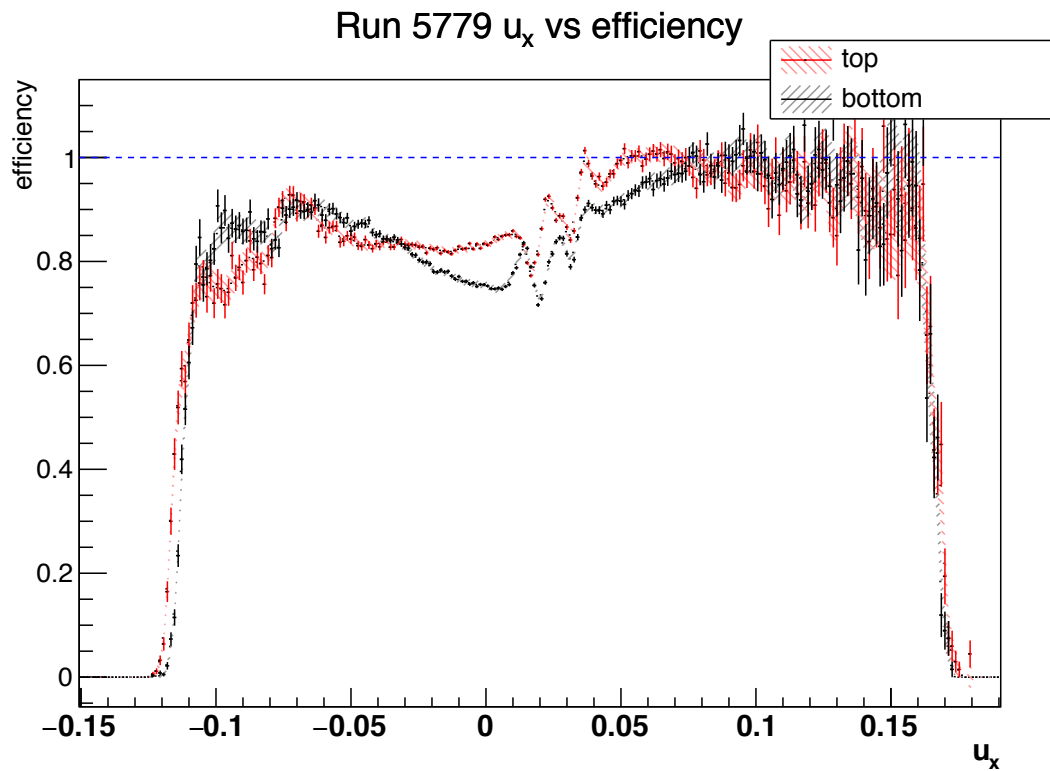


FIG. 6.9: Ratio of measured to predicted cross-sections for FEEs in run 5779 (1.056 GeV), projected in  $u_x$ . The slices are  $-0.050 < u_y < -0.036$  (black) and  $0.036 < u_y < 0.050$  (red). Vertical error bars represent the statistical errors; hatched regions represent combined statistical and systematic errors.

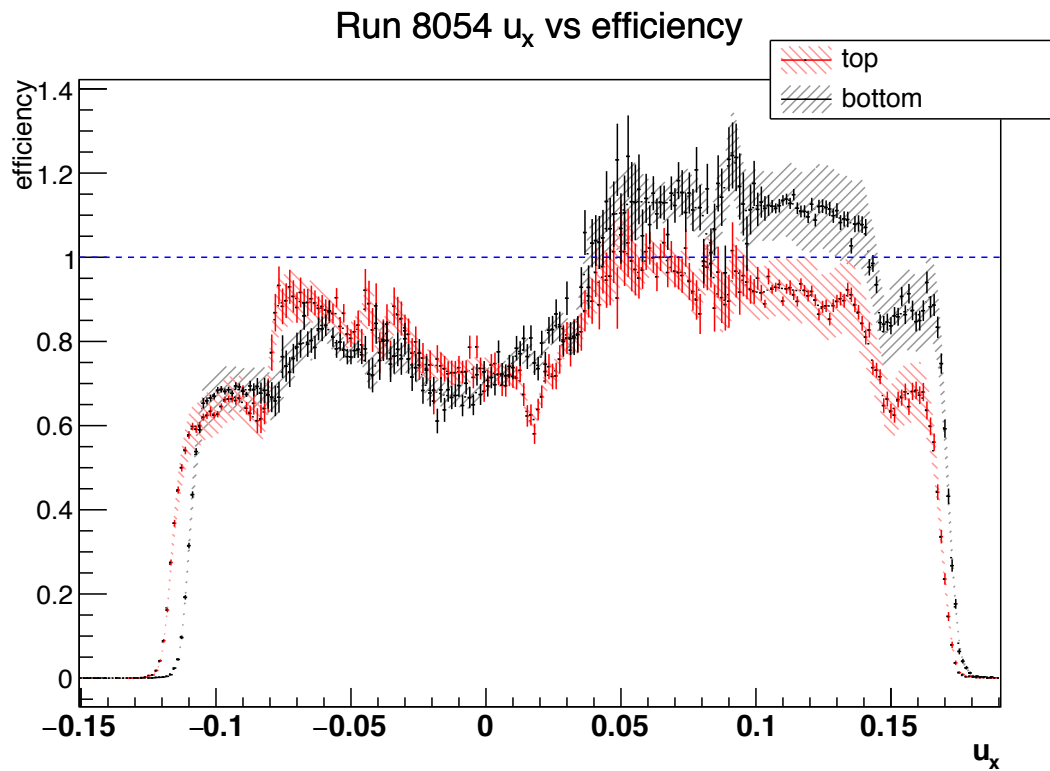


FIG. 6.10: Ratio of measured to predicted cross-sections for FEEs in run 8054 (2.306 GeV), projected in  $u_x$ . The slices are  $-0.050 < u_y < -0.036$  (black) and  $0.036 < u_y < 0.050$  (red). Vertical error bars represent the statistical errors; hatched regions represent combined statistical and systematic errors.

## 6.4 Interpretation

The negative  $x$  side of the detector has worse efficiency than the positive  $x$  side of the detector. A possible explanation is that the reason for this is that there are more negatively charged particles (which curve towards the negative  $x$  side of the detector) than positively charged particles that hit the detector. The last three layers of the SVT are split horizontally into two sensors, one on the left and one on the right. When multiple particles hit the same strip on any sensor within a short period of time as one another, their signal waveforms overlap, and unless there is sufficient separation between the two, it becomes impossible to distinguish between them. This phenomenon, known as pileup, causes some of the hits in the SVT to become lost. Since more particles bombard the electron-side sensors, the per-hit efficiency on those sensors is less than that of the positron-side sensors. Therefore, there is a larger probability of the tracks on the electron side being lost.

There are also three dips in between the high and low efficiency sides of the detector, which may be caused by the gap between the left and right sensors in the SVT in its last three layers. Near the edges of the acceptance in both the positive and negative  $x$  directions, there is another sharp drop-off in efficiency. This may be because at these higher angles, the electrons pass through the first five SVT layers and then barely miss the 6th layer. If any of these five hits fail for these tracks, the whole track is lost, since we require 5 hits per track. At smaller angles, the electrons pass through all 6 layers of the track, and so if one of the six hits fails, then the track is not lost.

There are regions of the detector where the calculated efficiency is lower for the top half than it is for the bottom half (and vice versa). The reason for this is not yet understood. It is possible that this reflects a systematic deviation in the direction of

the beam relative to each half of the SVT, which would cause systematic shifts on the measured  $\theta$ .

The most concerning feature in the efficiency spectrum is the cutaway in the middle of the Ecal. In the final design for the Ecal, nine crystals were removed from the inner most row on both halves, where the hit rates would be too high for the data-acquisition system. This causes irregularities in the acceptance as a function of  $\theta$  at the edges of this gap.

The presence of these features of the FEE efficiency spectrum does not necessarily imply that there will be discontinuities in the invariant mass spectrum for  $e^+e^-$  pairs. For any position on the Ecal or SVT, there is a wide range of pair invariant masses in which one of the two particles will hit that part of the detector. Therefore, if that part of the detector has an irregularity in its efficiency, then the effect of that discontinuity will be smeared out in the invariant mass spectrum. The worst case would be if there were two points roughly antipodal to one another where the efficiency spikes. If a bump is found in the resonance search, the features of the efficiency spectrum found in this analysis should be further investigated.

# CHAPTER 7

## Resonance Search Part 1: Preparing a Mass Spectrum

### 7.1 Bump-Hunt Algorithm Overview

To search for the dark photon, we used a bump-hunt algorithm to look for a narrow resonance in the invariant-mass spectrum of detected  $e^+e^-$  pairs. This chapter presents the steps I took to prepare an invariant-mass spectrum for the bump-hunt analysis to be performed on the 2.306 GeV dataset taken in 2016. Chapter 8 describes the bump-hunt analysis itself. Earlier analyses had been done on the previous dataset taken in 2015 with the 1.056 GeV beam [72–74].

The first step was to choose a set of criteria for determining which events with  $e^+e^-$  pairs to accept in the resonance search. The second step was to create a histogram of the invariant masses of the pairs, using a bin size considerably smaller than the mass resolution. (Although an un-binned fit would have had no bias from bin-size, it would have been considerably slower and therefore less practical). I then

iterated through possible  $A'$  mass hypotheses, testing if a signal-plus-background fit is significantly better than a background-only fit. For this, I used a likelihood ratio test, accounting for the look-elsewhere effect in the calculation of statistical significance. For every  $A'$  mass hypothesis I looked at, I then determined an upper limit (at  $2\sigma$  confidence level) on the coupling  $\epsilon^2$ .

In this chapter, I describe the selection and composition of the event sample. Chapter 8 will describe the details of the resonance search itself, the fitting methods, etc.

## 7.2 Dataset

The data used in the analysis are from the 2016 physics dataset. Table 7.1 lists all of the runs used in this analysis, which were chosen using the following criteria:

- There were no problems with the Data Acquisition (DAQ) system during the run.
- The current used in the run was either the nominal 200 nA, (or 150 nA used in runs prior to our decision to increase the beam current).
- The 4  $\mu\text{m}$  tungsten target was in place.
- The SVT was at 0.5 mm from the beam (most of the run).

If the majority of the run met these criteria, but an isolated set of files within the run failed the criteria, then only the part of the run for which these conditions held was included in the analysis. Since this is a blinded analysis, only the files whose file numbers end with 0 were used in this analysis. After unblinding, all of the (good) files in these runs will be used in the future full analysis.

TABLE 7.1: List of “golden” runs from the 2016 HPS dataset used in this analysis, correcting for livetime, excluding files with DAQ errors and periods where the SVT bias was off, and eliminating other unusual run conditions. An asterisk next to a run number indicates that some of the files in the run are excluded from the analysis. In this case, the numbers of events and luminosity listed are of the remaining files in the run.

Run Number	Total Events	Luminosity ( $\text{nb}^{-1}$ )
7629	48,445,040	57.28
7630	60,975,330	70.92
7636	148,219,610	170.48
7637	12,100,110	14.30
7644	150,288,740	187.59
7653	25,128,650	29.68
7779	131,186,351	130.49
7780	121,447,750	106.64
7781	151,580,510	142.13
7782	19,410,430	17.01
7783	3,677,110	4.24
7786	4,746,870	3.91
7795	119,559,730	120.47
7796	150,763,230	132.44
7798	167,693,140	174.72
7799*	149,954,553	164.51
7800	159,933,840	167.17
7801*	140,431,569	117.33
7803*	145,443,839	142.55

Continued on next page



TABLE 7.1: List of “golden” runs from the 2016 HPS physics run used in this analysis. (continued)

Run Number	Total Events	Luminosity (nb <sup>-1</sup> )
7804	150,163,340	151.63
7805*	130,983,413	134.32
7807*	110,738,242	114.52
7947	100,003,560	164.41
7948	112,391,630	186.06
7949	105,624,080	177.60
7953	25,034,370	32.58
7962*	23,011,403	37.58
7963	100,690,930	166.44
7964	100,426,760	158.62
7965	47,883,630	78.44
7966	102,294,530	159.30
7968	100,021,800	148.71
7969	9,593,000	15.33
7970	100,430,650	143.56
7972	72,335,630	125.13
7976	25,210,890	43.62
7982	16,805,500	29.93
7983	100,237,730	167.36
7984	105,389,430	187.04
7985	103,263,260	182.40
7986	102,740,620	182.09

Continued on next page

TABLE 7.1: List of “golden” runs from the 2016 HPS physics run used in this analysis. (continued)

Run Number	Total Events	Luminosity (nb <sup>-1</sup> )
7987	104,291,800	185.95
7988	100,041,960	173.63
8025	100,257,350	170.86
8026	100,229,880	172.84
8027	103,477,890	176.24
8028	119,665,800	200.13
8029	100,850,170	169.84
8030	68,263,790	115.31
8031	58,215,590	98.33
8039*	94,955,778	164.82
8040	100,283,730	172.91
8041	29,615,580	50.97
8043*	28,089,049	49.46
8044	100,089,230	174.61
8045	101,535,140	149.92
8046	101,280,500	150.71
8047	100,918,360	165.40
8048	100,013,000	172.62
8049	22,101,030	37.61
8051	29,492,890	49.18
8055	54,455,460	99.06
8057	100,049,810	181.69

Continued on next page

TABLE 7.1: List of “golden” runs from the 2016 HPS physics run used in this analysis. (continued)

Run Number	Total Events	Luminosity (nb <sup>-1</sup> )
8058	100,069,290	175.69
8059	110,092,750	193.91
8072	108,117,590	197.67
8073	103,940,210	164.48
8074	88,071,400	153.78
8075	34,367,160	63.35
8077	57,189,610	103.81
8085	59,817,680	119.24
8086	97,369,240	185.47
8087	109,983,980	178.96
8088	27,287,810	52.69
8090	31,698,590	58.73
8092	99,450,940	180.94
8094	100,575,040	186.33
8095	105,290,240	160.32
8096	100,177,890	159.82
8097	99,131,050	168.27
8098	101,838,720	190.14
8099	128,774,050	237.01
Total	7,237,677,827	10753.2716

### 7.3 Event Selection

I applied cuts on the  $e^+e^-$  data sample to remove events in which 1) there were unacceptable run conditions, 2) the tracks and clusters were mismatched with one another, 3) the tracks were poorly fit or reconstructed or 4) the kinematics were inconsistent with an  $A' \rightarrow e^+e^-$  signal. Appendix B describes the process of fine-tuning these cuts in order to maximize the significance of events consistent with the  $A' \rightarrow e^+e^-$  kinematics.

The following preliminary cuts were applied before any kinematic cuts:

- The event must be triggered by the primary trigger (Pair 1).
- All SVT/DAQ condition flags for the event are good.
- Both tracks in the SVT are matched to a cluster in the Ecal.
- The tracks are of opposite charge.
- The clusters are on opposite halves of the Ecal.

As Figure 7.1 shows, there is a strong correlation between the timing of the top and bottom clusters in the Ecal, since pairs of particles produced in the same beam bucket should hit the Ecal at the same time (neglecting the difference in path lengths between particles). To filter out pairs of particles that came from different beam buckets, I require the clusters to be within 2 ns of one another.

Since the track-cluster matching criteria in the event reconstruction is very loose (geometric matching<sup>1</sup>  $n_\sigma < 15$ , with no timing cuts), I placed tighter cuts on the matching. For this analysis, I required  $n_\sigma < 6.1$ , and the time difference between the track and the cluster<sup>2</sup> to be less than 4.4 ns.

---

<sup>1</sup>See Equation 2.2

<sup>2</sup>after applying a -55 ns offset to the cluster time.

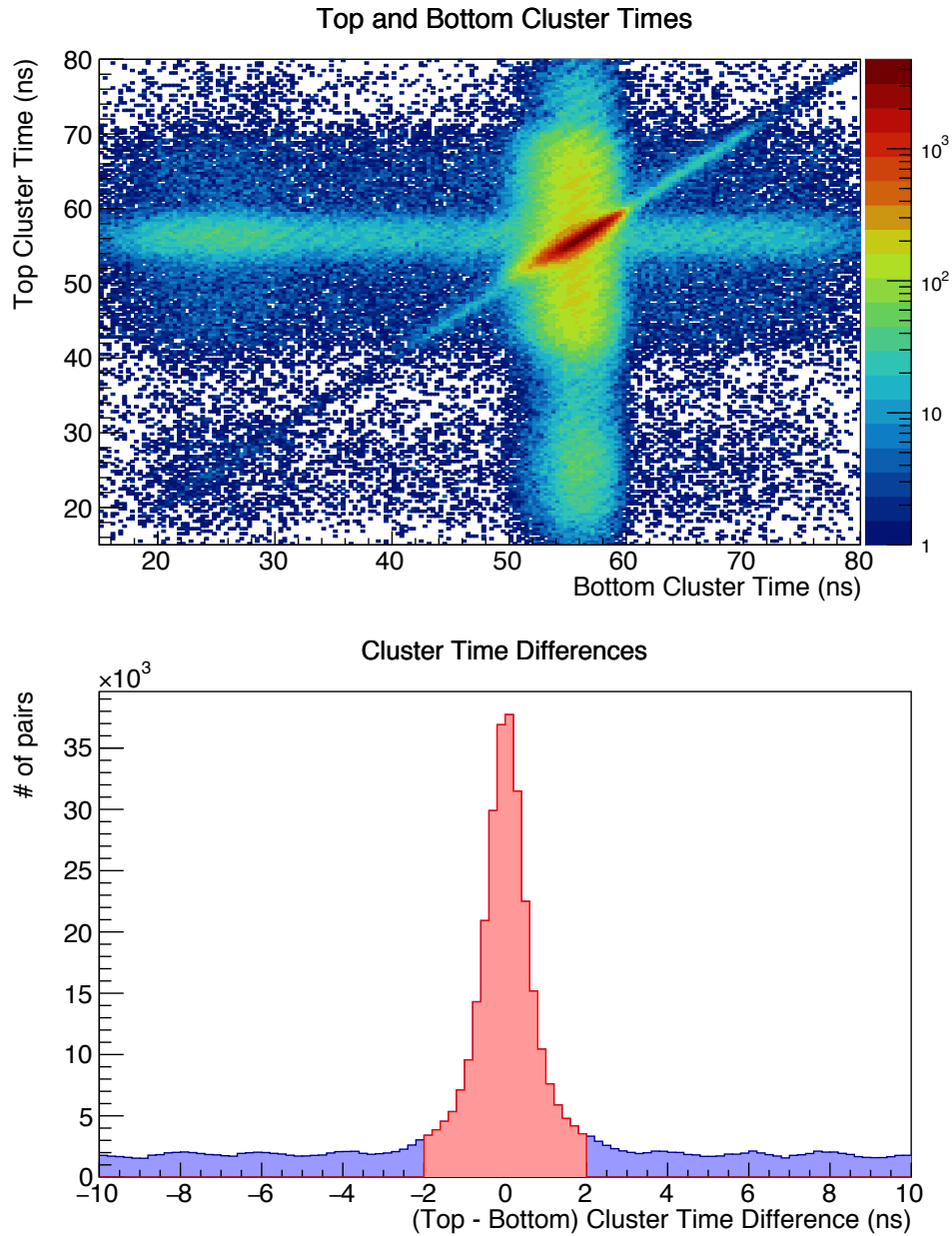


FIG. 7.1: Time spectra of clusters in Ecal. Top: reconstructed time for clusters in the top half of the Ecal versus for the clusters in the bottom half, for all combinations of two clusters on opposite sides of the detector. Bottom: difference between the times of the top cluster and the bottom cluster. The central peak is from the pairs of clusters from particles from the same reactions and beam buckets as one another. These correspond to the pairs in the diagonal in the top graph. The other peaks are from pairing a cluster from one beam bucket with a cluster from another beam bucket. The events cut out by a 2 ns cut are shown in blue.

The cuts listed so far select a pair of coincident clusters matched to tracks with opposite charges, consistent with an  $e^+e^-$  pair. The remaining cuts reduce contributions from unwanted  $e^+e^-$  coincidences, poorly reconstructed tracks, and converted WABs.

To remove full energy electrons from the data sample, I require that the electron track has momentum less than 1.76 GeV. Additionally, since the combined momentum of the paired particles cannot be more than the beam energy, I make a cut on the paired momentum sum at 2.90 GeV in order to further reduce accidentals. To increase the fraction of radiative tridents in the event sample (which are kinematically identical to the  $A'$  signal), I cut out the events with total momentum less than 1.51 GeV. This cut was chosen to optimize the ratio  $\frac{N_{\text{rad}}(p)}{\sqrt{N_{\text{tot}}(p)}}$ , where  $N_{\text{rad}}(p)$  is the number of radiative tridents that pass the cut, and  $N_{\text{tot}}(p)$  is the total number of  $e^+e^-$  pairs passing the cut, as determined by Monte-Carlo simulations.

In order to remove very poorly fit tracks, I require that both tracks' fit  $\chi^2$  be less than 70. If multiple tracks share at least one hit (e.g., two variations of the same track found using different tracking strategies), I retain the one with the smaller  $\chi^2$ .

To reduce the contribution from converted WABs, I require that the positron track has a hit in the first layer of the SVT, and that its extrapolated position at the target in the beam-curve direction ( $d_0$ ) is less than 1.07 mm. The reason for the latter cut is that in converted WAB events, the positron is usually not produced at the target, but rather in the first or second layer of the SVT.

Table 7.2 summarizes all of the cuts, and tabulates the number of events that pass each of the successive cuts in data and in Monte-Carlo. “Cutflows” such as Figures 7.2 through 7.8, which show the effect of successive cuts on the shape of a given variable (such as invariant mass or cluster time differences), are a useful visual representation of the information in Table 7.2.

Cut	Fraction of events remaining after cut (%)				
	data	60 MeV $A'$	WABs	tridents	radiative tridents
preliminary	100.0	100.0	100.0	100.0	100.0
$n_\sigma < 6.1$	73.8	80.1	67.2	82.8	80.5
electron $p < 1.76$ GeV	68.6	74.1	59.8	75.4	73.9
total $p < 2.90$ GeV	67.9	73.7	57.9	75.2	73.6
track fit $\chi^2 < 70$	60.2	66.8	44.9	68.9	67.1
$ t_{\text{cl}} - t_{\text{trk}} - 55 \text{ ns}  < 4.4 \text{ ns}$	59.1	60.0	38.0	61.1	60.3
positron has L1 hit	43.9	57.0	18.2	58.8	57.4
positron $d_0 < 1.1$ mm	37.8	55.9	13.1	57.6	56.2
$ t_{\text{cl},1} - t_{\text{cl},2}  < 2 \text{ ns}$	34.4	55.1	12.3	56.6	55.4
total $p > 1.51$ GeV	20.5	48.7	9.8	31.9	45.9

TABLE 7.2: Comparison of event acceptance after each cut on the data and on several Monte-Carlo simulations: 60 MeV  $A'$ , WAB, all tridents and radiative tridents. \*The row labeled “preliminary cuts” refers to the following cuts: Pair 1 trigger; both tracks are matched to clusters; if multiple tracks share more than 3 hits, use the track with the best  $\chi^2$ ; and the clusters associated with the electron and positron must be on opposite halves of the detector.

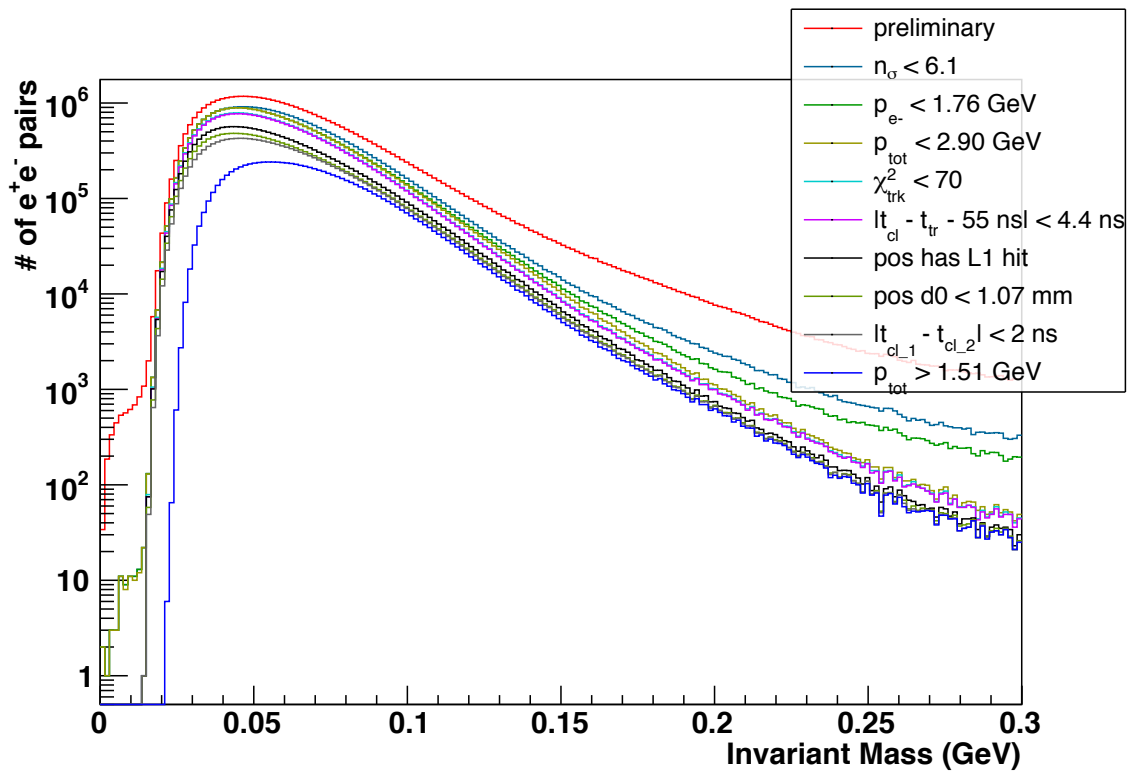


FIG. 7.2: Cutflow of the invariant-mass spectrum of  $e^+e^-$  pairs. The bottom-most blue mass distribution will be the starting point for the bump-hunt analysis. The histogram shown here has been re-binned for visualization purposes.



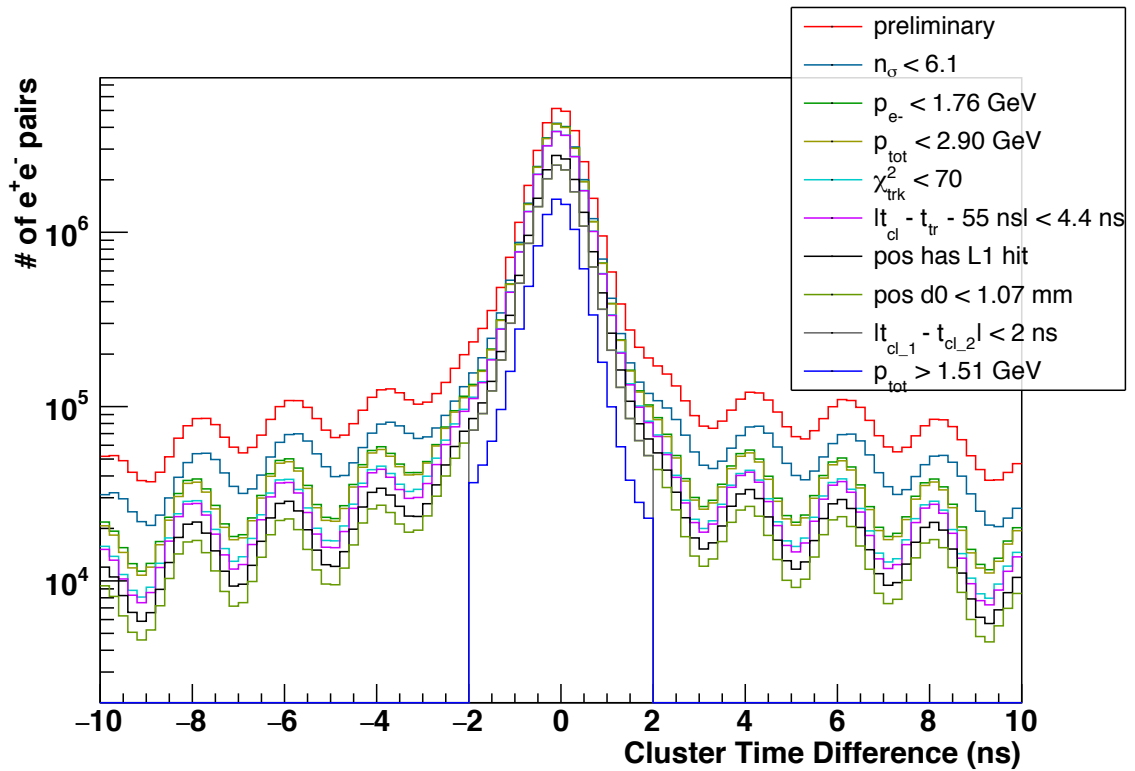


FIG. 7.3: Cutflow of the time difference between cluster times of paired particles. After all cuts have been made, the contamination from accidentals is about 1%.

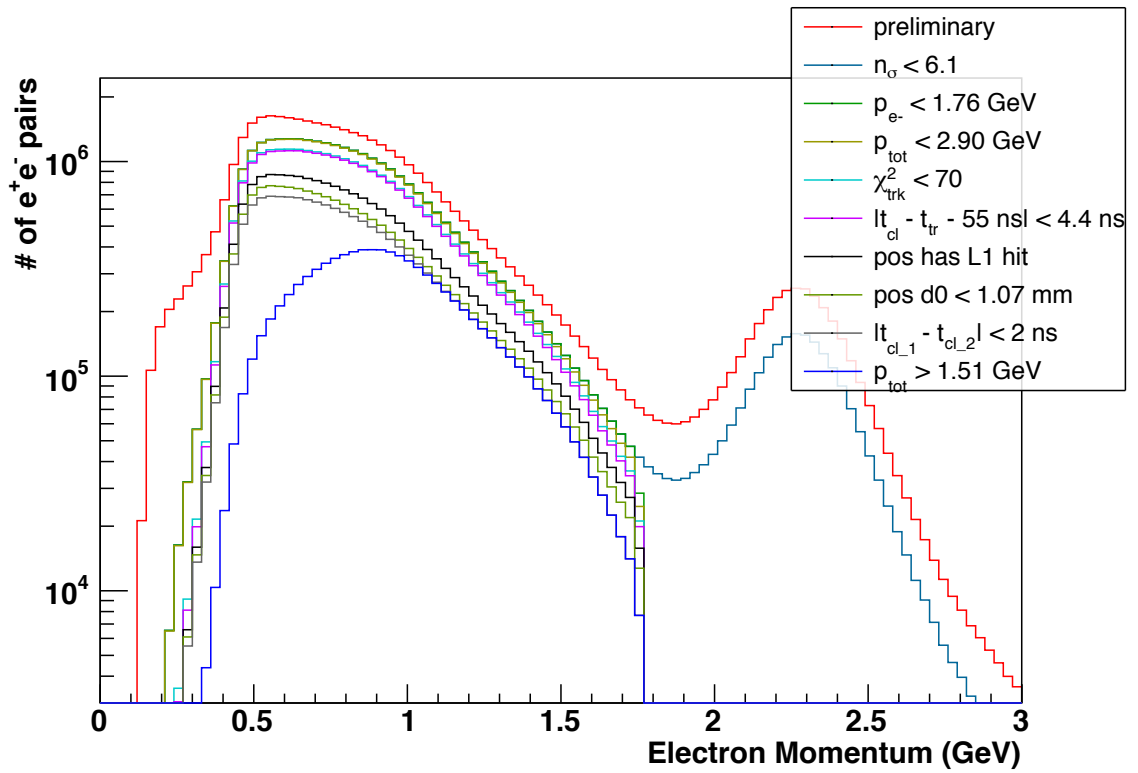


FIG. 7.4: Outflow of the electron momentum.

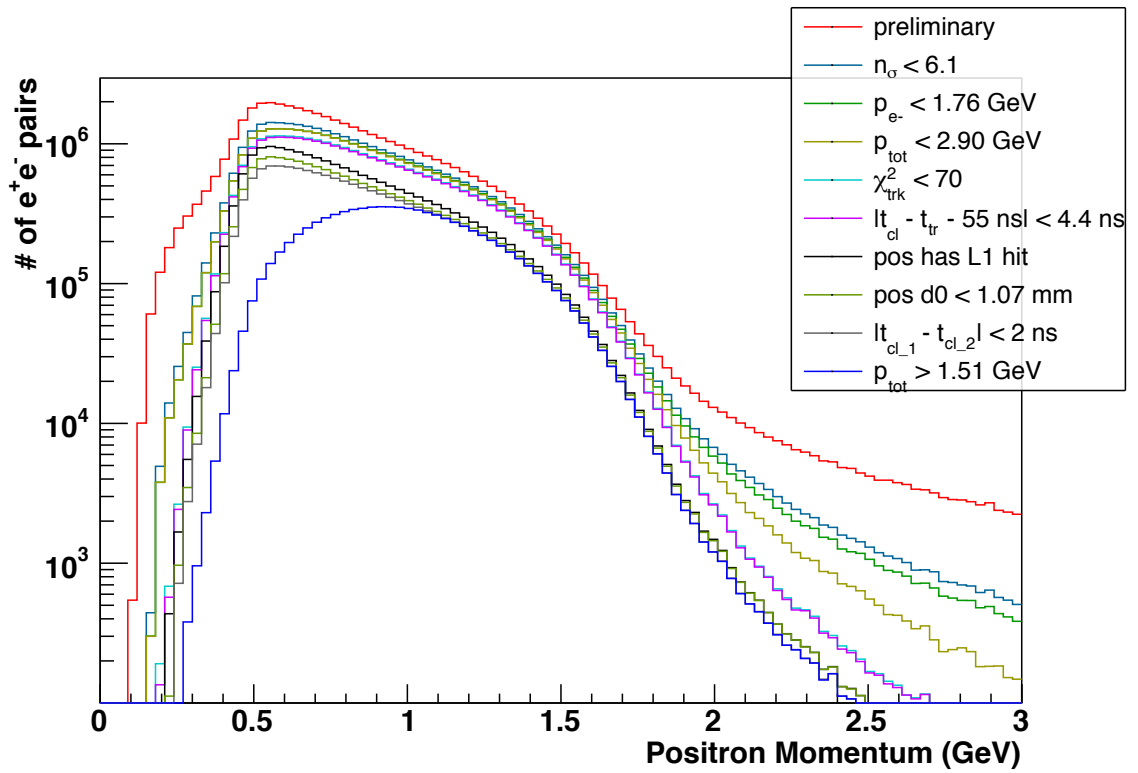


FIG. 7.5: Cutflow of the positron momentum.

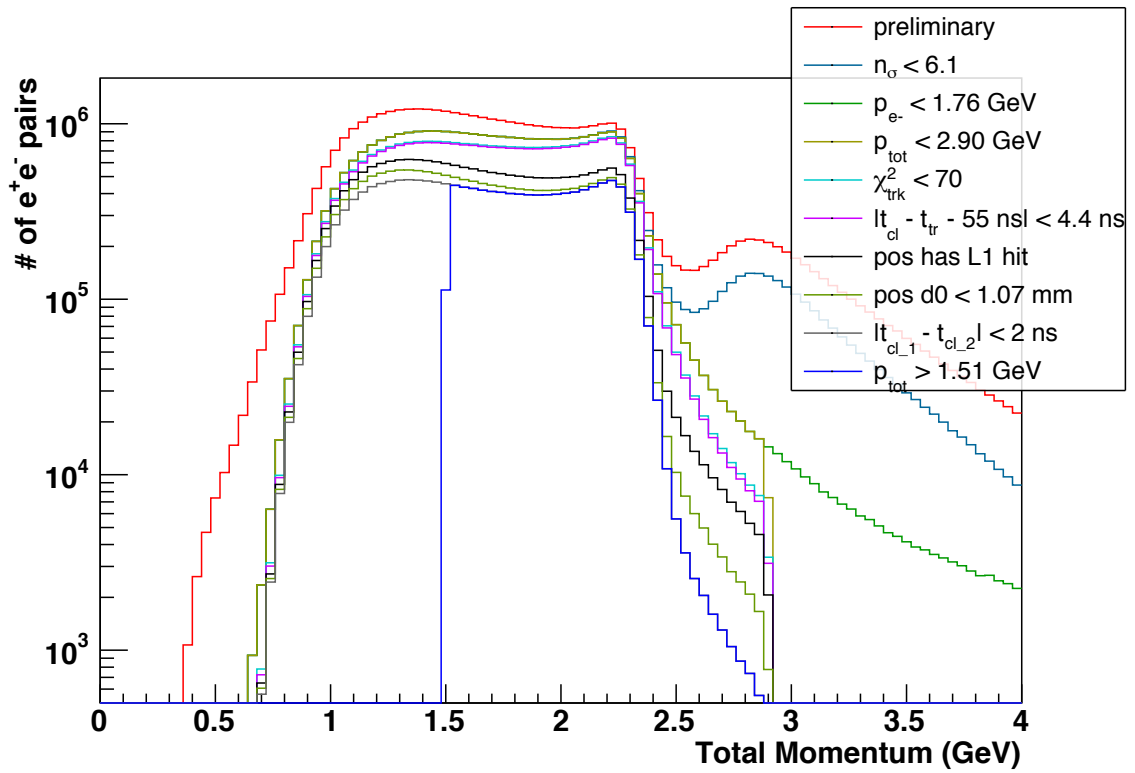


FIG. 7.6: Cutflow of the total momentum of  $e^+e^-$  pairs.

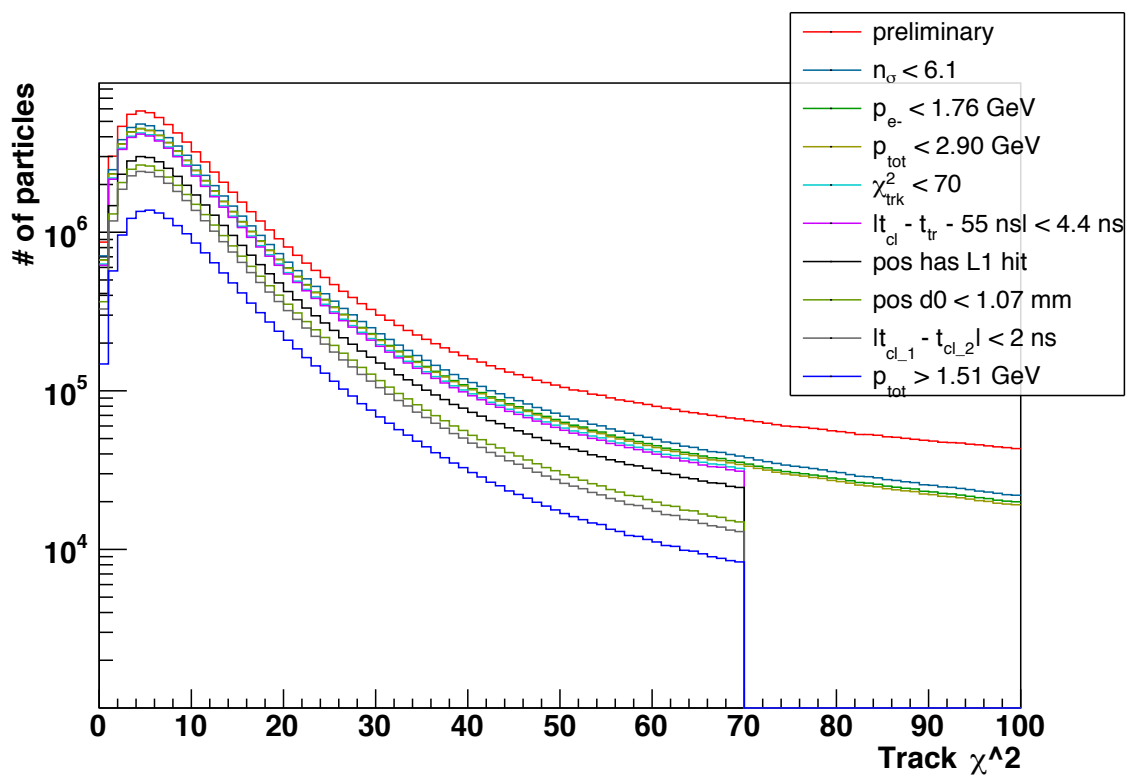


FIG. 7.7: Cutflow of the track fit  $\chi^2$  values.

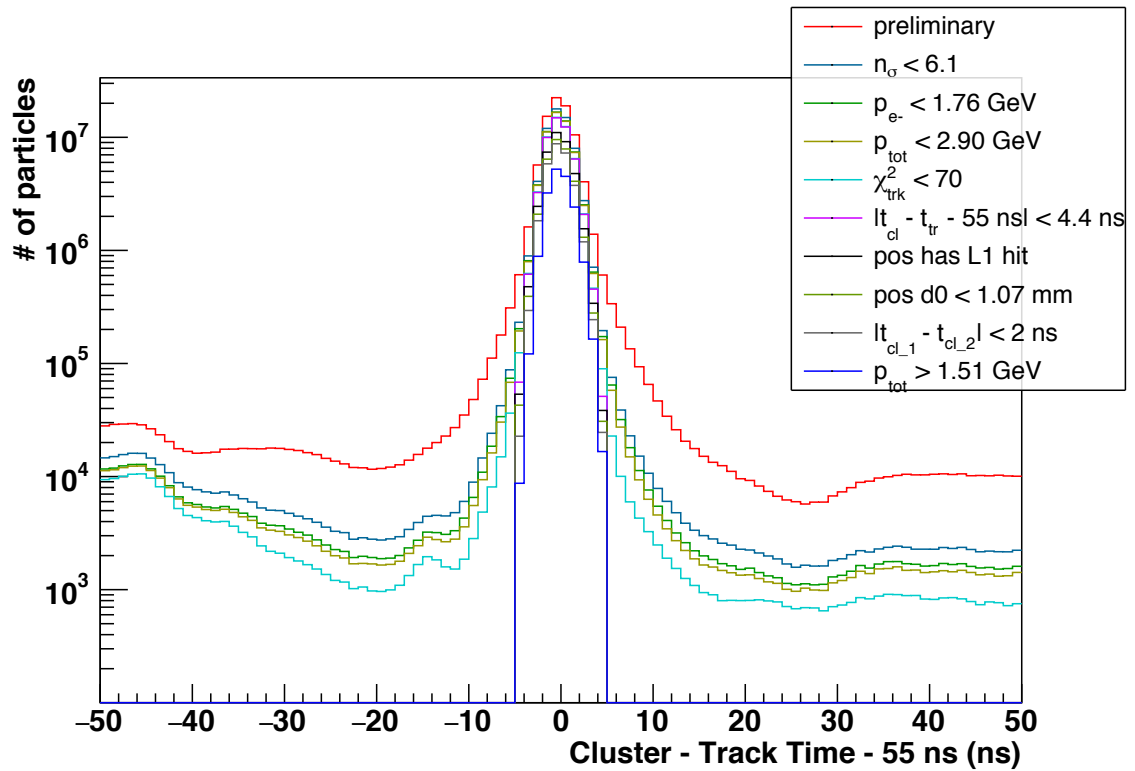


FIG. 7.8: Cutflow of the difference in cluster-track time difference (with a 55 ns offset).

## 7.4 Composition of the $e^+e^-$ Event Sample

After choosing a sample of events from the data, it is necessary to determine what fraction  $f_{\text{rad}}$  of the events in the sample are radiative tridents. This ratio will later be used when converting upper limits on the signal yield to upper limits on the  $A'$  coupling  $\epsilon^2$ .

To determine this fraction, we used three of the Monte-Carlo simulations: radiative tridents, both types of tridents (tritrig<sup>3</sup>) and WABs<sup>4</sup>. The radiative fraction is the ratio of the cross section passing the event selection cuts in the radiative trident sample ( $\sigma_{\text{rad}}$ ) divided by the sum of the cross sections of events passing the same cuts in the full trident and WAB simulations ( $\sigma_{\text{tot}}$ ). The difference in kinematics between the radiative tridents and the rest of the event sample is the most pronounced in the momentum sum spectra (Figure 7.9, top). In order to maximize the statistical significance of the  $A'$  signal events (which are kinematically similar to the radiative tridents), the lower cut on the momentum sum (1.51 GeV) was chosen by maximizing the ratio  $\frac{\sigma_{\text{rad}}}{\sqrt{\sigma_{\text{tot}}}}$ . Figures 7.9 through 7.12 show a comparison between the distributions of several variables in data and in Monte Carlo. I found that the fraction of radiative events in the event sample (after making all cuts) depends on the pair mass, as shown in Figure 7.13, and parametrized in Equation 7.1 below:

$$f_{\text{rad}} = 0.1549 - 0.2473 \exp \left[ \frac{-m}{0.0276 \text{ GeV}} \right]. \quad (7.1)$$

---

<sup>3</sup>“Tritrig” is short for “Trident trigger”, referring to the generator-level cuts that select only events that could potentially cause a Pair 1 trigger.

<sup>4</sup>All three of these simulations include WAB, beam and trident background as described in Section 4.3.

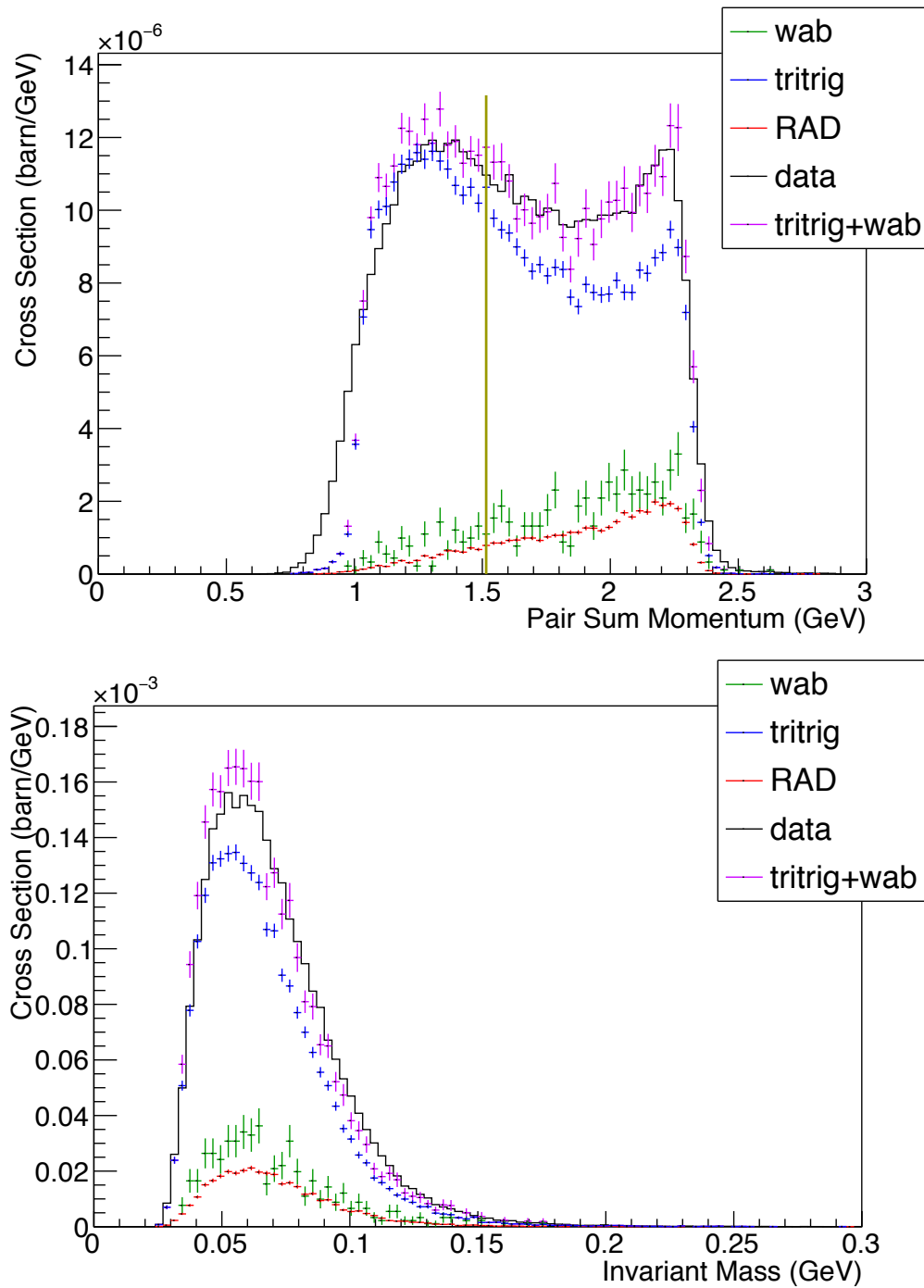


FIG. 7.9: Comparison of pair momentum (top) and invariant-mass (bottom) spectra of  $e^+e^-$  events between data and Monte Carlo. Data from run 7796 are shown in black. The golden vertical line shows the cut chosen for the minimum momentum sum (1.51 GeV).



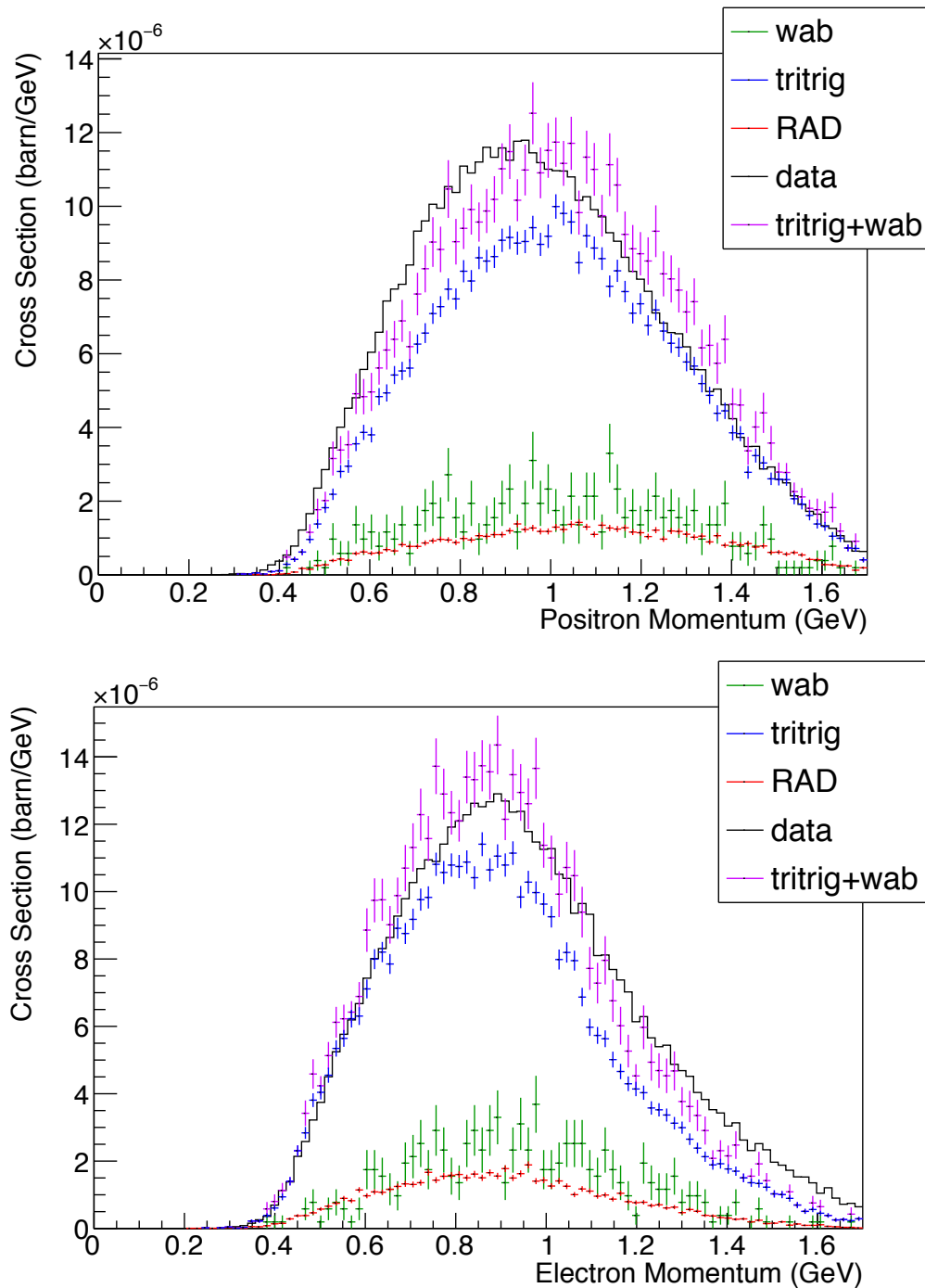


FIG. 7.10: Comparison of particle momenta in  $e^+e^-$  events between data and Monte Carlo. Data from run 7796 are shown in black. The positron momentum spectrum appears to be shifted towards slightly higher momenta in Monte Carlo compared to data, and the opposite trend appears in the electron momentum spectrum. The cause of this is unknown, though it may be caused by problems with the SVT alignment.

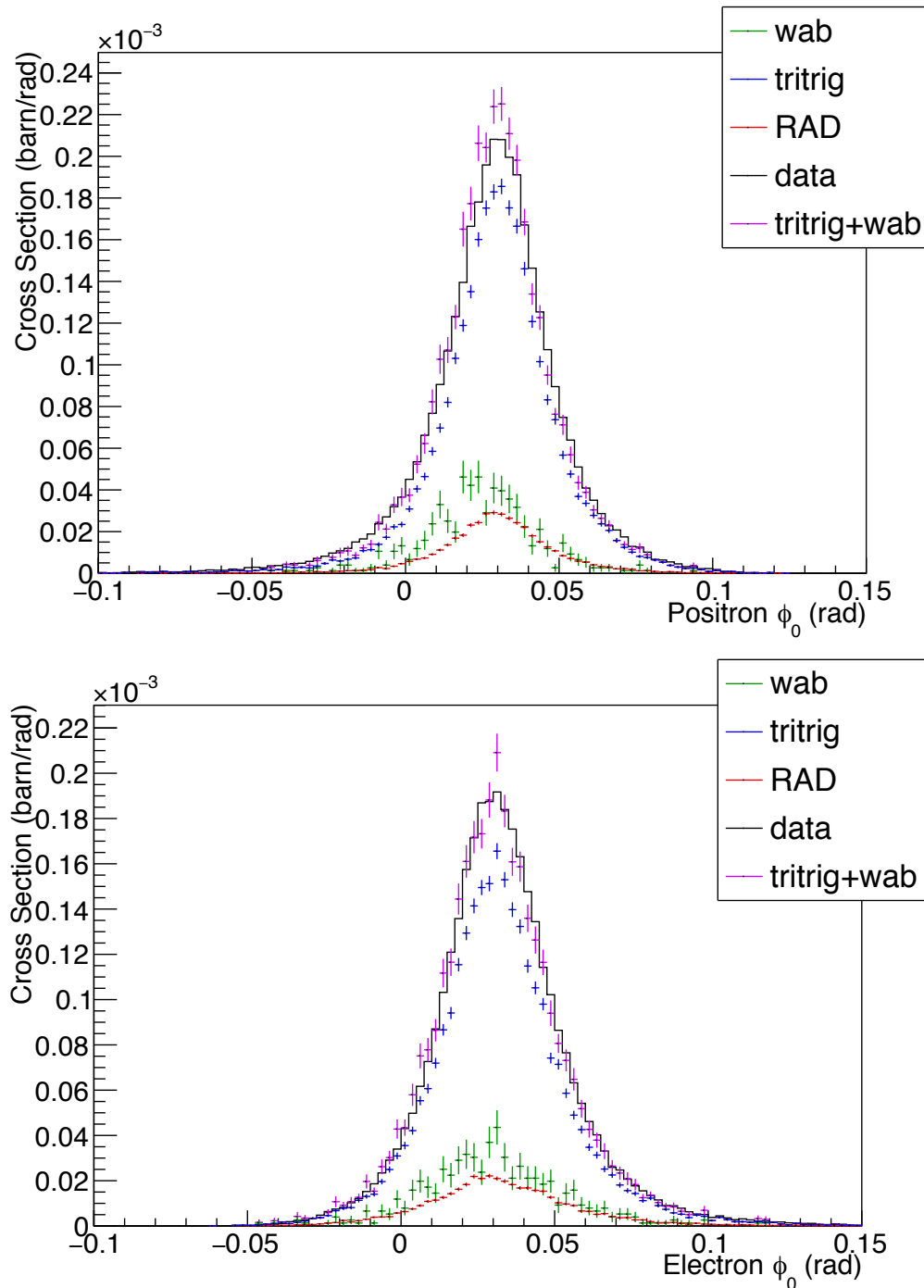


FIG. 7.11: Comparison of particle initial direction (in  $x$ ) in  $e^+e^-$  events between data and Monte Carlo. Data from run 7796 are shown in black.

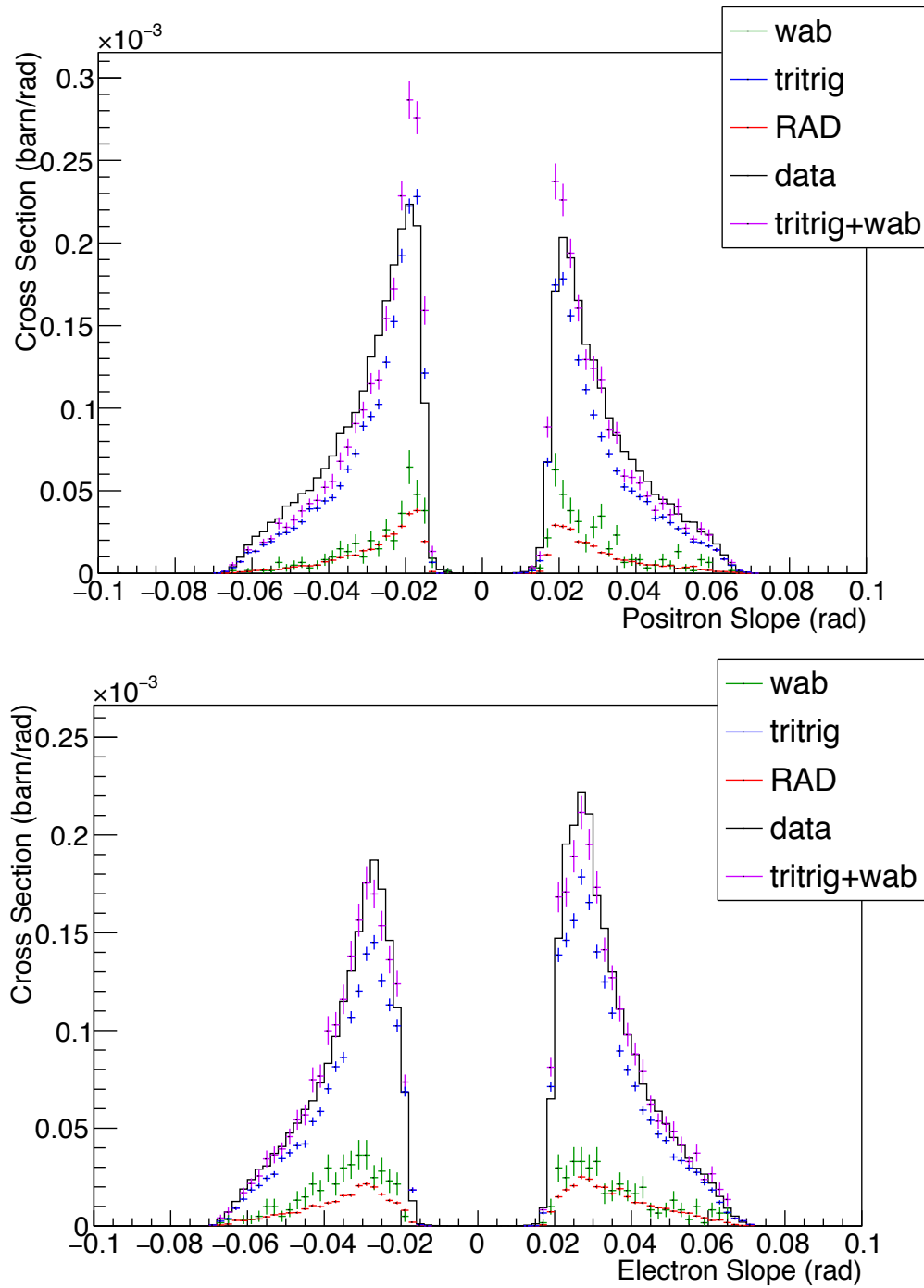


FIG. 7.12: Comparison of particle initial direction (in  $y$ ) in  $e^+e^-$  events between data and Monte Carlo. Data from run 7796 are shown in black.

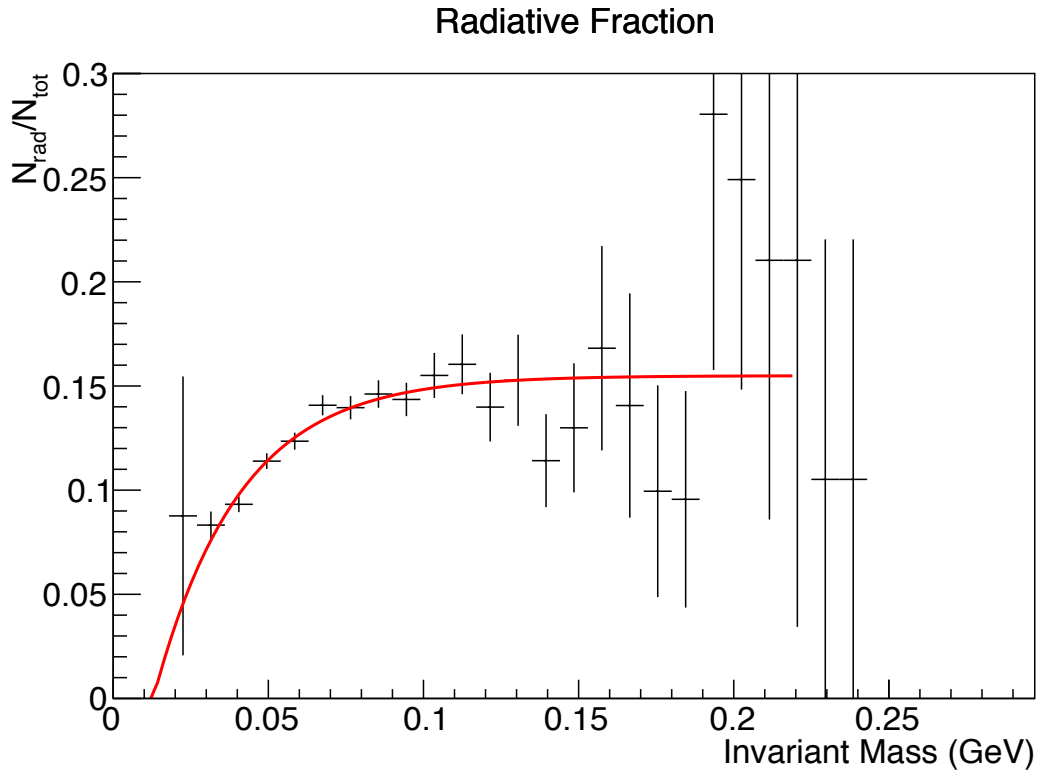


FIG. 7.13: Dependency of the radiative fraction on the invariant mass, as calculated using Monte-Carlo simulations. The red curve represents the parameterization in Equation 7.1. At large masses, statistics are limited both in simulations and data, due to the small cross-sections. Since there is very little sensitivity to dark photons with mass more than 120 MeV, the large uncertainties on  $f_{\text{rad}}$  are not as important as at smaller masses.

## 7.5 Mass Resolution and Signal Shape

After the events have been selected, the invariant masses of the remaining  $e^+e^-$  pairs are calculated via:

$$M = \sqrt{2\sqrt{\mathbf{p}_+^2 + m_e^2}\sqrt{\mathbf{p}_-^2 + m_e^2} + 2m_e^2 - 2\mathbf{p}_- \cdot \mathbf{p}_+} \quad (7.2)$$

where  $\mathbf{p}_+$  and  $\mathbf{p}_-$  are the reconstructed momenta of the two particles, after constraining both of their tracks to have come from the target, at (0, 0, 0.5) mm.

Neglecting the contribution from the electron mass  $m_e$ , this is equivalent to:

$$M = 2 \sin \frac{\theta}{2} \sqrt{p_+ p_-} \quad (7.3)$$

where  $\theta$  is the measured opening angle between the tracks.

Before proceeding with a bump-hunt, it is necessary to know what the expected width and the shape of the signal should be in the invariant-mass spectrum. The intrinsic width of the  $A'$  resonance,  $\Gamma = \frac{\hbar c^2}{\tau} = \frac{N_{eff} \alpha \epsilon^2}{3} m_{A'}$ , is negligible compared to the measurement resolution. I decided to use a Crystal Ball function [75], (consisting of a Gaussian core and a power-law tail on the lower mass side) as a model for the signal shape:

$$f(x) = N \begin{cases} \exp\left(-\frac{(x-\mu)^2}{2\sigma^2}\right), & \frac{x-\mu}{\sigma} > -\alpha \\ A\left(B - \frac{x-\mu}{\sigma}\right)^{-n}, & \frac{x-\mu}{\sigma} < -\alpha \end{cases} \quad (7.4)$$

where  $A = \left(\frac{n}{|\alpha|}\right)^n \exp\left(-\frac{|\alpha|^2}{2}\right)$  and  $B = \frac{n}{|\alpha|} - |\alpha|$ . The function's tail accounts for energy lost by the electron and/or positron as it travels through the SVT layers resulting in a smaller measured mass. The Crystal Ball function has 5 parameters:

- $N$ : an overall normalization factor.
- $\mu$ : the position of the peak of the distribution (that is the mean of the gaussian core).

- $\sigma$ : the standard deviation of the gaussian core.
- $\alpha$ : determines the boundary between the gaussian core and the power-law tail, located at  $\mu - \alpha\sigma$ .
- $n$ : the power in the power-law tail.

To determine the values of  $\sigma$ ,  $\alpha$  and  $n$ , I began by selecting events from the  $A' \rightarrow e^+e^-$  Monte-Carlo samples<sup>5</sup>, each with different  $A'$  masses, using the cuts in Section 7.3. I then plotted the invariant-mass spectrum for each simulated sample, and fit each of these spectra to a Crystal-Ball function. Figure 7.14 shows the reconstructed mass spectra for two of the  $A'$  mass values.

Next, I plotted the values of  $\sigma$ ,  $\alpha$  and  $n$  as functions of the simulated  $A'$  mass (Figures 7.16 and 7.17). I found that  $n$  and  $\alpha$  do not have a significant dependency on the mass, and have approximately constant values of  $2.85 \pm 0.26$  and  $1.23 \pm 0.04$  respectively. The width  $\sigma$  depends strongly on mass, as parameterized by Equation 7.5 below.

$$\sigma(m) = 0.000955 - 0.004198m + 0.2367m^2 - 0.7009m^3 \quad (7.5)$$

where  $m$  is in GeV.

At large  $A'$  masses, the reconstructed mass peak varies slightly from the simulated  $A'$  mass (Figure 7.16, bottom), but never by more than 1%. This discrepancy is parameterized below.

$$\frac{\mu(m) - m}{m} = 0.001598 - 0.03807m + 0.1622m^2 + 0.5723m^3 \quad (7.6)$$

To cross-check the resolutions with the data, we used Møller pairs (which have a known pair-mass) as a “standard candle” to compare the mass-resolutions in data with the Monte

---

<sup>5</sup>This includes background from WABs, beam, and tridents within the trigger window for realism, as described in Section 4.3.

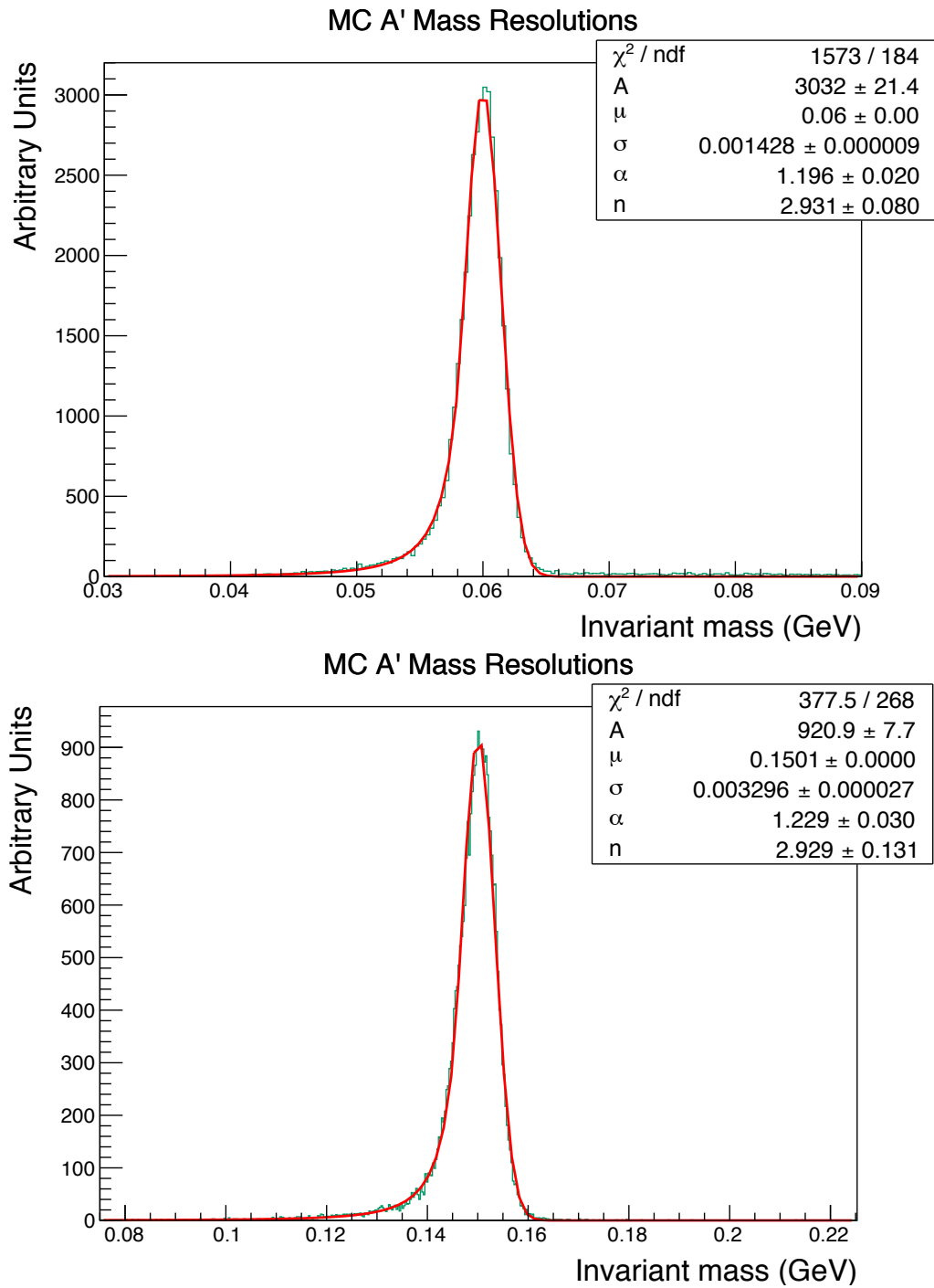


FIG. 7.14: Invariant mass spectrums for  $A'$  Monte Carlo with  $m_{A'} = 60$  MeV (top) and  $m_{A'} = 150$  MeV.

Carlo. For the data Møller sample, I used run 8054, which used the carbon-12 target (rather than the production runs with the tungsten target) since the signal-to-background ratio is larger for lower  $Z$  nuclei, as the Møller signal cross section is proportional to  $Z$  while the electronuclear background is proportional to  $Z^2$ . I used the following cuts to further reduce background in both the data and Monte-Carlo:

- All flags for the SVT status for the event are good.
- Exactly one of the SVT tracks is matched to a cluster in the Ecal with  $n_\sigma < 7$ , while the other track is not matched to any cluster.
- The time difference between the  $e^-$  tracks must be less than 3 ns. This is to reduce out-of-time background accidentals.<sup>6</sup>
- The track fit  $\chi^2$  per degree of freedom for both tracks are less than 7.
- The pair momentum is between 1.8 and 2.9 GeV.
- Both particles' momenta are less than 1.75 GeV.
- The target-constrained vertex fit  $\chi^2$  is less than 100.
- The trigger of the event is Single 0.

Similar to the  $A'$  Monte Carlo, I fit the mass spectra for the Møller data and Monte Carlo to Crystal-Ball functions to determine the mass resolutions (Figure 7.15). I found that the value of  $\sigma$  for the Møller pairs in Monte Carlo was 1.11 MeV, whereas in the data, it was 1.72 MeV, which is worse by 55%.<sup>7</sup> The values of  $\alpha$  were 1.36 and 1.07 for Monte

---

<sup>6</sup>This is place of an Ecal cluster time difference cut, which I used for the  $e^+e^-$  spectrum. With the 2.306 GeV beam energy, only a tiny fraction of the Møller pairs have both electrons producing signals the Ecal due to the small opening angle, therefore I do not require the tracks to be matched to Ecal clusters.

<sup>7</sup>The SVT alignment used in the reconstruction pass that this analysis is based on is very preliminary. Effort is underway to improve the alignment using Millepede, but a new reconstruction pass of the 2016 dataset, with improved alignment, was not available at the time of the writing of this dissertation.



Carlo and data respectively. For  $n$ , these values were 1.8 and 5.3. Also, there is a small discrepancy (-0.34% in Monte Carlo and -2.57% in data) between the fitted peak position and the expected value  $m_{\text{exp}} = \sqrt{2(E_{\text{beam}} + m_e)m_e} = 48.5$  MeV.

To account for the discrepancy between the widths of the Møller pair mass spectra in data and simulation, the values of  $\sigma$  used in the bump-hunt analysis are scaled up using the ratio of the resolutions from the two samples, as shown in Equation 7.7 below. I used the average values of  $n$  and  $\alpha$  from the  $A'$  Monte Carlo in the bump hunt, without applying any corrections from Møller pairs.<sup>8</sup>

$$\begin{aligned}\sigma(m) &= \left( \frac{\sigma_{\text{Møller,data}}}{\sigma_{\text{Møller,MC}}} \right) \times \sigma_{A',\text{MC}}(m) \\ &= \frac{1.72 \text{ MeV}}{1.11 \text{ MeV}} \times (0.000955 - 0.004198m + 0.2367m^2 - 0.7009m^3) \\ &= 1.56 \times (0.000955 - 0.004198m + 0.2367m^2 - 0.7009m^3)\end{aligned}\tag{7.7}$$

---

<sup>8</sup>I did not include the corrections to  $n$  and  $\alpha$  for several reasons. First, it was unclear if the corrections should be additive or multiplicative. Additionally, this would be a second-order correction, and would have a much smaller impact than the correction on  $\sigma$ . Thirdly, the  $A'$  and Møller simulations used different event generators, so it would be difficult to determine whether or not this is the cause of the difference in the tail-shape parameters.

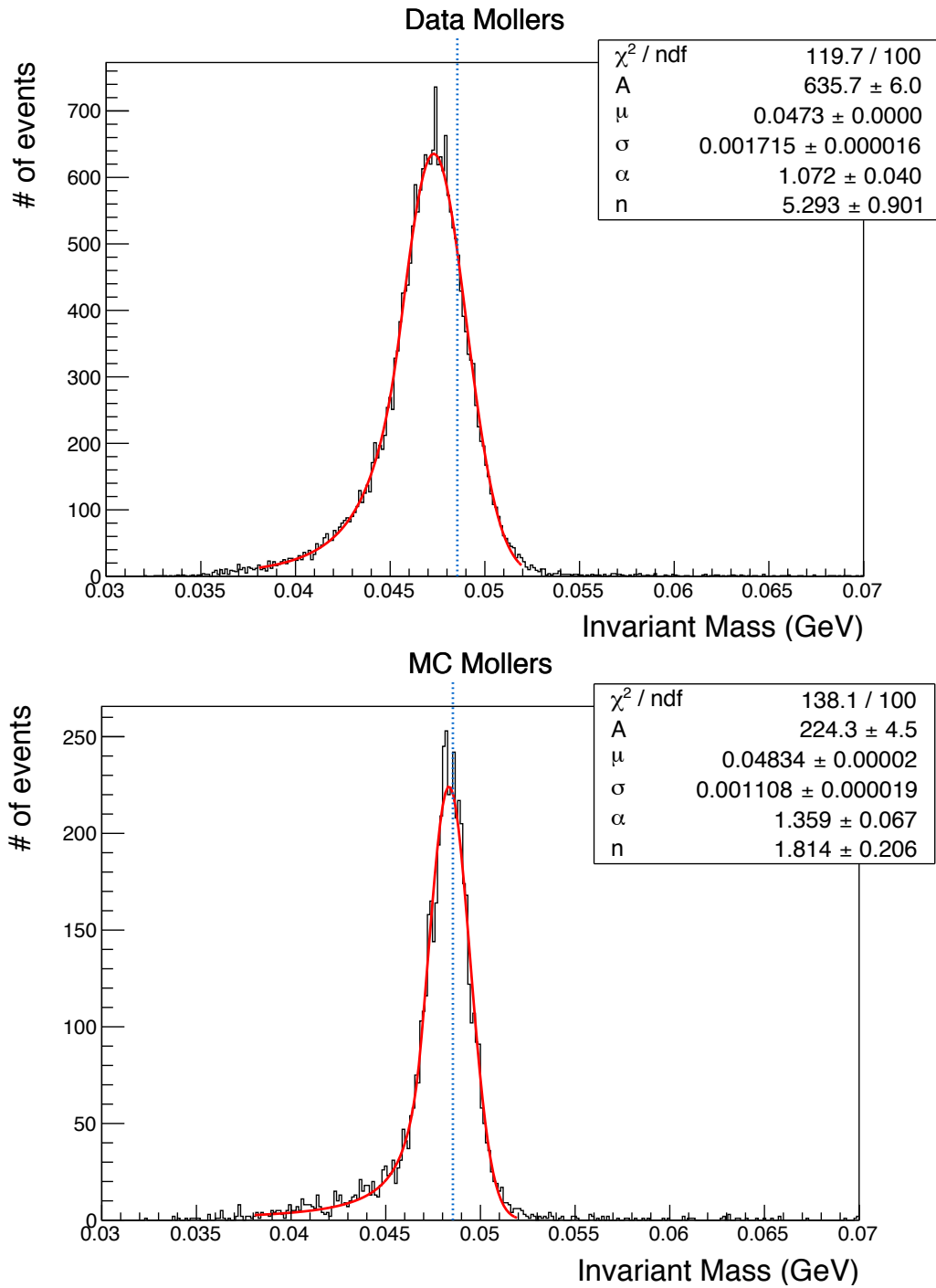


FIG. 7.15: Fitted mass spectra for Møller pairs in data (top) and Monte Carlo (bottom). The blue dashed line represents the expected value,  $\sqrt{2(E_{\text{beam}} + m_e)m_e} = 48.5$  MeV.

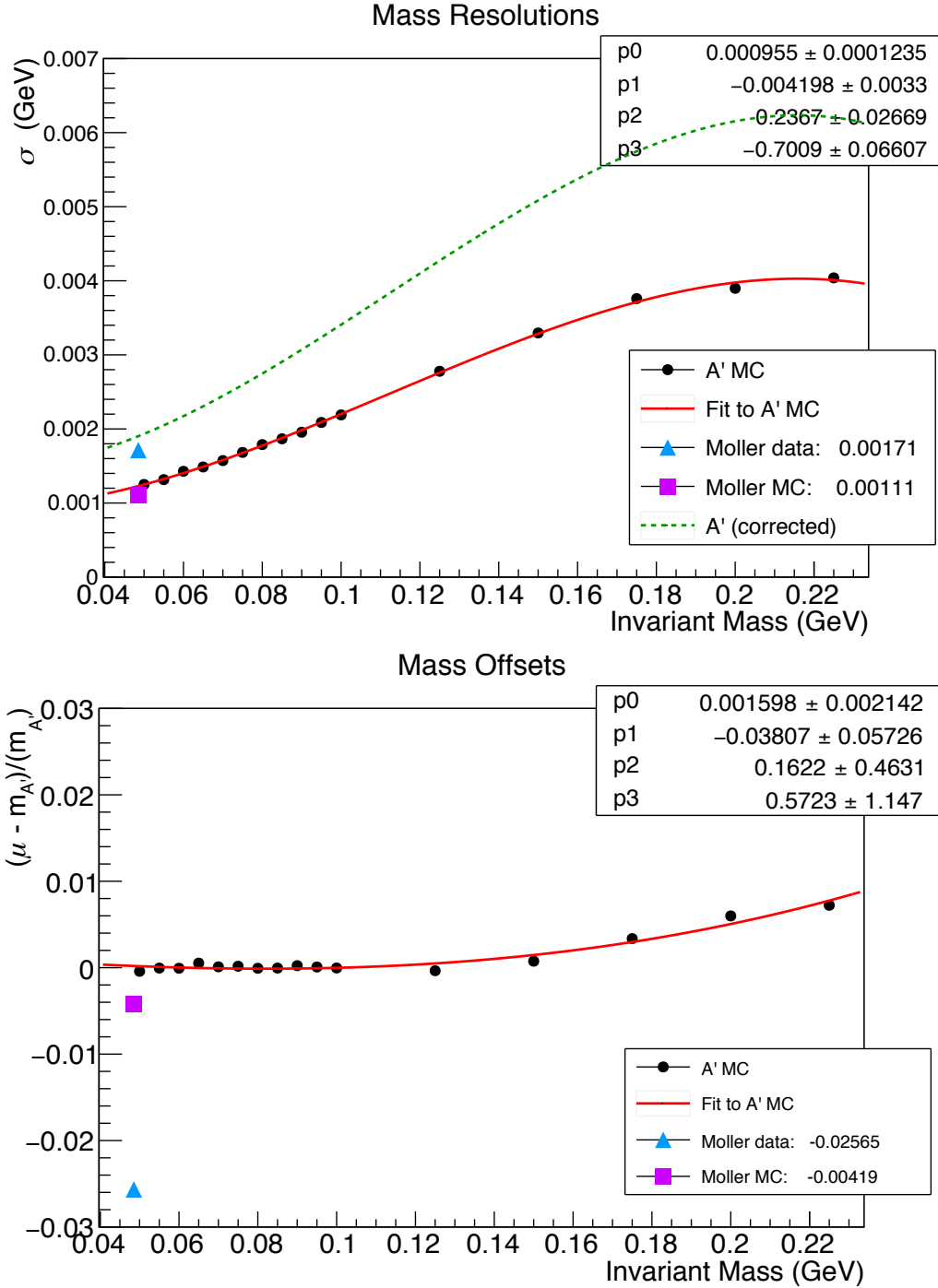


FIG. 7.16: Fit parameters of the reconstructed mass spectra of simulated  $A'$  events, as well as Møller pairs in both data and simulations. Top: widths  $\sigma$  of the gaussian part of the Crystal Ball fits. The dashed green curved represents the “corrected” resolution (Equation 7.7). Bottom: relative shift in mass between the peak and the expected mass ( $m_{A'}$  in  $A'$  simulations,  $\sqrt{2(E_{\text{beam}} + m_e)m_e}$  for Møller pairs).

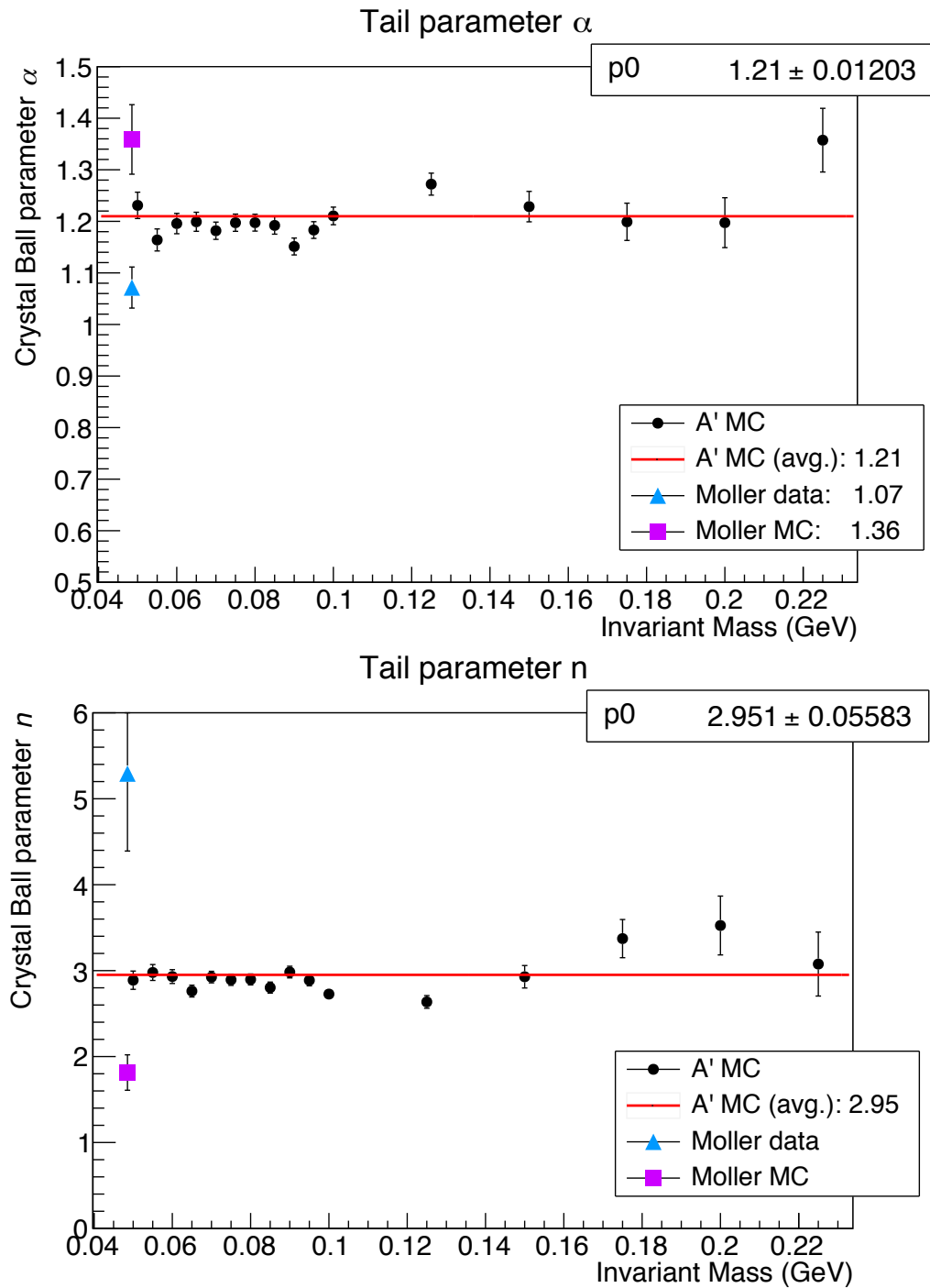


FIG. 7.17: Fit parameters of the reconstructed mass spectra of simulated  $A'$  events, as well as Møller pairs in both data and simulations Top:  $\alpha$ . Bottom:  $n$ .

## CHAPTER 8

# Resonance Search Part 2: Fitting the Mass Spectrum

A dark-photon resonance would appear as a bump on top of the background in the  $e^+e^-$  mass spectrum. Simulations have shown that a Crystal-Ball function is a sufficient model for the shape of the signal, as described in Section 7.5. The mean of this distribution would be at the mass  $m_{A'}$  of the dark photon<sup>1</sup>, with a mass-dependent resolution width  $\sigma_m$  and mass-independent tail parameters  $\alpha$  and  $n$ . The starting point for the resonance search in this chapter is the invariant-mass spectrum measured by HPS (the blue curve in Figure 7.2). The width of the bins in the histogram is 0.05 MeV, which is  $< 1/20$  of the mass resolution for all mass hypotheses.

Since the mass of an  $A'$  is not known *a priori*, it is necessary to step through multiple hypotheses of its mass, scanning the entire  $e^+e^-$  mass spectrum for a significant bump. Around each mass hypothesis a window is constructed, and the distribution of masses is

---

<sup>1</sup>plus some tiny systematic offset.

modeled by the function

$$P(m_{e^+e^-}) = \mu \cdot \phi(m_{e^+e^-} | m_{A'}, \sigma_m, \alpha, n) + B \cdot p(m_{e^+e^-} | \mathbf{t}). \quad (8.1)$$

where  $\mu$  is the signal yield (number of signal events),  $\phi(m_{e^+e^-} | m_{A'}, \sigma_m, \alpha, n)$  is the signal-distribution shape (in this analysis, a normalized Crystal-Ball function with parameters  $(m_{A'}, \sigma_m, \alpha, n)$ ),  $B$  is the number of background events and  $p(m_{e^+e^-} | \mathbf{t})$  is the probability-distribution shape of the background with parameters  $\mathbf{t}$  (in this analysis, the background is a 7th-order Chebyshev polynomial and its coefficients are  $\mathbf{t}$ ).

## 8.1 Formalization of Likelihood-Ratio Test

For a histogram of invariant masses with  $n_i$  events in the  $i^{\text{th}}$  bin, the model in Equation 8.1 predicts that the expectation value of  $n_i$  is

$$E[n_i] = S_i + B_i, \quad (8.2)$$

where

$$S_i = \mu \int_{\text{bin}_i} \phi(m_{e^+e^-} | m_{A'}, \sigma_m, \alpha, n) d(m_{e^+e^-}) \quad (8.3)$$

and

$$B_i = B \int_{\text{bin}_i} p(m_{e^+e^-} | \mathbf{t}) d(m_{e^+e^-}) \quad (8.4)$$

and the integral limits are the edges of the  $i^{\text{th}}$  bin. The parameters of the background,  $(B, \mathbf{t})$ , also called “nuisance parameters”, will hereafter be denoted as  $\theta$ . The Poisson likelihood

for a given  $\mu$  and  $\theta$  is then defined as [76]

$$\mathcal{L}(\mu, \theta) = \prod_{i=1}^{n_{\text{bins}}} \frac{(S_i + B_i)^{n_i}}{n_i!} e^{-(S_i + B_i)}, \quad (8.5)$$

where the product is over all the bins in the window. The values  $\hat{\mu}$  and  $\hat{\theta}$  which maximize  $\mathcal{L}(\mu, \theta)$  provide an estimate for the signal yield and nuisance parameters<sup>2</sup>.

The purpose of a resonance search is to discriminate between two scenarios, as illustrated in Figure 8.1:

- background-only (null hypothesis):  $\mu = 0$
- signal+background (alternative hypothesis):  $\mu > 0$

To accomplish this, a test statistic is used to compare the likelihoods of each of the two scenarios. A typical test statistic is the ratio of the maximized likelihoods between the signal+background hypothesis and the background-only hypothesis (where in the latter,  $\mu$  is constrained to zero):

$$\lambda(\mu) = \frac{\mathcal{L}(\mu, \hat{\theta})}{\mathcal{L}(\hat{\mu}, \hat{\theta})} \quad (8.6)$$

where  $\hat{\theta}$  is the “conditional estimator” of  $\theta$ , that is the value which maximizes  $\mathcal{L}(\mu, \theta)$  for a fixed value of  $\mu$  (in this case, 0)<sup>3</sup>. In our situation, however, a more appropriate test statistic is

$$q_0 = \begin{cases} -2 \ln \frac{\mathcal{L}(0, \hat{\theta})}{\mathcal{L}(\hat{\mu}, \hat{\theta})} & \hat{\mu} \geq 0 \\ 0 & \hat{\mu} < 0 \end{cases} \quad (8.7)$$

---

<sup>2</sup>Under certain limits with large datasets,  $-2\ln\mathcal{L}$  is equivalent to the Pearson  $\chi^2$ ; therefore maximizing  $\mathcal{L}$  is equivalent to minimizing  $\chi^2$ .

<sup>3</sup>In this notation system, borrowed from [76],  $\hat{\mu}$  and  $\hat{\theta}$  are used when both the signal and nuisance parameters are allowed to vary, and  $\mu$  and  $\hat{\theta}$  are used when we fix the signal and only allow the nuisance parameters to vary.

This test statistic has two advantages over  $\lambda(0)$ : First, the logarithm keeps the size of  $q_0$  reasonable. Secondly, since a dark photon can only cause a positive signal, the test statistic is set to zero if  $\hat{\mu} < 0$  (This is equivalent to defining  $(\hat{\mu}, \hat{\theta})$  to be the values of  $(\mu, \theta)$  that maximize  $\mathcal{L}(\mu, \theta)$  while requiring  $\mu \geq 0$ ). In the large sample limit, this test statistic would be distributed according to a  $\frac{1}{2}\chi^2$  distribution, defined as [76]

$$f(q_0|0) = \frac{1}{2} \left( \delta(q_0) + \frac{1}{\sqrt{2\pi}} \frac{1}{\sqrt{q_0}} e^{-q_0/2} \right) \quad (8.8)$$

The two terms inside the parentheses are a delta function at zero and a  $\chi^2$  distribution with one degree of freedom, respectively. How extreme a measurement of  $q_0$  is can be quantified by the  $p$ -value, defined by

$$p = \int_{q_{0,\text{obs}}}^{\infty} f(q_0|0) dq_0, \quad (8.9)$$

which is the probability, given  $\mu = 0$  of obtaining a value of  $q_0$  more extreme than  $q_{0,\text{obs}}$ , as illustrated in Figure 8.2. This quantity is typically compared to some significance level  $\alpha$  to determine whether or not to reject the null hypothesis in favor of the alternative hypothesis. In particle physics, it is typical to use  $\alpha = 3 \times 10^{-7}$  (that is,  $5\sigma$ ) as the standard for discovery of a new phenomenon or particle. In other words, if the null hypothesis is true, then the probability of getting a  $p$ -value at that level due to a statistical fluctuation in the background (and thus mistakenly rejecting the null hypothesis) would be 1 in 3.5 million.



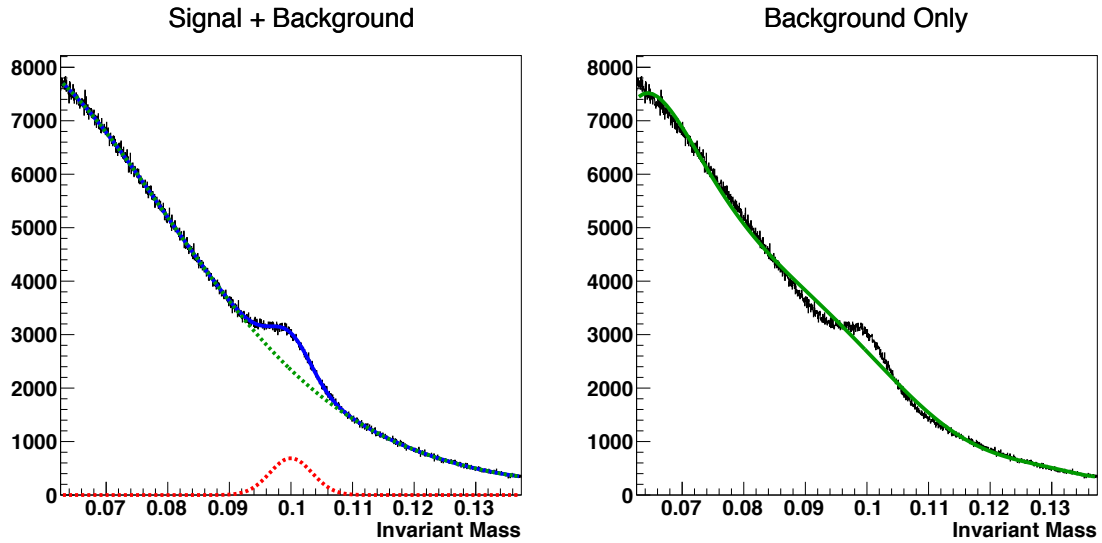


FIG. 8.1: Illustration a signal+background fit (blue, left) and background-only fit (green, right) for a simulated mass spectrum.

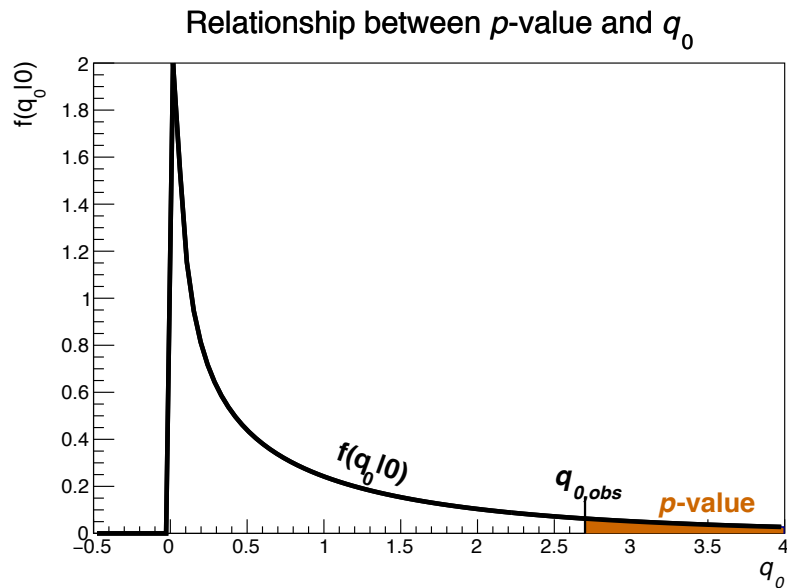


FIG. 8.2: Relationship between the test-statistic  $q_0$  and the associated  $p$ -value. The black curve represents the probability distribution function  $f(q_0|0)$ . If a measurement  $q_{0,obs}$ , then the  $p$ -value is the probability of obtaining a larger value of  $q_0$ , and is represented by the area in brown.

## 8.2 Background and Signal Models

The signal part of the signal-plus-background model is a Crystal Ball function with the mean fixed at the mass hypothesis, and with the other parameters fixed at  $\alpha = 1.21$  and  $n = 2.85$  and the  $\sigma$  value calculated from Equation 7.7. The only remaining free parameter of the signal part of the model is the normalization factor,  $\mu$ .

For the background, I tested several models but ultimately decided to use a 7th-order Chebyshev polynomial, fit within a window centered at the mass hypothesis that is 18 times wider than the mass resolution from Equation 7.7.

To quantify the goodness of a choice of a background model and/or fit window size, pseudo-datasets were employed. A global fit to the mass spectrum was made using the smooth function in Equation 8.10, and is shown in Figure 8.3, while Figure 8.4 shows its residuals. I then generated  $\sim 10^4$  pseudo-datasets by randomizing the height of each bin in a histogram, according to a Poisson distribution whose mean is the value of the global-fit function at the center of that bin.

$$f(m) = Ae^{-k(m-60 \text{ MeV})} \left( \frac{m - m_0}{60 \text{ MeV} - m_0} \right)^b \left[ 1 + \sum_{i=1}^7 a_i \left( \frac{m}{60 \text{ MeV}} \right)^i \right] \left[ 1 + \sum_{i=1}^7 a_i \right]. \quad (8.10)$$

Two types of metrics determine the viability of a given choice of a background model. The first type of metric is the signal pull, defined by

$$\text{pull} = \frac{\mu_{\text{fit}} - \mu_{\text{inj}}}{\mu_{\text{fit\_error}}}, \quad (8.11)$$

where  $\mu_{\text{fit}}$  is the mean value of the signal yields,  $\mu_{\text{inj}}$  is the signal injected into the pseudo-dataset<sup>4</sup> and  $\mu_{\text{fit\_error}}$  is the standard deviation of the signal yields. The second metric is the statistical upper limit on the signal yield. Figures 8.5 show the signal pulls and median values of upper limits calculated from the pseudo-datasets for several choices

---

<sup>4</sup>In this case, the injected signal is set to zero. In other studies of systematics, an injected signal may be added.

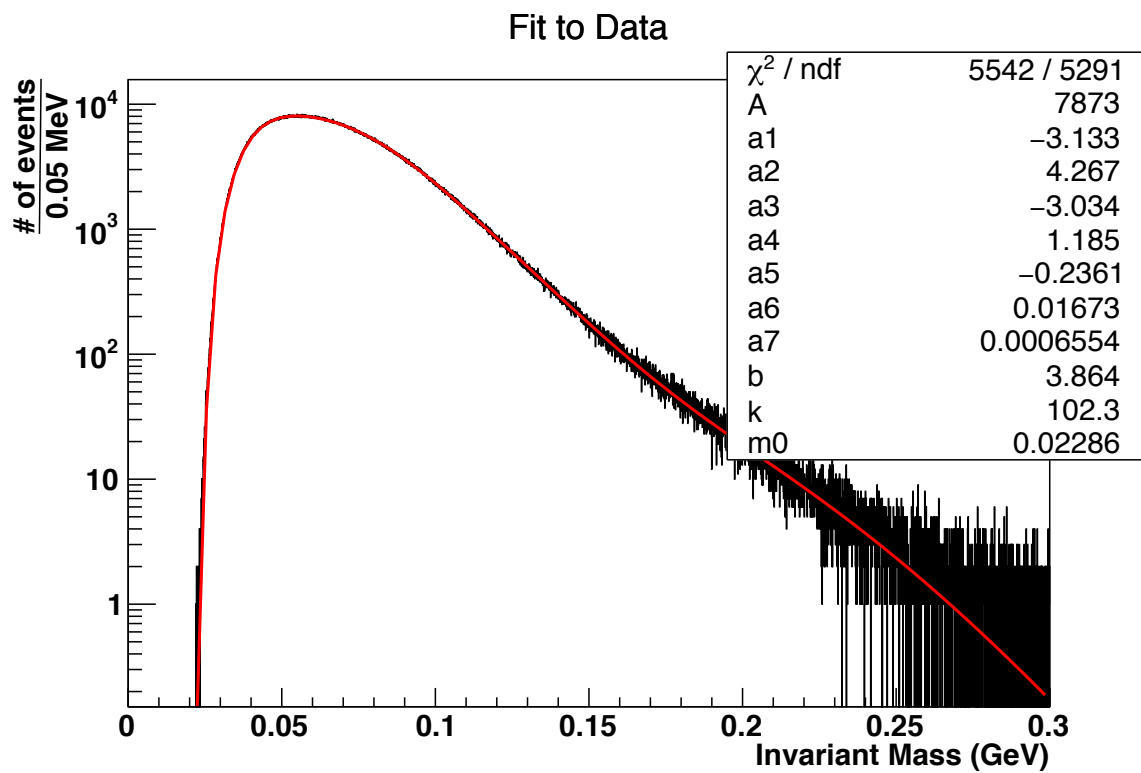


FIG. 8.3: Function used for generating pseudo-datasets (Equation 8.10).

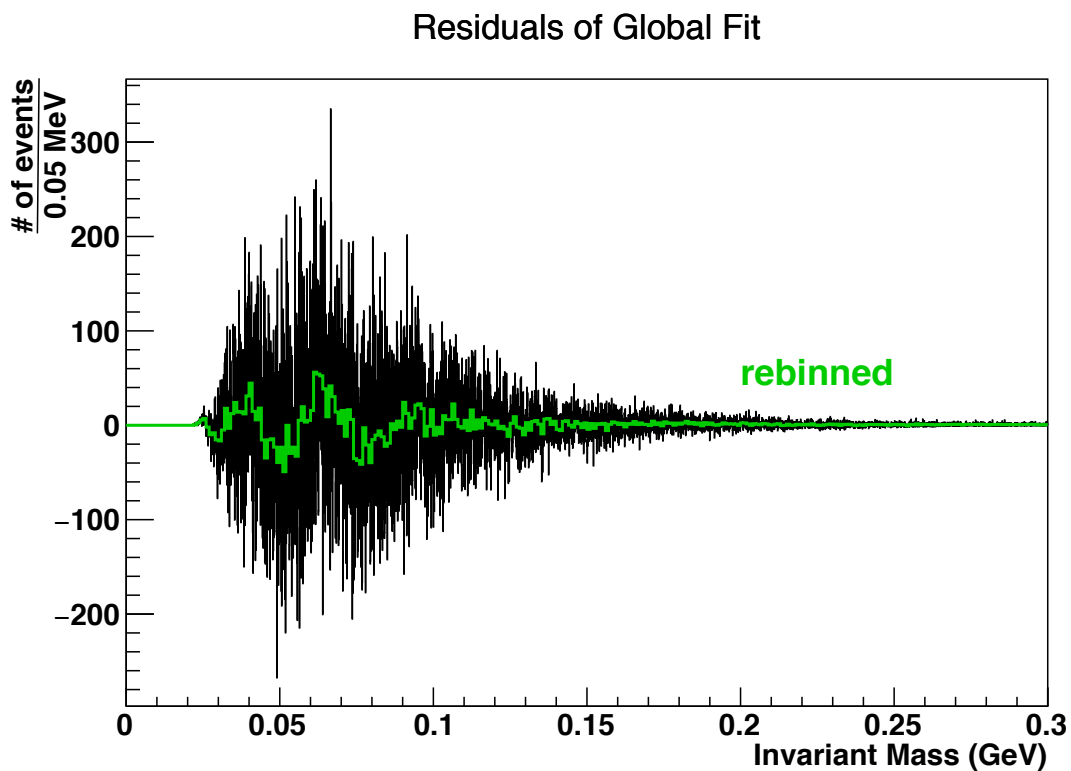


FIG. 8.4: Residuals of the global fit (black). The green histogram shows the average residuals in sets of 20 consecutive bins, to make trends in the residuals easier to visualize.

of background models and window sizes. For a background model to be viable, the signal pulls must be reasonably small; I require them to be less than 20% for any mass hypothesis. Among the choices of background models for which the pulls are reasonably small, I chose the one with the smallest statistical upper limit on the signal yield.

The mass hypotheses are 0.25 MeV apart for mass hypotheses between 45 to 70 MeV, 0.5 MeV from 70 to 140 MeV, and 1 MeV from then onward. This ensures that the spacing between consecutive mass hypotheses is less than  $1/5$  of the mass resolution, thus reducing systematics.

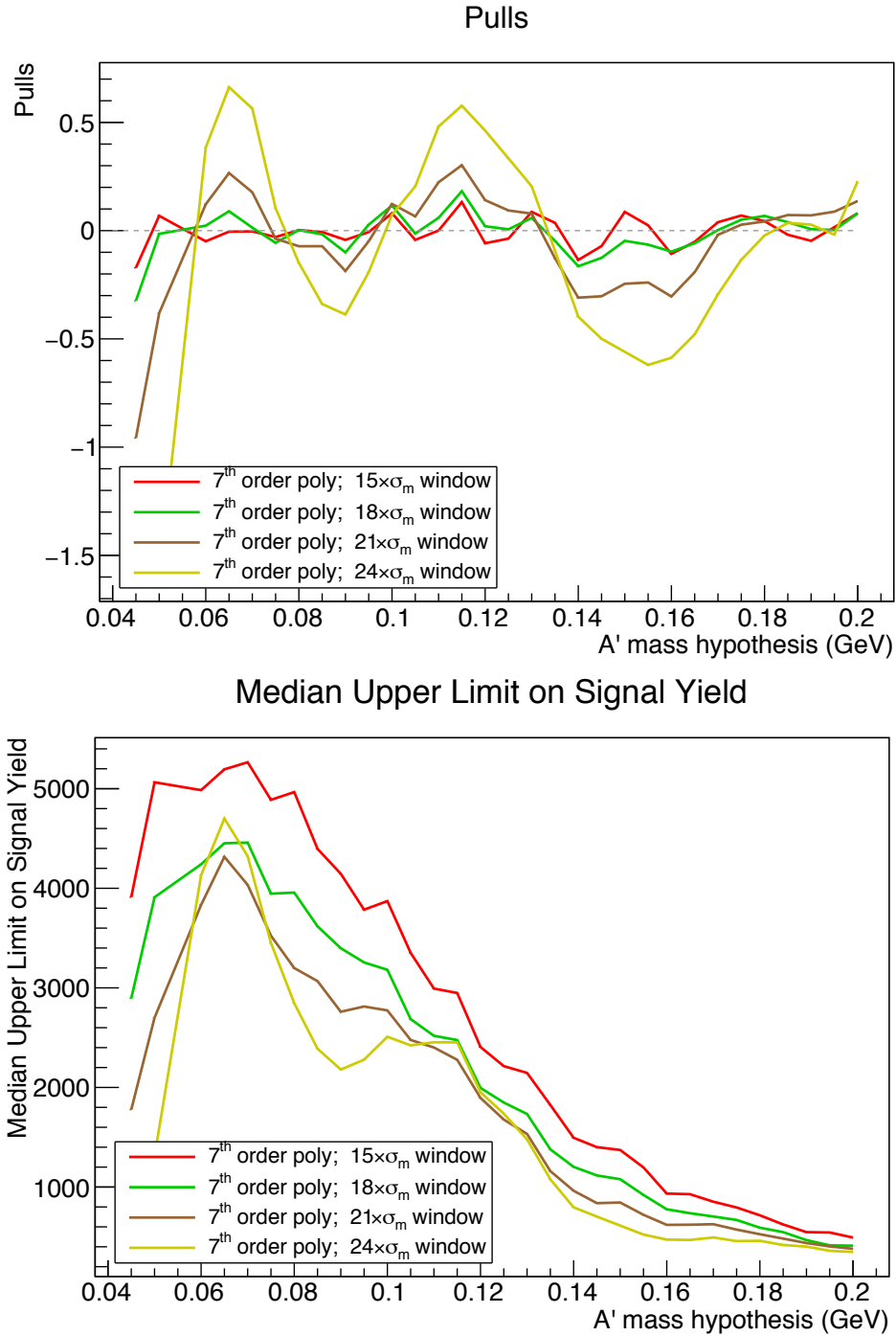


FIG. 8.5: Comparison of various choices of background polynomial order and window sizes. The metrics compared are the pulls (top) and median signal upper limits (bottom) from the pseudo-datasets, which are plotted here as functions of the invariant mass.

### 8.3 Look-Elsewhere Effect

As was discussed in the previous section, the  $p$ -value corresponds to the probability of producing a result that is more extreme than the observed result due to statistical fluctuations. However, this is only the case if we run the analysis for only a single mass hypothesis. Since we do not know *a priori* the mass of the dark photon, we loop through  $n \sim \mathcal{O}(100)$  mass hypotheses to search for a resonance. This means that the actual probability of getting at least one  $p$ -value less than some significance  $\alpha$  is not  $\alpha$  but  $\mathcal{O}(n \times \alpha)$ .

We define the “local”  $p$ -value as the lowest fit  $p$ -value found for any of the mass hypotheses. Then the “global”  $p$ -value is defined as the probability of getting a local  $p$ -value less than some value due to statistical fluctuations alone. To determine how significant a bump really is requires determining the global  $p$ -value for the calculated  $p$ -value.

The relationship between the global and local  $p$ -values cannot be determined analytically, since there are non-zero correlations between the  $p$ -values at nearby mass hypotheses. Therefore in order to get the relationship between the global and local  $p$ -values shown in Figure 8.6, I used the  $\sim 10^4$  pseudo-datasets described in the previous section and ran the bump-hunt algorithm for each of the mass hypotheses to calculate the lowest  $p$ -value in the pseudo-dataset. Then I calculated the global  $p$ -value by ranking the local  $p$ -values. (This allows us to see find the relationship between the local and global  $p$ -values down to a global  $p$ -value of  $\sim 10^{-4}$ , however, the asymptotic relationship between the two  $p$ -values should hold for smaller  $p$ -values.) Asymptotically, the global  $p$ -value is about 2 orders of magnitude larger than the local  $p$ -value, which is what one would expect for  $\sim 100$  mass hypotheses.

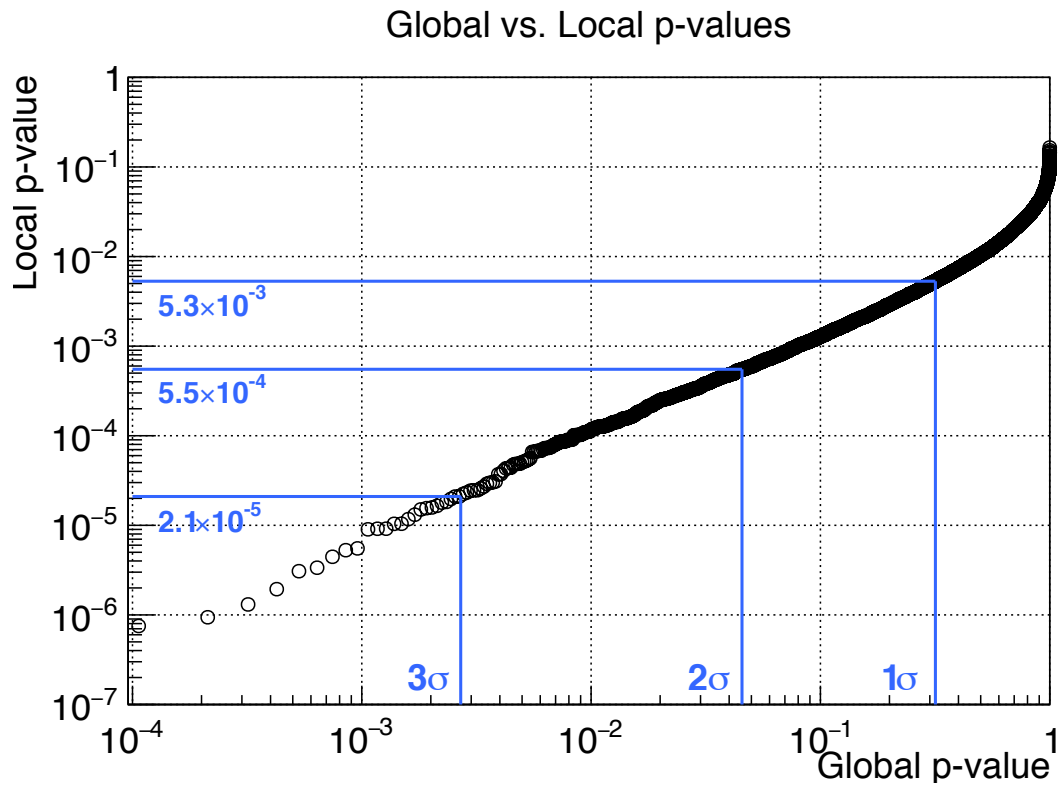


FIG. 8.6: Relationship between global and local  $p$ -values. Blue lines indicate 1, 2, and 3  $\sigma$  global significance levels.



## 8.4 Exclusion-Region Calculation

If we do not find a dark photon signal, we determine the range of  $A'$  masses and couplings for which we can exclude at 95% confidence level. The first step is to determine the upper limits on the signal yield,  $\mu_{\text{up}}$ . This is accomplished by scanning through values of  $\mu$ , and performing a log-likelihood ratio test to compare the likelihoods of the signal + background model with signal yield fixed at  $\mu$  to the case where the signal yield is  $\max(\hat{\mu}, 0)$ . The scan begins with  $\mu = \hat{\mu}$ , and continues incrementing  $\mu$  until the  $p$ -value reaches 0.05. As the  $p$ -value approaches 0.05, the increment gets smaller, in order to fine-tune the upper limit. The  $p$ -value in this case is the probability that the signal part of the fit would be less than or equal to  $\max(\hat{\mu}, 0)$ , under the assumption that the dark photon exists and that its coupling  $\epsilon^2$  is such that the expected signal yield is  $\mu$ . The test statistic in this case is [76]:

$$q_\mu = \begin{cases} -2 \ln \frac{\mathcal{L}(\mu, \hat{\theta})}{\mathcal{L}(0, \hat{\theta})} & \hat{\mu} < 0 \\ -2 \ln \frac{\mathcal{L}(\mu, \hat{\theta})}{\mathcal{L}(\hat{\mu}, \hat{\theta})} & 0 \leq \hat{\mu} \leq \mu \\ 0 & \mu < \hat{\mu} \end{cases} \quad (8.12)$$

where  $\mathcal{L}(\mu, \hat{\theta})$  is the likelihood evaluated with the signal yield fixed at  $\mu$  and the  $\hat{\theta}$  that maximizes the likelihood given the constraint on  $\mu$ . The corresponding  $p$ -value is then

$$p = \int_{q_{\mu, \text{obs}}}^{\infty} f(q_\mu | \mu) dq_\mu \quad (8.13)$$

where  $f(q_\mu | \mu)$  is calculated using the  $\frac{1}{2}\chi^2$  distribution discussed earlier in Equation 8.8. The unconstrained upper limit,  $\mu_{\text{up}}$  is then the value of  $\mu$  such that  $p_\mu = 0.05$ , corresponding to 95% confidence.

To avoid underestimating the upper limit on the signal yield in regions where the observed signal yield fluctuates downward, a power-constrained upper limit is used [77]. This clips off the downward fluctuations at the points where the sensitivity is too low.

To do this, I generated and fitted  $\sim 10^4$  pseudo-data sets at each mass hypothesis, and calculated the median (50% percentile) of the signal-yield upper limits for the fits ( $\mu_{\text{median}}$ ). Then the power-constrained upper limit of the signal yield ( $\mu_{\text{pc}}$ ) is defined as the larger of the unconstrained or median upper limits for a given mass hypothesis:

$$\mu_{\text{pc}} = \max(\mu_{\text{up}}, \mu_{\text{median}}). \quad (8.14)$$

Figure 8.7 illustrates the relationship between the unconstrained, median and power-constrained upper limits for our dataset.

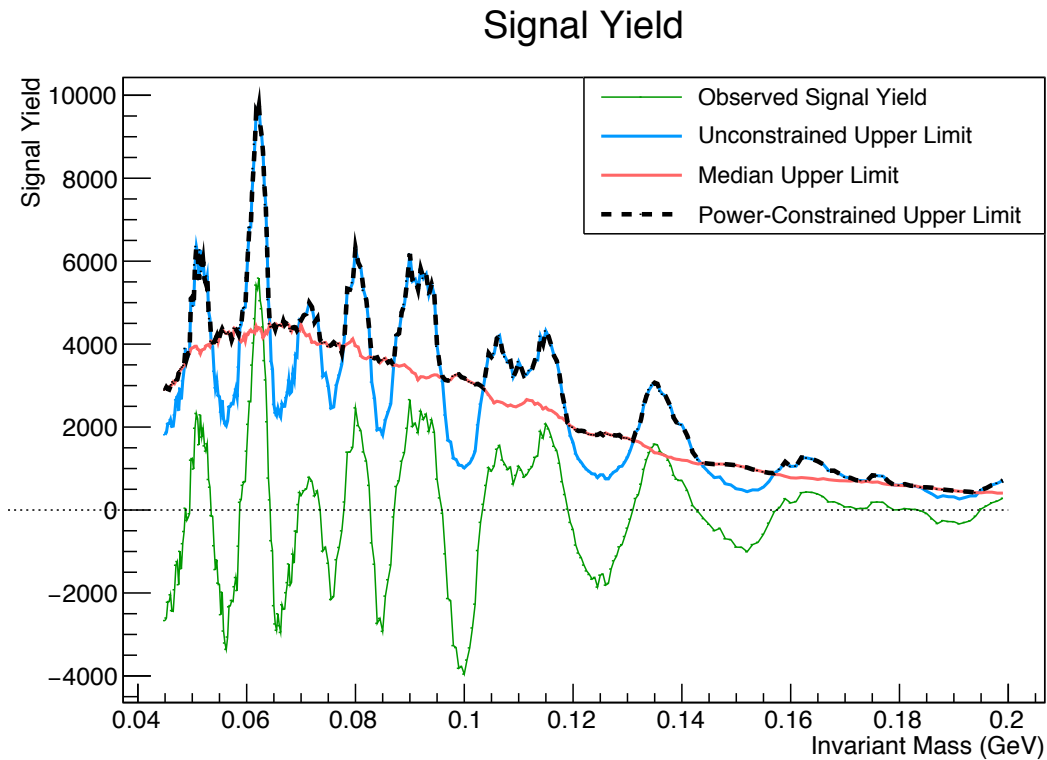


FIG. 8.7: Upper limits on the signal yield at each mass hypothesis. The power-constrained upper limit (black dashed line) is used for calculating exclusion limits.

From the power-constrained upper limit on the signal yield, the upper limit on the coupling  $\epsilon^2$  for a given mass hypothesis can be calculated:

$$\epsilon^2 = \frac{\mu_{\text{pc}}}{f_{\text{rad}} \Delta B / \Delta m} \frac{2N_{\text{eff}} \alpha}{3\pi m_{A'}} \quad (8.15)$$

where  $f_{\text{rad}}$  is the fraction of the background events that are radiative tridents<sup>5</sup> (as calculated using Monte Carlo in Section 7.4),  $\Delta B / \Delta m$  is the number of background events in the mass window centered at the mass hypothesis (by convention, this window is  $[m_{A'} - 1.28\sigma_m, m_{A'} + 1.28\sigma_m]$ ) divided by the size of that window ( $2.56\sigma_m$ ),  $N_{\text{eff}}$  is the effective number of decay products that the  $A'$  can decay into (which is 1 in the mass region of interest, since the  $A'$  in this range is too light to decay into an  $\mu^+\mu^-$  pair) and  $\alpha$  is the fine-structure constant  $\approx \frac{1}{137}$ .

---

<sup>5</sup>Systematic errors on  $f_{\text{rad}}$  are not taken into account in this analysis, but will be taken into account later in the complete analysis of the full dataset.

# CHAPTER 9

## Results of Resonance Search

Figure 9.1 shows the local and global  $p$ -values for finding a dark photon resonance at each mass hypothesis. The smallest local  $p$ -value was 0.020, for a mass hypothesis of 62.25 MeV. The next best candidate was at 135 MeV, with a  $p$ -value of 0.042. Both of these local  $p$ -values have less than  $1\sigma$  global significance, and their fits are shown in 9.2. As a sanity check, Figure 9.3 compares the spectra of test-statistics  $q_0$  and  $p$ -values at all mass hypotheses to their theoretical distributions. Figure 9.4 shows the exclusion region from the data used in this analysis, superimposed over the results from other experiments.

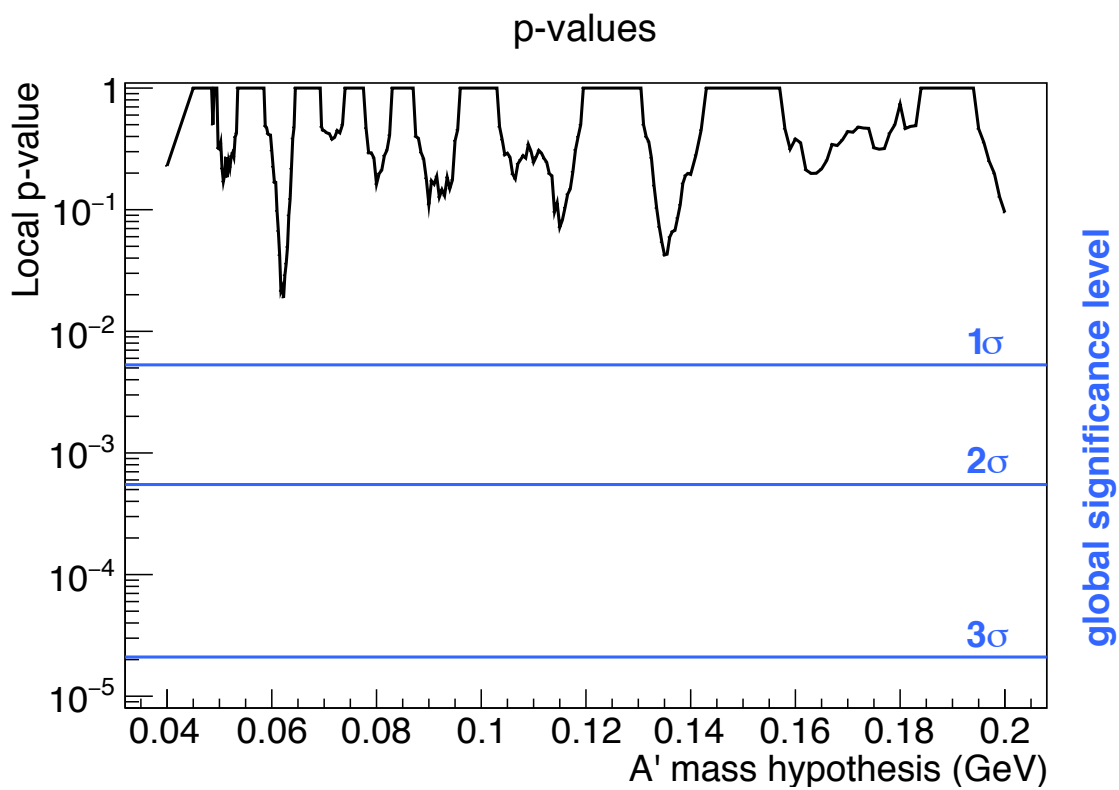


FIG. 9.1: Local  $p$ -values as a function of the mass hypothesis.

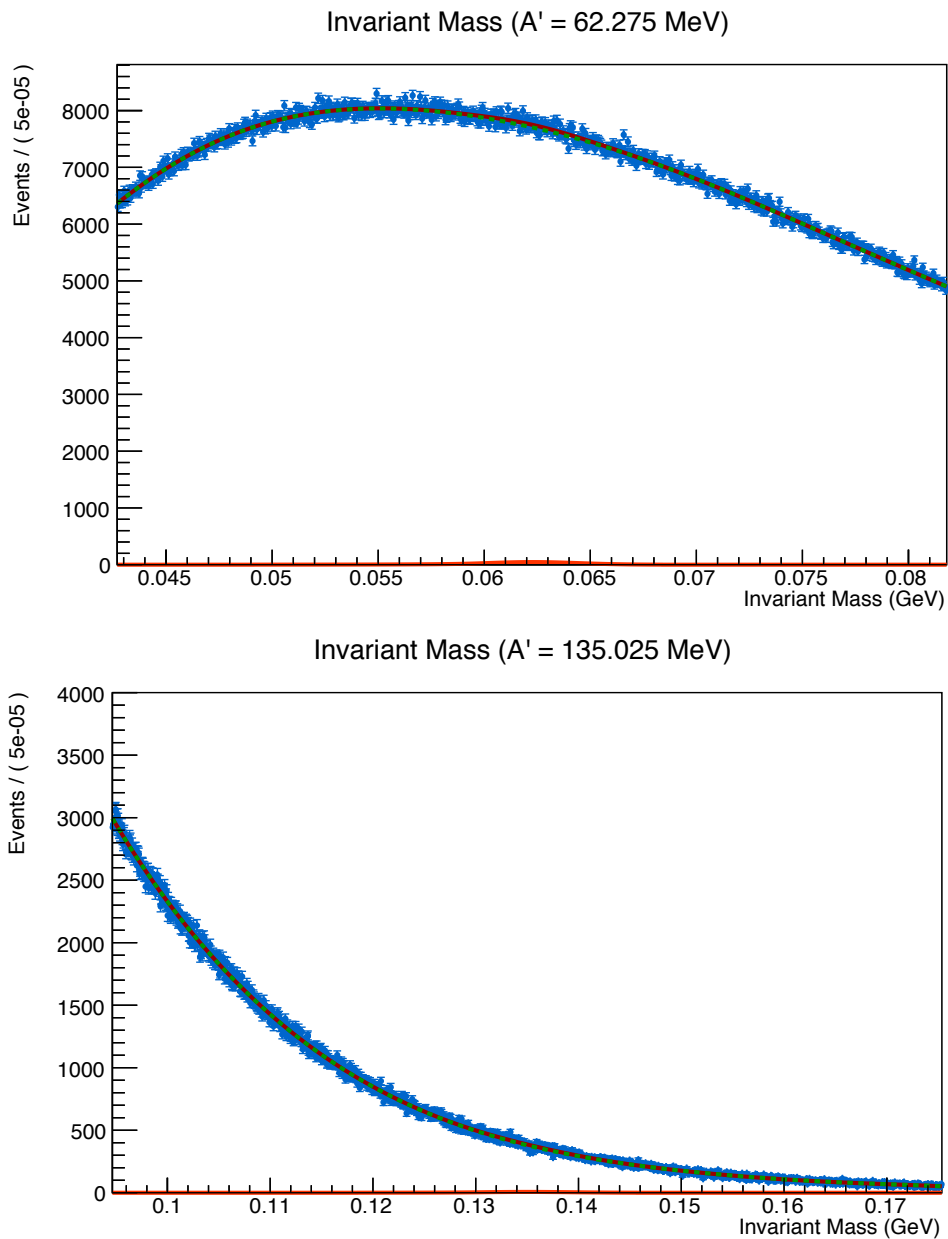


FIG. 9.2: Fits to signal plus background models for mass hypotheses of 62.25 (upper plot) and 135 MeV (lower plot), which have the smallest and second smallest local  $p$ -values respectively.

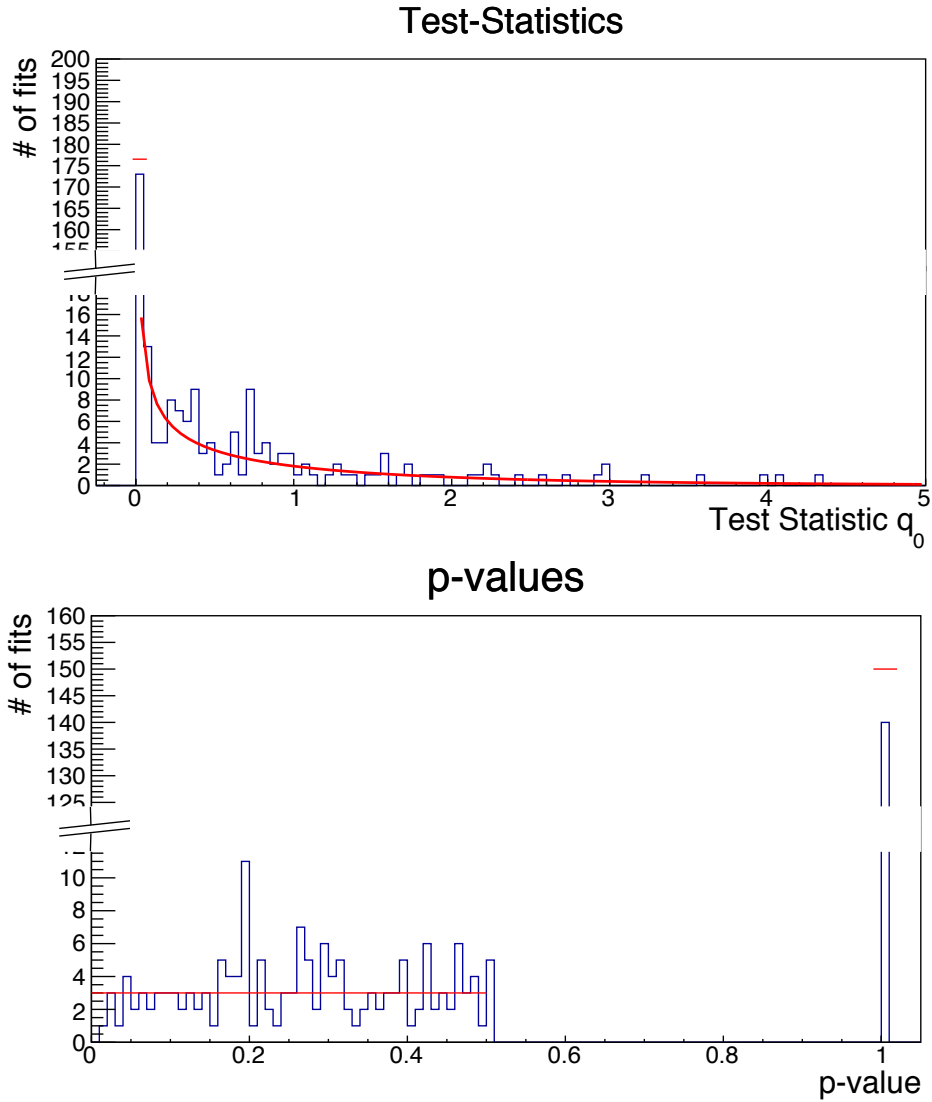


FIG. 9.3: Spectra of test statistics  $q_0$  (top) and p-values (bottom) of the signal+background vs. background-only tests for each mass hypothesis, compared to their theoretical distributions (red). The test statistics  $q_0$  are expected to follow a  $\frac{1}{2}\chi^2$  distribution (Equation 8.8). The expected distribution of the p-values is

$$\frac{1}{2}\delta(p-1) + \begin{cases} 1, & p \in [0, \frac{1}{2}] \\ 0, & \text{else} \end{cases} .$$

The reason for the delta function at  $p = 1$  is that this is a one-sided test, searching for a positive signal only. Comparing the two spectra to their respective functions yields  $\chi^2/\text{dof}$  equal to  $\frac{88.3}{101} = 0.87$  for the  $q_0$  spectrum and  $\frac{63.7}{51} = 1.25$  for the p-value spectrum, both of which are consistent with 1.

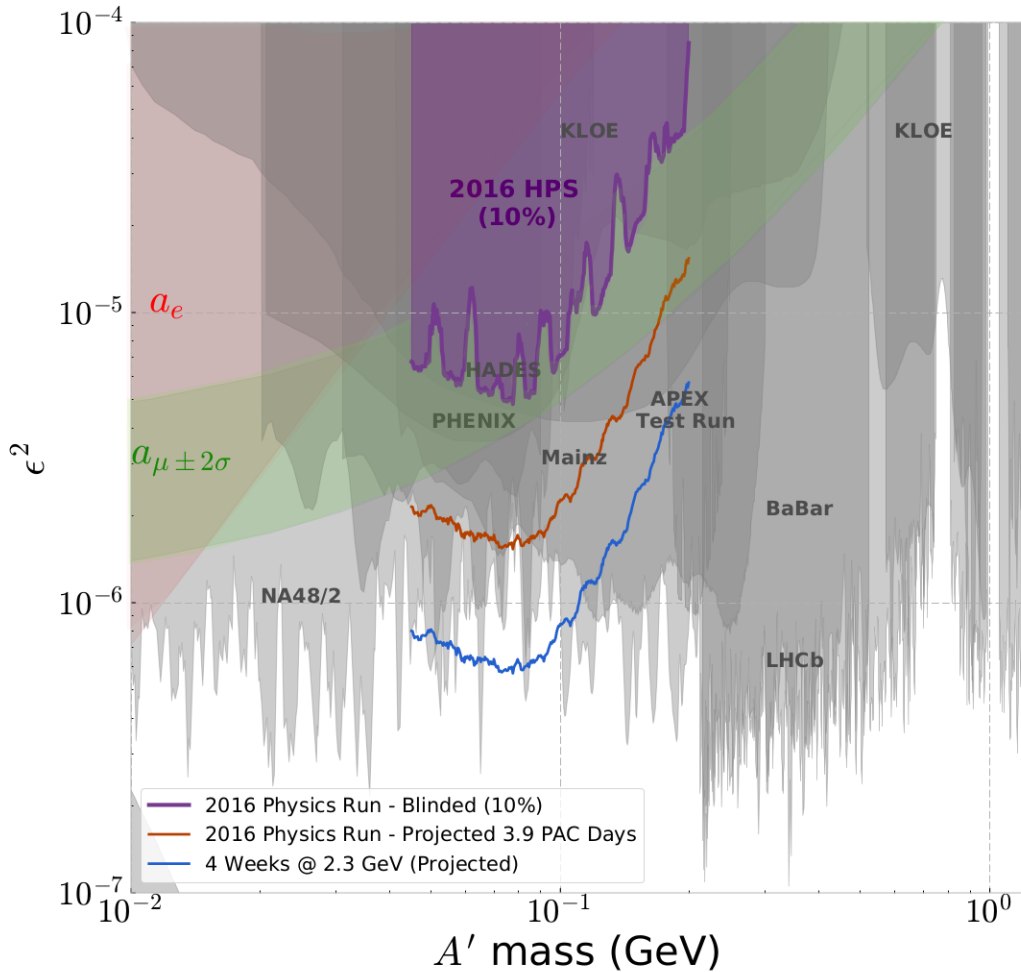


FIG. 9.4: Preliminary exclusion region from bump hunt on 10% of the 2016 HPS dataset (purple), as well as projections of the reach for the full 2016 dataset (brownish red) and for 4 weeks of continuous running. These limits are at the 95% confidence level and are compared to existing constraints (see references in the caption of Figure 1.2). The projections are calculated by scaling the median upper limits on  $\epsilon^2$  from pseudo-datasets by the inverse square root of the ratio of the luminosities in the datasets. They therefore do not take into account corrections to the tracker alignment in the 2016 dataset (see Section 5.1), nor upgrades to the detector for future datasets as discussed in Section 10.1.



# CHAPTER 10

## Conclusion and Outlook

A bump-hunt search for a dark photon was performed in the 40-200 MeV mass range using 10% of the 2016 HPS dataset, and no evidence for a dark photon was found. Moreover, limits at the 95% confidence level ( $\sim 2\sigma$ ) were set on the couplings down to  $\epsilon^2 \sim 5 \times 10^{-6}$  in that mass range. We expect to run a similar analysis using the same techniques presented here on the full 2016 dataset, using a future reconstruction pass with improved alignments in the SVT. The upper limits on  $\epsilon^2$  set by the full dataset analysis are expected to be  $\sim 4$  times smaller than those presented in this analysis, down to  $\epsilon^2 \sim 1.3 \times 10^{-6}$ , mostly due to the factor of 10 increase in statistics, and to a lesser extent due to improvements in mass resolution through improved alignment. The full analysis will also include corrections to the  $\epsilon^2$  upper limits to take into account the systematics due to uncertainties in the radiative fraction, mass resolution and fitting (pulls).

### 10.1 The Future of HPS

HPS is scheduled to take a larger data sample starting in 2019, with two major upgrades. The first upgrade is an additional “positron-only” trigger running concurrent with the other triggers. The reason for this is that many electrons miss the Ecal because 9 crys-

tals were removed per row in the high background region on the electron side. The positron side of the detector, on the other hand, has fewer particles hitting it, greatly reducing the background rate on it. Therefore, if a particle hits the positron side of the detector and there is no corresponding hit on the electron side, it is not unlikely that there was an electron that missed the Ecal by passing through the hole. The second upgrade is adding an additional “Layer 0” to the SVT halfway between the target and the existing Layer 1. This would greatly improve the resolution of the vertex position, decreasing the minimum  $A'$  decay length detectable by HPS.

As a bonus, HPS may be able to create true muonium, that is, bound states between a muon and an anti-muon pair, which has been predicted by QED but has not yet been observed [78, 79]. Several of the true muonium states ( $1^3S_1$ ,  $2^3S_1$ , and  $2^3P_2$ ) are predicted to decay into  $e^+e^-$  pairs with lifetimes on the picoseconds to tens-of-picoseconds scale. After a relativistic boost, this corresponds to the centimeter to tens-of-centimeters scale, which may be detected in a displaced-vertex search such as that of HPS.

# APPENDIX A

## Muon Detector

For the first year and a half of my participation the HPS collaboration, I spent the majority of my efforts on designing a muon detector to augment the existing HPS equipment. Its purpose was to increase the reach of the detector in the region where  $M_{A'} > 2m_\mu = 211.4$  MeV. It would have provided another trigger in addition to the one provided by the Ecal.

However, while I was in the midst of designing this detector, another experiment, BaBar, excluded the region of  $A'$  parameter space that HPS would be able to add to its reach with this detector. Therefore, the muon detector was never constructed. The purpose of including this appendix about the muon detector design into my dissertation is document the design of it, as well as the experience that I had gained from designing it, should HPS wish to add one at a later date.

Our proposal was to build a small muon counter, only about a cubic meter in volume, to search for a possible dark photon in the mass range of 200-500 MeV with couplings as small as  $10^{-6}$  that of electromagnetism. This muon counter would sit behind the other detector components of HPS and would not only provide a much

larger sensitivity to dark photons, with completely different sources of background, but it would also allow discovery potential if dark photons couple differently to electrons and muons. A summary of the physics case for this search can be found in [35].

## A.1 Description of Research Instrumentation and Needs

A muon detector will match the geometrical acceptance of the tracker, and will be about a cubic meter in size. Since the muon tracks are expected to be cleaner than those of electrons (due to significantly less bremsstrahlung), we are able to reduce the number hits in the tracker needed for a muon track, and therefore the geometrical coverage for muons in the tracker is greater than for electrons under the prescribed configurations for both particle types. With electrons, the standard procedure is to require hits from at least 5 layers per track in the tracker. With muons, however, we have found that the improvement in  $A' \rightarrow \mu^+\mu^-$  detection efficiency from requiring only 3 tracker layers outweighs the costs of poorer momentum resolution. With such geometrical coverage, the efficiency of detecting high mass  $A'$ s in the  $\mu^+\mu^-$  decay channel will be higher than for  $e^+e^-$  decays, see Figure A.1.

The di-muon decay channel of the  $A'$  has the advantage of a greatly reduced electromagnetic background. In this case, the only particle background in a muon counter would come from photoproduction of  $\pi^+$  and  $\pi^-$  pairs that are not fully stopped in the Electromagnetic Calorimeter (Ecal) or absorber. The rejection rate of pion pairs relative to those of muon pairs is shown in Figure A.2. Expected low background and high efficiency makes the di-muon final state an attractive complement to the  $A'$

## $A' \rightarrow \ell + \ell^-$ Detection Efficiency

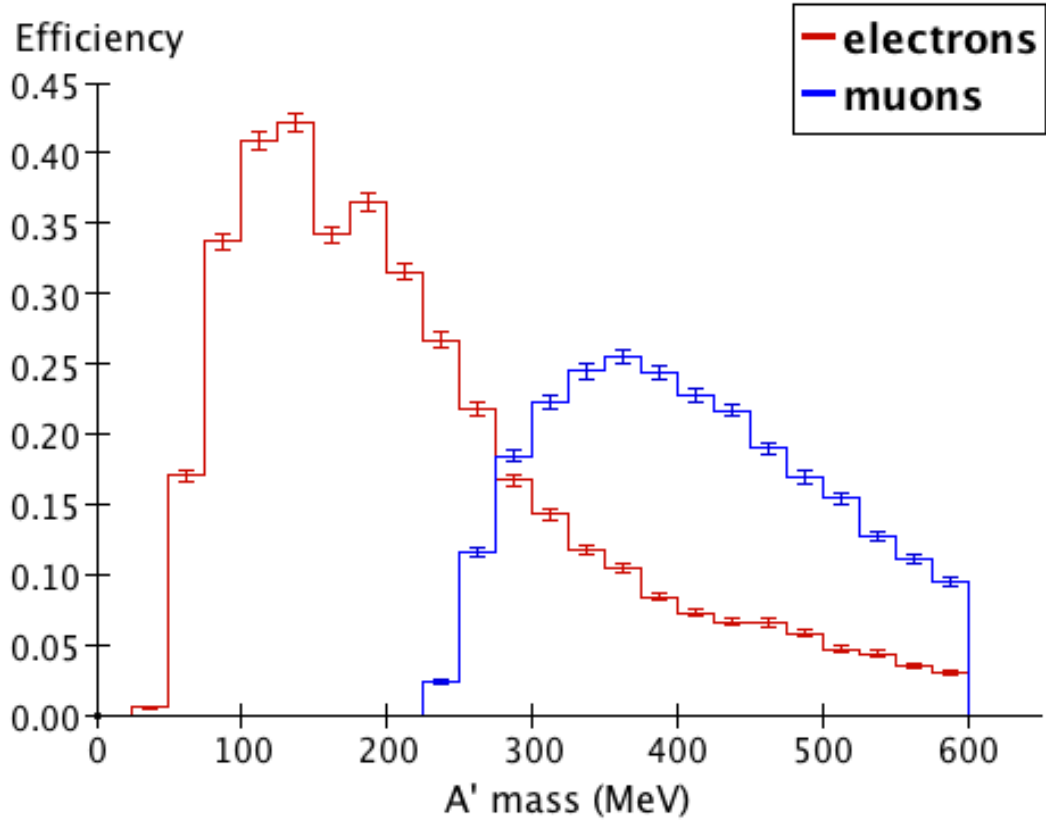


FIG. A.1:  $A'$  detection efficiency through  $\mu^+\mu^-$  (blue) and  $e^+e^-$  (red) decay channels as a function of mass for 4.4 GeV beam energy. We simulated events where an  $A'$  decays into either a  $\mu^+\mu^-$  pair or an  $e^+e^-$  pair at the target, and ran them through the triggering program to determine what fraction of the pairs of particles would be accepted. For the electrons tracks, we required at least 5 hits in the tracker for each particle. For the muons, however, we required hits on only 3 layers of the tracker for each particle, and also that the muon-detector's trigger condition, explained in more detail in Section A.2, is satisfied. For each value of the  $A'$  mass we generated 10k muon events and 10k electron events, and the  $A'$  masses used for each data-set were evenly spaced 25 MeV apart from one another.

search using the  $e^+e^-$  final state, and will add substantial territory in the mass and coupling parameter space as show in Figure A.3.

The muon system can be constructed with layers of scintillator hodoscopes sandwiched between iron absorbers, and can be added downstream from the rest of the HPS detector components. The total thickness of the absorbers is limited by the space available to us: about 53 cm, between the flange just downstream of the Ecal which connects the vacuum boxes and the downstream Frascati magnet. See Figure A.4.

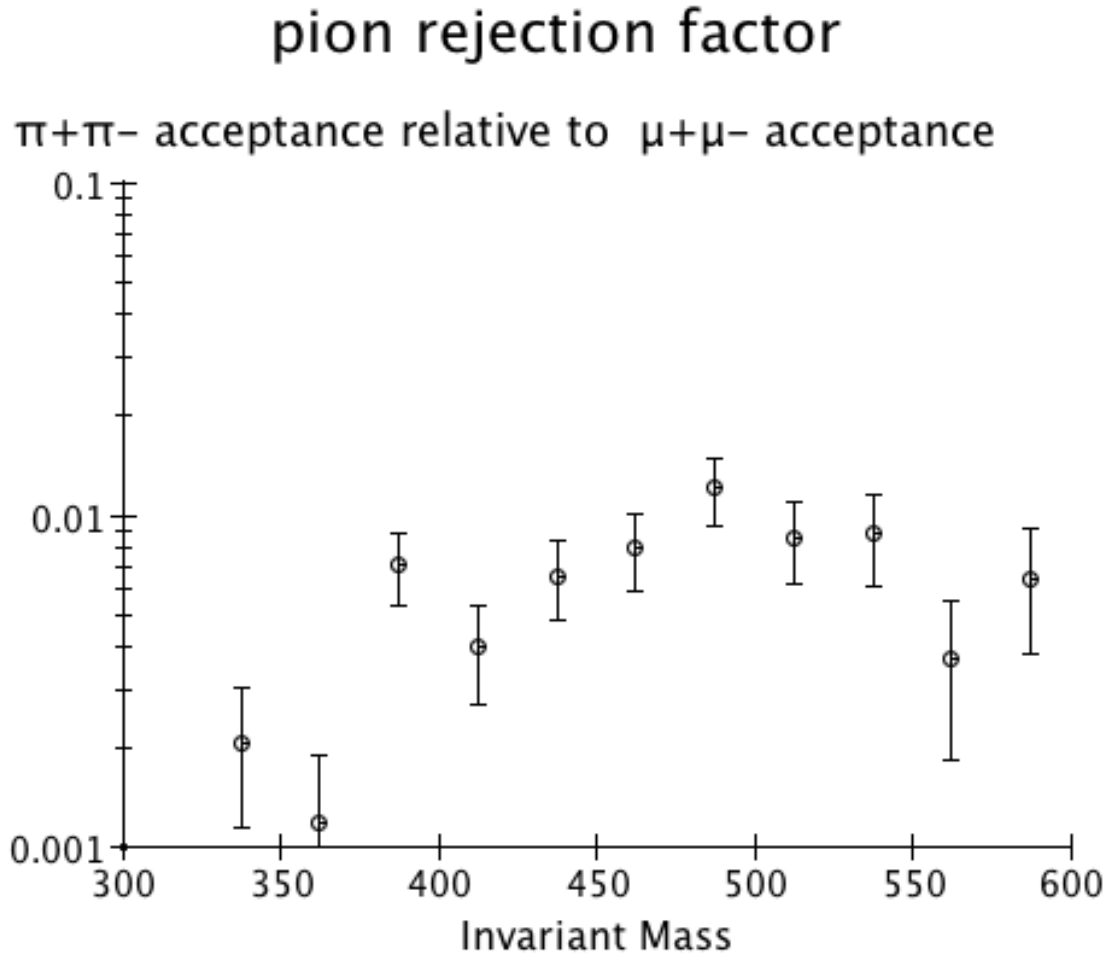


FIG. A.2: Pion rejection in the muon detector. Analogous to Figure A.1, we generated  $A' \rightarrow \pi^+\pi^-$  events in addition to the existing  $A' \rightarrow \mu^+\mu^-$  events. Our acceptance condition for the pions was identical to the one used when generating Figure A.1. We then calculated the ratio of accepted events to total events for both types of events. The quantity shown on the  $y$  axis is the ratio of the detection efficiency of pion pairs to that of muon pairs when the same number (10k) of events were generated for each type of reaction.

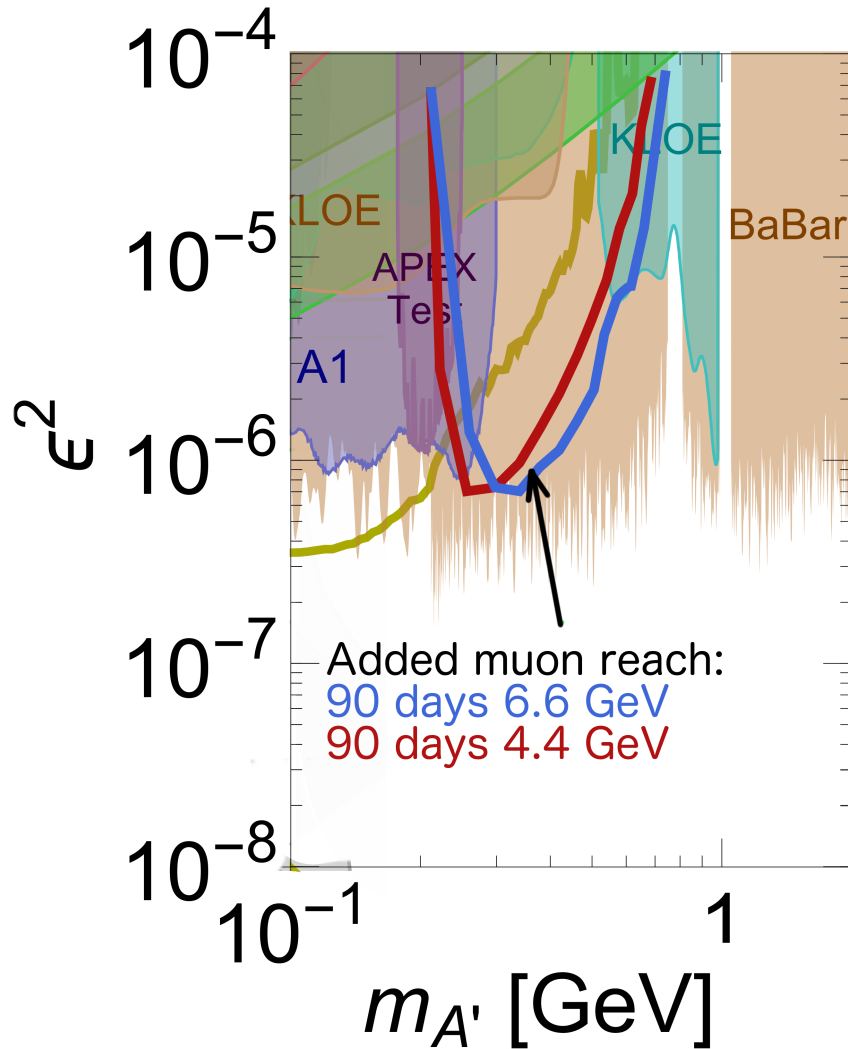


FIG. A.3: Additional reach from the muon detector. The filled regions represent excluded regions from other experiments. The gold curve represents an early estimate of HPS’s reach without the muon detector (This early estimate overestimated the reach by not taking into account the effects of converted WABs in the background for the  $A' \rightarrow e^+e^-$  search, which we were unaware of at the time. However, WABs would not contribute to the background of a muon analysis, since both the  $\mu^+$  and  $\mu^-$  would go to the same half of the detector). The red curve represents the reach added with a 90 day run with 4.4 GeV beam, and the blue curve represents the reach added through a 90 day run with 6.6 GeV beam. The new reach added by the HPS muon detector will exist near the roots of the stalactites of BaBar’s exclusion region.



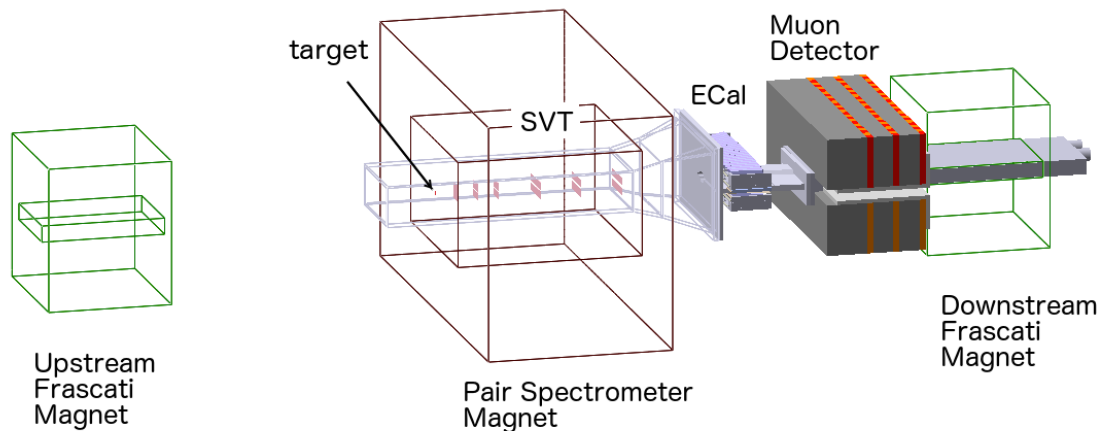


FIG. A.4: Position of the proposed muon detector in relation to other components of HPS. The muon detector will sit just downstream of the vacuum flange downstream from the Ecal, and just before the downstream Frascati magnet. The magnets and the vacuum box surrounding the Silicon Vertex Tracker (SVT) are shown as outlines.

### A.1.1 Conceptual Design

On the basis of these constraints as well as simulations of background rates, we have designed a muon detector composed of three iron absorbers (total length of  $20 + 10 + 10 = 40$  cm) with a single-layer scintillator hodoscope positioned after each absorber. The muon detector will be mounted behind the Ecal, in front of the downstream Frascati magnet. The front face of the first absorber will be at 180 cm from the target, just after the flanges that connect the vacuum boxes. Similar to the Ecal, the muon detector will consist of two halves, one above and one below the beam plane. This segmentation is necessary in order to minimize the effects of the “sheet of flame,” that multitude of low-energy particles in the horizontal plane, swept into the detector acceptance by the dipole analyzing magnet. Additional features in the design for reducing background related to the sheet of flame are discussed in Section A.1.3. These include two tungsten shields and a modification to the vacuum box called a “sheet-of-flame window”. Figure A.5 shows the placement of the various parts of the detector.

The dimensions of the hodoscopes and absorbers are defined using simulations of  $A' \rightarrow \mu^+\mu^-$  for the accessible kinematics. For these hodoscopes, we plan to use the same extruded scintillator strips with embedded wavelength-shifting fiber and photomultiplier tube (PMT) readout as was developed for the CLAS-12 Preshower Calorimeter. These scintillator strips are  $45 \text{ mm} \times 10 \text{ mm}$  in cross section, and can be cut to any lengths. Widths can be reduced as needed for the muon counter. Each strip contains two long tunnels, created in the original extrusion process, into which wave-length shifting fibers can be inserted.

The system will be instrumented with less than 256 readout channels, in which case the requisite electronics will fit into a single VME/VXS crate. Signal from each

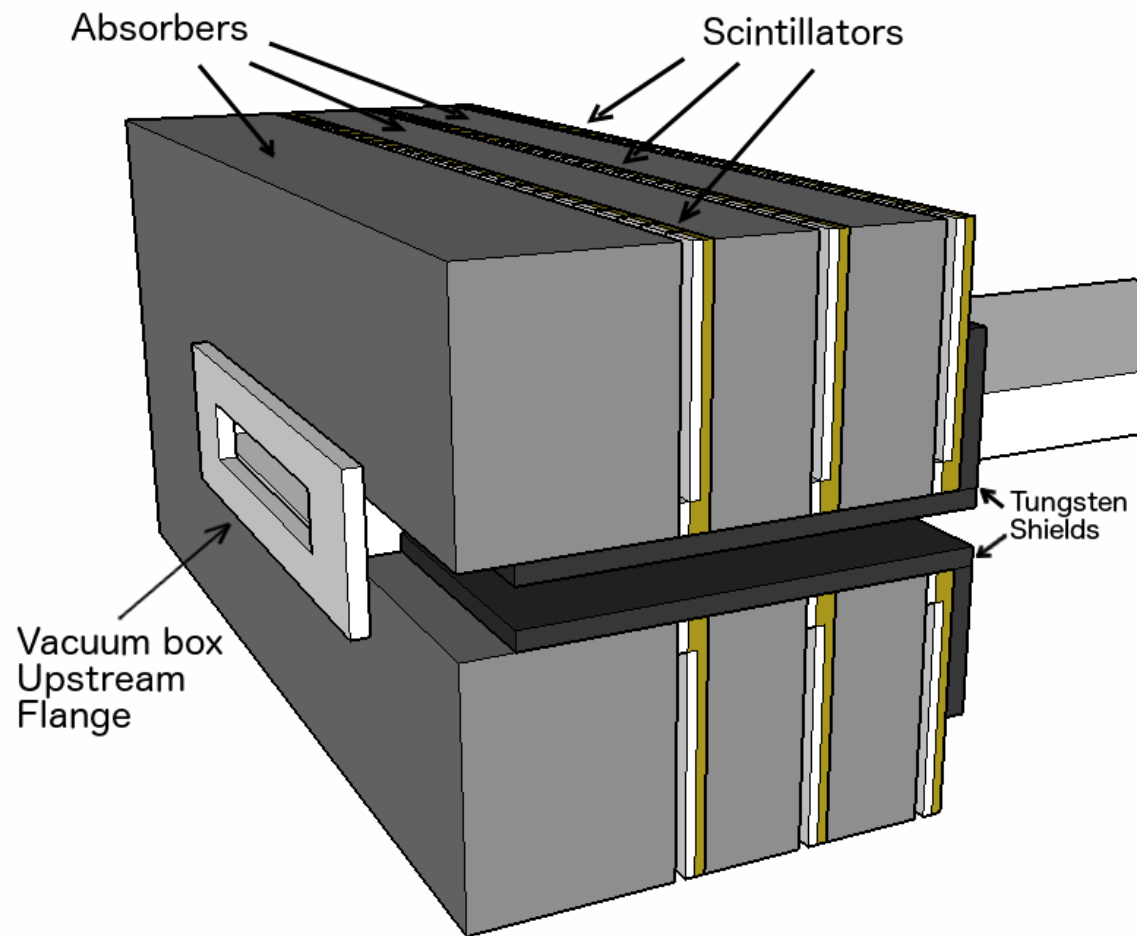


FIG. A.5: Schematic diagram detailing the various components of the muon detector.

PMT channel will be sent to an FADC. We intend to borrow the CLAS-12 Preshower Calorimeter electronics and HV system. Similar to the Ecal, FADCs will be used to construct a muon trigger for the experiment.

### A.1.2 Absorbers and Scintillators

The first absorber will start 180 cm downstream from the target and will be 20 cm thick; the second and third absorbers will be 10 cm thick and begin at 203 and 226 cm from the target, respectively. The space between the absorbers is 3 cm, which is just enough to fit the scintillators and their backboards (that is, the support structures that the scintillators will be glued to). The shapes of these will be a blocky horseshoe shape as shown in Figure A.6. The scintillators will form vertical stripes, 4.5 cm wide in  $x$ . The  $x$  index of the scintillators, starts with  $i_x = 1$  on the far right, and increments up to  $i_x = 26$  on the far left. There are three different designs used for the scintillator stripes/backboards which are used in regions of different levels of background. In the low background region (where the scintillator position index  $i_x$  is in the 17-26 range) the stripe consists of a single scintillator 25 cm long. In the medium background regions ( $i_x = 1-10, 14-16$ ) there are 2 scintillators in each vertical stripe; with the shorter scintillator (3 cm) closer to the vacuum box, and the longer one (22 cm in length) further outward. For the very high background region above/below the electron beam ( $i_x = 11-13$ ), there is a small deadzone (2 cm) where there is no scintillator material, then a 2 cm short scintillator, and then a 19 cm long scintillator. The short scintillators are offset on a ledge built into the backboard, so that there is space for the wavelength-shifting fibers for reading out from the inner scintillators. (see Figures A.8 and A.7).

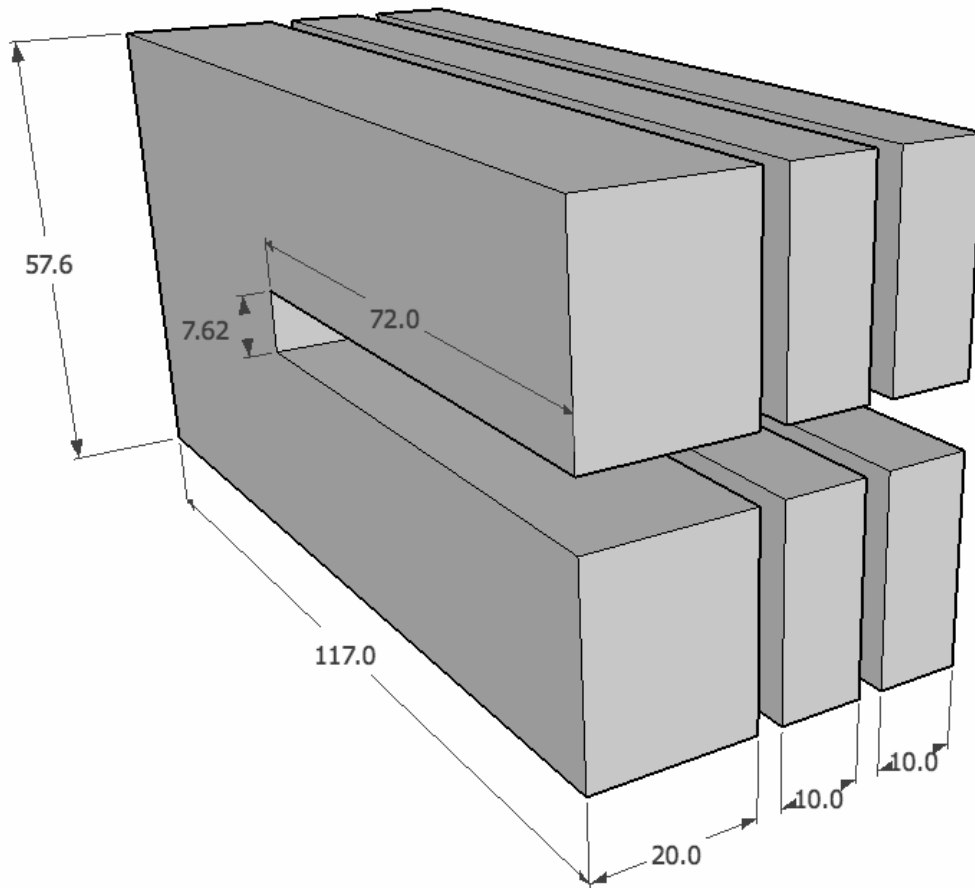


FIG. A.6: Schematic for the iron absorbers. All dimensions that are shown are in cm.

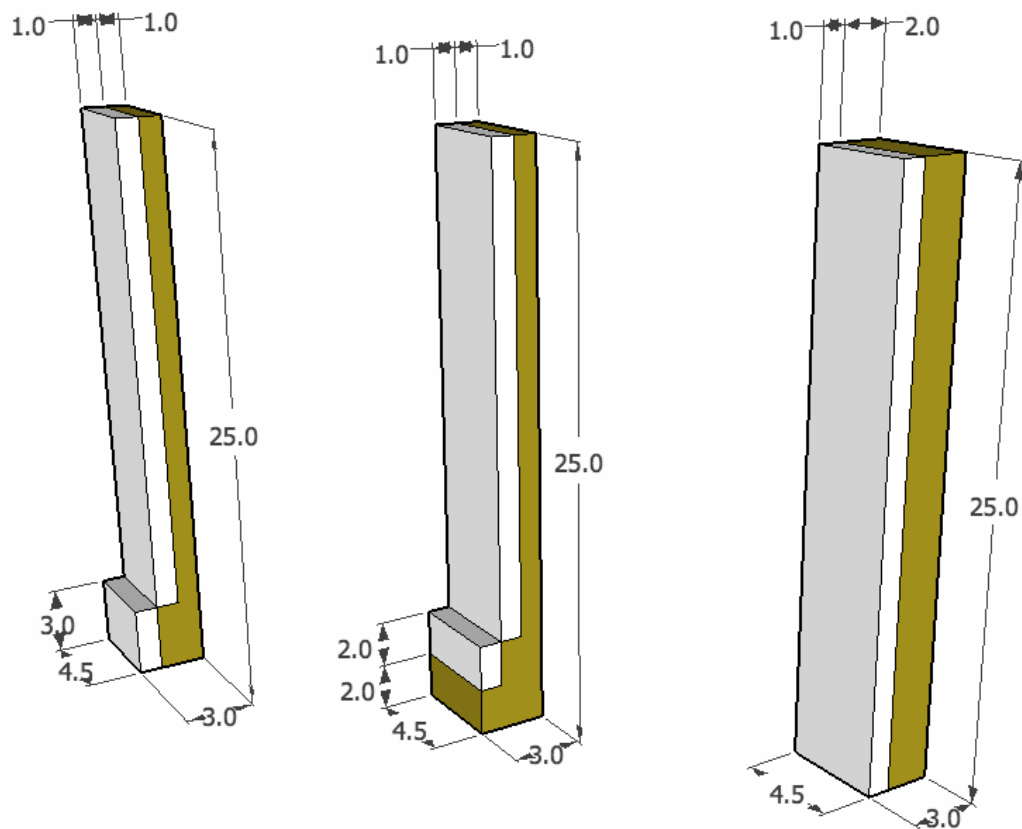


FIG. A.7: Schematics of scintillators (white) with their backboards (yellow). On the left is the design for scintillators in the regions with medium amount of background. The middle is the design for the scintillators in high background regions, and the one on the right is for low background regions. All dimensions are in cm.

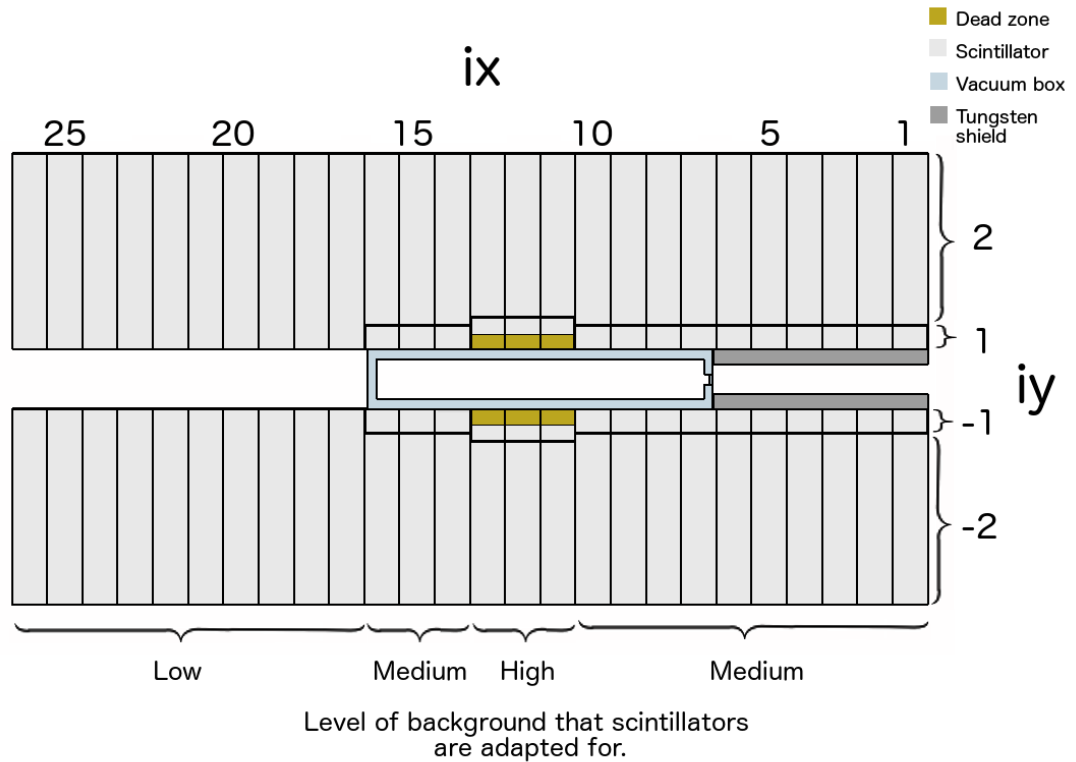


FIG. A.8: Layout of scintillators. The horizontal index increases from right to left. The vertical index increases from bottom to top. In addition to the scintillators, a cross-section of the vacuum box, the sheet-of-flame window, and the horizontal tungsten shields are shown. The yellow regions are where the scintillators are trimmed to reduce background, and the backboards are visible. The height of each half of the scintillator layer is 25 cm, and the width is 117 cm. On the top, the horizontal indices (increasing from one from right to left) of some of the scintillators are shown, and on the right, the vertical indices are shown.

### A.1.3 Background Reducing Features

There are several features in this design that exist in order to reduce background rates in the more exposed parts of the detector caused by the beam. The justification for the dimensions of these features are discussed in Section A.6. When the electrons in the beam pass through the target, they lose energy, some much more so than others. As they pass through the pair spectrometer field (which is vertically aligned), the ones that lost more energy than normal have their trajectories fanned out bent to the right. This phenomenon is called the “sheet of flame”, and it is a major cause of beam background in the detector. Some of these sheet-of-flame electrons hit the right side of the vacuum box, scatter, and cause the nearby scintillators to have high background rates. To mitigate this effect, I have included two design features, which together bring the background rates to a reasonable level.

The first feature is called the “sheet-of-flame window”, which consists of a slit in the side of the vacuum box, 44 cm in length, by 1.25 cm in width, sealed over with a 5 mm thick aluminum plate. This begins 15 cm upstream of the front face of the first scintillator ( $z = 185$  cm), and ends at the back face of the last scintillator ( $z = 229$  cm). Schematic diagrams of this cut are shown in Figure A.9.

The second of these features is a pair of horizontal tungsten shields, each of which consists of two plates that are attached at right angles to one another. The first plates in each shield are horizontal and are placed above and below the sheet of flame, extending from the right wall of the vacuum box, as far as the scintillators reach. These plates block the scattered sheet-of-flame electrons from going up or down into the scintillators. These start at  $z = 185$  cm (measured from the target) and end at  $z = 231$  cm, (2cm downstream of the last scintillator). These plates connect to a



set of vertical backslash plates<sup>1</sup> just downstream of the last scintillator layer. This second pair of plates protects the last scintillator layer from beam background that is scattered backwards from places downstream of the last scintillator. The dimensions of these plates are shown in Figure A.10.

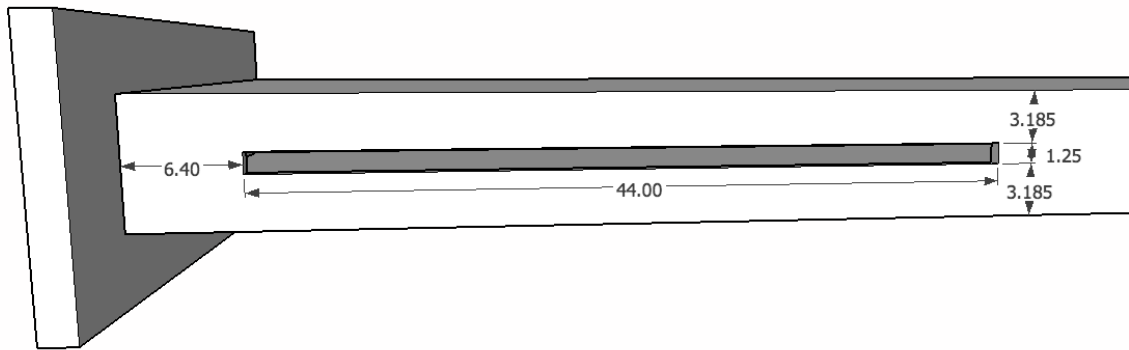


FIG. A.9: Dimensions and position of the sheet-of-flame window cut. All dimensions are in cm.

### A.1.4 Readout and Electronics

Each of the scintillators will have two wavelength-shifting fibers coming out of them, and each pair of fibers will be fed into a PMT channel. The output of these PMTs will in turn be fed into an FADC channel to be digitized.

As there are 252 total scintillators (42 per half-layer), we will require a single crate (16 FADC boards which in turn each process 16 channels) for the digitization, with 4 extra channels left over. The electronics in this crate will furthermore be tasked with checking for triggers, and sending digitized data to other hardware.

---

<sup>1</sup>These are also made of tungsten.

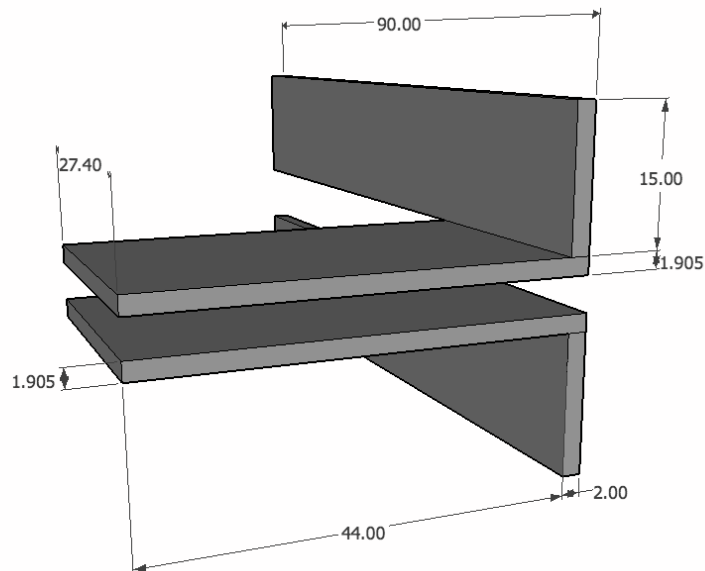


FIG. A.10: Dimensions of tungsten shields. All dimensions are in cm.

## A.2 Trigger Conditions

The trigger will fire when there are two tracks which may be matched to one another in the muon detector. There are conditions on what constitutes a track, and which tracks may be matched to which other tracks.

A “hit” is recorded on a channel when the sum of 4 consecutive samples (taken once every 4 ns by the FADCs) exceeds a certain threshold. The threshold corresponds to 4.5 MeV deposited in the scintillator. The FADC readout value depends not only on the energy deposited in the scintillator, but also on the details of the photomultiplier tubes, which have yet to be determined.

To form a track, there must be at least two hits that satisfy four criteria. First, they must be on different layers in  $z$ . We require 2 hits on different layers because a passing muon will cause hits on all of the layers that it passes through, whereas beam-background hits are uncorrelated with one another. Secondly the hits must be

in the same row in  $y$ . This is because as the muons pass through the detector, their positions in  $y$  are unlikely to change very much from one layer to another. Third, they must have the same index in  $x$ , plus or minus one. The allowance for plus or minus one is because we found in our simulation that a muon track may change its position in  $x$  from one cell in one layer, to the adjacent cell in  $x$  in the next layer because the tracks may have a nonzero slope in the  $x$  direction. The fourth criteria is that the hits must take place within 16 ns of one another.

For the trigger to occur, the two tracks must satisfy two criteria. First, one of the tracks must be on the top half of the detector, and the other must be on the bottom half of the detector. Secondly, the  $x$  indices of the two tracks (defined as the  $x$  index of the first hit in the track if they are different) must be within the range of values that we deem to be acceptable. From looking at our simulated  $A' \rightarrow \mu^+\mu^-$  events, we determined which pairs of values of  $x$  are acceptable. The accepted ranges are given in Table A.1. Thirdly, all of the hits causing the trigger must take place within the same 16 ns window.

$x$ index of track 1	$x$ index of track 2
1-13	16-26
14	12-22
15	8-16
16	1-16
17-22	1-14
23-26	1-13

TABLE A.1: Ranges of acceptable pairs of  $x$  indices for paired tracks. To determine if a pair of tracks on opposite vertical halves of the detector can cause a trigger: First, look through the left column to find the range containing the  $x$  index of the first track. Then look at the range in the next index. If the second track's  $x$  index is in the range on the right, then the trigger is generated

### A.3 Methods of Simulation

For the calculations of trigger and individual channel hit rates, we generated data using GEMC, a Monte-Carlo program built on Geant-4. The goal was to simulate a 450 nA electron beam at 4.4 GeV hitting a  $8.75 \mu\text{m}$  tungsten target. These simulations enabled me to optimize methods of reducing background to reasonable rates (i.e., less than 2 kHz of total triggers, and less than 1 MHz of hits on any given channel under the run conditions specified).

To calculate beam-background hit rates, we generate 5617 electrons per event, (corresponding to the 2 ns bunches of electrons in the beam), for about 50k events per simulated run. Each simulated electron begins with 4.4 GeV just upstream of the tungsten target, and scatters as it passes through the target, scattering. These scattered electrons are then traced through the muon detector, as they deposit energy in the materials of the detector. After simulating hits in the scintillators, we ran a program that sums up the energies of all hits in each channel within a 16 ns window. If the sum is above a threshold, we then count that as a hit contributing to the total background rate for its channel. The threshold corresponds to the energy that a minimum ionizing muon deposits (based on muon simulations), which is 1.5 MeV per cm thickness of the scintillators. After reading through the whole simulated run, the program then divides the number of recorded hits in each channel by the total amount of time simulated.

To determine bump-hunt reach, we generated events representing QED reactions that will be background in the detector, both radiative and Bethe-Heitler, with a 4.4 GeV beam, and also for a 6.6 GeV beam. We reconstructed these events to determine the mass resolution and multiplied that by 2.5 to get the mass bin width. Then, we determined the number of background events per bin by counting the number of

events that would fulfill trigger conditions among the simulated events of each type, multiplying by their cross sections and by other factors related to the run conditions. To determine the number of signal events that would exist in such a run, I used the fact that the number of  $A' \rightarrow \mu^+\mu^-$  events is proportional to the number of radiative events within a given bin using Equation A.1 from [11].

$$\frac{\sigma_{A' \rightarrow \mu^+\mu^-}}{\sigma_{radiative}} = \frac{3\pi\epsilon^2}{2N_{\text{eff}}\alpha} \frac{m_{A'}}{\delta m}, \quad (\text{A.1})$$

where  $N_{\text{eff}}$  is the effective number of decay products, and  $\delta m$  is the width of the bin. We will assume that 80% of the  $A'$  events that are reconstructed are in the correct bin (which is reasonable, since such is the case if we assume that the measurement error is approximately Gaussian), and that all other background is much smaller than the muon QED tridents. The bottom curve of the reach plot is then determined by solving for  $\epsilon^2$  for each bin where

$$N_{\text{signal}}/\sqrt{N_{\text{background}}} = 2 \quad (\text{A.2})$$

If the total run time exceeds about 6 years, then we will be able to get reach from a displaced vertex search in addition to the bump-hunting, although this scenario is not likely.

## A.4 Background Sources

There are several types of background that will be present in the detector. One of these is beam background. Another type of background comes from QED reactions at the target which produce  $\mu^+\mu^-$  pairs. And finally, a third type is from pions. The

rates we want to consider are how frequently each individual channel records a hit, and how frequently the trigger is activated. We have simulated data that corresponds to a 4.4 GeV 450 nA beam on a 8.75  $\mu\text{m}$  tungsten target. Based on these simulations, we expect no more than 1 kHz of total triggers, and no more than 1 MHz of hits on any given channel.

### A.4.1 QED Reactions Producing Muons

There are two types of QED reactions that produce  $\mu^+\mu^-$  pairs. The first are Bethe-Heitler events, and the other type are radiative events. The Bethe-Heitler events are the more common of the two, however, most of them can be filtered out from the  $A'$  decay by putting a cut on the total momentum of the two muons in the pair. The radiative events are kinematically identical to the  $A'$  decay events, and there is a simple formula relating the rates of the radiative events to the  $A'$  production rate which is given in [11]. Since these events take place inside the target, they can be filtered out post trigger from  $A' \rightarrow \mu^+\mu^-$  events via a cut on the vertex position in  $z$ .

Our Monte-Carlo simulations predict that the trigger rates from the QED reactions are  $28.8 \pm 0.8$  Hz for Bethe-Heitler reactions, and  $1.54 \pm 0.02$  Hz for the radiative reactions.

### A.4.2 Pions

In addition to the QED reactions that produce  $\mu^+\mu^-$  pairs, there are also similar reactions that produce  $\pi^+\pi^-$  events, with  $\sim 1/20$  of the cross-section for muon events. Most of the pions will be absorbed by the absorbers, however, a large enough fraction of them will not be absorbed and then show up as background in the SVT and the

muon detector. The iron absorbers alone only brings down the pion acceptance by only one order of magnitude.

Therefore, in addition to the absorption, we will also take advantage of the fact that pions produce electronic showers in the absorbers, and therefore the total energy that they deposit in the detector will in general be greater than that of muons. Therefore we intend to use a cut on the sum of the readouts of all muon detector channels. This brings the pion-acceptance rate down by another order of magnitude.

In Figure A.2 we plot the ratio of accepted 2-pion events to accepted 2-muon events as a function of the invariant mass of the pair, using the trigger condition explained in Section A.2. We see that the paired-pion events are suppressed by a total of between 2 and 3 orders of magnitude compared to muon events.

A small percent of the pions will decay via  $\pi^+ \rightarrow \mu^+ \nu_\mu$  (or  $\pi^- \rightarrow \mu^- \bar{\nu}_\mu$ ) before they reach the detector. For a typical pion momentum of 2 GeV, it will travel an average of  $\ell_{\text{avg}} = c\tau_{\pi^\pm}\gamma\beta = 112$  m, which indicates that the fraction of pions that decay before the detector is  $f_{\text{decay}} = 1 - \exp\left(\frac{-180 \text{ cm}}{112 \text{ m}}\right) = 1.5\%$ .

Finally, it is possible that there will be some background from accidental coincidences of two single-pion events that take place close in time to one another. Single pion events have a high cross-section ( $\sim 3$  millibarns), however, the acceptance of these types of events is very small ( $\sim 1\%$ ) due to the large scattering angles. Taking into consideration the probability of 2 such events taking place within a 16 ns time window (and the paired-track constraints) we can estimate the rate of such background triggers from paired-pion triggers to be around 0.3 Hz, and can be further reduced in the offline analysis by cuts on the kinematic variables of the pair.

### A.4.3 Beam Background

Almost all of the hits will come from beam background, however, since the hits are uncorrelated, their rates are relatively low (between 300 and 400 Hz according to simulations) and therefore they account for only about a fourth of all triggers. Furthermore, these events can be rejected post-trigger by checking if a similar track exists in the SVT; if not, then the event will be rejected. Features of the design for decreasing beam background are discussed in Section A.1.3 and the methods used to optimize their effectiveness are discussed in A.6. The simulated background hit rates are shown in Figure A.11.

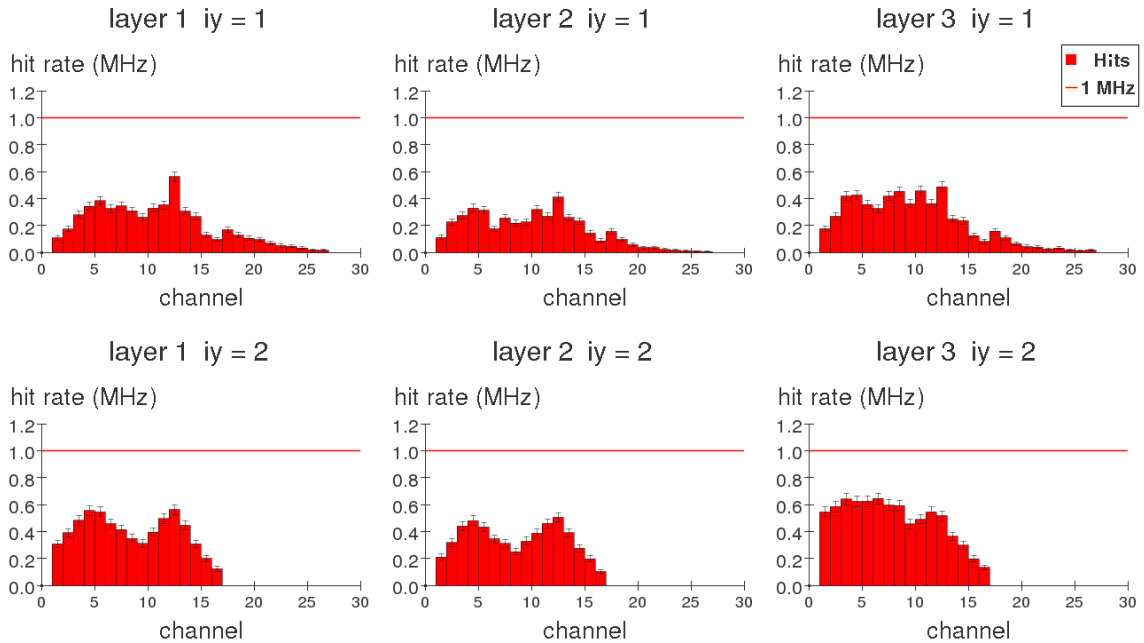


FIG. A.11: Beam background hit rates on each channel for a 4.4 GeV 450 nA beam on a  $4.375 \mu\text{m}$  thick tungsten target. The red line corresponds to 1 MHz.

One would naively think that the ideal way to simulate the beam-background trigger rate would be to simulate several tens of milliseconds of data, count the number



of triggers, and divide by the amount of time that the simulation covers. However, this takes a large amount of computing power and is impractical, especially when one must generate several versions of the detector geometry in the optimization process.

Instead, what we do in practice only requires us to generate only about  $100 \mu\text{s}$  of simulated events. We then determine the probability of a hit on each channel within the required time window by multiplying that channel's hit rate by the window's size. For every possible combination of channels that could generate a trigger, we calculate the probability of a trigger by multiplying the probabilities of the individual hits within the trigger window together. I then sum these up the rates for each possible generate combination together to get the total trigger rate.

## A.5 Additional Filters on Events

In order to reduce the amount of background from Bethe-Heitler muon events, we will reject all events where the sum of the momenta of the two tracks is less than a certain threshold. For the purpose of this proposal, we used the values 3.5 GeV for a 4.4 GeV beam, and 6.0 GeV for 6.6 GeV beam. These have been optimized to maximize the dark photon mass-vs-coupling reach.

## A.6 Optimization of Dimensions

In this section, we shall discuss the procedure used to optimize the parameters of the detector design, including angular coverage and the background-reducing features.

### A.6.1 Angular Coverage

In order to determine how tall and wide to make the muon detector, we simulated  $A' \rightarrow \mu^+\mu^-$  events and plotted the positions where the particles hit a vertical plane at  $z=200$  cm, and filtered out all events except ones in which both of particles in the pair hit at least 3 of the 6 layers of the SVT. Given the constraint that we can only look for particles above and below the vacuum box, we need to put a gap in between the top and bottom parts of the muon detector. The results are shown in Figure A.12. Based on this, each half of the muon detector will be 25 cm tall, and 117 cm wide, offset in  $x$  by +9 cm.

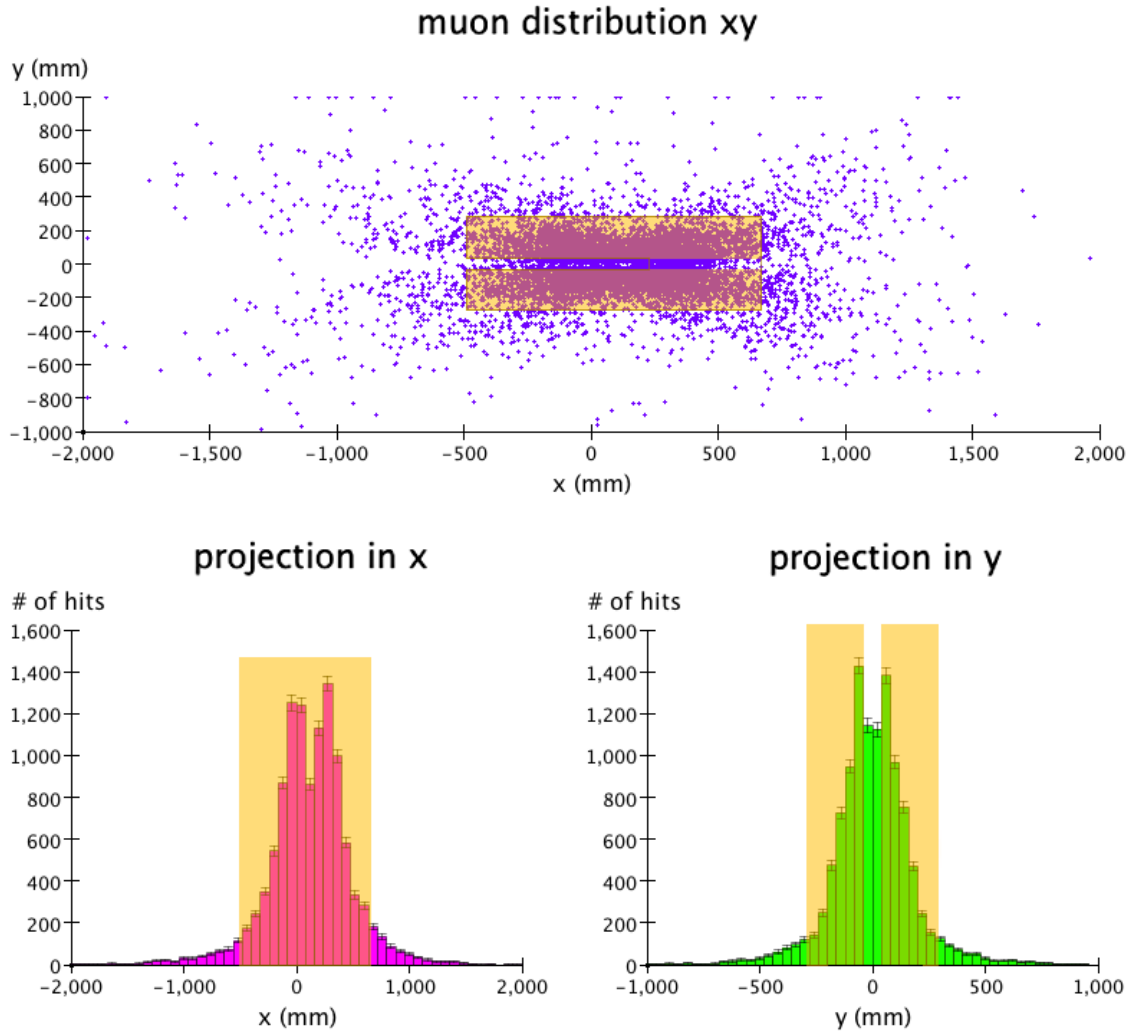


FIG. A.12: Angular coverage of the muon detector. The dots in the top graph are positions where simulated trackable particles pass through the  $z = 200$  cm plane (where the first scintillator layer of the muon detector will go). Overlaid is an outline of the sensitive region that we decided on based on the simulation. By trackable, we mean particles that passes through at least 3 of the SVT layers. The pairs are produced by simulating the decay of an  $A'$  with varying masses between 211.4 MeV, the mass of 2 muons, and 600 MeV, from a 4.4 GeV beam. The other two graphs are projections of these positions on the  $x$  and  $y$  directions.

## A.6.2 Sheet-of-Flame Window

In order to minimize the cost and difficulty of installation of the sheet-of-flame window (see Figure A.9), its total area should be as small as possible without significantly increasing the amount of background, and the plate of aluminum that seals over the window must be thick enough to be structurally stable. This gives us 4 variables to optimize: the starting and ending positions in  $z$ , the height, and the thickness of the aluminum sealing plate.

In Figure A.13 we see that the background rates using a 5 mm thick aluminum plate versus a 100  $\mu\text{m}$  aluminum plate are nearly identical, despite being 50 times thicker. Since the background rates are nearly independent of the thickness of the plate, we can use a 5 mm thick plate. We find that as we decrease the window's height below 1.27 cm, background rates increase, as demonstrated in Figure A.14. Therefore, we will keep its height at 1.27 cm. We also find that as we move the upstream end of the the sheet-of-flame window further downstream (closer to the first scintillator), background rates increase, most noticeably in the first layer, therefore we plan to keep the starting position of the window at 185 cm (15 cm before the first scintillator layer's front face). This is demonstrated in Figure A.15. We found that the background rates are not improved by extending the downstream end of the window beyond the last scintillator layer (see Figure A.16).

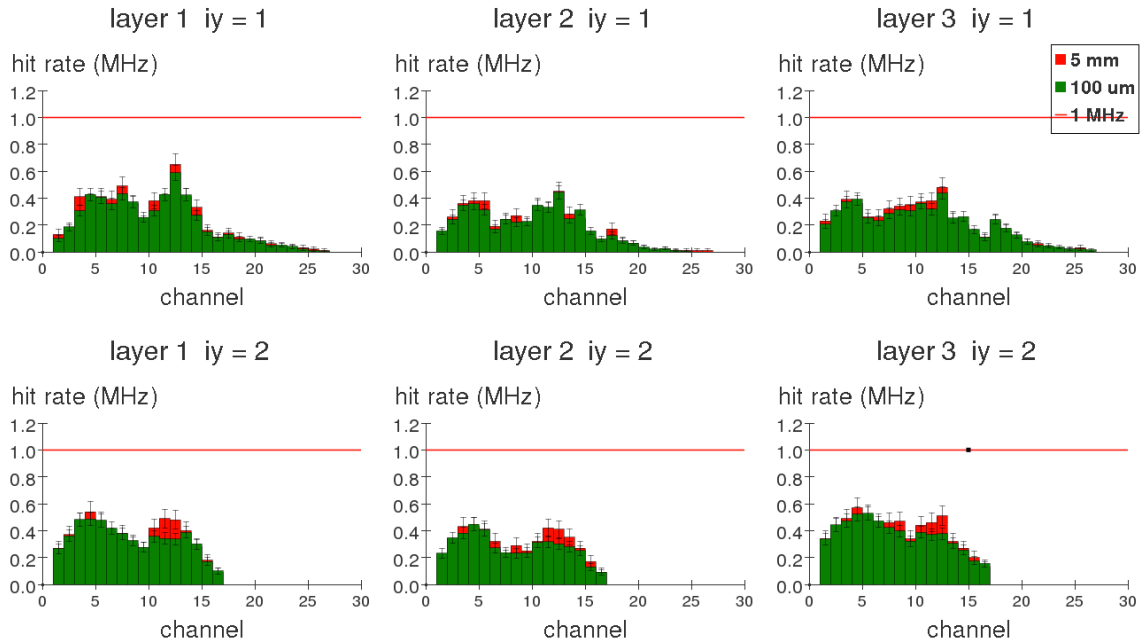


FIG. A.13: Background rates on each channel for various thicknesses of the aluminum plate covering the sheet-of-flame window. In this figure, and in all other subsequent figures in this section, we created several versions of the detector geometry with only one variable modified (in this case the width of the sheet-of-flame window covering plate), and calculated background rates on all channels for each of them. The background rates for each of the versions of the geometry are shown in these figures superimposed on top of one another with different colors for a comparison.

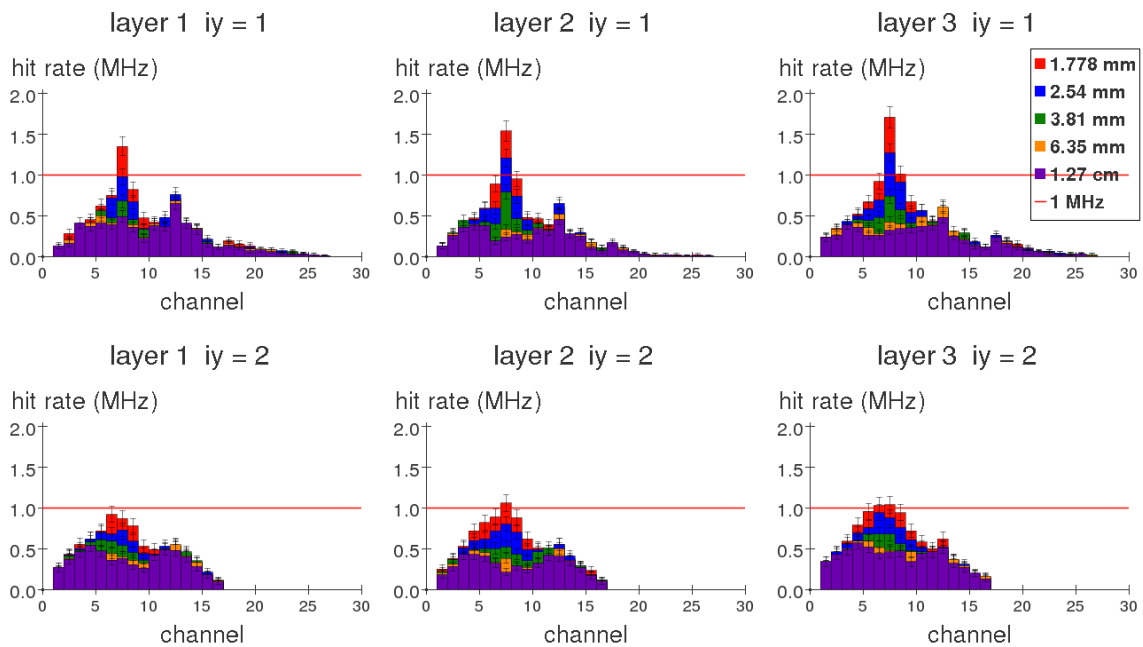


FIG. A.14: Background rates on each channel for various heights of the sheet-of-flame window. Most of values of the heights used for this test were chosen because they are simple fractions of the height of the vacuum box.

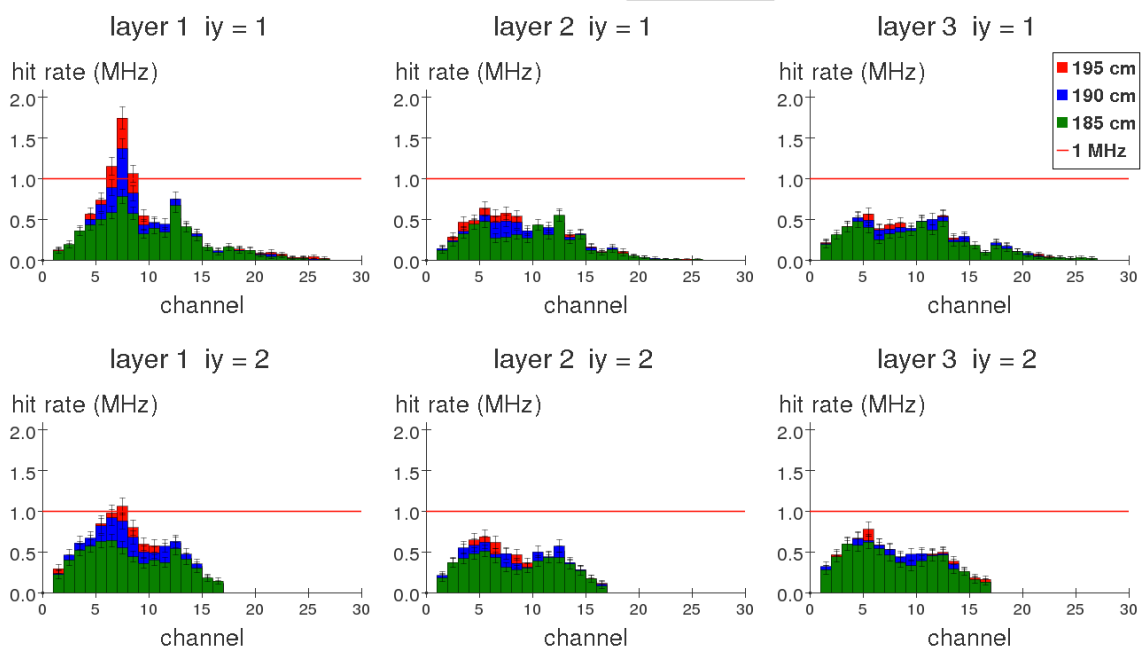


FIG. A.15: Background rates on each channel for various positions of the upstream end of the sheet-of-flame window.

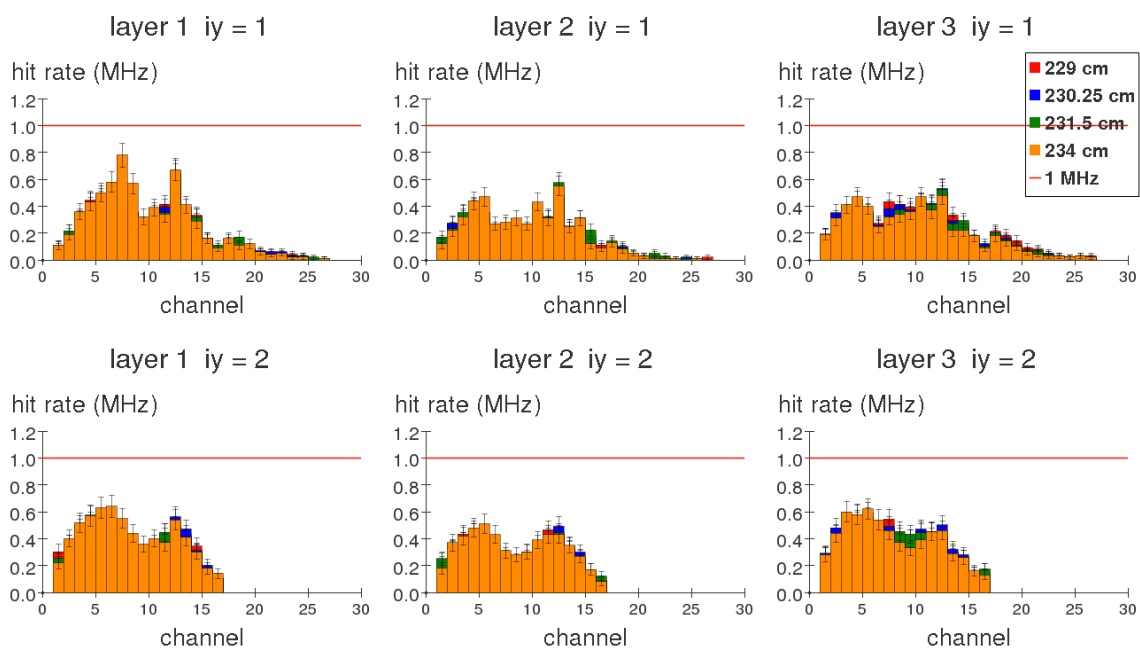


FIG. A.16: Background rates on each channel for various positions of the downstream end of the sheet-of-flame window.



### A.6.3 Inner Tungsten Shield

In order to minimize the cost of material costs for the inner tungsten shields, they should be as small as possible without significantly increasing the background. Since the far right channels exceed 1 MHz without this shielding, the width of the plates must extend far enough to cover them. The position of the downstream end in  $z$  corresponds to the back face of the backsplash shield. This leaves us with 2 remaining variables to optimize: the downstream position in  $z$  (which determines the length) and the thickness.

As the shields are made thinner, we find that the background rates increase significantly for the far right scintillators in all layers, as is shown in Figure A.17. Therefore, we will keep these shields' thicknesses at 19.05 mm. Beginning the shields any further downstream increases background rates. The optimum position for the upstream end of the inner tungsten shield is 190 cm downstream from the target, as shown in Figure A.18.

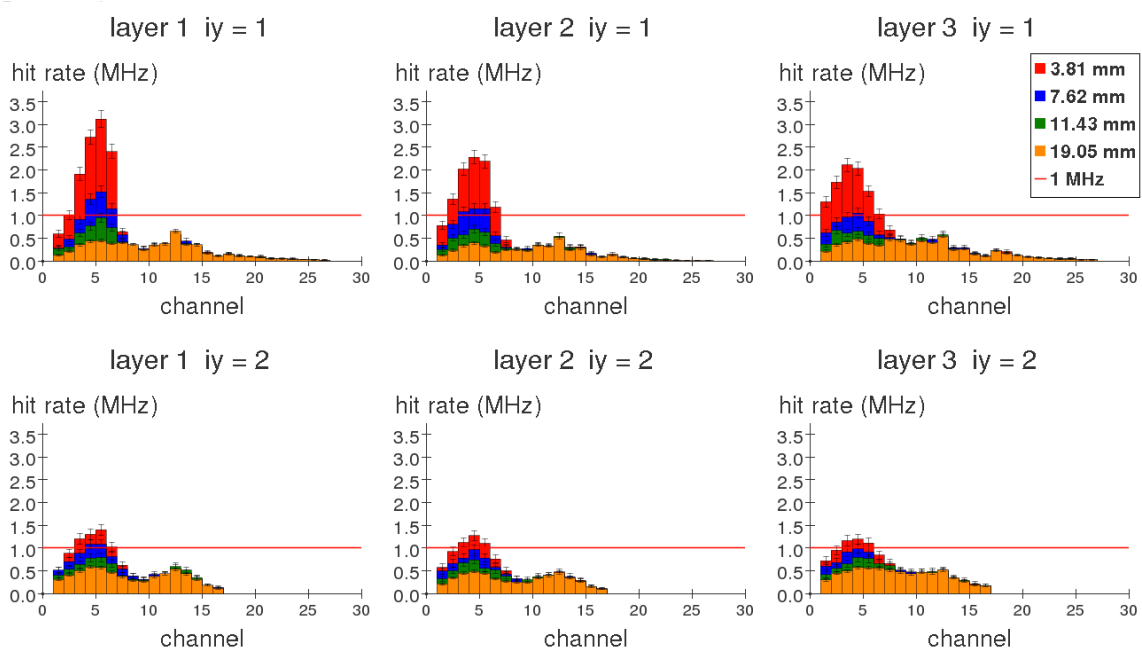


FIG. A.17: Background rates on each channel for various thicknesses of the inner tungsten shields.

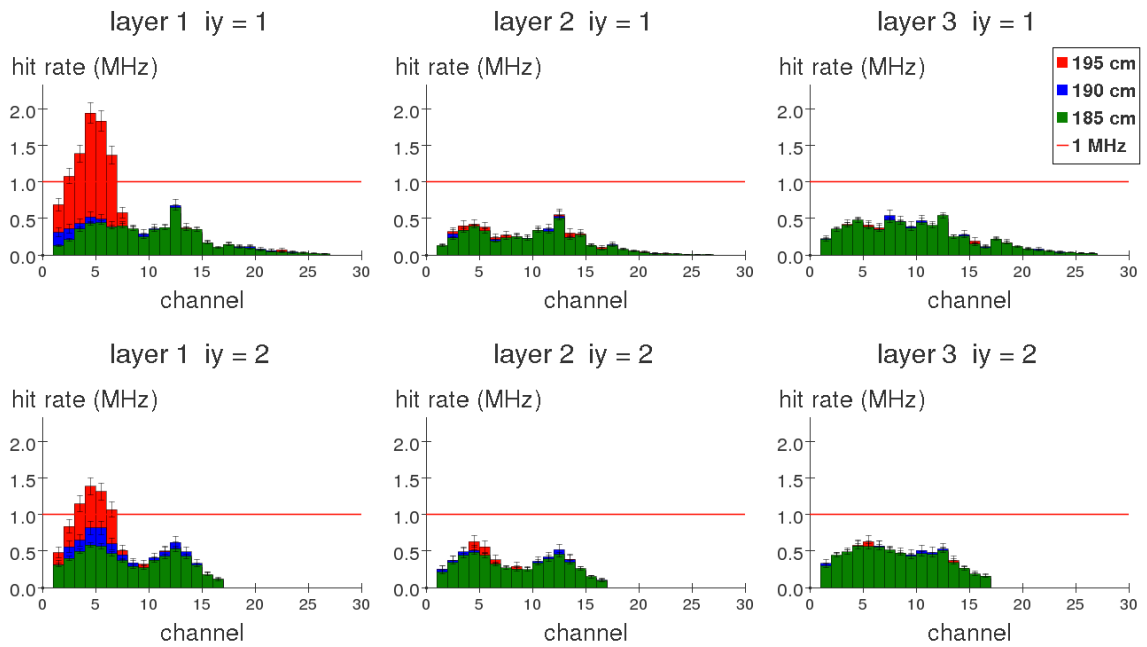


FIG. A.18: Background rates on each channel for various starting positions of the inner tungsten shield. Note that the beam-right scintillators in the first layer are the ones most heavily affected by these changes.

### A.6.4 Tungsten Backsplash Shield

Similar to the inner tungsten shields, the backsplash shields should be as small as possible without significantly increasing background rates. Some of the parameters can be chosen based on qualitative reasoning. For instance, the right edge of the backsplash shield should be aligned with the right edge of the scintillators, because without it, the background rates are too high. The bottom edge of the top shield (top edge of the bottom shield) should rest on top (below) the vacuum box, and the back face of the shield should be just downstream of the last scintillator layer's backboard. Since these positions are already predetermined, we have 3 variables to optimize: width, height and thickness. The optimum height of these shields is 15 cm (see Figure A.19). Above that, the background rates on some channels reaches excessive levels. Their thickness should be 2 cm, (see Figure A.20) and they should be 90 cm wide in order to provide the best protection against backsplash (See Figure A.21).

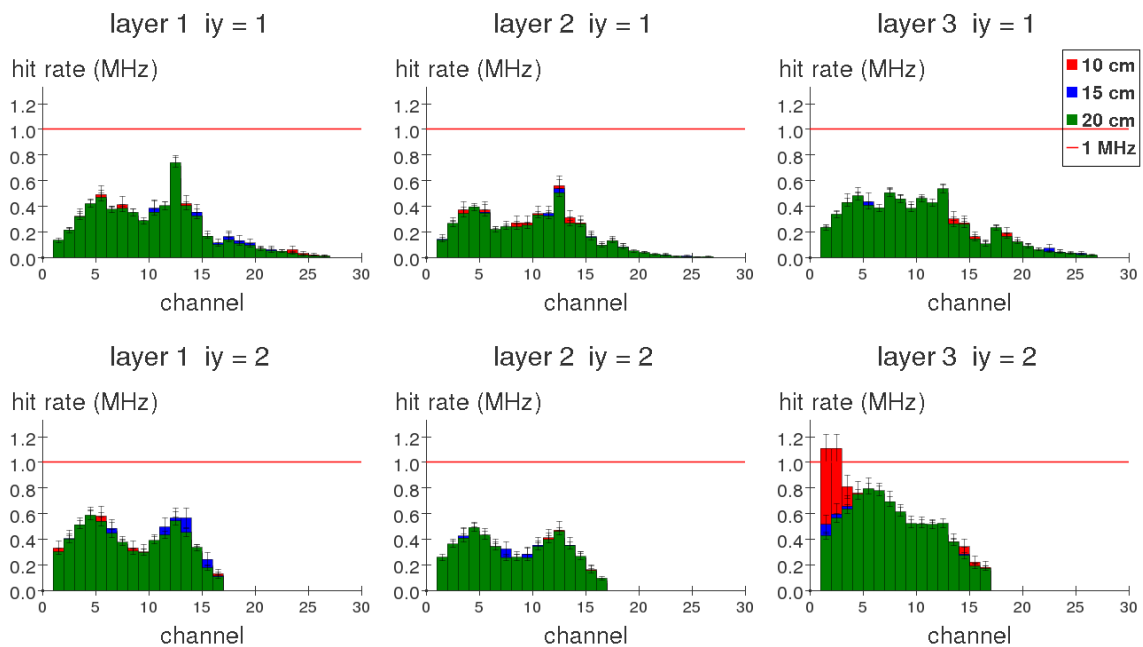


FIG. A.19: Background rates on each channel for various backslash shield heights.

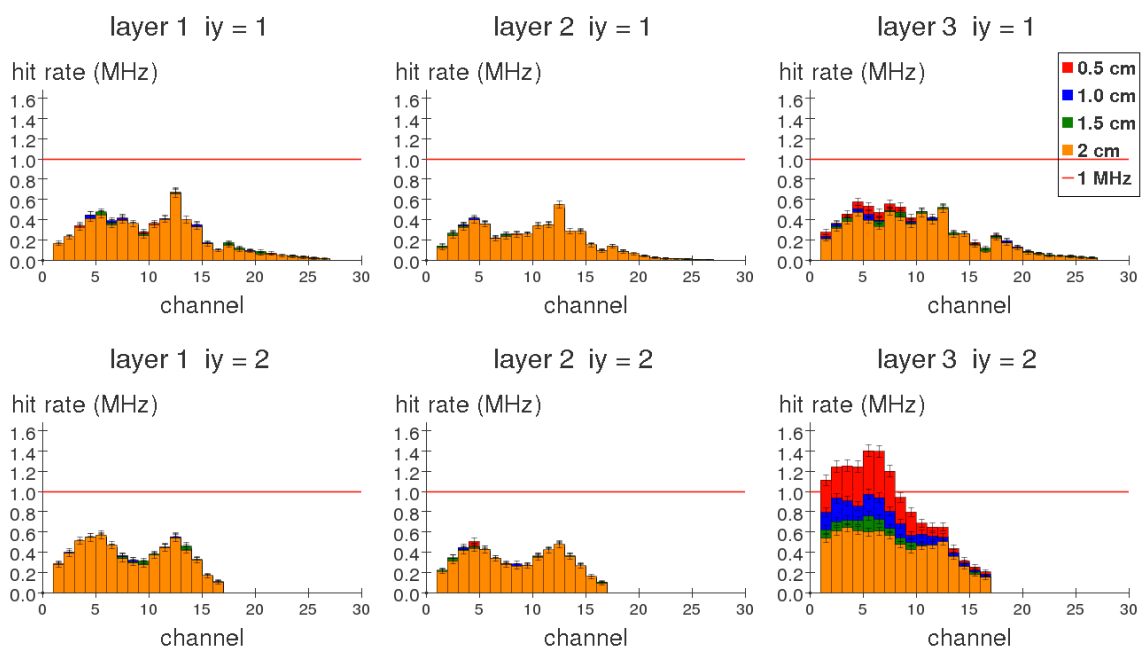


FIG. A.20: Background rates on each channel for various backslash shield thicknesses.

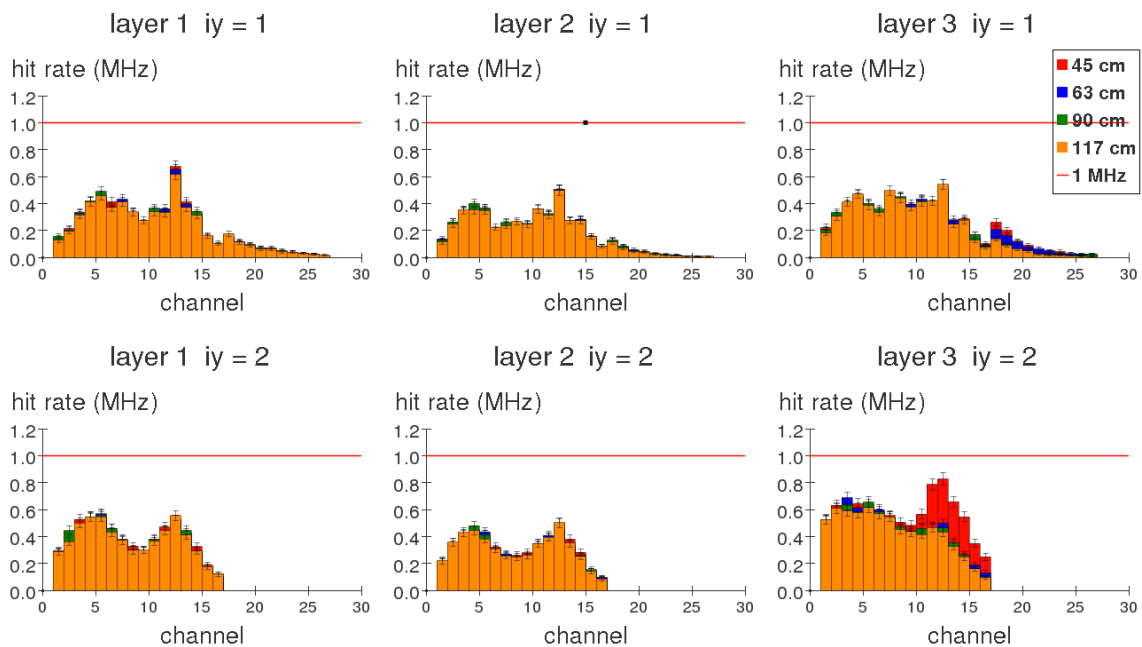


FIG. A.21: Background rates on each channel for various backplash shield widths.

### A.6.5 Scintillator Thickness

The results of the simulations shown up until now in this section have used 3 cm thick scintillators, which takes up all of the space between the absorbers. This is not acceptable, since this does not allow space for a backboard, nor for the readout fibers of the scintillators on the scintillators in the rows closest to the vacuum box. In Figure A.22 we compare the beam backgrounds with 1cm thick scintillators and a 1.5 MeV cutoff on the energy deposited, versus with 3 cm thick scintillators with a 4.5 MeV energy cutoff. The reason for the difference in energy cuts is because muons deposit energy proportional to the thickness of the scintillators. It is clear that the difference in the signal-to-noise levels for the 1 cm and 3 cm cases is very minimal, and therefore, we will use the 1 cm thick scintillators.

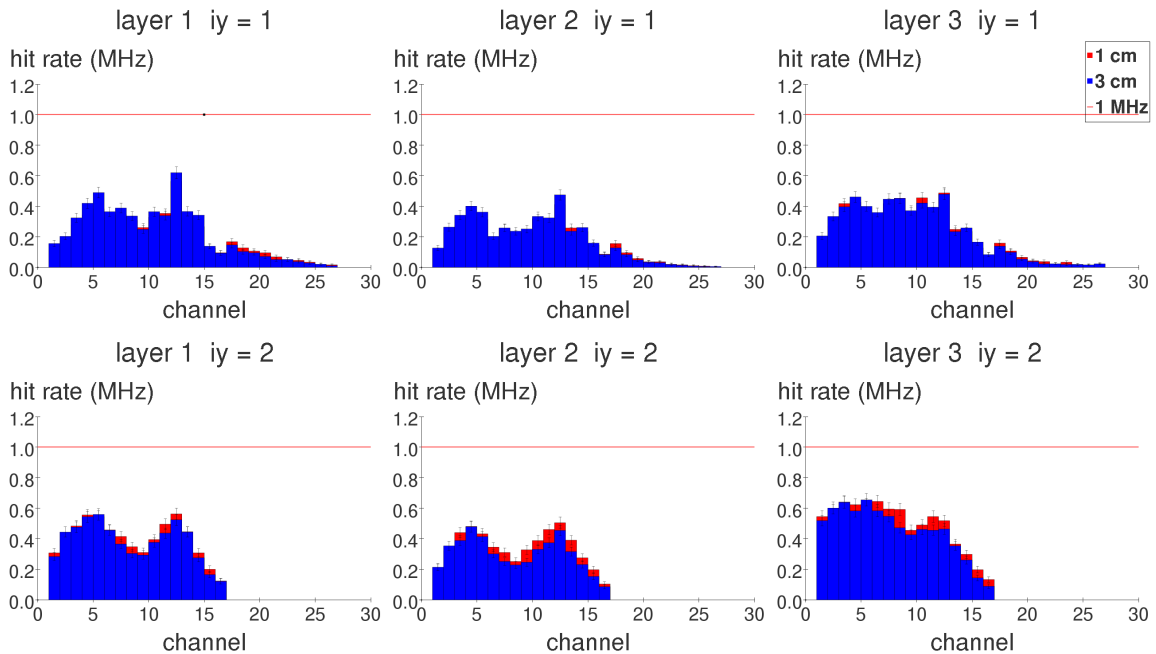


FIG. A.22: Comparison of background rates on each channel with 3 cm and 1 cm thick scintillators.



## APPENDIX B

# Optimization of Resonance-Search Cuts in the 2016 HPS Dataset

Ideally, event selection cuts in a resonance search should maximize the signal significance,  $\kappa = \frac{N_S}{\sqrt{N_S+N_B}}$ , where  $N_S$  and  $N_B$  are the number of events that pass a particular cut in a “signal-like” sample and a “background-like” sample. For the WAB and Bethe-Heitler reduction cuts, I used Monte-Carlo simulations, with simulated radiative tridents as the signal-like sample and a properly-normalized combined WABs and tridents simulation as a “signal+background”-like sample.

For the track-cluster matching cuts and the accidental reduction cuts, I used several schemes to select “signal-like” and “background-like” samples from the data, in order to optimize the cuts on each variable using another variable as a selector. Since the “signal-like” sample contains a few background events, I used the following alternative method to determine what cutoff values to use, rather than  $\frac{N_S}{\sqrt{N_S+N_B}}$ . For these cuts, I plot the spectra for the variable being cut for both the signal-like and background-like samples, and made the cut at the point where the density of

background-like events begins to exceed the density of signal-like events.

All of the  $e^+e^-$  samples used in this study have the following preliminary cuts applied to them:

- Pair 1 trigger is fired.
- One of the clusters is on top half of Ecal and the other is on the bottom half.
- All event flags are good.
- The track fit has  $\chi^2 < 100$  for both tracks (this is just a loose preliminary cut).

In addition, unless otherwise noted, whenever fine-tuning any cut in this appendix, I apply all of the previously fine-tuned cuts to both the signal-like and background-like  $e^+e^-$  samples used.

## B.1 Track-Cluster Matching

The first cut to be optimized was the geometric track-cluster matching parameter<sup>1</sup>  $n_\sigma$ . I chose the “signal-like” sample to be  $e^+e^-$  events where both tracks are within 2 ns of their respective cluster<sup>2</sup>, and the “background-like” sample to be those where either of the two tracks is more than 5 ns of its respective cluster (Figure B.1). Figure B.2 shows the  $n_\sigma$  spectrum for the signal-like and background-like samples.

---

<sup>1</sup>This is defined in Equation 2.2 in terms of the displacement between the cluster position and the extrapolated position of the track at the Ecal.

<sup>2</sup>after subtracting the 55 ns offset from the cluster time.

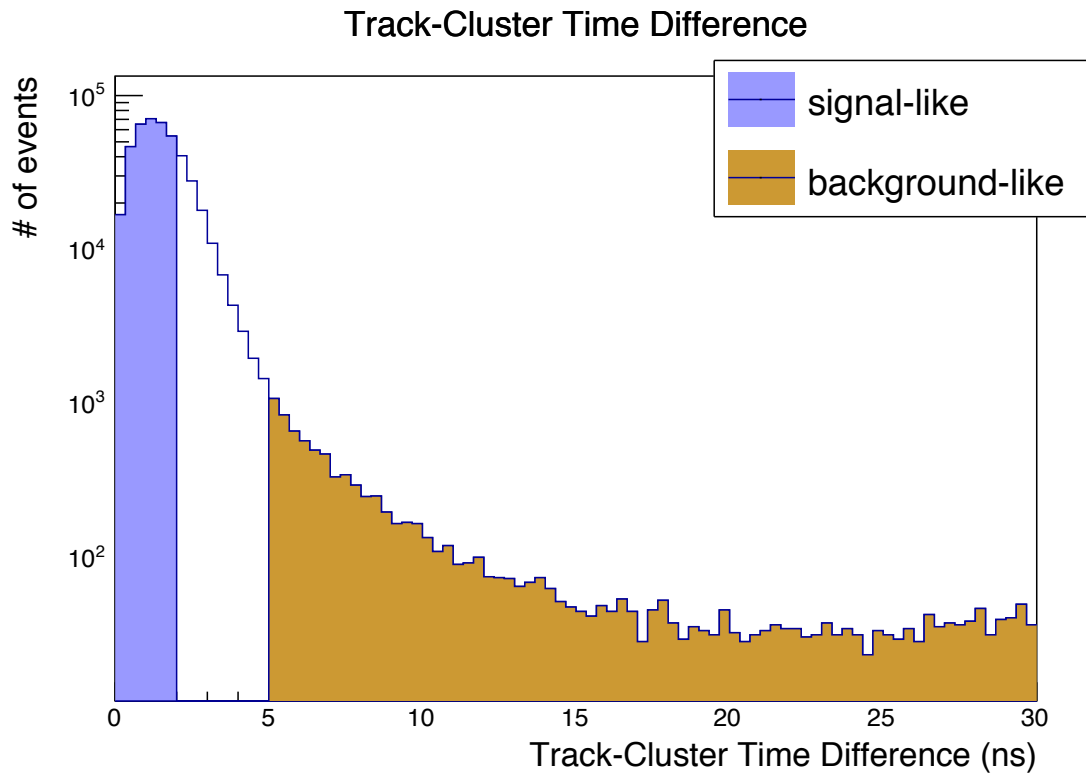


FIG. B.1: Time difference between clusters and tracks for “signal-like” (blue) and “background-like” (brown) events for fine-tuning the cut on  $n_\sigma$  in the track-cluster matching. The  $x$  axis represents the larger of the two track-cluster time differences for the two paired particles in the event.

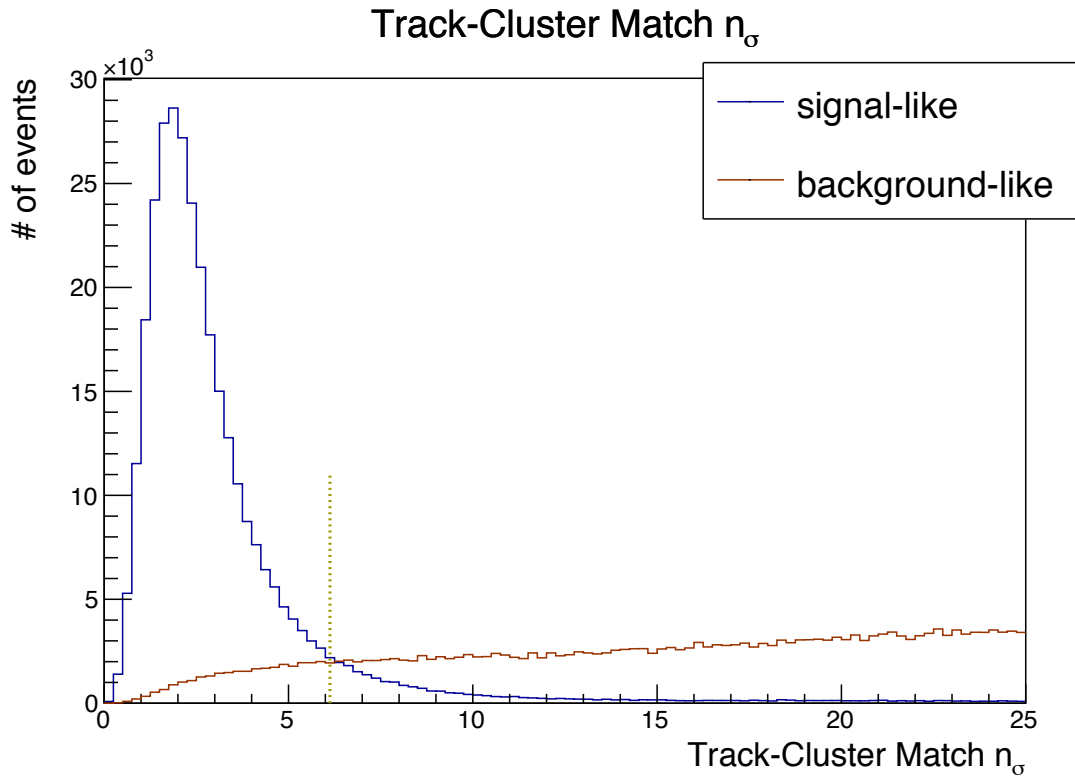


FIG. B.2:  $n_\sigma$  spectra for “signal-like” (blue) and “background-like” (brown) events. On the  $x$  axis is the larger of the two  $n_\sigma$  values for the two particles. Signal-like events (where both track times are within 2 ns of their respective clusters) tend to have  $n_\sigma$  less than 6, whereas background-like events (where at least one particle has track-cluster time difference greater than 5) tend to much larger  $n_\sigma$  values. The golden vertical dashed line represents the optimal cut in  $n_\sigma$ , beyond which the rate of background-like events exceeds that of signal-like events.

When optimizing the track-cluster time difference, I used  $e^+e^-$  events where the  $n_\sigma$  values for both particles are  $< 3$  for the “signal-like” sample, and those where at the  $n_\sigma$  value for at least one particle is  $> 7$  as the “background-like” sample (Figure B.3). The track-cluster time difference spectrum of both samples is shown in Figure B.4.

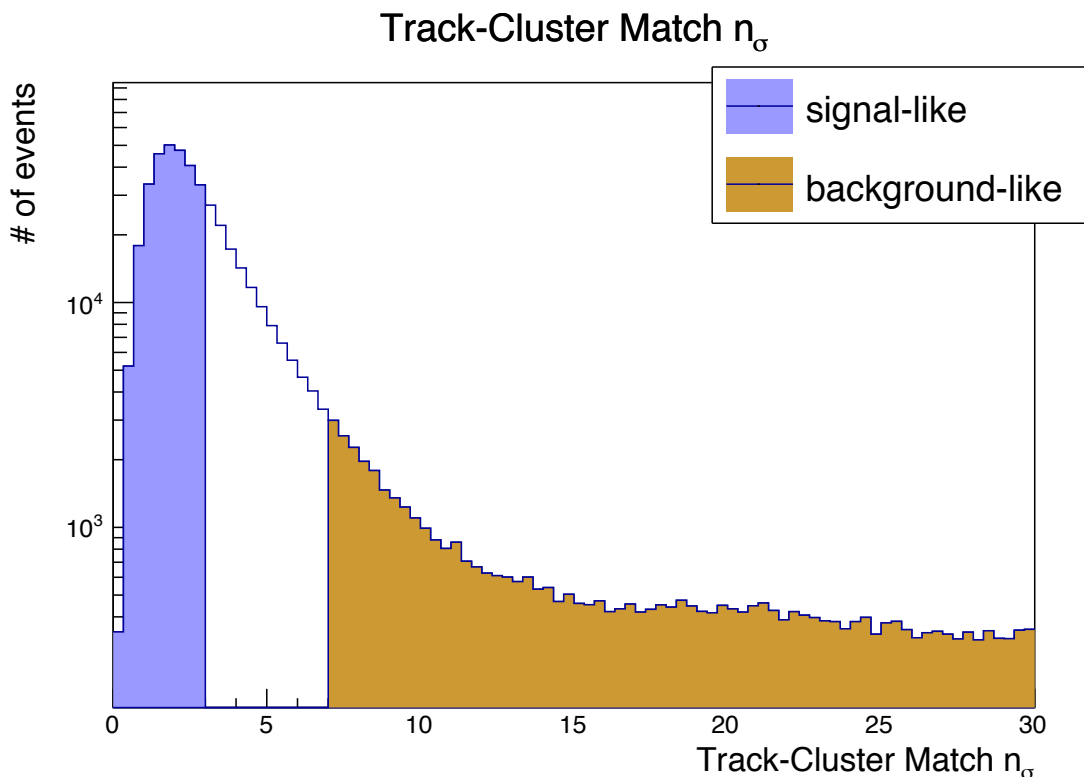


FIG. B.3:  $n_\sigma$  values for “signal-like” (blue) and “background-like” (brown) events for fine-tuning the track-cluster time difference cut. The background-like events are defined to be in the tail end of the spectrum, with large  $n_\sigma$  (i.e., the track extrapolates further away from the cluster), whereas the signal-like events are defined to be near the peak (ie, the track extrapolates near the cluster).

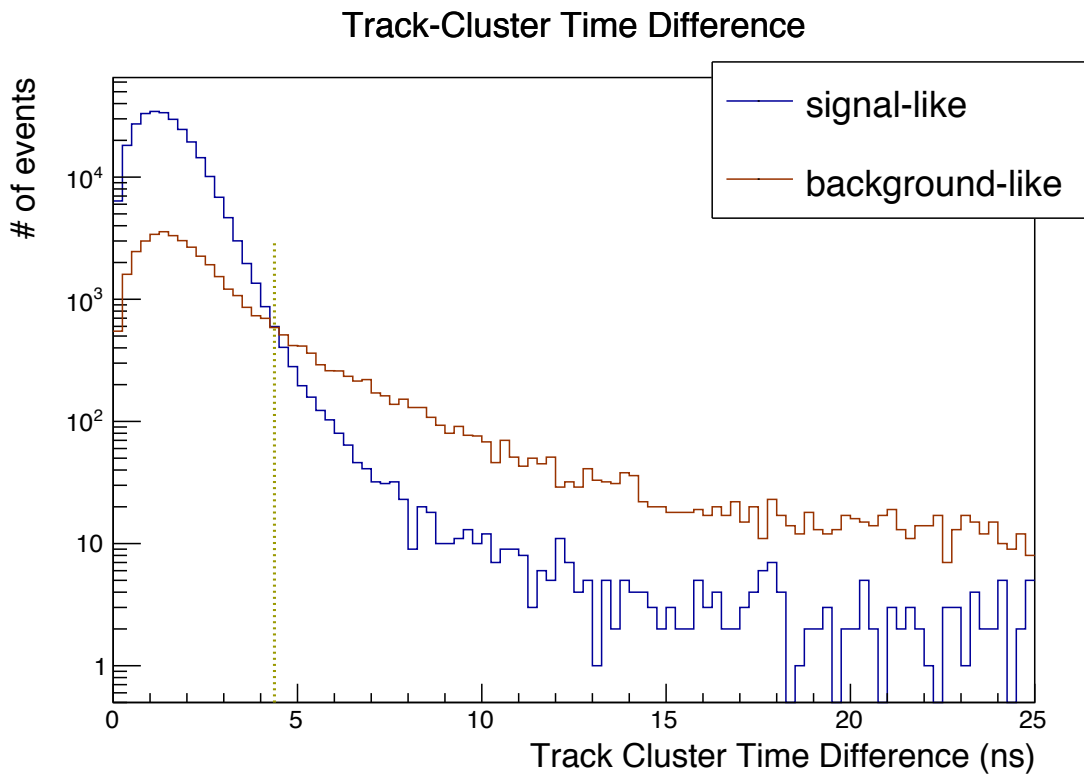


FIG. B.4: Track-cluster time difference spectra for “signal-like” (blue) and “background-like” (brown) events. The variable plotted on the  $x$  axis is the maximum of the track-cluster time differences between the two particles. These spectra for signal-like events and background-like events both peak near 1 ns, but background-like events drop off slower than the signal-like events at larger time differences.

## B.2 Accidental Reduction

The cuts to remove accidentals are optimized using time-coincidence. The cluster time difference spectrum (Figure B.5) clearly shows a region dominated by signal events (near 0), and the rest of the spectrum ( $\delta t \gtrsim 3$  ns) is dominated by accidental coincidences. In this case, I choose a “background” sample consisting of events where the cluster time difference is greater than 3 ns and a “signal” sample consisting of events where the difference is less than 1 ns. The track-cluster matching cuts in the previous section have already been applied to these events, as well as the loose preliminary track fit  $\chi^2 < 100$  cut.

The cuts optimized using these samples are

- maximum electron momentum  $p_e$  cut: removes events where an elastically scattered electron is mismatched with a positron.
- maximum total momentum  $p_{\text{tot}}$  cut: removes events that are inconsistent with the total energy in the reaction (including that of the usually-undetected recoil electron) being equal to the beam energy.

Both of these cuts are optimized using the  $\frac{S-B}{\sqrt{S}}$  metric after making cuts on the variables that precede them (including the track-cluster matching cuts). The cuts obtained from this optimization are  $p_e < 1.76$  GeV and  $p_{\text{tot}} < 2.90$  GeV. The signal-like and background-like spectra for  $p_e$  are shown in Figure B.6, and the corresponding plots for  $p_{\text{tot}}$  are shown in Figure B.7.

To further reduce accidentals between particles from different beam buckets, a cut is made on the time difference between the clusters at 2 ns, equal to the time separation between beam buckets.

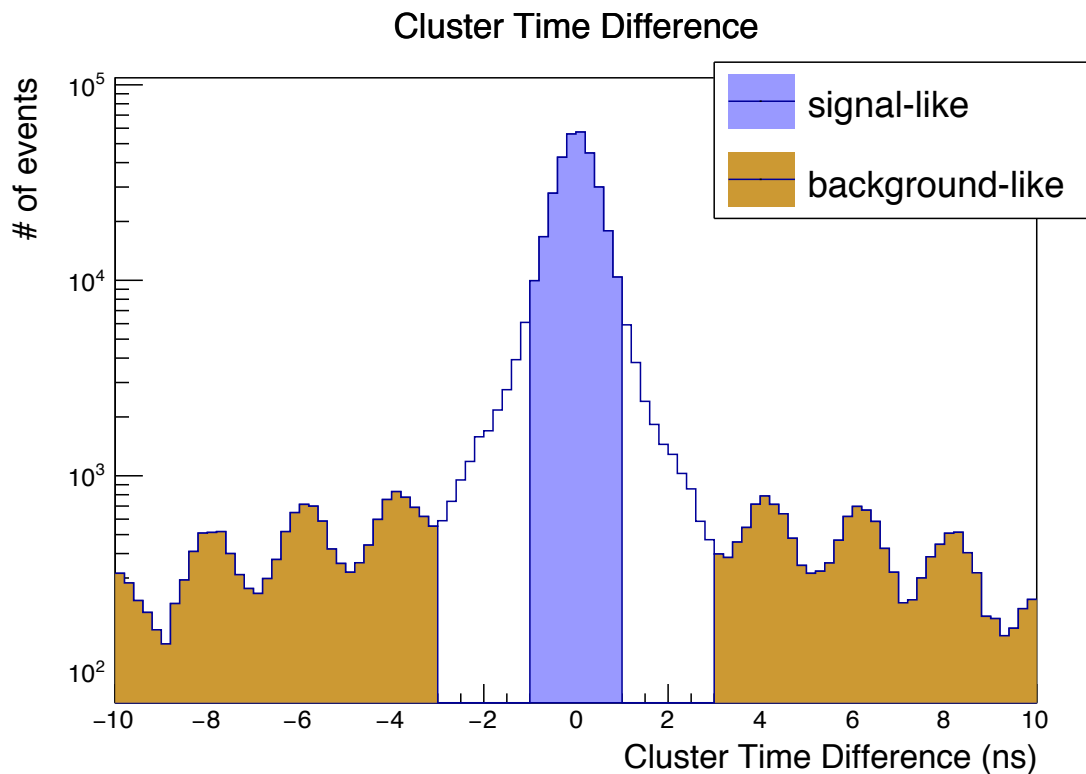


FIG. B.5: Cluster-time difference spectra for “signal-like” (blue) and “background-like” (brown) events for fine-tuning the accidental-reduction cuts. The signal-like sample consists of events where the paired particles are from the same beam bucket, whereas the background-like sample consists of accidental coincidences from different beam buckets.



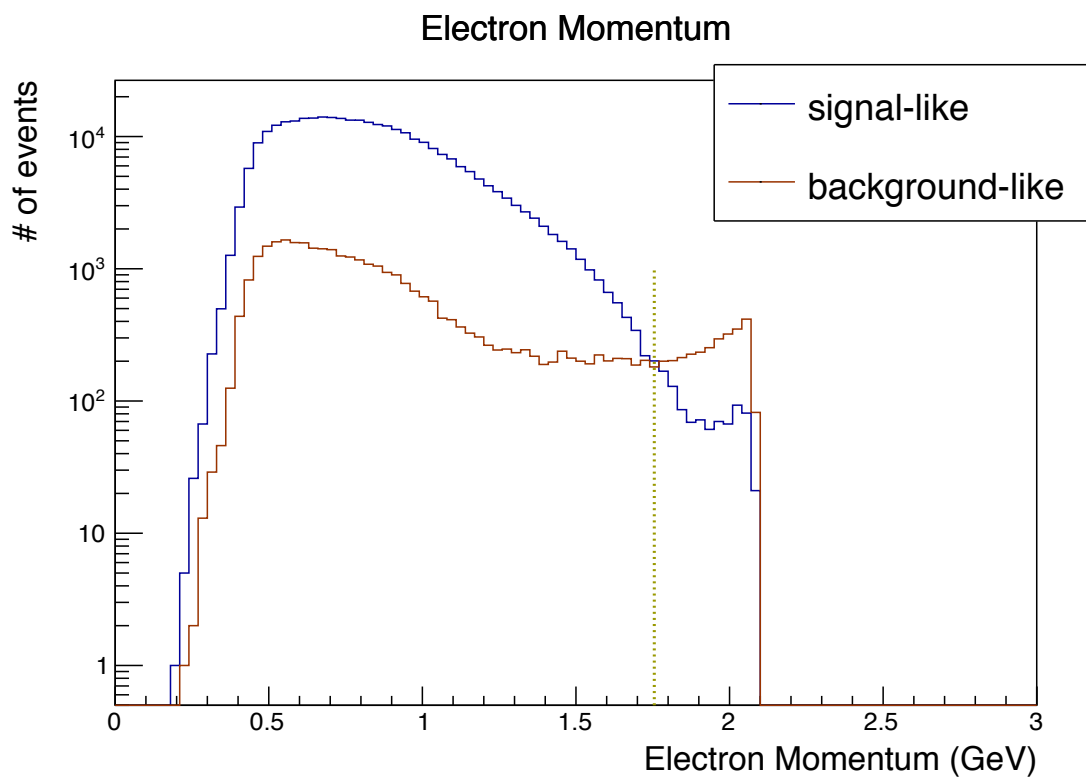


FIG. B.6: Electron momentum spectra for background-like (brown) and signal-like (blue) events. The high momentum region ( $> 1.76$  GeV) is dominated by background-like events.

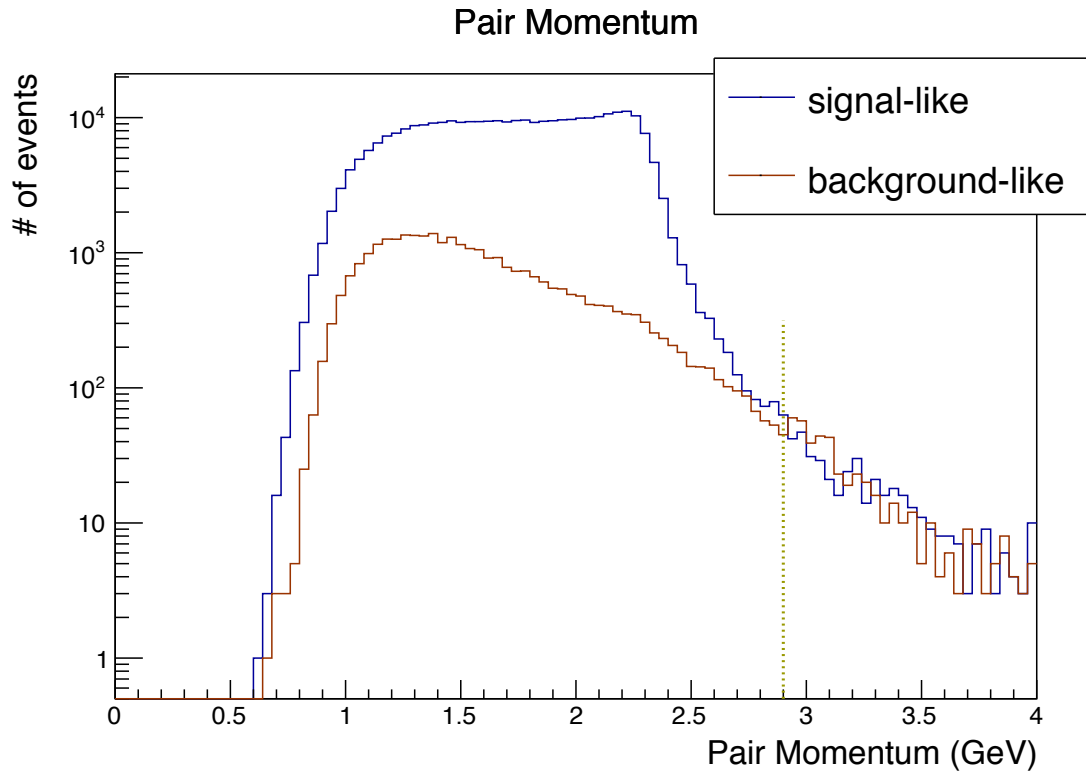


FIG. B.7: Total momentum spectra for background-like (brown) and signal-like (blue) events. Beyond  $\sim 2.7$  GeV, the rates of background-like events are approximately equal to those of signal-like events. Events with electron momentum beyond the 1.76 GeV cut have already been removed from both the signal-like and background-like event samples.

### B.3 Track $\chi^2$

The track  $\chi^2$  cut removes tracks in which one of the hits is a noise or ghost hit or the particle was scattered at a relatively large angle in one of the SVT layers. In either case, the mass resolution of events with large track  $\chi^2$ s is much worse than for events with small track  $\chi^2$ s. To optimize the cuts on track  $\chi^2$ , I took a sample of Møller pairs, using the following criteria:

- all event quality flags are good.
- track time difference  $< 3$  ns.
- both electrons' momenta  $< 1.75$  GeV.
- exactly one of the tracks is matched to a cluster ( $n_\sigma < 6.1$ , track-cluster time difference  $< 4.4$  ns), while the other track is not matched to any cluster ( $n_\sigma > 20$ )
- the cluster is on the electron side ( $x < 0$  mm) of the Ecal.
- tracks are on opposite halves of the detector.

Figure B.8 (top) shows the invariant mass of the Møller pairs in this sample compared to  $\chi_{\max}^2$ , which is the maximum of the two tracks'  $\chi^2$  values. From this I calculated the full width at half max ( $m_{\text{FWHM}}$ ) and peak value  $m_{\text{peak}}$  of the mass for the Møller pairs in the sample for which  $\chi_{\max}^2$  is below the 95% quantile. I chose the cut value  $\chi_{\text{cut}}^2$  which maximizes  $N_S/\sqrt{N_S + N_B}$  where  $N_S$  and  $N_S + N_B$  are the number of events in the signal-like and background-like samples. The signal-like sample is defined by:

$$|m - m_{\text{peak}}| < \frac{m_{\text{FWHM}}}{2} \tag{B.1}$$

$$\chi_{\max}^2 < \chi_{\text{cut}}^2$$

and the background-like sample is defined by

$$\chi_{\max}^2 < \chi_{\text{cut}}^2. \quad (\text{B.2})$$

The optimum cut I found in this analysis was  $\chi_{\text{trk}}^2 < 70$ .

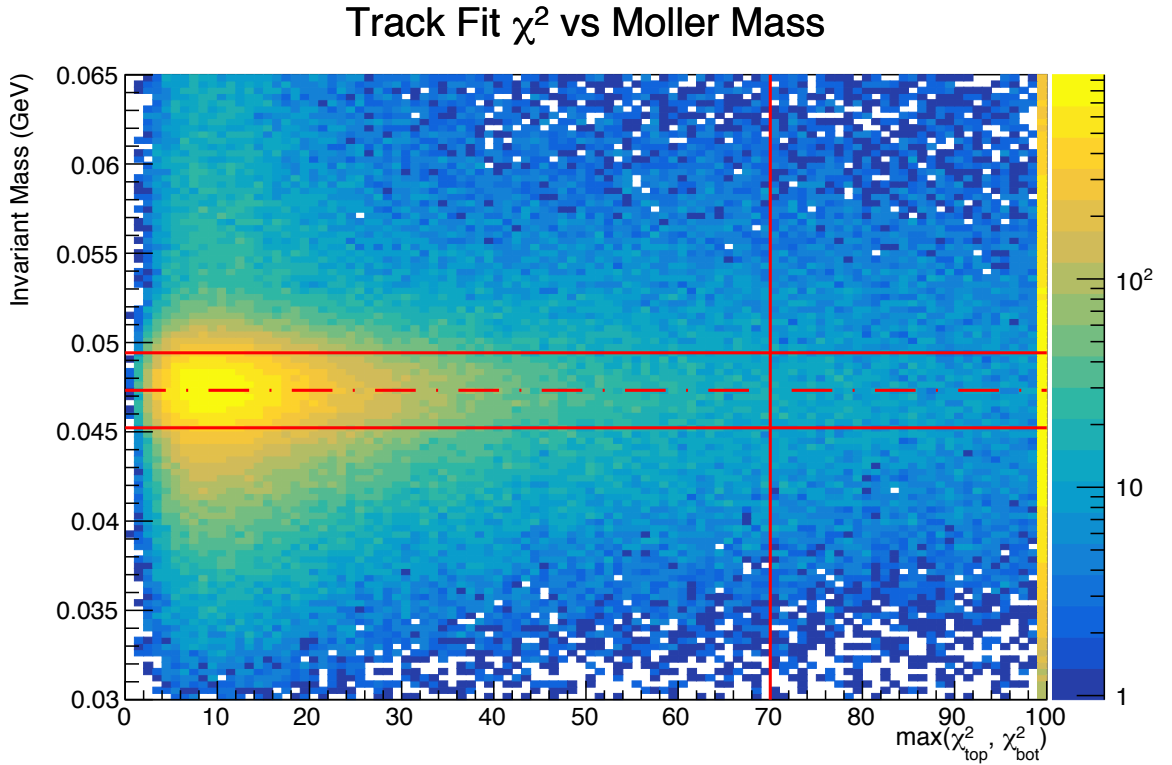


FIG. B.8: Track fit  $\chi^2$  vs Møller invariant masses. The “signal” region is defined to be between the horizontal red lines (at  $m_{\text{peak}} \pm \frac{m_{\text{FWHM}}}{2}$ ). The dashed red line indicates  $m_{\text{peak}}$ . The vertical line indicates the cut determined by the analysis. A large fraction of the events where the fit  $\chi^2$  for both tracks is low have invariant pair masses in the  $m_{\text{peak}} \pm \frac{m_{\text{FWHM}}}{2}$  range (between the solid red lines). If at least one of the tracks has a large  $\chi^2$ , then there is a smaller probability of the invariant mass being in that range.

## B.4 WAB and Bethe-Heitler Reductions

The two cuts to reduce the contribution of converted WABs in the  $e^+e^-$  sample require that the positron track has a hit in the first layer, and extrapolates back to the target. The former removes events where the photon converts either in the first SVT layer (but it doesn't deposit enough energy to record a hit) or in the second layer (but the conversion takes place early enough that a hit is recorded in the second layer). Figure B.9 shows the number of events with and without an SVT Layer 1 hit in the positron track for data, and simulations, after making all of the cuts optimized in the previous sections of this appendix. It is clear that requiring the Layer 1 hit for the positron improves the significance (in this case  $\frac{N_{\text{trident}}}{\sqrt{N_{\text{trident}}+N_{\text{WAB}}}}$ ).

Figure B.10 shows the spectrum of the distances of closest approach ( $d_0$ ) of the positron tracks to the target in data and simulations. Since the resolution in the data is much worse than in the simulation (owing to poor preliminary alignments), it would be inappropriate to optimize this variable using the simulations alone. Therefore instead I set the cut on  $d_0$  by fitting the core of the spectrum from the data to a gaussian and then took the mean plus 2 sigma, which is 1.0 mm.

Finally, the reduction of Bethe-Heitler events is performed by setting a lower-bound cut on  $p_{\text{tot}}$  that maximizes  $\frac{N_{\text{rad}}}{\sqrt{N_{\text{tridents}}+N_{\text{WAB}}}}$ . Figure B.11 shows the cross sections as a function of  $p_{\text{tot}}$  in data and in radiative trident, total trident and WAB simulations. The value of the  $p_{\text{tot}}$  cut that optimizes  $\frac{N_{\text{rad}}}{\sqrt{N_{\text{tridents}}+N_{\text{WAB}}}}$  is 1.51 GeV.

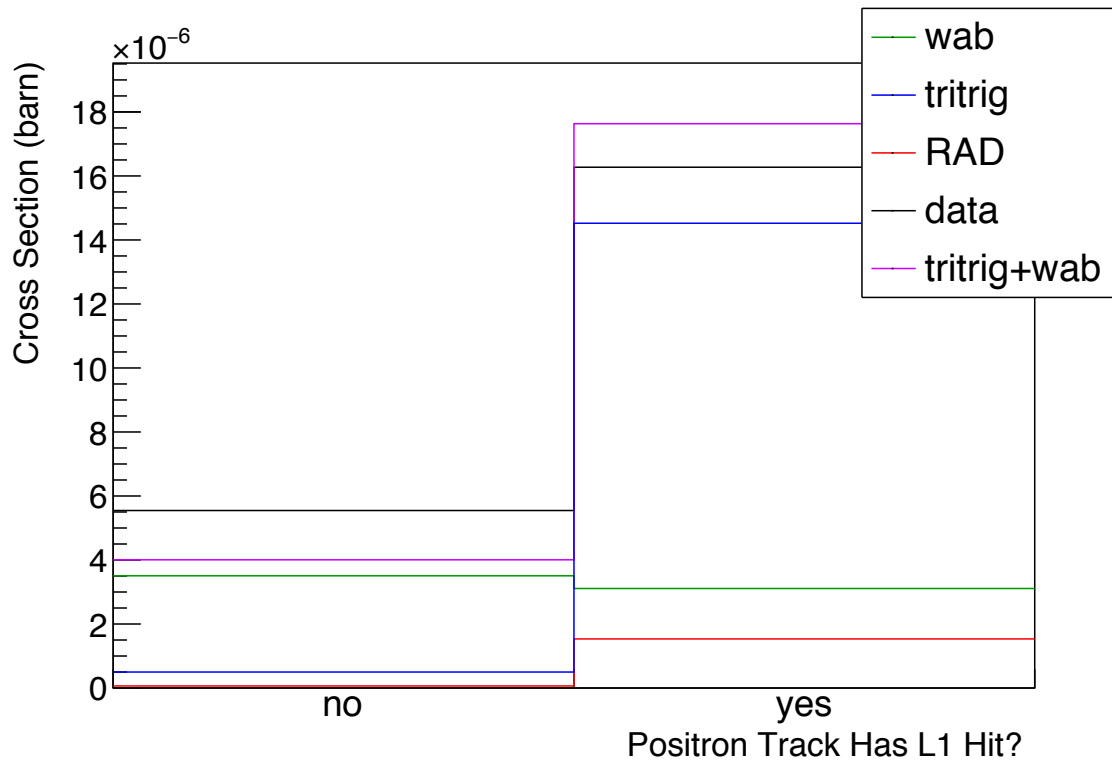


FIG. B.9: Comparison of the cross sections of events with/without SVT Layer 1 (L1) hits in data and Monte Carlo simulations. Data from run 7796 are shown in black. Requiring a hit in L1 has only a small impact on the acceptance of tridents (blue) but greatly reduces the number of WABs (green).

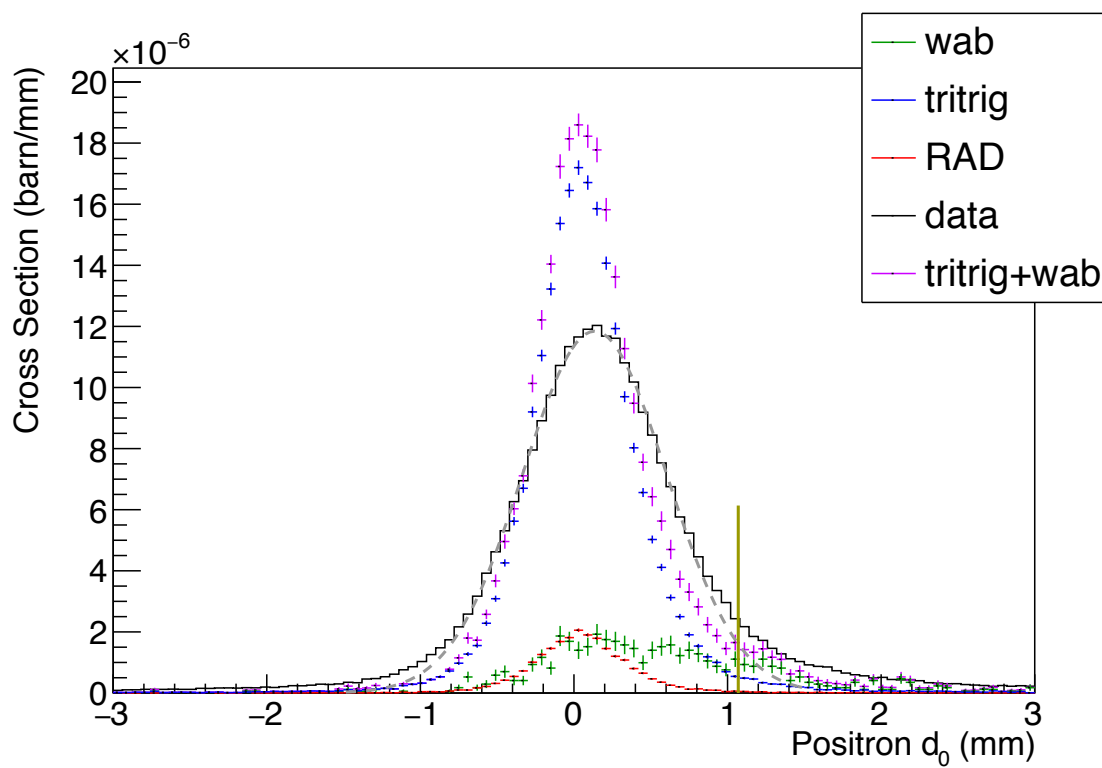


FIG. B.10: Comparison of positron track's distance of closest approach in data and Monte Carlo. The core of the distribution from data (black) is fit to a gaussian (grey dashed). The cut to reduce the WAB contribution is then  $\mu + 2\sigma = 1.07$  mm (vertical golden line).

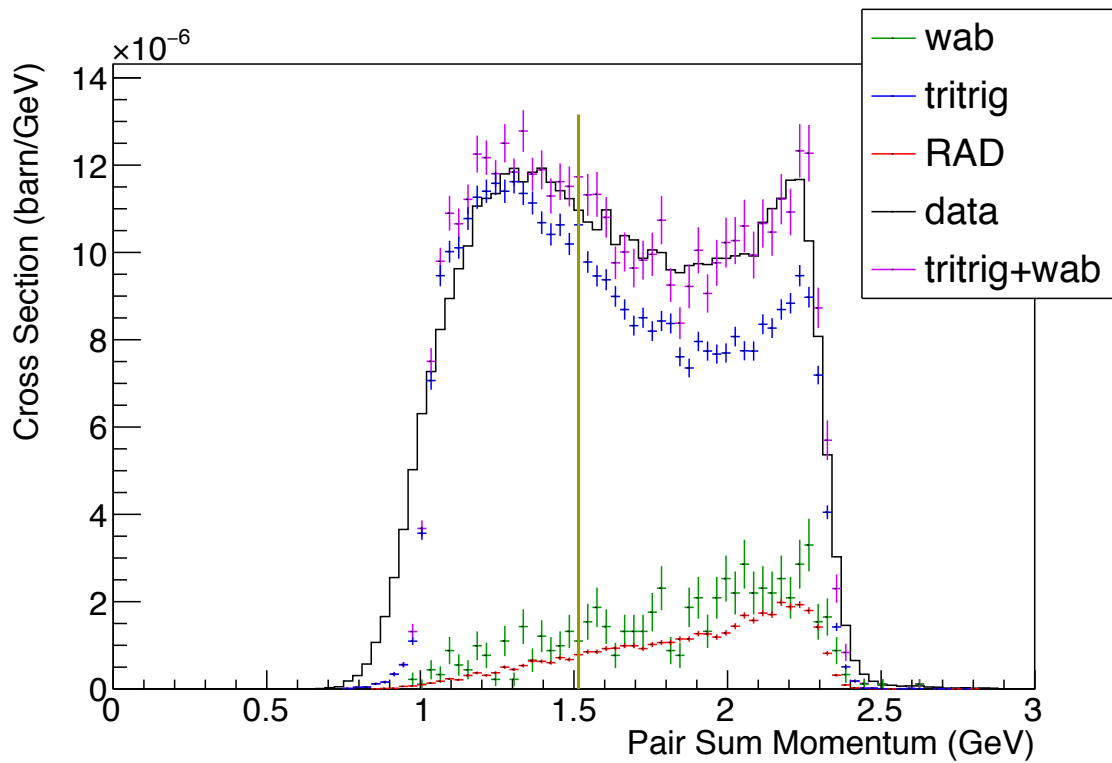


FIG. B.11: Comparison of  $e^+e^-$  pair sum momenta in data and Monte Carlo. Data from run 7796 are shown in black. The optimal cut, which maximizing  $\frac{N_{\text{rad}}}{\sqrt{N_{\text{tridents}} + N_{\text{WAB}}}}$ , is at 1.51 GeV, (vertical golden line).



# APPENDIX C

## List of Abbreviations

***A'*** Dark photon. A hypothesized elementary particle, which HPS is searching for.

Also known as a “heavy photon”.

**ADC** Analog to Digital Converter.

**APD** Avalanche Photo Diode. A device converting photon signals in the Ecal crystals into electrical signals via photoelectric effect.

**CEBAF** Continuous Electron Beam Accelerator Facility. The accelerator at Jefferson Lab.

**cl** Shorthand for “cluster”.

**CLAS** CEBAF Large-Acceptance Spectrometer. The primary detector system in Hall B of Jefferson Lab.

**CLAS-12** Upgraded version of CLAS to accommodate a 12 GeV beam, which is twice the maximum beam energy used in CLAS experiments prior to the upgrade.

**DAQ** Data Acquisition. System responsible for online recording data and storing it in files.

**DM** Dark Matter. A type of unseen material that is believed to account for the missing mass in galaxies.

**dof** Degrees of Freedom. Number of data points minus the number of fit parameters.

**Ecal** Electromagnetic Calorimeter. One of the two main detector components of HPS.

**extrap** Shorthand for “extrapolated”, as in, the extrapolated position of a track to the Ecal face.

$\epsilon^2$  Square of the coupling between the dark photon and the Standard Model photon. The ratio of the  $A'$  production cross-section to that of radiative tridents in HPS is proportional to  $\epsilon^2$ .

**FADC** Flash Analog to Digital Converter. A type of electronic board that converts analog signals to digital signals.

**FEE** Full-Energy Electrons. Collective term for elastically scattered electrons, and electrons from any other reaction where the energy loss is much smaller than the resolution of HPS.

**FSD** Fast Shutdown. A system to quickly shut down the CEBAF beam during unusual beam conditions.

**GBL** Generalized Broken Lines. An algorithm for fitting tracks to a set of helix segments, allowing for small kinks at the connection points due to multiple scattering [49].

**Geant4** A toolkit for the simulation of the passage of particles through matter [54–56].

**GTP** General-Trigger Processor. One of the types of electronic boards in the trigger system.

**HEP** High-Energy Physics.

**HPS** Heavy Photon Search. An experiment at Jefferson Lab which searches for dark photons (otherwise known as  $A'$ , or heavy photons).

**JLab** The Thomas Jefferson National Accelerator Laboratory. Also known as Jefferson Lab.

**L1 ... L6** Layer 1 ... Layer 6 (of the SVT)

**LCSIM** Linear Collider Simulator. A Java-based framework for event simulation, reconstruction and analysis originally developed for the Linear Collider Detector at SLAC, but is used in other HEP experiments, such as HPS.

$n_\sigma$  A metric for determining the goodness of track-cluster matching, using the displacement between the extrapolated position of the track at the Ecal and the cluster position, normalized for resolution. This is parameterized in Equation 2.2.

**PAC** Physics-Acceptable Conditions. Runtime of an experiment is typically measured in PAC days, that is, the equivalent amount of time that the experiment would have to run continuously, sans setup time and beam trips, in order to acquire the same amount of data.

**Pair 0** Loose trigger on paired clusters in the Ecal, used for calibrations.

**Pair 1** Tight trigger on paired clusters in the Ecal. This is the primary trigger used in HPS.

**PC** Power Constraint. A technique for clipping off downward fluctuations in the spectrum of upper limits on signal yields (or coupling) in a resonance search [77].

**PMT** Photomultiplier Tube. A device that is used for converting photon signals into electrical signals.

**PS** Pair Spectrometer [magnet]. The main magnet for curving electron and positron tracks, so that their momenta can be calculated using their curvatures.

**QED** Quantum Electrodynamics. A field theory describing the interactions of charged particles and the photon.

**rad** Shorthand for “radiative tridents”, a type of background event in HPS.

**RF** Radio Frequency.

**Single 0** Loose trigger on a single cluster in the Ecal, used for calibrations.

**Single 1** Tight trigger on a single cluster on the Ecal, used for calibrations.

**SLAC** Stanford Linear Accelerator. One of several institutions collaborating in the HPS experiment.

**SLIC** Simulator for the Linear Collider. A simulator package for particles passing through detector systems, using the Geant4 toolkit.

**SM** Standard Model. An effective field theory developed in the 1970s describing 17 types of elementary particles (6 types of leptons, 6 types of quarks, 4 gauge bosons and 1 Higgs) and their interactions.

**SSP** Subsystem Processor. One of the electronic boards in the trigger system.

**SVT** Silicon Vertex Tracker. One of the two main detector components of HPS.

**TI** Trigger Interface. One of the electronic boards in the trigger system.

**tritrig** Trident-Trigger [event generator]. A trident event generator in Monte Carlo with cuts to include only events with kinematics that might cause a trigger.

**trk** Shorthand for “track”.

**WAB** Wide-Angle Bremsstrahlung. Reactions where a photon is produced via bremsstrahlung at a large enough angle that it is within our detector acceptance ( $\theta \gtrsim 15$  mrad).

**wbt** WAB + beam + tridents. Monte Carlo configuration in which background from WABs, beam interaction and tridents within the trigger window are added to the simulated event.

## BIBLIOGRAPHY

- [1] J. Alwall, R. Frederix, S. Frixione, V. Hirschi, F. Maltoni, O. Mattelaer, H. S. Shao, T. Stelzer, P. Torrielli, and M. Zaro, *JHEP* **07**, 079 (2014), 1405.0301.
- [2] G. Aad et al. (ATLAS), *Phys. Lett.* **B716**, 1 (2012), 1207.7214.
- [3] S. Chatrchyan et al. (CMS), *Phys. Lett.* **B716**, 30 (2012), 1207.7235.
- [4] F. Zwicky, *Helv. Phys. Acta* **6**, 110 (1933), [*Gen. Rel. Grav.*41,207(2009)].
- [5] V. C. Rubin, N. Thonnard, and W. K. Ford, Jr., *Astrophys. J.* **238**, 471 (1980).
- [6] F. Iocco, M. Pato, and G. Bertone, *Nature Phys.* **11**, 245?248 (2015), 1502.03821.
- [7] D. Clowe, M. Bradac, A. H. Gonzalez, M. Markevitch, S. W. Randall, C. Jones, and D. Zaritsky, *Astrophys. J.* **648**, L109 (2006), astro-ph/0608407.
- [8] J. Alexander et al. (2016), 1608.08632, URL <http://inspirehep.net/record/1484628/files/arXiv:1608.08632.pdf>.
- [9] R. Essig, A. Manalaysay, J. Mardon, P. Sorensen, and T. Volansky, *Phys. Rev. Lett.* **109**, 021301 (2012), 1206.2644.
- [10] R. Adam et al. (Planck), *Astron. Astrophys.* **594**, A1 (2016), 1502.01582.
- [11] J. D. Bjorken, R. Essig, P. Schuster, and N. Toro, *Phys. Rev.* **D80**, 075018 (2009), 0906.0580.

- [12] B. Holdom, Phys. Lett. **166B**, 196 (1986).
- [13] D. H. Weinberg, J. S. Bullock, F. Governato, R. Kuzio de Naray, and A. H. G. Peter, Proc. Nat. Acad. Sci. **112**, 12249 (2014), [Proc. Nat. Acad. Sci.112,2249(2015)], 1306.0913.
- [14] R. Corliss (DarkLight), Nucl. Instrum. Meth. **A865**, 125 (2017).
- [15] B. Echenard (BaBar), Nucl. Part. Phys. Proc. **273-275**, 2427 (2016).
- [16] J. P. Lees et al. (BaBar), Phys. Rev. Lett. **119**, 131804 (2017), 1702.03327.
- [17] R. Aaij et al. (LHCb) (2017), 1710.02867.
- [18] P. Ilten, J. Thaler, M. Williams, and W. Xue, Phys. Rev. **D92**, 115017 (2015), 1509.06765.
- [19] P. Ilten, Y. Soreq, J. Thaler, M. Williams, and W. Xue, Phys. Rev. Lett. **116**, 251803 (2016), 1603.08926.
- [20] R. Aaij, B. Adeva, M. Adinolfi, Z. Ajaltouni, S. Akar, J. Albrecht, F. Alessio, M. Alexander, A. Alfonso Albero, S. Ali, et al. (LHCb Collaboration), Phys. Rev. Lett. **120**, 061801 (2018), URL <https://link.aps.org/doi/10.1103/PhysRevLett.120.061801>.
- [21] L. S. Barabash et al., Instrum. Exp. Tech. **46**, 300 (2003), [Prib. Tekh. Eksp.46,no.3,20(2003)].
- [22] J. Blumlein et al., Z. Phys. **C51**, 341 (1991).
- [23] J. Blmlein and J. Brunner, Phys. Lett. **B731**, 320 (2014), 1311.3870.

- [24] J. D. Bjorken, S. Ecklund, W. R. Nelson, A. Abashian, C. Church, B. Lu, L. W. Mo, T. A. Nunamaker, and P. Rassmann, Phys. Rev. **D38**, 3375 (1988).
- [25] E. M. Riordan et al., Phys. Rev. Lett. **59**, 755 (1987).
- [26] E. Izaguirre, G. Krnjaic, P. Schuster, and N. Toro, Phys. Rev. **D88**, 114015 (2013), 1307.6554.
- [27] M. Battaglieri et al. (BDX) (2017), 1712.01518.
- [28] P. Coloma, B. A. Dobrescu, C. Frugiuele, and R. Harnik, JHEP **04**, 047 (2016), 1512.03852.
- [29] A. Bross, M. Crisler, S. H. Pordes, J. Volk, S. Errede, and J. Wrbanek, Phys. Rev. Lett. **67**, 2942 (1991).
- [30] B. Batell, R. Essig, and Z. Surujon, Phys. Rev. Lett. **113**, 171802 (2014), 1406.2698.
- [31] J. R. Batley et al. (NA48/2), Phys. Lett. **B746**, 178 (2015), 1504.00607.
- [32] H. Merkel et al., Phys. Rev. Lett. **112**, 221802 (2014), 1404.5502.
- [33] H. Merkel et al. (A1), Phys. Rev. Lett. **106**, 251802 (2011), 1101.4091.
- [34] S. Abrahamyan et al. (APEX), Phys. Rev. Lett. **107**, 191804 (2011), 1108.2750.
- [35] R. Essig, P. Schuster, N. Toro, and B. Wojtsekhowski, JHEP **02**, 009 (2011), 1001.2557.
- [36] D. Babusci et al. (KLOE-2), Phys. Lett. **B720**, 111 (2013), 1210.3927.
- [37] A. Palladino (KLOE-2), Nucl. Part. Phys. Proc. **273-275**, 608 (2016).



- [38] D. Babusci et al. (KLOE-2), Phys. Lett. **B736**, 459 (2014), 1404.7772.
- [39] A. Anastasi et al. (KLOE-2), Phys. Lett. **B757**, 356 (2016), 1603.06086.
- [40] F. Curciarello (2015), [Acta Phys. Polon.B46,39(2015)], 1501.04424.
- [41] A. Anastasi et al., Phys. Lett. **B750**, 633 (2015), 1509.00740.
- [42] Y. Yamaguchi (PHENIX), Nucl. Phys. **A956**, 882 (2016).
- [43] Y. Yamaguchi, PoS **DIS2015**, 129 (2015).
- [44] R. Holzmann and M. Gumberidze (HADES), in *Proceedings, 20th International Conference on Particles and Nuclei (PANIC 14): Hamburg, Germany, August 24-29, 2014* (2014), pp. 382–385, URL <http://inspirehep.net/record/1375612/files/9.pdf>.
- [45] M. Pospelov, Phys. Rev. **D80**, 095002 (2009), 0811.1030.
- [46] I. Balossino et al. (HPS), Nucl. Instrum. Meth. **A854**, 89 (2017), 1610.04319.
- [47] N. A. Graf and J. McCormick, in *Proceedings, 2012 IEEE Nuclear Science Symposium and Medical Imaging Conference (NSS/MIC 2012): Anaheim, California, USA, October 29-November 3, 2012* (2012), pp. 1016–1023, URL <http://www-public.slac.stanford.edu/sciDoc/docMeta.aspx?slacPubNumber=SLAC-PUB-15297>.
- [48] M. Diamond and O. Moreno, *The Heavy Photon Search reconstruction pipeline*, HPS Analysis Note (2018), currently in draft form.
- [49] C. Kleinwort, Nucl. Instrum. Meth. **A673**, 107 (2012), 1201.4320.
- [50] G. D. Lafferty (BaBar), Nucl. Part. Phys. Proc. **263-264**, 63 (2015).

- [51] J. Alwall, P. Demin, S. de Visscher, R. Frederix, M. Herquet, F. Maltoni, T. Plehn, D. L. Rainwater, and T. Stelzer, *JHEP* **09**, 028 (2007), 0706.2334.
- [52] H. Hirayama, Y. Namito, A. F. Bielajew, S. J. Wilderman, and W. R. Nelson (2005).
- [53] N. Graf and J. McCormick, *AIP Conf. Proc.* **867**, 503 (2006), [,503(2006)].
- [54] J. Allison, K. Amako, J. Apostolakis, P. Arce, M. Asai, T. Aso, E. Bagli, A. Bagulya, S. Banerjee, G. Barrand, et al., *Nuclear Instruments and Methods in Physics Research Section A: Accelerators, Spectrometers, Detectors and Associated Equipment* **835**, 186 (2016), ISSN 0168-9002, URL <http://www.sciencedirect.com/science/article/pii/S0168900216306957>.
- [55] J. Allison, K. Amako, J. Apostolakis, H. Araujo, P. A. Dubois, M. Asai, G. Barrand, R. Capra, S. Chauvie, R. Chytrcek, et al., *IEEE Transactions on Nuclear Science* **53**, 270 (2006), ISSN 0018-9499.
- [56] S. Agostinelli, J. Allison, K. Amako, J. Apostolakis, H. Araujo, P. Arce, M. Asai, D. Axen, S. Banerjee, G. Barrand, et al., *Nuclear Instruments and Methods in Physics Research Section A: Accelerators, Spectrometers, Detectors and Associated Equipment* **506**, 250 (2003), ISSN 0168-9002, URL <http://www.sciencedirect.com/science/article/pii/S0168900203013688>.
- [57] E. Wolin, D. Abbott, V. Gurjyan, G. Heyes, E. Jastrzembski, D. Lawrence, and C. Timmer, in *Proceedings, 2007 IEEE Nuclear Science Symposium and Medical Imaging Conference (NSS/MIC 2007): Honolulu, Hawaii, October 28-November 3, 2007* (2007), pp. 856–859.
- [58] H. Vance, Ph.D. thesis, Old Dominion University (2017).

- [59] S. Uemura, Ph.D. thesis, Stanford University (2016).
- [60] V. Blobel, *Millepede II - Draft Manual*, Hamburg University (2007), URL [http://www.desy.de/~kleinwrt/MP2/doc/html/draftman\\_page.html](http://www.desy.de/~kleinwrt/MP2/doc/html/draftman_page.html).
- [61] V. Blobel and C. Kleinwort, in *Advanced Statistical Techniques in Particle Physics. Proceedings, Conference, Durham, UK, March 18-22, 2002* (2002), pp. URL-STR(9), hep-ex/0208021, URL <http://www.ipp.dur.ac.uk/Workshops/02/statistics/proceedings//blobel1.pdf>.
- [62] H. De Vries, C. W. De Jager, and C. De Vries, *Atom. Data Nucl. Data Tabl.* **36**, 495 (1987).
- [63] A. Nakada, Y. Torizuka, and Y. Horikawa, *Phys. Rev. Lett.* **27**, 745 (1971), URL <http://link.aps.org/doi/10.1103/PhysRevLett.27.745>.
- [64] H. Crannell, *Phys. Rev.* **148**, 1107 (1966), URL <http://link.aps.org/doi/10.1103/PhysRev.148.1107>.
- [65] E. J. Moniz, I. Sick, R. R. Whitney, J. R. Ficenec, R. D. Kephart, and W. P. Trower, *Phys. Rev. Lett.* **26**, 445 (1971), URL <http://link.aps.org/doi/10.1103/PhysRevLett.26.445>.
- [66] D. Higinbotham, private communication.
- [67] J. J. Kelly, *Phys. Rev.* **C70**, 068202 (2004).
- [68] C. Patrignani et al. (Particle Data Group), *Chin. Phys.* **C40**, 100001 (2016).
- [69] J. Lightbody Jr. and J. O'Connell, *Computers In Physics* pp. 57-64 (1988).
- [70] L. W. Mo and Y.-S. Tsai, *Rev. Mod. Phys.* **41**, 205 (1969).

- [71] I. Wolfram Research, software, URL <https://www.wolfram.com/mathematica/>.
- [72] O. Moreno, Ph.D. thesis, UC Santa Cruz (2016).
- [73] O. Moreno, N. Baltzell, M. Graham, and J. Jaros, *Search for a heavy photon in electro-produced  $e^+e^-$  pairs with the HPS experiment at JLab*, HPS Analysis Note (2018).
- [74] A. Simonyan, Ph.D. thesis, Université Paris-Sud (2017).
- [75] J. E. Gaiser, Ph.D. thesis, SLAC (1982), URL <http://www-public.slac.stanford.edu/sciDoc/docMeta.aspx?slacPubNumber=slac-r-255.html>.
- [76] G. Cowan, K. Cranmer, E. Gross, and O. Vitells, *Eur. Phys. J.* **C71**, 1554 (2011), [Erratum: *Eur. Phys. J.*C73,2501(2013)], 1007.1727.
- [77] G. Cowan, K. Cranmer, E. Gross, and O. Vitells (2011), 1105.3166.
- [78] H. Lamm and Y. Ji, in *6th International Conference on Exotic Atoms and Related Topics (EXA2017) Vienna, Austria, September 11-15, 2017* (2017), 1712.03429, URL <http://inspirehep.net/record/1642451/files/arXiv:1712.03429.pdf>.
- [79] A. Banburski and P. Schuster, *Phys. Rev.* **D86**, 093007 (2012), 1206.3961.

## VITA

### Sebouh Paul

Sebouh Paul was born on October 31, 1987 in Vienna, Virginia. Since his youth he has always been curious about many things related to science and math. He began his formal education in 1993 at Marshall Road Elementary School in Vienna, Virginia, but then transferred to Oakton Elementary in 1998. In 2000, he entered Thoreau Middle School, also in Vienna, VA. In 2002, he entered James Madison High School, also in Vienna VA which he graduated from in 2006. In the same year, he joined Christopher Newport University in Newport News, VA, where he got his Bachelors Degree in Physics in 2010 and then a Masters Degree in Physics and Computer Foundations in 2012. He entered College of William & Mary in Williamsburg, Virginia in the fall of that same year. In 2013 he joined the Heavy Photon Search collaboration. After graduating, Sebouh will begin a research postdoc position at Tel Aviv University.